AWARD NUMBER: W81XWH-12-1-0336

TITLE: Molecular Innovations Toward Theranostics of Aggressive Prostate Cancer

PRINCIPAL INVESTIGATOR: Xiankai Sun, PhD

CONTRACTING ORGANIZATION: University of Texas Southwestern Medical Center at Dallas
Dallas, TX 75390

REPORT DATE: November 2017

TYPE OF REPORT: Final

PREPARED FOR: U.S. Army Medical Research and Materiel Command
Fort Detrick, Maryland 21702-5012

DISTRIBUTION STATEMENT: Approved for Public Release;
Distribution Unlimited

REPORT DOCUMENTATION PAGE

Form Approved
OMB No. 0704-0188

1. REPORT DATE *(DD-MM-YYYY)*
November 2017

2. REPORT TYPE
Final

3. DATES COVERED *(From - To)*
1Sep2012 - 31Aug2017

4. TITLE AND SUBTITLE
Molecular Innovations Toward Theranostics of Aggressive Prostate Cancer

5a. CONTRACT NUMBER

5b. GRANT NUMBER
W81XWH-12-1-0336

5c. PROGRAM ELEMENT NUMBER

6. AUTHOR(S)

Xiankai Sun

Email: Xiankai.Sun@UTSouthwestern.edu

5d. PROJECT NUMBER

5e. TASK NUMBER

5f. WORK UNIT NUMBER

7. PERFORMING ORGANIZATION NAME(S) AND ADDRESS(ES)

University of Texas Southwestern Medical Center
Department of Radiology
2201 Inwood Rd., NE3.120A
Dallas, Texas 75390

8. PERFORMING ORGANIZATION REPORT NUMBER

9. SPONSORING / MONITORING AGENCY NAME(S) AND ADDRESS(ES)
U.S. Army Medical Research and Materiel Command
Fort Detrick, Maryland 21702-5012

10. SPONSOR/MONITOR'S ACRONYM(S)

11. SPONSOR/MONITOR'S REPORT NUMBER(S)

12. DISTRIBUTION / AVAILABILITY STATEMENT

Approved for public release; distribution unlimited

13. SUPPLEMENTARY NOTES
N/A

14. ABSTRACT: In this project, we proposed to develop a new drug delivery vehicle based on dendrimer nanotechnology for personalized medicine. This new class of nanoplatforms contains imaging probe and molecular medicine with a cancer-specific targeting capability which is able to target cancer cells, monitor drug delivery and tumor response to achieve a "see and treat" strategy as a new concept of molecular medicine. Specifically, One partner PI's lab will make dendrimers bearing functional handles to conjugate with chelating agents provided by the initiating PI's lab for PET imaging and therapeutic peptides provided by another partner PI's lab for the treatment of aggressive prostate cancer. Within the funding period, we have designed and synthesized the proposed bifunctional chelator scaffold system, CB-TE2A(^{t}Bu)$_2$-N$_3$ for the further construction of theranostic agents and multi-modality imaging probes for aggressive prostate cancer. In the meanwhile, we have designed a targeted theranostic small molecule drug conjugate (T-SMDC) system, and successfully synthesized a sample compound of T-SMDC, which consists of a PSMA-specific ligand, a PET imaging moiety, and a cytotoxic drug. The resulted T-SMDC retains the PSMA binding affinity and exhibits PSMA-dependent toxicity. Built upon the theranostic platforms and experimental data obtained, two new projects have been proposed and submitted to funding agencies including this prostate cancer research program.

15. SUBJECT TERMS

None listed

16. SECURITY CLASSIFICATION OF:			**17. LIMITATION OF ABSTRACT**	**18. NUMBER OF PAGES**	**19a. NAME OF RESPONSIBLE PERSON** USAMRMC
a. REPORT	**b. ABSTRACT**	**c. THIS PAGE**			**19b. TELEPHONE NUMBER** *(include area code)*
U	U	U	U	92	

Standard Form 298 (Rev. 8-98)
Prescribed by ANSI Std. Z39.18

Table of Contents

Page

Introduction

This project combines the recent advances in prostate cancer (PCa) research from three different labs integrated with a strong interest and dedication to develop a new molecular medicine approach towards the eventual cure of PCa. Like other cancer types, the current available therapeutic regimens for metastatic PCa are not PCa specific. With respect to PCa cells harboring various genetic alterations, the development of small molecular agents targeting these genetic defects to achieve a better therapeutic efficacy is foreseeable. In this project, we propose to develop a new drug delivery vehicle based on dendrimer nanotechnology for personalized medicine. This new class of nanoplatforms contains imaging probe and molecular medicine with a cancer-specific targeting capability which is able to target cancer cells, monitor drug delivery and tumor response to achieve a "see and treat" strategy as a new concept of molecular medicine. This platform system will be flexible to adopt any new cell targeting molecule or any therapeutic agents. Specifically, Dr. Simanek's lab will make dendrimers bearing functional handles to conjugate with chelating agents provided by Dr. Sun's lab for PET imaging and therapeutic peptides provided by Dr. Hsieh's lab for the treatment of aggressive PCa.

Keywords

Prostate cancer, Theranostics, Nanoconjugates, Molecular Imaging

Accomplishments

1. **The proposed dendrimer conjugates were successfully constructed. To serves the purpose of developing prostate cancer theranostics, the conjugates contain specific cell permeation peptides, peptide therapeutic(s) and a bifunctional chelator for PET imaging (Aim 1)**

Task 1: Synthesis and Characterization of Dendrimers - Scaffold Library (Simanek)

For the completion of this task, please see Dr. Simanek's report for details. Briefly, the design and construction of the dendrimer conjugates were accomplished by 1) varying in size from generation 3-7 with a functional alkyne core; 2) installing a chelate for imaging at the alkyne site; 3) Surveying the surface groups for optimal behavior; and 4) incorporating therapeutic peptides for assessment. In the no-cost extension period, we further constructed a targeted dendrimer conjugate using a prostate-specific membrane antigen (PSMA) ligand, 2-[3-(1,3-dicarboxypropyl)ureido] pentanedioic acid (DUPA: Ki = 8 nM) for PCa theranostics.

Task 2. Synthesis and Characterization of CB-TE2A-based Bifunctional Chelator (Sun)

An azide-modified form of CB-TE2A, CB-TE2A(^{t}Bu)$_2$-N$_3$, was synthesized to conjugate with the alkyne-introduced dendrimers *via* the well-established "click chemistry" procedure. Given the in vivo stability of its copper (II) complex, we chose a bicyclo[6.6.2] tetraamine (CB-TE2A: 4,11-bis-(carboxymethyl)-1,4,8,11-tetraazabicyclo [6.6.2] hexadecane) to serve as the ^{64}Cu chelating core for the construction of dendrimer conjugates. The synthetic route to CB-TE2A(^{t}Bu)$_2$-N$_3$ is outlined below.

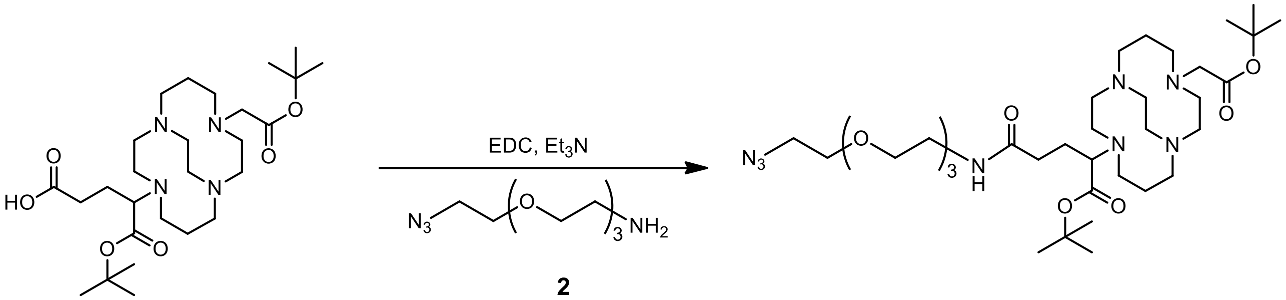

1

2

3

Briefly, to the solution of **1** (0.050 g, 0.095 mmol) in dry acetonitrile (0.5 mL) was added triethyl amine (0.014 g, 0.142 mmol) and 1-ethyl-3-(3-dimethylaminopropyl)carbodiimide hydrochloride (0.027 g, 0.142 mmol). The resulting solution was stirred overnight at room temperature. The solvent was then removed under vacuum to afford the crude product, which was purified by HPLC (Elution time: 22 min) and the resulting fraction lyophilized to give **3** (0.040 g, 0.055 mmol, 58%) as a yellow viscous liquid. ^{1}H NMR (400 MHz, $CDCl_3$): δ 3.73-3.59 (m, 12H), 3.55 (m, 4H), 3.50-3.34 (m, 8H), 3.33-3.04 (m, 12H), 2.97-2.74 (m, 11H), 1.44 (s, 18H). MS (MALDI) *m/z* calcd for $C_{35}H_{66}N_8O_8$: 726.5; found: 727.8 ($[M + H]^+$). Of note, the two internal carboxylate groups are kept protected with t-butyl so as to avoid the chelation of Cu(II), which might be resulted from the Cu(I) catalyst. In total, we provided > 100 mg of Compound **3** to Dr. Simanek's lab for the construction of our proposed dendrimer conjugates.

2. **Potent compounds with screening systems were selected based on specific mechanism(s) of action (Aim 2)**

For the completion of this Aim, please see Dr. Hsieh's Progress Report for details. Briefly, a panel of different prostate cell lines without DAB2IP expression were used for the selection. In addition, a biomarker expression assay and a migration assay were established to detect EMT. The potency of each dendrimer conjugate was determined based on the same molar ratio of therapeutic peptide with the positive control.

3. **Proposed biodistribution, pharmacokinetics, and potential cytotoxicity evaluation experiments were accomplished.**

Task 4: Radiochemistry and in vitro assay of the synthesized theranostic agents (Sun/Hsieh)
Task 5: In vivo and PET/CT imaging evaluation of the synthesized theranostic agents (Sun)
We designed and synthesized the proposed bifunctional chelator scaffold system, CB-TE2A(^{t}Bu)$_2$-N_3 for the further construction of dendrimer-based theranostic agents for aggressive prostate cancer. Specifically, three enantiopure BFC scaffolds for copper radiopharmaceuticals were designed, synthesized and evaluated using a well-validated model ligand (integrin $\alpha_v\beta_3$ ligand). Our work suggests that the chirality of BFC scaffolds plays an insignificant role in integrin $\alpha_v\beta_3$ targeted copper radiopharmaceuticals (Singh et al. *Eur. J. Med. Chem.* **2014**, 80, 308-315). Although this observation does not support our design rationale, the importance of BFC chirality in radiopharmaceutical agents cannot be undervalued without discretion when it is applied to other biological targets. In addition, we have designed a targeted theranostic small molecule drug conjugate (T-SMDC) system, and successfully synthesized a sample compound of T-SMDC, which consists of a PSMA-specific ligand, a PET imaging moiety, and a cytotoxic drug. The resulted T-SMDC retains the PSMA binding affinity and exhibits PSMA-dependent toxicity. When labeled with ^{68}Ga, the T-SMDC is capable of specific imaging PSMA-expressing cancer xenografts in mice. We recognize that the DM1 drug carried by the T-SMDC in the injected dose for PET imaging is low (*ca.* 0.1 nmol) to elicit the desired anti-cancer effects. In

addition to taking advantage of the multi-valent NOTA scaffold for multi-presentation of DM1, we will consider three other approaches in our future work to realize the goal of the theranostic design concept for precision cancer patient care: i) increase the injection dose to the level that specific PSMA binding allows; ii) fractionate a therapeutic dose into multiple imaging doses. The PSMA-mediated internalization mechanism can be exploited for multiple administrations of an imaging dose until the desired DM1 dose is delivered, of which only one ^{68}Ga-NO3A-DM1-Lys-Urea-Glu dose is needed while others are its cold gallium counterpart to avoid unnecessary radiation exposure; iii) have PET imaging with ^{68}Ga-NO3A-DM1-Lys-Urea-Glu only serve the companion purpose for precision chemotherapy of DM1 delivered by the T-SMDC formulated with cold Ga(III). It is noteworthy that the T-SMDC design is versatile in that it can be applied to other targeting systems for developing theranostics of the corresponding diseases.

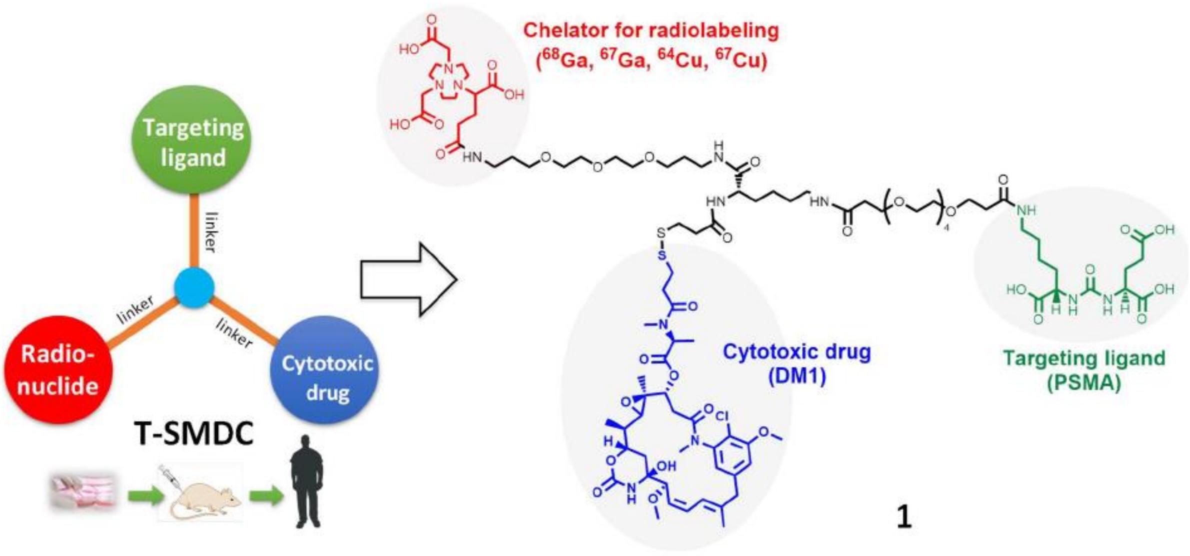

Figure 1. Design of Prostate Specific Membrane Antigen (PSMA) Targeted Theranostic Small-Molecule Drug Conjugate (T-SMDC **1**) (Kumar et al. *Bioconjugate Chemistry* **2016**, 27, 1681-1689).

4. Therapeutic efficacy using various re-clinical models were accomplished (Aim 4)

Task 6: *Preparation of dendrimer conjugates for Aim 4 (Simanek)*
Task 7: Target validation of dendrimer conjugates (Hsieh)
For the completion of these two tasks, please see the reports submitted by Drs. Simanek and Hsieh, respectively, for details.

Task 8: Therapeutc efficacy of dendrimer conjugates (Hsieh/Sun)
Given that the application of ^{68}Ga-NO3A-DM1-Lys-Urea-Glu for anti-tumor therapy might be limited by a big dose gap between the uses of diagnosis and therapy, we developed a pair of ^{18}F/^{19}F-labeled theranostic agents ([$^{18/19}$F]FB-Lys-DM1-Lys-Urea-Glu) with identical chemical and biological properties on the basis of T-SMDC design. The theranostic regime could be formulated by using desired ratios of the paired ^{18}F/^{19}F agents for cancer diagnosis and therapy. The synthetic procedures to make the paired ^{18}F/^{19}F agents are quite different from those of ^{68}Ga-NO3A-DM1-Lys-Urea-Glu because the ^{68}Ga and ^{18}F radiochemistry is essentially different. Similar to ^{68}Ga-NO3A-DM1-Lys-Urea-Glu, the [^{18}F]FB-Lys-DM1-Lys-Urea-Glu specifically

binds to PSMA and displayed a PSMA-mediated internalization in a time dependent manner. The anti-proliferative activity of the new version of T-SMDC showed a strong correlation with the PSMA expression level. Small animal PET imaging with [^{18}F]FB-Lys-DM1-Lys-Urea-Glu demonstrated significantly higher uptake ($p < 0.01$; $n = 3$) in the PSMA positive PC3-PIP tumors (11.2 ± 1.1 % ID/g) at 1 h post-injection than in the PSMA negative PC3-Flu tumors (1.8 ± 0.1% ID/g). These values are significantly higher than those of ^{68}GaNO3A-DM1-Lys-Urea-Glu in PC3-PIP (4.30 ± 0.20%ID/g) and PC3-Flu (1.12 ± 0.42%ID/g) tumors ($p < 0.01$; $n = 3$). The paired $^{18/19}$F agents showed great potential for cancer diagnosis and therapy.

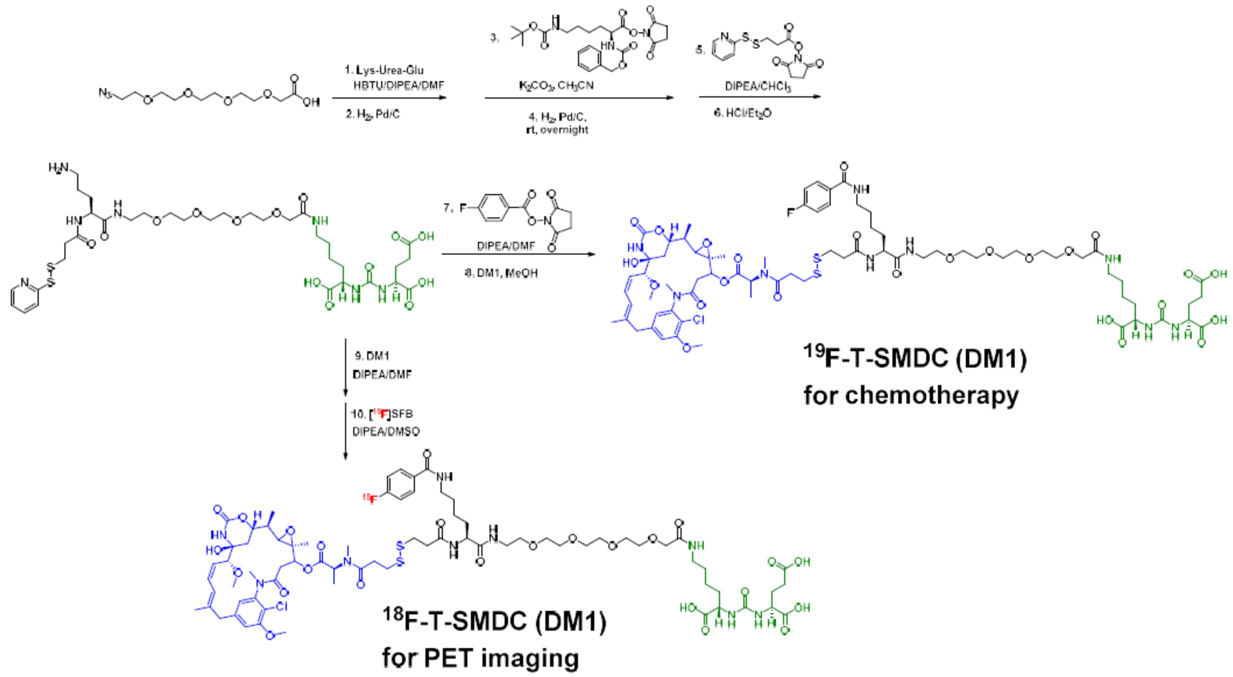

Figure 2. Design and synthesis of an identical pair of ^{18}F/^{19}F PSMA-targeted small-molecule drug conjugates (T-SMDC) for theranostics of prostate cancer.

Therapeutic efficacy studies of ^{18}F/^{19}F-T-SMDC: We performed treatment studies in SCID mice bearing subcutaneous PC3-PIP (PSMA+) tumors to evaluate both imaging and therapeutic performance of T-SMDC (DM1). Based on a reported dose with a DM1-derived SMDC, we firstly intravenously injected 75 nmol ^{19}F-T-SMDC (DM1) in 10 % ethanol solution per mouse for five consecutive days. Starting from day 3, all mice showed a clear trend of tumor size reduction along with rapid body weight loss. Due to the significant toxicity, we terminated this first set of treatment on day 7.

We further reduced the dose to 15 and 40 nmol and adjusted injection schedules to three

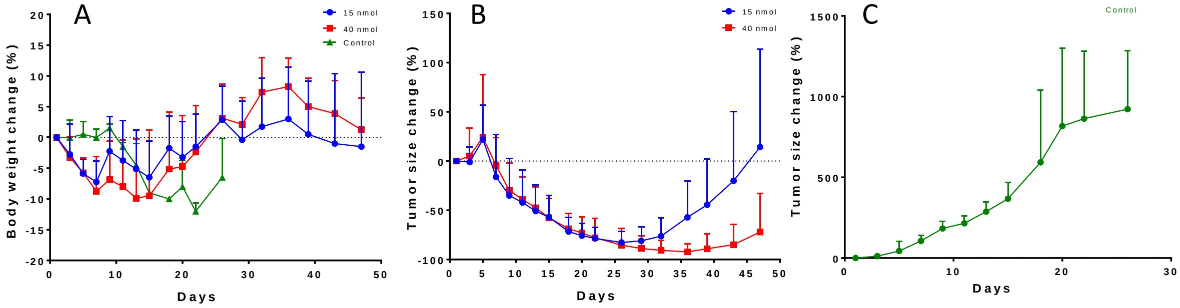

Figure 3. Treatment studies of T-SMDC (DM1) in PC3-PIP (PSMA+) mice. (**A**) Body weigh change; (**B**) Tumor volume change of 15 nmol and 40 nmol groups; (**C**) Tumor volume

times a week for total four injections. Since the aim is to perform concurrent or sequential PET/CT imaging with ^{18}F-T-SMDC (DM1) during treatment with ^{19}F-T-SMDC (DM1), we wanted to ensure no significant therapeutic impact by the trace amount of drug contained in the ^{18}F-T-SMDC (DM1) dose. Therefore, we added 0.075 nmol ^{19}F-T-SMDC (DM1) to the 10% ethanol formulation solution for the control group, which was calculated based on radioactivity (0.15 mCi) and radiotracer specific activity (2,000 mCi/μmol) used for PET/CT imaging. Shown in **Figure 3A**, our adjusted dosing schedule indeed controlled the acute toxicity, with the body weight loss within -15%. The 40 nmol group showed a greater body weight loss than the 15 nmol group, but both groups started to gain weight from day 18. Then, they lost weight again due to the tumor regrowth from about the 5th week. Interestingly, the average tumor sizes of both treatment groups were almost identical during the first half of the treatment period. This is likely because the PSMA sites on tumors became saturated under either of the dosing conditions. Consequently, the increased dose did not benefit the tumor reduction but instead cause slightly higher toxicity. Tumor growth stopped by day 7. After then, all tumors started shrinking over the course of the treatment (**Figure 3B**). However, the tumor started to regrow between day 25 and day 35, with distinct difference between the 15 nmol and 40 nmol group. The higher dose group demonstrated advantages over the lower dose group for the second half of the treatment period. In contrast, the control group was observed with fast and continuous tumor growth, and mice showed body weight loss from day 10 when the tumor burden became severe (**Figure 3C**). Based on the promising treatment data, we believe that our SMDC design addresses the systemic toxicity issue and improves the chemotherapy efficacy. For future studies, we will include an additional course of treatment before the tumor regrowth, in order to prevent the tumor relapse.

Concurrent and follow-up PET/CT imaging enabled by the theranostic design: To evaluate the major designed feature of our theranostic SMDC design, we conducted PET imaging before (*day 0: inject ^{18}F-T-SMDC (DM1) only for imaging*), during the 1st-dose treatment (*day 1: co-injection of ^{19}F-T-SMDC (DM1) for treatment*), and post-treatment (*day 44: inject ^{18}F-T-SMDC (DM1) only for imaging*) for both 15 and 40 nmol groups (n = 3). Compared to the pre-treatment PET imaging results, both groups showed significantly reduced tumor uptake when administering a large amount of ^{19}F-T-SMDC (DM1) for therapy. However, the 40 nmol group showed much more tumor uptake reduction than the 15 nmol group (**Figure 4**). Indeed, the quantitative imaging data analysis demonstrated 63 ± 10% and 36 ± 5% tumor uptake reduction ($\text{Uptake}_{\text{day1}}/\text{uptake}_{\text{day0}}$) for the 15 nmol and 40 nmol groups, respectively. Correspondingly, the 40 nmol group only delivered about 1.5 folds more ^{19}F-T-SMDC (DM1) dose to tumors than the 15 nmol group, which is lower than the 2.7-fold initial dose difference between the two groups.

$$Ratio\ of\ average\ tumor\ uptake = \frac{40\ nmol}{15\ nmol} \times \frac{36\%}{63\%} = 1.5$$

$$Ratio\ of\ initial\ dose = \frac{40\ nmol}{15\ nmol} = 2.7$$

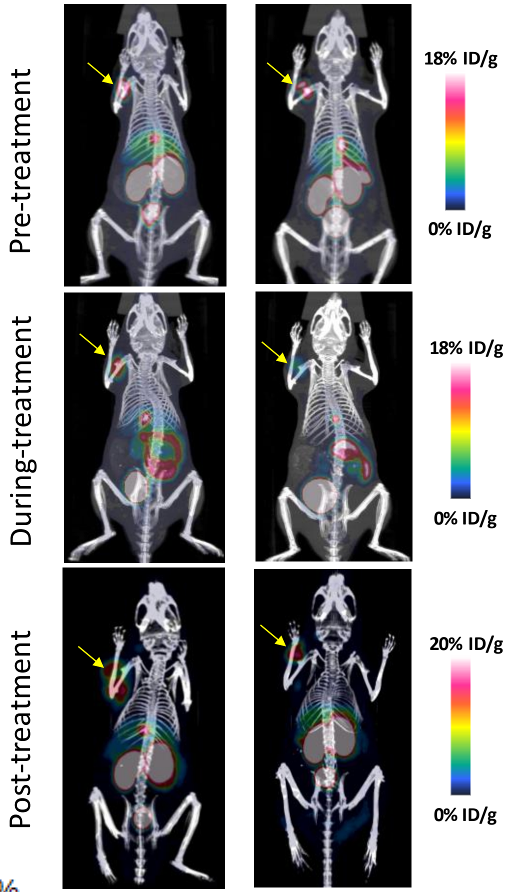

Figure 4. Representative MIP images with ^{18}F-T-SMDC (DM1) before (day 0), during (day 1), and post (day 44) the 1st-dose treatment. PET scans were conducted at 1 hr p.i. Yellow arrows

Apparently, the tumor-specific delivery efficiency of the higher dose group was much lower than the lower dose group based on the imaging results. This quantitative analysis enabled by the imaging function of $^{18/19}$F-T-SMDC (DM1) provided a clear explanation to the treatment results. ***Another intriguing finding is that the kidney uptake from imaging was nearly completely suppressed by the injection of therapeutic doses, which is highly desirable in terms of reducing toxicity and radiation burden to kidneys.*** On day 44 post-treatment, the tumor uptake shown from ^{18}F-T-SMDC (DM1) imaging returned to a similar level as pre-treatment, while the tumors regrew to a bigger size. This implies that we can add another course of treatment before tumor regrowth, since PSMA binding sites are readily available after the 1st course of treatment. It would be better if we had acquired PET/CT images right before the tumor regrowth, so we can access the PSMA expression levels when tumors were treated in the smallest size.

Besides the PET imaging with ^{18}F-T-SMDC (DM1), we also conducted ^{18}F-FDG PET imaging in the 15 nmol group mice (n = 3) before and post treatment (day 22, before tumor regrowth). Two out of three mice did not show visible tumor uptake at all at day 22. The only mouse with visible tumor uptake at day 22 showed approximately 50% of PET signal reduction as compared to the pre-treatment scans (2.1 %ID/g vs. 4.5 ± 0.3 %ID/g) (**Figure 5**), further confirming the effectiveness of the treatment. Taken together, the concurrent and follow-up PET/CT imaging provide a valuable measure to evaluate drug delivery efficacy, monitor treatment response, and optimize the dosing plan.

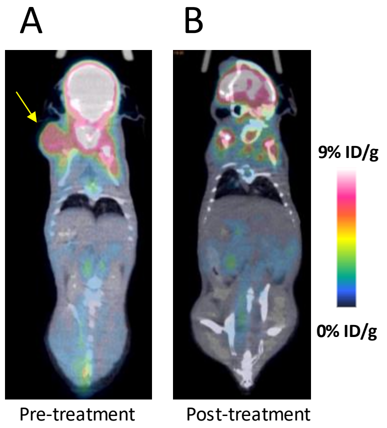

Figure 5. Representative coronal FDG-PET images at 1 hr p.i. (**A**) before and (**B**) post the treatment from the same mouse. Yellow arrow indicates PC3-PIP tumors.

In summary, we have successfully designed and synthesized a pair of $^{18/19}$F-labeled small-molecule theranostic agents for prostate cancer. The structure can be readily modified for other cancer types by changing the targeting vectors as necessary. We are currently evaluating the imaging and therapy efficacies of the new agents.

The accomplishments summarized above has been published in the following manuscripts:

1. Lo S-T, Kumar A, Hsieh J-T, and Sun X: Dendrimer Nanoscaffolds for Potential Theranostics of Prostate Cancer with a Focus on Radiochemistry. *Molecular Pharmaceutics* **2013**, 10:793-812.
2. Hao G, Kumar A, Dobin T, Oz OK, Hsieh, J-T, and Sun X: A Multivalent Approach of Imaging Probe Design to Overcome an Endogenous Anion Binding Competition for Noninvasive Assessment of Prostate Specific Membrane Antigen. *Molecular Pharmaceutics*. **2013**, 10:2975-2985
3. Singh AN, Dakanali M, Hao G, Ramezani S, Kumar A, Sun X: Enantiopure bifunctional chelators for copper radiopharmaceuticals - Does chirality matter in radiotracer design? *Eur. J. Med. Chem.* **2014**, 80, 308-315.
4. Lo S-T, Kumar A, and Sun X: Delivery and controlled release of therapeutics via dendrimer scaffolds. Chapter 10 of "*Nanoparticle Delivery of Biotherapeutics*" edited by Vooght-Johnson. Published by Future Science Group, **2015**

5. Kumar A, Zhang S, Hao G, Hassan G, Ramezani S, Lo S-T, Sagiyama K, Takahashi M, Sherry AD, Oz OK, Kovacs Z, and Sun X: Molecular Platform for Design and Synthesis of Targeted Dual-modality Imaging Probes. *Bioconjugate Chemistry*, **2015**, 26(3):549-558. ***ACS Editor's Choice***
6. Kumar A, Hao G, Liu L, Ramezani S, Hsieh JT, Oz OK, and Sun X: Click-Chemistry Strategy for Labeling Antibodies with Copper-64 via a Cross-Bridged Tetraazamacrocyclic Chelator Scaffold. *Bioconjugate Chemistry*, **2015**, 26(4), 782-789.
7. Kumar A, Mastren T, Wang B, Hsieh JT, Hao G, and Sun X: Design of a Small-Molecule Drug Conjugate for Prostate Cancer Targeted Theranostics, Bioconjugate Chemistry, **2016**, 27:1681-1689.

There are at least two more manuscripts under preparation, which will detail the progress we made toward the development of prostate cancer targeted theranostic agents.

Impact

This project was designed to take advantage of the advances in prostate cancer research recently reported by the laboratories of the three PIs to address the above challenges with the ultimate goal to develop a new molecular medicine approach towards the eventual cure of prostate cancer. Metastasis is the main cause of cancer-related deaths. While metastasis is a complex process, published data indicate that cancer cells undergo epithelium-to-mesenchymal transition (EMT), in which cells become motile and acquire invasiveness to the surrounding tissue upon the initiation of metastasis. Highly specialized in prostate cancer research, this three-PI team focuses their proposed work in this project on the function reinstalling of DA2IP, a DOC-2/DAB2 interactive protein firstly identified by one of the PI's labs (Hsieh) as a tumor suppressor associated with several cancer types. The basic rationale of this work was based on our published evidence that EMT can be reversed to prevent prostate cancer metastasis by DAB2IP. The approach was to present three small therapeutic peptides derived from the proline-rich (PR) domain, which have been proven by us with the same inhibitory function of DOC-2/DAB2 in blocking growth factor-elicited signal pathways, on a validated dendrimer scaffold system (Simanek/Sun) for targeted intracellular delivery when coupled with a prostate specific cell permeation peptide, which again was identified by us (Hsieh/Sun).

We have designed different chemical modification of small peptide and characterized their in vitro biologic activities using several metastatic prostate cancer cell lines. Our data have shown the better activity of chemical modified peptide than prototype peptide. However, we did not observe any enhancement of activity after dendrimer conjugation, suggesting that peptide conjugation to dendrimer might have altered its structure. Overall, we conclude small peptide therapeutics remains a potential specific targeting agent. Nevertheless, there are still some issues regarding to drug delivery such as type of nanoparticle, chemistry of conjugation needed to be resolved in order to achieve an efficient delivery.

Changes/Problems

However, the failure of the multivalent strategy to deliver a biological effect that matches or exceeds the bioactive monomers have led us to prepare new monomers that might be more effective than those previously reported. The therapeutic sequence is maintained, but the targeting domain, and $(Arg)_{11}$ sequence is being replaced by the PSMA ligand called DUPA. During this period, the DUPA ligand (**Figure 6**) has been prepared and conjugated to a triazine linking group as shown below. The bioactive monomer and three PSMA-targeted dendrimeric constructs have been prepared and their biological evaluations are ongoing (Sun/Simanek) with publishable data expected within three months.

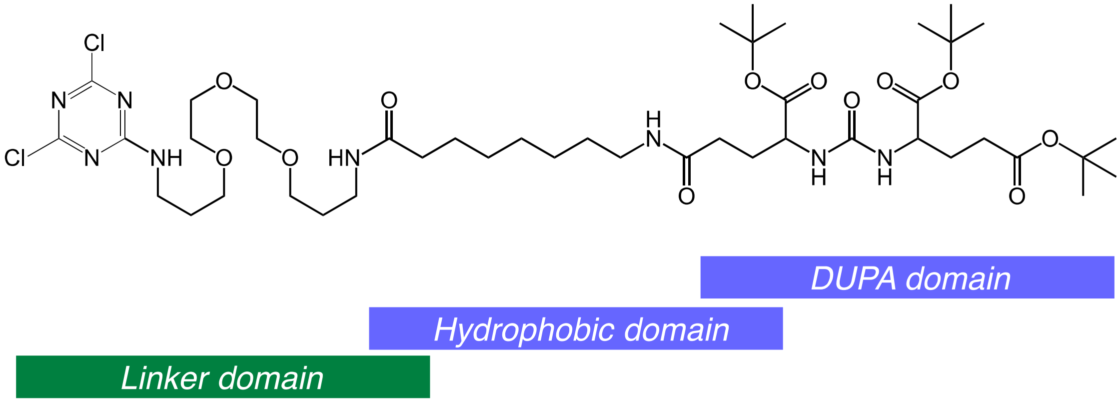

Figure 6. The DUPA domain subdivided to show the required hydrophobic domain and hydrophilic linker domain upon which the bioactive peptide can be appended.

Products

N/A

Participants & Other Collaborating Organizations

Xiankai Sun, PhD, Associate Professor, 09/2013 – 08/2017
Marianna Dakanali PhD, Postdoctoral Researcher II, 09/2013 – 08/2014
Su-Tang Lo, PhD, Postdoctoral Researcher II, 10/2013 – 04/2014
Aditi Arun Mulgaonkar PhD, Postdoctoral Researcher II, 09/2017 – 08/2017
Daniel Abraham Rodriguez De Anda, Graduate Student, 06/2017 – 07/2017

Special Reporting Requirements

None.

Appendices

Seven peer-reviewed publications

molecular pharmaceutics

Review

pubs.acs.org/molecularpharmaceutics

Dendrimer Nanoscaffolds for Potential Theranostics of Prostate Cancer with a Focus on Radiochemistry

Su-Tang Lo,[†] Amit Kumar,[†] Jer-Tsong Hsieh,[‡] and Xiankai Sun*[,†,§]

[†]Departments of Radiology and [‡]Urology, [§]Advanced Imaging Research Center, University of Texas Southwestern Medical Center, Dallas, Texas 75390, United States

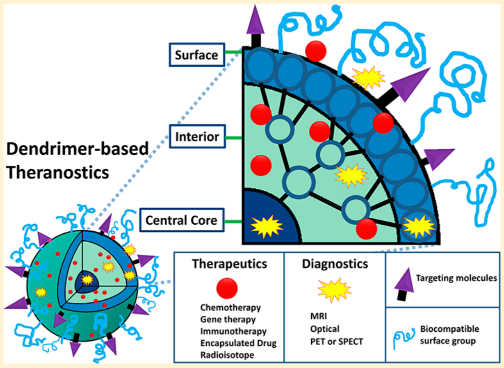

ABSTRACT: Dendrimers are a class of structurally defined macromolecules featured with a central core, a low-density interior formed by repetitive branching units, and a high-density exterior terminated with surface functional groups. In contrast to their polymeric counterparts, dendrimers are nanosized and symmetrically shaped, which can be reproducibly synthesized on a large scale with monodispersity. These unique features have made dendrimers of increasing interest for drug delivery and other biomedical applications as nanoscaffold systems. Intended to address the potential use of dendrimers for the development of theranostic agents, which combines therapeutics and diagnostics in a single entity for personalized medicine, this review focuses on the reported methodologies of using dendrimer nanoscaffolds for targeted imaging and therapy of prostate cancer. Of particular interest, relevant chemistry strategies are discussed due to their important roles in the design and synthesis of diagnostic and therapeutic dendrimer-based nanoconjugates and potential theranostic agents, targeted or nontargeted. Given the developing status of nanoscaffolded theranostics, major challenges and potential hurdles are discussed along with the examples representing current advances.

KEYWORDS: *dendrimer, theranostics, prostate cancer, molecular imaging, drug delivery*

■ INTRODUCTION

Current therapeutic strategies often target one disease with the same regimen in different individual patients. In general, the delivery schedule and treatment dosage of each agent is given based on a limited number of parameters of the disease such as the stage, symptom, and physical condition of patient. Overwhelming literature reports have indicated that distinct different genetic makeup exists among patients even diagnosed with the same disease. For example, the success of Herceptin attests to the viability of personalized therapies for cancer. Herceptin is a monoclonal antibody that binds to the human epidermal growth factor receptor 2 (HER2/neu) receptor that is overexpressed on the cell surface of approximately 25% of breast cancers.[1] Only HER2 positive cancers are responsive to treatment. The need for more refined, tailored treatment was also made clear by Iressa for lung cancer treatment. While highly effective in 10% of lung cancer patients, it failed to enhance survival in the other treated patients. Recently it has been discovered that patients who respond to Iressa have a somatic mutation in the tyrosine kinase domain of epidermal growth factor receptor (EGFR).[2−5] These examples stress the need for a detailed molecular diagnosis and correspondingly a more tailored therapy regime.[6] The concept of personalized medicine becomes more apparent because molecular medicine has clearly identified key genetic defects associated with many diseases. To formulate a specific regimen for each patient, noninvasive molecular imaging techniques are needed in addition to genetic profiling to better define the location and extent of disease and to better assess the disease response to drugs in a real-time manner.

Capable of providing highly specific information of the intact organism with respect to structural and functional phenotypes, molecular imaging has evolved to become an indispensable tool in biomedical research. The potential of molecular imaging has been well recognized for enhancing basic biological knowledge, better understanding molecular mechanisms of disease for early and accurate diagnosis, facilitating drug discovery and validation, and improving prediction and assessment of the response of a disease to various therapies. Most molecular imaging procedures are enabled by imaging probes, which usually consist of two components: a reporter group for detectable signal generation and a targeting moiety for localization of molecular events. Common reporter groups include fluorescent molecules for optical imaging, T_1 and T_2 contrast agents for magnetic resonance imaging (MRI), microbubbles for ultrasound imaging (US), radioisotopes for positron emission tomography (PET) and single photon emission computed tomography (SPECT). Targeting molecules are chosen based on the specific targets of interest.

Special Issue: Theranostic Nanomedicine with Functional Nanoarchitecture

Received: September 19, 2012
Revised: January 7, 2013
Accepted: January 7, 2013
Published: January 7, 2013

dx.doi.org/10.1021/mp3005325 | *Mol. Pharmaceutics* 2013, 10, 793−812

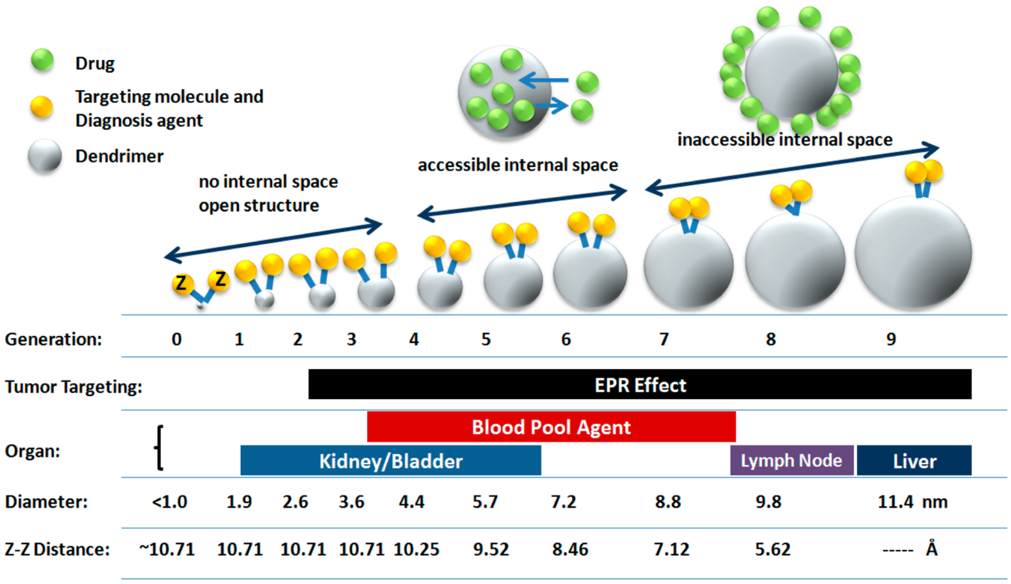

Figure 1. A dendrimer system often has tunable physical properties for different biomedical applications, which are mainly determined by the dendrimer's generation. This unique feature depicted here is represented by a PAMAM−DTPA (Gd) system (G0−G9) that was developed for MRI contrast agents. Different dendrimer systems may possess different tunable physical properties. The figure was adapted using data from Menjoge et al.[23] PAMAM: poly(amidoamine); DTPA: diethylene triamine pentaacetic acid.

Usually, they can be small organic molecules, peptides, oligonucleotides, macromolecules such as antibodies, or activatable enzyme substrates.

The recently emerged concept termed as "*Theranostics*", which integrates *thera*peutic and diag*nostic* agents into a single entity, is expected to play an important role in the personalized therapy.[7] The central hypothesis of this concept is that the integration of a molecular imaging component would enable the desired noninvasive imaging of the *in vivo* status of the molecular target during the personalized treatment, to which the therapeutic agent is intended to be delivered. Of course, the personalized treatment must be administered after the final molecular diagnosis of the disease status, which can be performed by either the theranostic agent itself but void of the therapeutic component or other diagnostic techniques. The former is exemplified by a nuclear medicine practice that can date back to the 1940s, which uses iodine-123 (a γ-emitter) for diagnosis and then iodine-131 that emits both γ-rays and β-particles for imaging and radiotherapy of differentiated thyroid therapy.[8] The latter would be a typical clinical practice, in which molecular diagnosis is first performed to identify and stratify patients based on the molecular signatures of their disease and then a corresponding theranostic agent is administered for both treatment and imaging-enabled noninvasive monitoring of the disease responses.

Not intended for an exhaustive coverage of literature on the design and potential application of theranostic agents, this review focuses on the recent advances of using dendrimer nanoscaffolds for the development of diagnostics or therapeutics and potential theranostic agents for prostate cancer with the emphasis on the radioisotope-enabled approaches. Comprehensive reviews on the design of dendrimer nanoscaffolds for drug delivery can be found elsewhere.[9−13] According to the American Cancer Society's 2012 Facts and Figures, prostate cancer has been the most commonly diagnosed cancer in males and consistently among the leading causes of cancer-related deaths of men in United States. Although surgery can effectively control the primary prostate cancer, for metastatic disease, androgen deprivation becomes a gold standard of therapy that only delays the onset of castration resistant prostate cancer (CRPC), which contributes to the majority of prostate cancer mortality. It is almost certain that the relapse of CRPC is inevitable for patients who are under hormonal therapy. With respect to current regimens available for the recurrent CRPC patients, some have shown therapeutic efficacy despite that there are many undesirable side effects (e.g., bone marrow suppression, alopecia, and sloughing of the epithelial cells in gut).[14] Although tremendous efforts have been seen on the development of novel diagnostics and therapeutics toward the eventual cure of prostate cancer, few effective agents have been reported.[15,16]

Dendrimers are a class of highly branched and symmetrical macromolecular constructs, which consist of repeating dendrons extending outward from a central core.[17−19] Compared to linear polymers, dendrimers can be synthesized reproducibly with low polydispersity, which is a highly desirable feature for drug delivery vehicles. The synthesis of dendrimers can be performed in a controlled manner, yielding products with predictable sizes termed as "generation". Because of this controlled feature, different generations of a dendrimer system can be exploited to fulfill desired *in vivo* pharmacokinetic requirements for a wide range of biomedical applications (Figure 1). In addition, as the dendrimer core branches out in the synthesis of each generation, the number of peripheral groups increases exponentially, which results in a shielded interior that can be used to load drugs for delivery. Obviously, the peripheral functional groups, often in the form of amine or carboxylate, can be used to conjugate with functional molecules in a multivalent format for imaging signal amplification and therapeutic efficacy enhancement. Given the unique structural features, undoubtedly, dendrimers can be used as nanoscaffolds to develop theranostic agents for oncologic and nononcological applications.

In the past decades, the developmental efforts of theranostics have been focused on the use of currently available nanotechnologies and nanomaterials.[7,20−23] In this review, we

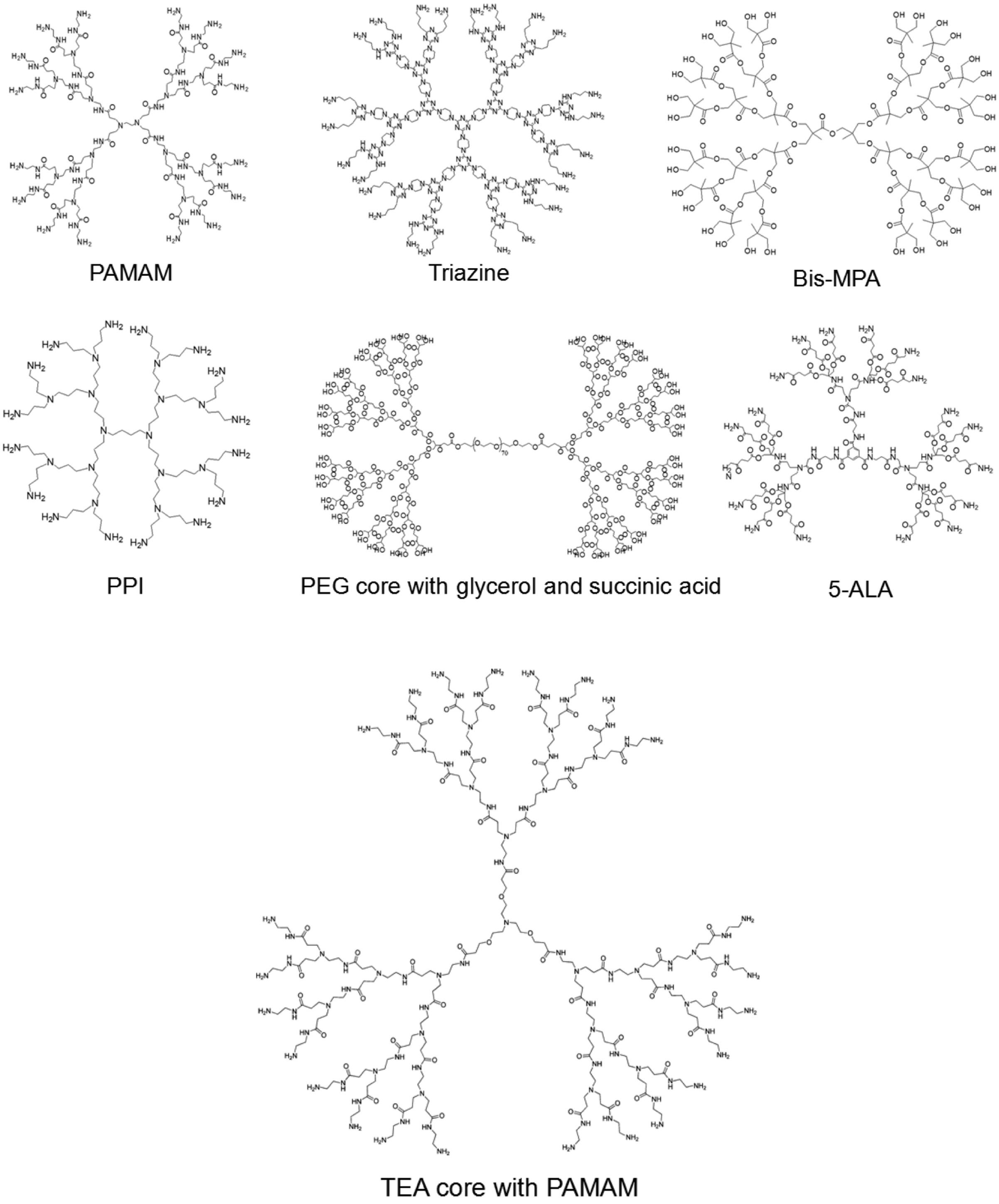

Figure 2. Structures of the dendrimer systems that have been used for the development of diagnostics and therapeutics of prostate cancer. PAMAM: poly(amidoamine); Bis-MPA: 2,2-bis(hydroxymethyl) propionic acid; PPI: polypropylenimine; PEG: poly(ethylene glycol); 5-ALA: 5-aminolevulinic acid; TEA: triethanolamine.

discuss potential methods in the development of dendrimer nanoscaffolds for theranostic agents of prostate cancer.

■ DENDRIMER NANOSCAFFOLDS

Nanotechnologies have been extensively explored for more effective cancer diagnosis and therapy in the past decades. Of the basic requirements for cancer therapeutic or diagnostic agents, the pharmacokinetic properties of potential nanosized platforms are critically important given the fact that they must be able to permeate the vascular wall, reach their biological targets, and retain there at a sufficiently high concentration for effective therapy or imaging. Further, if the oncologic targets are intracellularly located, they must be able to cross the cell membrane. Engineered nanoparticles with the size range of several nanometers to a couple of hundred nanometers in diameter can be potentially designed to have desired pharmacokinetics, multiple binding capacities, and the ability to fit into an endocytotic vesicle through endocytosis or phagocytosis as a carrier or transporter of imaging reporters and/or therapeutic agents.[24] The reader is referred to other review articles[25−27] for recent advances in nanoparticle-based molecular imaging research.

Among the nanoconstructs that have been reported for biomedical applications, dendrimers hold great promising in that they can be synthesized in a more controlled way with low polydispersity or monodispersity to achieve the desired *in vivo* pharmacokinetics for different applications by simply varying the generation (Figure 1). However, the tunable properties, such as passive and active tumor targeting, vary with different dendrimer systems. It is noteworthy that currently no general agreement has been reached on the size threshold of dendrimer systems that undergo the enhanced permeability and retention (EPR) tumor trapping mechanism. Like their polymeric counterparts, dendrimers can provide hundreds or even thousands of sites if necessary for multipresentation of various functional molecules to serve the purpose of interest, such as targeting ligands, imaging reporters, or therapeutic drugs. As discussed above, the major advantages of using dendrimers for cancer imaging or therapy include their more defined and readily tunable size and surface functionalities. Theoretically, the number of exterior functional groups branching out from the core increases exponentially generation-wise. Therefore, dendrimers can also be used as a nanocapsule system for drug loading (Figure 1). However, as the generation goes, the steric effects between the surface terminal groups and their spatial crowding would result in a higher generation dendrimer with less defined structure, which is not desirable for drug delivery. A dendrimer system, which is usually much smaller than its polymeric counterpart, exhibits rapid blood clearance and low accumulation in the reticuloendothelial system (RES) organs as compared to the *in vivo* behavior of other nanoconstructs. This provides compelling reasons to exploit dendrimers as biocompatible nanoscaffolds to carry imaging and/or therapeutic agents for biomedical applications. Indeed, specific tumor accumulation can be conveniently achieved by targeted nanoscaffolds as exemplified by a monoclonal antibody conjugated generation-4 poly(amidoamine) dendrimer (G4-PAMAM).[28] However, there is no guarantee that a dendrimer system would have an optimal *in vivo* pharmacokinetic profile. For a specific biological application, subjecting the dendrimer system to *in vitro* and *in vivo* evaluations is the only way to test its rational design.

Shown in Figure 2 are representative dendrimer scaffolds that have been seen in scientific literature with potential to be used as imaging and/or therapeutic agents for prostate cancer. Obviously, such dendrimer scaffolds can be also used for other cancer types and diseases.[29] To stay focused on the potential theranostic applications of dendrimers for prostate cancer, this review excludes the synthesis of the dendrimer scaffolds, which has been thoroughly discussed in recent reviews.[23,30]

■ STRATEGIES TOWARD CONTROLLED DRUG RELEASE

Dendrimers, on account of their unique supramolecular and interfacial features and chemically modifiable peripheral functional groups, are ideally suited as nanoscaffolds for bioactive agents. These nanoconstructs have successfully been utilized for the delivery of drugs, genes, diagnostic dyes, and biologically active metal ions[23,31−35] by two general methods (Figure 3). One entails the encapulation of functional agents within a dendrimer scaffold, and the other deals with covalently linkage of active agents to the functional groups located on the branching units. In case of the encapsulation, the agents physically interact with the nanoscaffolds by noncovalent secondary binding processes, such as hydrogen bonding, van der Waals interactions, and electrostatic attractions between oppositely charged species located within the agents and the nanocarrier. Dendrimers, owing to the presence of a large number of surface terminal groups within the same molecule, are widely used to provide multivalency in biology and targeted drug delivery systems.[18,36] Multivalency arises from the multipresentation of a functional molecule on a single platform, by which the interactions between the functional molecule and its biological targets can be significantly enhanced when compared to the individual bonding of an equivalent number of monovalent ligands to the same biological targets.[37] This phenomenon is widely used by biological systems, particularly for attachment,[38] signal transduction,[39] and cellular recognition.[40] Such enhancement termed as the “multivalent effect” is driven by the high entropic gain in the formation of a multivalent complex. Dendrimer nanoscaffolds, owing to the vicinal presence of active functional groups within an adjustable distance, can easily mimic “ligand clustering” for the desired multivalent effect.[41−44]

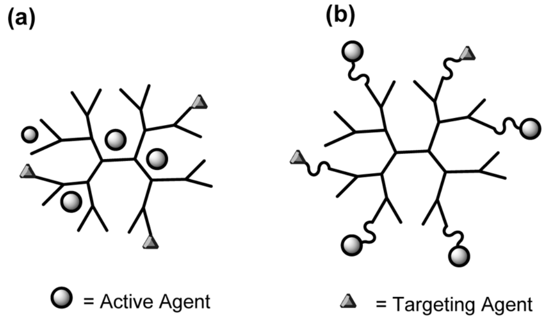

Figure 3. Two general methods of loading active drug to dendrimers: (a) noncovalent encapsulation and (b) covalent conjugation.

Noncovalent Encapsulation. Dendrimers are capable of noncovalently harboring drugs, dyes, diagnostic agents, and other biologically active species. The secondary interactions (e.g., hydrogen bonding, electrostatic interactions, dipole−dipole, and hydrophobic interactions) between the dendrimers and bioactive agents are responsible for stabilizing of these agents. The resulting supramolecular self-assembly offers several distinct advantages such as enhanced solubilization of nonpolar drugs in aqueous media and minimization of nonspecific interactions of the encapsulated drugs with plasma components.

In the early 1990s, the synthesis and characterization of “dendritic boxes” within poly(propyleneimine) dendrimers surrounded by a dense shell were published and adopted by other researchers in the development of drug delivery applications of dendritic polymers.[45,46] While the initial approaches dealt with non water-soluble systems, the subsequent dendritic molecules have been made water-soluble for the delivery of a wide variety of biologically active species with substantial therapeutic and pharmaceutical improvement. For instance, a full-and-half generation (G6.5) of PAMAM dendrimer was reported to aquate cisplatin, an effective anticancer drug. The noncovalently complexed cisplatin was proven more efficacious in the treatment of cancer.[47]

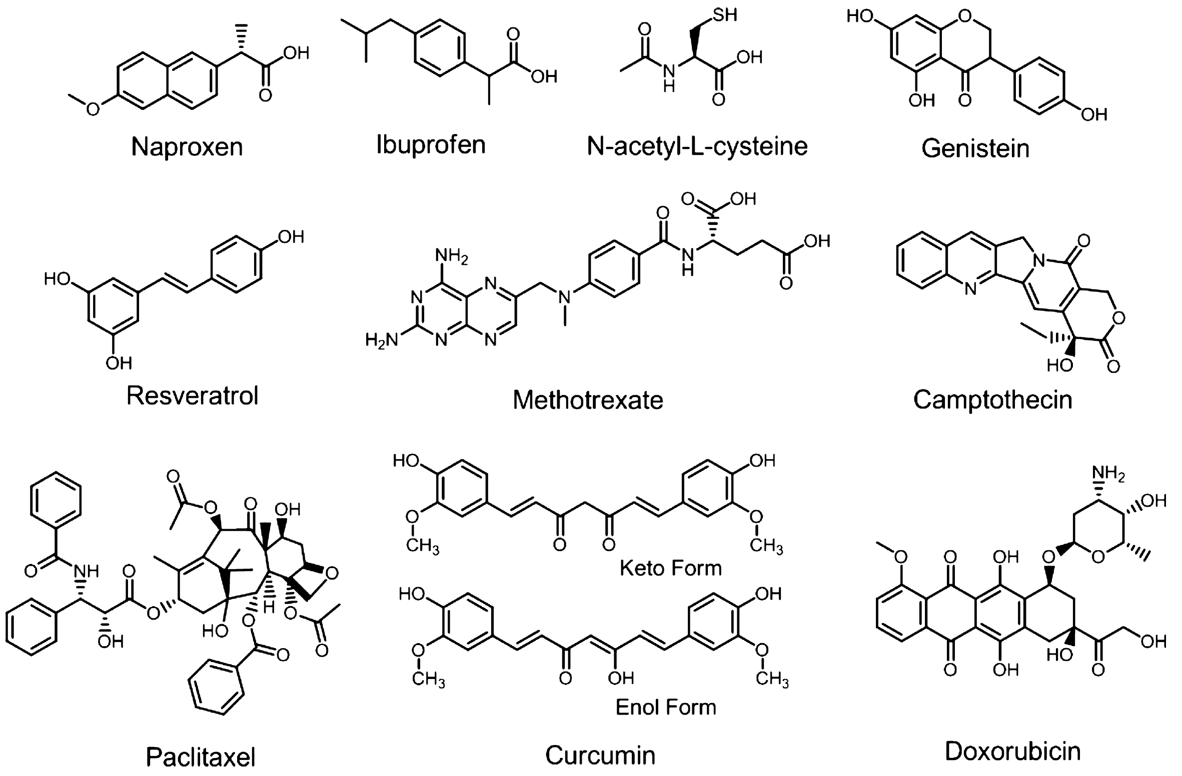

Figure 4. Structures of selected drugs used for the construction of dendrimer therapeutics.

The release of encapsulated drugs from their dendrimer scaffolds has been extensively studied as the responses to environmental conditions (e.g., pH, salts).[48−50] For instance, a multifunctional dendrimer scaffold, which consists of diaminobutane poly(propylene imine) dendrimers (DAB) with poly(ethylene glycol) chains and guanidinium moieties on its exterior, was able to release the encapsulated pyrene upon the pH and/or osmotic environment change.[49]

Covalent Delivery with Dendritic Molecules. Covalently linking drug molecules to dendrimers is the commonly used approach in the construction of dendrimer drug delivery systems. Peripheral end-groups of a dendrimer can be used as attachment points to couple drugs to the core scaffold. The key to the design of a dendrimer-drug conjugate lies in the fact that multiple copies of the same or different drug molecules can be attached to each dendrimer molecule by various bioconjugation reactions between the orthogonal and complementary functional groups. Release kinetics of the active agents from the dendrimer scaffold is largely governed by the chemical linkage by which the drug is coupled. The major advantage of this approach is that chemistry strategies can be applied with hope to realize the goal of controlled release by taking advantaging of the susceptibility of various chemical bonds to different *in vivo* conditions, such as the acidic tumor microenvironment, site-specific enzyme cleavage, or disease-specific metabolic alteration. Drugs have been linked to the dendrimer scaffold through amide,[51] ester,[52] hydrazone,[53] imine,[54] carbamate,[55] disulfide,[56] carbazate bonds,[57] and enzymatic cleavable peptide sequences.[58] Each of these linkages has their own differential mechanism of cleavage to separate the drug molecule from the scaffold. While ester, hydrazone, and carbamates depend on the surrounding pH for release, amides and peptidic sequences require an enzymatic involvement for their degradation and subsequent release of the active species.

Amide vs Ester Bonds. Amide and ester bonds are most frequently used in the conjugation design of dendrimer-based drug delivery systems. In most cases, dendrimer-drug conjugates undergo the lysosomal or endosomal pathway after entering the cell.[51,59] In the acidic environment, the drug can be released from the dendrimer carrier upon the acidic cleavage of the ester bonds. However, amide bonds are robust and undergo a very slow enzymatic degradation. Owing to their remarkable stability, the amide bond linkage is not the preferred for drug release.[51] The drug release rate can also be affected by the different chemical environment of the same bond. For example, diethylene glycol (deg) and lactic (lact) ester linkages were assessed for their drug release rate from a G0 PAMAM dendrimer using naproxen (Figure 4), a prescription non-steroidal anti-inflammatory drug with poor water solubility, as a model drug.[60] It was found that the deg linkage of G0-deg-NAP was much more quickly hydrolyzed than the lact ester bonds of G0-lact-NAP.

To understand the effect of architecture and linker on drug release, a recent study compared the drug release characteristics of a series of dendrimer−ibuprofen conjugates (see Figure 4 for the chemical structure of ibuprofen) built upon a G4 PAMAM dendrimer with an ester, amide, or a peptide as the drug and dendrimer linkage.[52] As expected, amide-linked conjugates were relatively stable against hydrolysis, whereas the ester-linked conjugates showed a pH-dependent release rate. Interestingly, the conjugates constructed by direct amide and ester bonding did not release ibuprofen enzymatically in either cathepsin B buffer or diluted human plasma. In contrast, the dendrimer−ibuprofen conjugate incorporated with PEG as a linker released its drug loads rather efficiently by cathepsin B activity, so was the peptide-linked conjugates. This demonstrates that the steric crowding at the surface of dendrimer−drug conjugates along with the linking chemistries govern the drug release mechanisms as well as kinetics. Therefore, understanding these structural and steric effects on their drug release characteristics is crucial for the design of dendrimer conjugates. Shown in Figure 4, methotrexate (MTX), an antimetabolite and antifolate drug, has two possible sites for conjugation owing to the presence of carboxylic and amine terminations. As such, MTX can serves as a good drug model to compare the drug release profiles from amide and ester linkages. In fact, the carboxylate group of MTX is preferred in the construction of dendrimer-MTX conjugates because MTX can be released once the internalized conjugates are exposed to the acidic endosomal environment.[61,62]

***cis*-Aconityl Bond.** *cis*-Aconityl is another pH-sensitive linker that has been extensively exploited for the design and construction of drug delivery systems.[63,64] For instance, dendrimer conjugates of doxorubicin (DOX) constructed by use of *cis*-aconityl linkage were able to show an acid-triggered DOX release, whereas the release from its amide counterpart was negligible.[65]

Disulfide Bond. The disulfide bond (−S−S−) is formed through the oxidation of two thiols. While relatively stable in mildly oxidizing environments (e.g., atmospheric oxygen or the bloodstream), disulfide bonds can be cleaved by a reducing agent reforming two thiols.[66,67] In the cell, the reduced form glutathione (GSH) is maintained at the millimolar concentration level through the cytosolic NADPH-dependent reaction catalyzed by glutathione reductase. GSH is found at much higher level in diseased cells. For example, it was found to be 7-fold higher in a human lung adenocarcinoma cell line (A549) than in a normal human lung fibroblast line (CCL-210).[68] With this feature, the strategy of using disulfide bond linkage through reacting with sulfhydryl groups on dendrimer has been used to facilitate the drug release. Study showed that by using this strategy the anti-inflammatory and antioxidant agent, *N*-acetyl-L-cysteine (NAC), can be tailored on dendrimer and released by the intracellular glutathione *in vivo*.[69,70] For PAMAM dendrimers possessing carboxylic or amine terminal groups, they must be first modified using glutathione or *N*-succinimidyl-(2-pyridyldithio)-propionate, respectively, and then coupled with the thiol moiety of NAC to form the dendrimer-drug conjugate through disulfide linkage. The construct was found to be able to avoid plasma protein binding, which is an additional advantage for the enhancement of drug bioavailability. Efficacy studies using this construct on microglial cells revealed that the dendrimer-NAC conjugate was 16 times more efficacious than the drug alone in the treatment of maternal fetal infections.[69−71] A similar study was also done using thiol terminated star poly(ethylene glycol) conjugates.[72] A similar design was also seen in a paclitaxel (PTX) conjugate constructed from a G2 triazine dendrimer for the intracellularly controlled release of PTX for prostate cancer treatment.[73] The conjugate showed a better therapeutic efficacy as compared to its counterparts without the intracellular glutathione sensitive disulfide linker.[74]

The conjugation methods mentioned above utilize diversified multifunctional and multivalent approaches and exhibited substantially positive biological results. Despite the success demonstrated by the conjugation methods, it must be noted that conjugating different classes of ligand molecules to the surface of the dendrimer scaffolds often results in a heterogenic distribution of ligand-bound dendrimer conjugates in terms of the number of ligands per conjugate. The ligand distribution on a dendrimer scaffold is related to the synthetic history of the dendrimer, and the product conjugate becomes more inhomogeneous with increasing synthetic steps, as more ligands and ligand types are involved.[75] Such a heterogeneous ligand distribution certainly would hinder the interpretation of biological and clinical results as the structure−activity relationship is compromised. To address this problem, efforts have been made through the implementation of new synthetic strategies and scalable purification techniques regarding the understanding of inhomogeneous ligand distribution.[76−83]

■ POTENTIAL CYTOTOXICITY OF DENDRIMER NANOSCAFFOLDS

Toward the eventual application as theranostic agents, the dendrimer nanoscaffolds must be able to maintain a certain degree of integrity under the physiological conditions, which provides desired cytotoxicity shielding of the carried therapeutic agents from nontarget organs or tissues. As such, ideal nanoscaffolds themselves should not induce immune-responses, cause hemolytic toxicity, or impose cytoxicity. However, nonmodified or intact dendrimer scaffolds might elicit immune-responses or be toxic due to the size and the surface termination of the dendrimers. The otherwise exposed building blocks, if toxic, must be shielded by the surface termination or modification, and the dendrimer nanoscaffolds must remain stable because fragmentation would release the toxic building blocks, which may redistribute back to the bloodstream and thus impose unnecessary harm to healthy tissues.

As exemplified by the surface-unmodified PAMAM dendrimer systems, the positively charged surface (quaternary ammonium ions) interacts with red blood cells and other healthy cells, which results in hemolytic toxicity and cytotoxicity.[84] It has been reported that both hemolytic toxicity and cytotoxicity of PAMAM dendrimers are dependent on the charge, concentration, and generation of the dendrimers,[85,86] and lower generation PAMAM dendrimers (i.e., G0−G1) exhibit considerably less cytotoxicity than the higher generation ones (i.e., G2−G4).[87] On the other hand, both anionic and neutral PAMAM dendrimers are found substantially less toxic than cationic dendrimers.[88] Based on these observations, surface chemistries play an essential role in the design of a dendrimer nanoscaffold system to reach the desired biocompatibility. Usually two common approaches are taken: (1) surface modification by polyethylene glycol (PEGylation) to neutralize the surface charge and improve the water solubility of the dendrimer system; and (2) surface termination with small molecules (e.g., acetylation) to neutralize the surface charge and enhance the cellular uptake.[89] It has been well-recognized that surface PEGylation renders nanoconstructs with desired stealthiness to the immune system and biocompatibility. In addition, long PEG chains are usually employed to optimize the *in vivo* kinetics and increase the biological half-lives of nanoconstructs.[90,91] A good example of the latter was set by a study on the effect of surface amidation of PAMAM dendrimers on their cytotoxicity,[88] in which a linear relationship was found between the number of the naked surface amine groups and the cytotoxicity of dendrimers while the desired transepithelial permeability was not compromised. Not surprisingly, the complete amidation led to a nontoxic dendrimer system.

Fatty acids, such as lauric acid (namely, dodecanoic acid: n-$C_{11}H_{23}COOH$), can also be used to modify dendrimer surface as a biocompatible penetration enhancer.[92] It was reported that lauroylation of cationic PAMAM dendrimers reduces the cytotoxicity along with the surface PEGylation and the degree of lauroylation can be used as an approach to improve the dendrimer's cell permeability.[93] Of course, further modification of a dendrimer nanoscaffold system with targeting or other functional molecules must take into consideration its effect on the biocompatibility of the system.

■ CONSTRUCTION OF TARGETED DENDRIMER NANOSCAFFOLDS

Targeting is important in that it can provide higher contrast to imaging of the targeted organ or more efficacious therapy to the specific diseased sites. Tumor targeting of nanoconstructs can be achieved by either passive or active targeting mechanisms. The passive-targeting approach takes advantage of the EPR effect,[94−96] which resulted from the rapid tumor growth during tumor angiogenesis because a defective vascular architecture is required to sustain the demand for adequate nutrient and oxygen supply as well as the waste disposal.[97] The defective vasculatures are characterized by unusually large gaps (ca. 300−800 nm) between adjacent endothelial cells of the tumor blood vessels resulting from an abnormal arrangement of the basement membrane and perivascular cells.[98] This led to the enhanced permeability of the blood vessels of solid tumors to blood-borne macromolecules or nanoparticles. However, it should be also remembered that the normally high interstitial pressure in angiogenic tumors along with the chaotic and disorganized neovasculatures may partially offset the extravazation of particles caused by the EPR.[97] Nonetheless, due to the lack of an effective lymphatic drainage system,[99] solid tumors can accumulate nanoconstructs that leak out of the permeable blood vessels, especially the ones stealthy of RES sequestration.[100,101] Many drug-loaded dendrimer systems have been reported with efficient uptake in prostate cancer for therapeutic treatment by taking advantage of this passive targeting mechanism.[73,74]

Active targeting strategies normally exploit the existence of specific molecular signatures of targeted sites. In general, tumor cells of a specific cancer type overexpress specific receptors or antigens. It would be straightforward to conjugate nanoconstructs with the specific ligands of the receptors or antigens for active targeting, which may allow early diagnosis, patient stratification, or personalized therapy at molecular level while alleviating cytotoxicity to normal tissues.[102] To date, varieties of nanoconstructs have been functionalized with small molecules, peptides, and antibodies to target endothelial receptors on the microvasculature of proliferating tumors.[103−107] Here we focus our discussion on two commonly exploited targets for targeted imaging or therapy of prostate cancers: prostate-specific membrane antigen (PSMA) and $\alpha_v\beta_3$-integrin.

Targeting the Prostate-Specific Membrane Antigen (PSMA). PSMA is a type II transmembrane glycoprotein that is overexpressed in prostate cancer and neovasculature, but not in the vasculature of the normal tissues.[108,109] A cell surface protein that presents a large extracellular domain (amino acids 44−750), PSMA has been utilized as an effective target for monoclonal antibody directed imaging agents or therapeutics for prostate cancer.[110−113] Indeed, the only U.S. Food and Drug Administration (FDA) approved prostate cancer imaging agent is an ^{111}In-labeled PSMA monoclonal antibody (7E11-C5.3).[110,112] Clinical trials showed that SPECT imaging with this agent had improved sensitivity in the detection of prostate cancer compared to CT or MRI, and it is in clinical use to define the stage of localized prostate cancer and metastases in conjunction with CT or MRI.[112] However, recent reports indicate problems in terms of imaging specificity and sensitivity given the fact that the antibody (7E11-C5.3) recognizes an internal epitope of PSMA.[110] To address the problems, many monoclonal antibodies have been developed (e.g., J591/MLN591, J533, J415, E99, and E6, etc.) that recognize the extracellular domain of PSMA.[111,114−118] As anticipated, imaging with these antibodies labeled radioisotopes have shown significantly improved sensitivity and specificity in the detection of prostate cancer. These antibodies have also been seen in the construction of targeted dendrimer systems. For instance, a PAMAM dendrimer conjugate with J591 showed the specific binding to the PSMA$^+$ LNCaP cells but not the PSMA$^-$ PC-3 cells.[119]

Targeting PSMA can also be achieved by using aptamers, a class of nuclease-stabilized oligonucleotides selected by a ligand screening technology, SELEX (systematic evolution of ligands by exponential enrichment).[120−127] Much smaller than antibodies and without immunogenicity, aptamers might be able to contest the roles of antibodies in therapeutics and diagnostics. In 2002, two RNA aptamers, xPSM-A9 and xPSM-A10, were identified with high binding affinity to the extracellular domain of PSMA. The first PSMA-targeted aptamer-nanoparticle conjugate was built from xPSM-A10. It was found that the nanoconjugate can efficiently target and accumulate in PSMA$^+$ LNCaP cells but not in PSMA$^-$ PC-3 cells.[128] Recently, a G4 PAMAM dendrimer was reported as a carrier of A10 aptamer-DOX complex for prostate cancer treatment,[129] and the PSMA-targeted dendrimer system displayed an antitumor efficacy comparable to DOX alone. Similarly, a G5 PAMAM dendrimer conjugate with A10-3.2, a truncated form of xPSM-A10, was reported with capability of delivering tumor suppressor genes to PSMA expressing target.[130]

Targeting $\alpha_v\beta_3$-Integrin. The progression rate of a solid tumor is strongly dependent on its ability to stimulate angiogenesis, a process in which new blood vessels grow from pre-existing vessels to supply tumor cells with oxygen and essential nutrients. Integrin adhesion receptors are the key factor for cell to interact with the extracellular matrix (ECM)[131] to activate the signaling pathways for regulating the cell functions such as motility, proliferation, and differentiation.[41] In 1994, $\alpha_v\beta_3$-integrin, the vitronectin receptor, was found highly upregulated on activated endothelial cells with a critical role in their survival, while its expression is weak in most normal organ systems.[132] To date, $\alpha_v\beta_3$-integrin has been well recognized as a receptor affecting tumor growth, local invasiveness, and metastatic potential.[133] Among over 25 identified integrin receptors, about two-thirds including $\alpha_v\beta_3$-integrin recognize and bind tightly to a tripeptide sequence Arg-Gly-Asp (RGD). In addition to numerous synthetic RGD peptido-mimetics, RGD-containing peptides, usually in the cyclized form, have been developed as $\alpha_v\beta_3$ antagonists with potential to decrease angiogenesis and induce tumor regression and apoptosis within the angiogenic blood vessels.[132,134−140] To date, cyclic RGD peptides and peptidomimetics have been extensively explored for $\alpha_v\beta_3$-integrin targeted imaging and therapy. The first $\alpha_v\beta_3$-integrin targeted nanoconstruct was built upon a polymerized lipid-based vesicle conjugated with an $\alpha_v\beta_3$ antagonist for targeted gene delivery to angiogenic blood vessels. Tumor cell apoptosis and regression was observed after the nanoconjugate administration to treat established primary and metastatic cancers.[105]

In prostate cancer, the expression of $\alpha_v\beta_3$-integrin is commonly observed in several cell lines including DU145 and PC-3. Interestingly, it was found that the adhesion and migration of cancer cells was mediated partly by $\alpha_v\beta_3$-integrin during distal metastasis of prostate cancer. Not surprisingly, $\alpha_v\beta_3$-integrin targeted dendrimers have been reported with the potential for targeted imaging and therapy of prostate cancer.[141,142]

IMAGING APPLICATION OF DENDRIMER NANOSCAFFOLDS

Given the unique structural features, dendrimers have been extensively utilized for molecular imaging research. The imaging application of dendrimer nanoscaffolds is mainly based on the facts: (1) the versatility of surface chemistries can tailor a common dendrimer scaffold for different applications and imaging signal amplification if necessary; (2) functionalities can also be incorporated into the core and the interior radial structures; and (3) most dendrimer scaffolds are robust under physiological conditions. In this section, we briefly discuss the imaging applications of dendrimer scaffolds categorized by common imaging modalities.

Magnetic Resonance Imaging (MRI). With exquisite spatial resolution and superior soft tissue contrast, MRI holds great promise in the diagnosis of prostate cancer. However, MRI with gadolinium-based contrast agents is inherently less sensitive as compared to PET or SPECT. This is where dendrimer scaffolds can come to play an important role. Earlier efforts were made on linear and hyperbranched polymers, to which multiple copies of contrast agent were attached for the desired signal enhancement.[143,144] However, their *in vivo* applications were hampered by the inherent polydispersity and inefficient renal excretion of the polymer conjugates. In contrast, dendrimer scaffolds are monodisperse, and their sizes are tunable for optimal biodistribution.[23] In addition, dendrimers can also be retained in solid tumors through EPR effect, where the Gd(III)-based T_1 relaxivity can be further enhanced via the confined moving and tumbling. To date, dendrimers have been reported for both T_1 and T_2 contrast agents: (1) dendrimers containing superparamagnetic iron oxide particles (SPIO) (magneto-dendrimers) and (2) dendrimer incorporated with high numbers of Gd(III)-chelates.[145,146] The former is exemplified by a G4.5 PAMAM dendrimer system loaded with iron oxide particles[147] with potential to be used as a cell tracking agent for monitoring the fate of stem cells. Such magneto-dendrimer scaffolds have also shown utility in gene delivery into cells. Interestingly, the cell uptake level of DNA-loaded cationic magneto-dendrimers can be dramatically enhanced in the presence of magnetic field due to the magnetic nature.[148] For instance, a G6 PAMAM dendrimer loaded with SPIO was used to transfect COS 7 cells.[149]

Compared to the magneto-dendrimers, Gd(III)-complex loaded dendrimers were much more widely used. Conjugation of Gd(III) complexes to dendrimer's peripheral functional groups results in a significant enhancement of relaxivity. For example, the r_1 relaxivities of G4 and G5 PAMAM dendrimers conjugated with Gd-DTPA (DTPA: diethylene triamine pentaacetic acid) can be considerably enhanced (G4: r_1 = 28 $\mathrm{mM^{-1}\ s^{-1}}$; G5: r_1 = 30 $\mathrm{mM^{-1}\ s^{-1}}$) as compared to the low molecular weight Gd-DTPA (Magnevist: r_1 = 5.5 $\mathrm{mM^{-1}\ s^{-1}}$). It is noteworthy that the proton relaxivity of the Gd(III)-loaded dendrimers are not enhanced proportionally as the dendrimer generation increases (G8: r_1 = 35 $\mathrm{mM^{-1}\ s^{-1}}$).[23] This can be attributed to the decreased water accessibility of Gd(III) in the high-generation dendrimer structure. Therefore, the G6 PAMAM dendrimer scaffold is the most frequently used for the r_1 enhancement of Gd(III)-based contrast agents.[150−153] Inherent from the nature of dendrimers, different generations of dendrimer can be used for different applications. As such, different generations of Gd(III)-dendrimer contrast agents have been reported for different imaging applications:the drainage lymph node, vasculature (angiograph), kidney, tumor, or even the whole blood pool.[23]

Computed Tomography (CT). An inherent anatomical imaging technique, CT provides excellent hard tissue contrast. To enable X-ray based angiography, a contrast agent that efficiently absorbs X-rays is needed through a systemic administration. In sharp contrast to the huge volume of reports using dendrimer scaffolds for MRI signal enhancement, few such efforts have been seen for CT contrast agents. The typical synthesis of CT contrast agents constructed from dendrimer scaffolds was seen in a recent report, in which a series of G3, G4, and G5 dendrimers with a PEG core were conjugated with tri-iodophthalamide moieties to the peripheral amino groups.[154] Among them, the G4 dendrimer conjugate showed the optimal intravascular contrast in a rat model, while all conjugates exhibited adequate water-solubility, low osmolality, and good chemical stability.

Optical Imaging. Optical imaging's popularity in molecular imaging can be partially attributed to the common use of a charge-coupled device (CCD) camera, which is portable and relatively inexpensive. In addition to its inherent high sensitivity,[155,156] it has excellent temporal and spatial resolution.[157−159] Even though the limited depth of tissue penetration of the light signals makes optical imaging cannot compete with PET, MRI, and CT in clinical applications, it still holds great potential for understanding the disease progression and therapeutic evaluation at preclinical level. Detail for the applications of optical imaging can be found in many review articles.[160−165] Because of the inherent high sensitivity of optical imaging, it is often unnecessary to apply a nanoconstruct to enhance its signal readout. In most cases, optical imaging probes were incorporated into a nanoscaffold for a secondary purpose, such as *ex vivo* validation of *in vivo* imaging results obtained from other imaging techniques.[150,166,167] For instance, a dual imaging probe can be constructed from a G5 dendrimer scaffold by conjugating three imaging reporters to the surface amine groups—two fluorophores (Cy5.5 and Rhodamine) for optical imaging and fluorescence microscopy, Gd(III)-DOTA for MRI, and a targeting molecule (angiopep-2) for transcytosis and glioblastoma targeting. The resulting nanoprobe was able to cross the blood−brain barrier and reach the target for optical and MR imaging of glioblastoma.[168]

Positron Emission Tomography (PET) and Single Photon Emission Computed Tomography (SPECT). PET and SPECT are two main nuclear imaging techniques that are capable of providing tomographic and quantitative functional information inside a living subject.[169,170] In theory, natural nonradioactive substance in an organism's physiological and biochemical processes can be measured by its radioactive counterpart based on the tracer principle. In reality, most PET and SPECT procedures are performed with radiolabeled compounds, called radiopharmaceuticals or radiotracers or nuclear imaging probes, which rarely have their biological counterparts. The physical difference of PET and SPECT in the

Table 1. Radioisotopes of Interest for the Development of Dendrimer-Based Diagnostics and Therapeutics for Prostate Cancer[a]

radioisotope	half-life ($t_{1/2}$)	decay mode	labeling moieties	principal applications	ref
^{64}Cu	12.7 h	β^+ (17.4%) γ (40%)	DOTA CB-TE2A	PET, radiotherapy	171, 172
^{67}Ga	3.3 d	EC (100%)	NOTA	SPECT	173, 174
^{68}Ga	68 min	β^+ (90%) EC (10%)	DOTA, NOTA	PET	175
^{86}Y	14.7 h	β^+ (33%)	DOTA	PET, radiation dosimetry	176, 177
^{90}Y	64.1 h	β^- (100%)	DOTA	radioimmunotherapy	178–180
^{111}In	67.9 h	EC (100%)	DOTA	SPECT, radiotherapy	181–183
^{123}I	13 h	EC (87%) γ (85%)	tyrosine residue or Bolton-Hunter moiety	SPECT	184
^{124}I	4.2 d	β^+ (22%) γ (78%)		PET	185
^{125}I	59 d	γ (100%)		SPECT	186
^{131}I	8.0 d	β^- (89%) γ (81%)		SPECT, radiotherapy	187
^{177}Lu	6.7 d	β^- (100%) γ (27%)	DOTA	SPECT, radiotherapy	179
^{186}Re	3.8 d	β^- (93.1%) EC (6.9%)	HYNIC	SPECT, radiotherapy	188–190
^{188}Re	16.9 h	β^- (100%) γ (15%)	HYNIC	SPECT, radiotherapy	190–193

[a] EC: electron capture; DOTA: 1,4,7,10-tetraazacyclododecane-1,4,7,10-tetraacetic acid; NOTA: 1,4,7-triazacyclononane-1,4,7-triacetic acid; CB-TE2A: 2,2′-(1,4,8,11-tetraazabicyclo[6.6.2]-hexadecane-4,11-diyl)diacetic acid; HYNIC: 6-hydrazinonicotinamide.

use of radioisotopes dictates the types of hardware and software for the detection, localization, and quantification of the decay events. While PET detects pairs of 511 keV γ-rays resulted from the annihilation of positions emitted from the PET imaging probe with electrons, SPECT acquires γ-rays directly emitted for the radiotracer. Unlike visible light, γ-rays can easily pass through the body and be detected for quantitative imaging construction and data analysis. The commonly used radioisotopes in PET and SPECT are listed in Table 1.

Dendrimer nanoscaffolds have been commonly seen in PET and SPECT studies.[26,194] The purpose of incorporating a nuclear imaging reporter into the nanoconstructs is to track the *in vivo* distribution and quantify the targeted delivery of the nanoconstruct system. The conjugation chemistry approach is virtually identical to what have been described above. The only difference is that different radioisotopes of choice require their corresponding chelators or labeling functionalities (Table 1). This is based on the concept that the radiolabel moiety must remain stably attached to the nanoconstructs; otherwise the imaging readouts will not reflect the biological behavior of the nanoconstructs. It is noteworthy that dendrimer scaffolds conjugated with 1,4,7,10-tetraazacyclododecane-1,4,7,10-tetraacetic acid (DOTA) can be labeled with many different radioisotopes, which include ^{177}Lu, ^{111}In, and ^{67}Ga for SPECT imaging[179,183,194] or ^{68}Ga, ^{64}Cu, and ^{86}Y for PET imaging.[195−197] When considering a proper radioisotope for a specific application, the biological half-life of the nanoconstruct determines the radioisotope options. For instance, a low-generation dendrimer (G0−G3) that has a rapid clearance profile through kidneys should be labeled with a short-lived radioisotope, such as ^{68}Ga or ^{64}Cu. In contrast, a high-generation dendrimer (>G7) with long biological half-life should be labeled with a long-lived radioisotope, such as ^{111}In or ^{177}Lu. In the latter cases, the *in vivo* stability of the metal chelate moiety must be considered.

Among the noninvasive imaging techniques, PET or SPECT is exceptionally sensitive but with poor spatial resolution, while MRI has high spatial resolution and exquisite soft tissue contrast but with low sensitivity. Therefore, the synergistic combination of PET/MRI or SPECT/MRI will certainly be advantageous over MRI, PET, or SPECT alone.[198] To date, integrated PET/MRI scanners have been successfully implemented with potential to become the mainstream of molecular imaging in near future. For PET/MRI or SPECT/MRI, imaging agents that enable both imaging procedures could provide complementary information for a better diagnosis. However, the major challenge is how to overcome the large difference in sensitivity of the two techniques. Nanoparticle-based agents have been extensively pursued in this regard. Obviously, the design and synthesis of such dual-modality imaging probes can be readily realized by attaching bifunctional chelators to the surface of dendrimers loaded with superparamagnetic iron oxide (SPIO) or Gd(III) chelates. Information obtained from the dual-modality imaging of PET/MRI are anticipated to enable the perfect colocation and cross-validation of MRI and PET agents in the target regions of interest. While the MRI scan provides the anatomical information, motion artifact correction, and PET partial volume correction, the PET scan can be used for better imaging quantification so that higher detection sensitivity can be achieved with more accurate molecular signature changes over the course of study.[199−201]

■ THERAPEUTIC APPLICATIONS OF DENDRIMER NANOSCAFFOLDS

Dendrimer nanoscaffolds have been used to carry a variety of therapeutic agents for either passively or actively targeted delivery with the aim to improve the therapeutic efficacy of cancer treatment. The design and synthesis of therapeutic dendrimer-based drug delivery systems takes a similar methodology as described in the previous sections. The major design

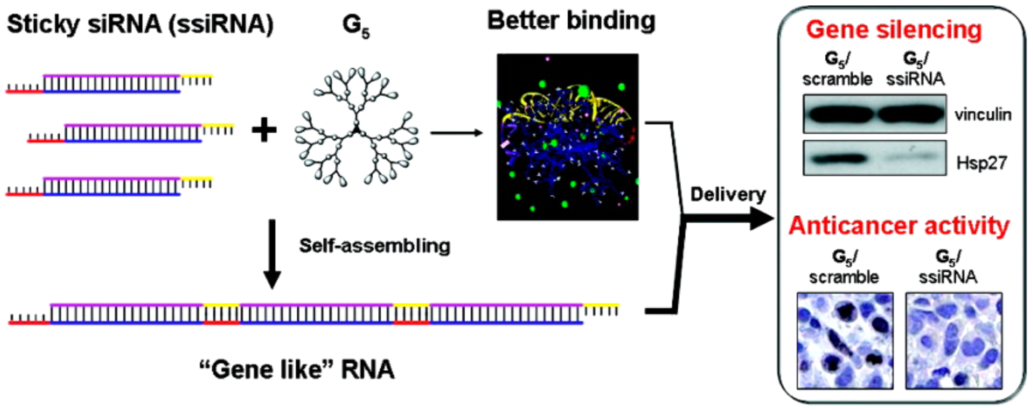

Figure 5. Self-assembly of siRNAs on a dendrimer scaffold for gene therapy of prostate cancer. The sticky siRNAs of heat shock protein 27 (Hsp27) bear complementary A*n*/T*n* (*n* = 5 or 7) 3′-overhangs (A*n*: yellow; T*n*: red). The overhangs serve two roles in this siRNA delivery vehicle design: facilitating the self-assembly of the siRNAs and noncovalently anchoring the siRNAs at the dendrimer scaffold for delivery. Reprinted from ref 221. Copyright 2012 American Chemical Society.

concerns include the biocompatibility of the nanocontructs, bioavailability of the loaded therapeutics (controlled release), and the *in vivo* kinetics of the dendrimer-based drug delivery system. In this section, we briefly discuss the therapeutic applications of dendrimer scaffolds categorized by common therapeutic interventions.

Chemotherapy. To date, many chemotherapy drugs have been seen in the construction of dendrimer-based drug delivery vehicles, which include Curcumin,[202−205] Genistein,[206] *cis*-diamminedichloroplatinum (Cisplatin),[147,188] PTX,[73,74] resveratrol,[207] DOX,[129] camptothecin (CPT),[148,149] and MTX.[40,150] Curcumin has shown potential to suppress *in vitro* prostate cancer cell proliferation in both androgen-sensitive prostate cancer cell line LNCaP and androgen-independent cell line DU145[202−205] and *in vivo* tumor growth in a LNCaP xenograft mouse model.[203] Similar inhibitive effects have been seen for Genistein to suppress prostate cancer growth.[206] The purpose of constructing a dendrimer-based drug delivery system is to improve the bioavailability and increase the payload of the drugs so as to achieve a more efficacious therapy while reducing the toxic effects on healthy tissues. It was found that the interior size of a dendrimer system plays an important role in the noncovalent packing of drugs. For instance, a high-generation dendrimer (G7−G9 PAMAM) has a tight structure, which provides less accessibility of drug molecules to the interior space. As such, a lower generation of PAMAM dendrimers (G4−G6) is preferred for the noncovalent loading of drugs into the interior space of the dendrimer (Figure 1).[29] Structural analysis showed that Cisplatin was able to bind to PAMAM dendrimers through the interaction between Pt cations and the hydrophilic region of peripheral amino groups.[208] PAMAM dendrimers were reported with great potential to encapsulate many chemotherapeutic drugs such as Curcumin, Genistein, and Resveratrol via noncovalent interactions. It was found that the encapsulation efficiency as measured by the binding affinity increases from G4 PAMAM to G4 PAMAM with PEG to G3 PAMAM with PEG, while the drug release rate was in the order of Curcumin > Cisplatin > Genistein > Resveratrol.[208] Hence, PAMAM-based dendrimer scaffolds are able to carry both hydrophilic and hydrophobic drugs depending on the spatial geometry of the dendrimer scaffolds. Poly(glycerol succinic acid) dendrimers (PGLSA dendrimers) were investigated to encapsulate hydrophobic CPTs, in which the peripheral groups of G4-PGLSA dendrimers were found with an important role in the encapsulation of a camptothecin analogue, 10-hydroxycamptothecin (10-HCPT).[209] While the G4-PGLSA dendrimer bearing hydroxyl groups (G4-PGLSA-OH) failed to encapsulate the drug molecules, the one with carboxylate groups (G4-PGLSA-COONa) succeeded. The G4-PGLSA-COONa dendrimer could also be loaded with 7-butyl-10-aminocamptothecin (BACPT). Encouragingly, both drug-encapsulated G4-PGLSA-COONa dendrimers showed a significant improved anticancer activity to various cancer cell lines.[210] The current challenge is how to overcome the lack of controlled release mechanisms.

In addition to the encapsulation approach, covalent linkages can also be utilized for drug loading. As discussed in the chemistry strategies of controlled drug release, chemical bonds selectively labile to different *in vivo* conditions are required. Given the two available conjugation sites of MTX, it can be nonvalently linked to a dendrimer scaffold through either carboxylate or amine groups.[211] While both dendrimer-MTX conjugates were formed by the amide linkage, the former showed an appreciable sensitivity increase against an MTX-resistant human leukemic lymphoblasts cell line, while no sensitivity increase was observed for the latter. This difference of therapeutic efficacy might be attributed to the dendrimer's surface charge after the release of MTX. Other dendrimer−drug conjugate systems were also reported for cisplatin,[212] indomethacin,[213] and paclitaxel.[74,214]

Gene Therapy: Suicide Gene, siRNA, and microRNA. Gene therapy is a therapeutic approach with the potential for prostate cancer therapy. However, with over 90 clinical protocols of gene therapy, only four of them progressed to phase III.[215] By far, viral systems are the most effective gene delivery carriers, but the safety concerns (e.g., acute toxicity, immunogenicity, and oncogenicity, etc.) remain the biggest hurdle for the translational and clinical trials.[216,217]

Recently, a nonviral delivery system constructed from a G5 PAMAM dendrimer was reported for herpes simplex virus (HSV)-thymidine kinase (TK)/ganciclovir (GCV) and connexin43 (Cx43) duo-suicide gene therapy. The G5-PAMAM conjugate delivered suicide genes TK-Cx43 led by a PSMA promoter, and this double-targeted and double-enhanced system was demonstrated being effective in inducing cell growth inhibition and apoptosis *in vitro* and suppressing tumor growth *in vivo* in PSMA$^+$ LNCaP tumors but not in PSMA$^-$ PC-3 tumors.[218]

RNA interference (RNAi) has emerged as a new promising approach for gene therapy. RNAi is a sequence-specific gene silencing process which is controlled by the RNA-induced silencing complex (RISC). With the specific sequence against the complementary mRNA, small interfering RNA (siRNA) can trigger RNAi activity, interfere mRNA translation, and further block the downstream protein synthesis. Given the great potential of this approach for gene therapy, tremendous efforts have been seen to apply available methods for siRNA delivery.[219−222] Of them, a cell-internalizing aptamer has shown great promise for gene therapy of prostate cancer by directing the siRNA delivery system to PSMA.[223] Recently, a PAMAM dendrimer with a triethanlamine (TEA) core was shown with the ability to directly serve as the vector of a siRNA targeting heat shock protein 27 (Hsp27),[224] an ATP-dependent molecular chaperone up-regulated during the hormone ablation and chemotherapies of prostate cancer treatment. The inhibition of Hsp27 expression leads to the increased level of caspase 3-dependent apoptosis thus suppressing tumor growth rate.[225,226] Through the self-assembly of the siRNA by adding complementary RNA with A_n/T_n 3′-overhangs, a lower-generation PAMAM dendrimer was found with potential to assemble siRNA for intracellular delivery. With this effective siRNA delivery system, silencing of Hsp27 gene was observed along with activated caspase 3-dependent apoptosis and inhibited tumor cell proliferation in a PC-3 xenograft mouse model (Figure 5).[221]

Although siRNA has been widely used, it is difficult to suppress the cancer progression via blocking a single gene activity. Recently, the discovery of microRNAs (miRNAs) has advanced RNAi into the mechanistic research of gene regulation.[227] A group of endogenous noncoding RNAs, microRNAs are able to either activate or inhibit protein translations.[228] Recent evidence indicates that miR-15a and miR-16-1 act as tumor suppressor genes in prostate cancer by down-regulating the expression of survival genes such as bcl2, ccnd1, and wnt3A.[229] When functionlized with maleimide groups, a G5 PAMAM dendrimer was reported with capability to deliver thiolated miR-15a and miR-16-1 into prostate cancer cells to induce the cell death.[130] This provides a new promising method to develop novel therapies against advanced prostate cancer.

Immunotherapy and Radioimmunotherapy. Due to the intrinsic low proliferation of prostate cancer, chemotherapy drugs aimed to ablate cancer cells with high proliferation index might not be effective. With the success of immunotherapy using Rituximab (anti-CD20) and Trastuzumab (anti-erbB2), monoclonal antibodies have become one of the fast-growing classes of cancer therapeutics,[230] which involves several prostate cancer related targets (e.g., prostate-specific antigen, mucin, and PSMA), and other cell surface receptors such as the epimermal growth factor receptor (EGFR) and the human epidermal growth factor receptor 2 (HER2/neu).[231] Cancer vaccine has also shown potential in prostate cancer therapy. To date, several prostate cancer associated antigens have been identified, which can serve as targets for vaccine development.[232] Moreover, by combining cancer vaccination and hormonal ablation therapy, a considerable expansion of vaccine-induced effector cells was observed. Therefore, active immunotherapy against prostate cancer might be more potent than the traditional chemotherapy against prostate cancer after androgen ablation treatment.[233] Not surprisingly, dendrimer has been used for vaccine delivery.[234]

Radioimmunotherapy is a straightforward extension of immunotherapy when the monoclonal antibody is labeled with a therapeutic radioisotope, such as ^{177}Lu, ^{90}Y, or ^{131}I.[235−237] The chemistry strategies involved in radioimmunotherapy are nearly identical to the approaches discussed in the imaging applications.

Cell receptor-based therapies also include the use of peptides or other small targeting molecules, which can be readily and cost-efficiently identified by combinatorial library approaches and synthesized by solid phase chemistry modules. Unlike monoclonal antibodies, these small receptor-specific ligands do not elicit immune-responses and can withstand harsh conditions for chemical modifications. Because small molecules often exhibit rapid *in vivo* kinetics, conjugating them with a dendrimer nanoscaffold is a convenient way of developing them for targeted cancer therapeutics.

■ TOWARD DENDRIMER-BASED THERANOSTICS OF PROSTATE CANCER THROUGH RADIOISOTOPE INCORPORATION

From the perspective of nuclear medicine, theranostics is just a new compound word. The concept and practice in nuclear medicine can be traced back to 1940s because of the straightforward dual use of radioisotopes that emit both β^- particles for therapy and γ-rays for scintigraphic diagnosis as in the routine clinical practice of using radioiodine nuclides for differentiated thyroid therapy. Indeed radioisotope imaging allows noninvasive and longitudinal assessment of drug delivery and thereafter treatment efficacy, which can also be elicited by radiotherapeutic particles emitted by the radioisotope itself. Similar radioisotopes to radioiodine are commonly seen in conventional nuclear medicine. For instance, both ^{186}Re ($t_{1/2}$ = 3.78 d) and ^{188}Re ($t_{1/2}$ = 16.9 h) can be used for SPECT imaging (γ-energies: 137 keV and 155 keV, respectively) and radiotherapy (β^- emissions: 1.07 MeV and 2.12 MeV, respectively) (Table 1).[188−193] Conveniently available from a commercially available generator, ^{188}Re is more commonly seen in research and clinical practice. The pair of ^{186}Re and ^{188}Re can be judiciously chosen for the radotherapeutic treatment of solid tumors with different sizes. While ^{188}Re is optimal for the radiotherapy of large tumors, the lower β^- emission energy makes ^{186}Re more suitable for small tumor treatment. To date, both ^{186}Re and ^{188}Re have been found in the construction of radioactive nanoconjugates.[192,238−240] For instance, ^{186}Re-labeled liposomes loaded with doxorubicin was reported for SPECT imaging and chemoradionuclide therapy of cancer in a head and neck squamous cell carcinoma xenograft rat model.[188] Multiple SPECT images acquired in a 120 h period showed the *in vivo* kinetics of the radioactive nanoconjugate, which had a slow blood clearance, low liver uptake, and an increasing deposition in both spleen and tumor. When labeled with ^{188}Re, PEGylated liposome-based nanoconjugates of doxorubicin were reported with therapeutic potential in various cancer animal models,[241−246] indicating that nanoscaffolding is a practical means to afford desired pharmacological and targeting properties for imaging and therapeutic agents.

Lutetium-177 ($t_{1/2}$ = 6.71 d) is also a radioisotope emitting both γ-rays (208 keV; 11%) and β^- particles (0.5 MeV), which can find applications in the development of theranostic agents. Obviously, approaches as described above are applicable to ^{177}Lu, and they have been seen in the literature. Mostly recently, a ^{177}Lu-labeled nanoconjugate constructed from C_{80}

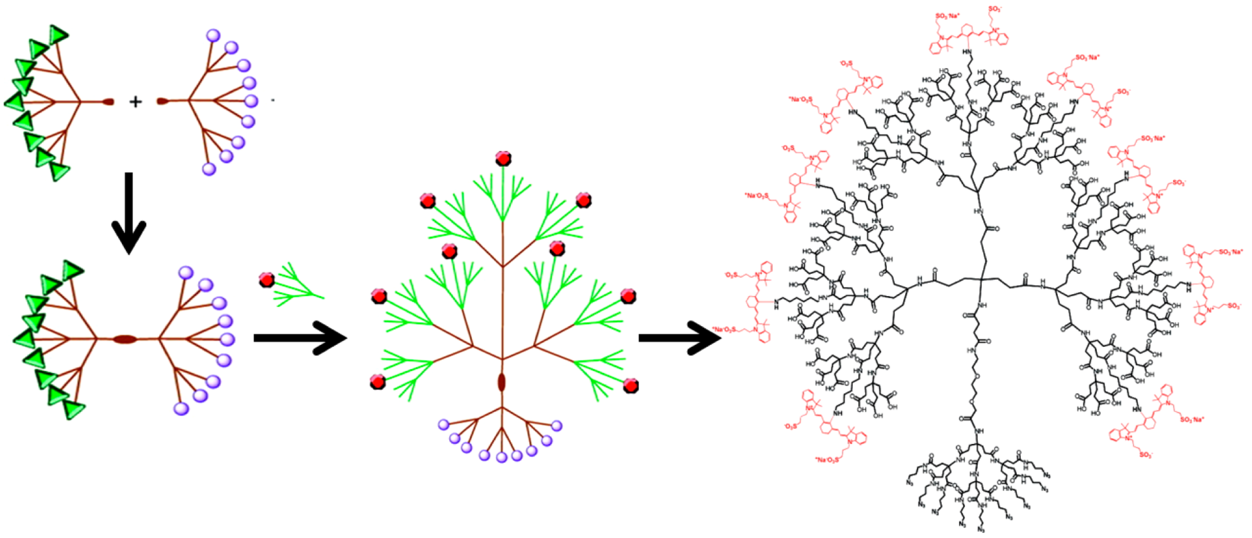

Figure 6. A Janus-like dendrimer system with potential to serve as scaffold to present stoichiometric multifunctionalities for the development of theranostic agents. The dendrimer core is depicted in dark red; azide groups in purple; amine termini in red; and the terminal acid groups in green. Reprinted from ref 78. Copyright 2011 American Chemical Society.

fullerenes (^{177}Lu-DOTA-f-$Gd_3N@C_{80}$) was reported as a theranostic agent to deliver effective interstitial brachytherapy in two orthotopic xenograft brain tumor models of glioblastoma multiforme (GBM).[247] Although the SPECT imaging potential with ^{177}Lu-DOTA-f-$Gd_3N@C_{80}$ was not performed or mentioned in the paper, it can definitely provide a noninvasive and quantitative tool to monitor the delivery and therapeutic efficacy of the radioactive nanoconstruct.

Obviously, other radioisotopes including ^{64}Cu and ^{111}In that emit positrons or γ-rays for PET or SPECT imaging and β^- or Auger electrons for radiotherapy can be simply used to construct theranostic agents in the form of either small molecules or nanoconjugates.

However, even with straightforward approaches for the design and synthesis of radioactive nanoconstructs for theranostic agent development, using radioisotopes is not always considered as an ideal method in this endeavor. Unnecessary radiation exposure and public fear of radiation are among the main concerns. Another major issue with the radioisotope-enabled theranostics is that radioactive decay is always going on and irradiates the whole body when systemically administered. From the perspective of *in vivo* pharmacokinetics, radioisotope-labeled nanoconjugates might not be able to find a practical application in clinics because of the excessive irradiation to nontarget organs resulting from the inevitable passive accumulation in the RES organs and the long blood circulation half-life of the nanoconjugates unless they can be efficiently cleared from kidneys.[248,249] On the other hand, small molecules with organ-specific targeting properties and an efficient clearance profile can be well-positioned in the development of radioisotope-enabled theranostic agents as in the conventional nuclear medicine practice with radioiodine.

The design and synthesis of theranostic agents other than radioisotope-enabled ones remains challenging. In this regard, nanoscaffolds are advantageous over small molecules in that a nanoscaffold typically presents multiple functionalities and a high potential payload for functional molecules. In other words, the capability of multipresentation of a molecule and multiplexing of different functionalities makes nanoscaffolds an appealing class of carriers for targeted delivery of both diagnostics and therapeutics in a single entity, namely, a theranostic agent. As discussed above, given the unique structural features and proven potential in both imaging and therapy applications, dendrimers are a practical class of nanoscaffolds that can find active roles in the development of theranostics. However, in spite of the functional versatility of dendrimers, a theranostic agent cannot simply be prepared by presenting three different functionalities (diagnostics, therapeutics, and targeting vector) on a single dendrimer nanoscaffold. Although a dendrimer system has a well-defined structure, presenting different functionalities may incur unexpected chemical interference between different functional groups or regions, which would result in a failed or an irreproducible reaction. From the perspective of chemistry, an ideal dendrimer nanoscaffold should present different functional groups with a defined stoichiometry for orthogonal functionalization so as to achieve the designed theranostics reproducibly in a controlled manner. Such examples exist in the literature. For instance, a Janus-like dendrimer scaffold formed by combining two separately synthesized dendrons was recently reported. Shown in Figure 6, this Janus-like dendrimer system presents different functionalities with defined stoichiometry: 9 azide, 9 amine, and 54 carboxylate groups,[78] which enabled an orthogonal functionalization to present the defined number of each functional molecule for a potential theranostic agent.

The systematic development of theranostic agents based on nanoscaffolds is still in its infancy, although promising examples have been shown in the literatures. To illustrate the basic concept and current status of nanoscaffold-based theranostic agent development, we summarized the key components that have been used for the construction of theranostic agents in Table 2.

In summary, while advances in the field of theranostic agent development are obvious, challenges still remain to be addressed even in the preclinical development status: (1) dosage difference between the components of therapeutics and diagnostics if a dual-use radioisotope is used; (2) passive uptake in RES organs; (3) toxicity and aggregation of dendrimer scaffolds after functionalization; (4) bioavailability or controlled release of loaded therapeutics; (5) different requirements of *in*

Table 2. Functional Components with Proven Potential for the Design and Construction of Prostate Cancer Theranostics

application	type or module	functionalities	references
active targeting	peptide	RGD peptide (cRGDyk)	141, 142
	PSMA-targeted antibody	J591/MLN591	115, 119
		7E11-C5.3	110, 112, 115
		E6	111
		J415	115
	PSMA-targeted aptamer	A10 aptamer	129
		A10-3.2 aptamer	130
passive targeting	EPR effect	Carrier's size	73, 74, 100, 101
diagnostics	MRI	gadolinium (Gd), SPIO	145−147, 149
	CT	tri-iodophthalamide	154
	optical imaging	near-infrared fluorophore (Cy5.5 and Rhodamine)	168
	PET or SPECT	PET: ^{64}Cu, ^{68}Ga, ^{86}Y	195−197
		SPECT: ^{111}In, ^{67}Ga, ^{177}Lu, $^{186/188}$Re, $^{123/125/131}$I	188, 241−247, 250−252
therapeutics	chemotherapy drug	curcumin	202−205
		genistein	206
		cisplatin	208, 253
		paclitaxel (PTX)	73, 74, 208, 214, 253
		resveratrol	207
		doxorubicin (DOX)	129
		camptothecins (CPT)	209, 210
		methotrexate (MTX)	62, 211
	gene therapy	suicide gene (HSK-TK/Cx43)	218
		small interfering RNAs	224
		miR-15a and miR-16-1	130, 224
	immunotherapy	rituximab (anti-CD20)	230
		trastuzumab (anti-erbB2)	230, 231
		hMAb425 (anti-EGFR antibody)	231
	radiotherapy	^{90}Y, ^{64}Cu, ^{177}Lu, $^{186/188}$Re, ^{131}I	188, 235−237, 241−247

vivo pharmacokinetics for therapeutics and diagnostics; and (6) administration routes and dosing plan for optimal diagnostic value and therapeutic efficacy. The FDA regulations governing the diagnostic and therapeutic agents are expected to become the main hurdles when a nanoscaffold-based theranostic agent reaches the translational status toward the eventual applications in human trials. For small molecular theranostics enabled by dual-use radioisotopes, especially those that have been in FDA's approval, the translational human trials could be more straightforward.

Knowing the status of molecular target(s) of disease before, during, and after therapy, theranostic agents are expected to play a critical role in personalized medicine. While challenges remain, the perspective of theranostic agents is promising. The future realization of clinical theranostic practice requires tenacious multidisciplinary efforts from chemists to oncologists and cross-specialty coordination between radiologists and oncologists in today's preclinical development.

■ AUTHOR INFORMATION

Corresponding Author

*Phone: 214-645-5978. Fax: 214-645-2885. E-mail: Xiankai.Sun@UTSouthwestern.edu.

Notes

The authors declare no competing financial interest.

■ ACKNOWLEDGMENTS

The authors acknowledge the funding support to their work on developing theranostic agents for prostate cancer by the National Institutes of Health (R01CA159144, J.T.H.) and the Prostate Cancer Research Program of the United States Army Medical Research and Materiel Command (W81XWH-12-1-0336P1, X.S. and W81XWH-12-1-0336P2, J.T.H.).

■ REFERENCES

(1) Slamon, D. J.; Godolphin, W.; Jones, L. A.; Holt, J. A.; Wong, S. G.; Keith, D. E.; Levin, W. J.; Stuart, S. G.; Udove, J.; Ullrich, A. Studies of the HER-2/neu proto-oncogene in human breast and ovarian cancer. *Science* **1989**, *244* (4905), 707−712.

(2) Lynch, T. J.; Bell, D. W.; Sordella, R.; Gurubhagavatula, S.; Okimito, R. A.; Brannigan, B. A.; Harris, P. L.; Haserlat, S. M.; Supko, J. G.; Haluska, F. G.; Loius, D. N.; Christiani, D. C.; Settleman, J.; Haber, D. A. Activating mutations in the epidermal growth factor receptor underlying responsiveness of non-small-cell lung cancer to gefitinib. *N. Engl. J. Med.* **2004**, *350* (21), 2129−2139.

(3) Paez, J. G.; Janne, P. A.; Lee, J. C.; Tracy, S.; Greulich, H.; Gabriel, S.; Herman, P.; Kaye, F. J.; Lindeman, N.; Boggon, T. J.; Naoko, K.; Sasaki, H.; Jujji, Y.; Eck, M. J.; Sellers, W. R.; Johnson, B. E.; Meyerson, M. EGFR mutations in lung cancer: correlation with clininical response to gefitinib therapy. *Science* **2004**, *304* (5676), 1497−1500.

(4) Minna, J. D.; Gazdar, A.; Sprang, S. R.; Herz, J. Cancer. A bull's eye for targeted lung therapy. *Science* **2004**, *304* (5676), 1458−1461.

(5) Dancey, J. E. Predictive factors for epidermal growth factor receptor inhibitors- the bull's-eye hits the arrow. *Cancer Cell* **2004**, *5* (5), 411−415.

(6) Arteaga, C. L. Selecting the right patient for tumor therapy. *Nat. Med.* **2004**, *10* (6), 577−578.

(7) Janib, S. M.; Moses, A. S.; MacKay, J. A. Imaging and drug delivery using theranostic nanoparticles. *Adv. Drug Delivery Rev.* **2010**, *62* (11), 1052−1063.

(8) Lee, D. Y.; Li, K. C. Molecular theranostics: a primer for the imaging professional. *Am. J. Roentgenol.* **2011**, *197* (2), 318−324.

(9) Grayson, S. M.; Frechet, J. M. J. Convergent dendrons and dendrimers: from synthesis to applications. *Chem. Rev.* **2001**, *101* (12), 3819−3867.

(10) Lee, C. C.; MacKay, J. A.; Frechet, J. M. J.; Szoka, F. C. Designing dendrimers for biological applications. *Nat. Biotechnol.* **2005**, *23* (12), 1517−1526.

(11) Liu, M. J.; Frechet, J. M. J. Designing dendrimers for drug delivery. *Pharm. Sci. Technol. Today* **1999**, *2* (10), 393−401.

(12) Frechet, J. M. J. Functional polymers and dendrimers: reactivity, molecular architecture, and interfacial energy. *Science* **1994**, *263* (5154), 1710−1715.

(13) Svec, F.; Frechet, J. M. J. New designs of macroporous polymers and supports: From separation to biocatalysis. *Science* **1996**, *273* (5272), 205−211.

(14) Luo, Y.; Prestwich, G. D. Cancer-targeted polymeric drugs. *Curr. Cancer Drug Targets* **2002**, *2* (3), 209−226.

(15) Chen, Z.; Penet, M. F.; Nimmagadda, S.; Li, C.; Banerjee, S. R.; Winnard, P. T., Jr.; Artemov, D.; Glunde, K.; Pomper, M. G.; Bhujwalla, Z. M. PSMA-targeted theranostic nanoplex for prostate cancer therapy. *ACS Nano* **2012**, *6* (9), 7752−7762.

(16) Lukianova-Hleb, E. Y.; Oginsky, A. O.; Samaniego, A. P.; Shenefelt, D. L.; Wagner, D. S.; Hafner, J. H.; Farach-Carson, M. C.;

Lapotko, D. O. Tunable plasmonic nanoprobes for theranostics of prostate cancer. *Theranostics* **2011**, *1*, 3−17.

(17) Svenson, S.; Tomalia, D. A. Dendrimers in biomedical applications—reflections on the field. *Adv. Drug Delivery Rev.* **2005**, *57* (15), 2106−2129.

(18) Gillies, E. R.; Frechet, J. M. J. Dendrimers and dendritic polymers in drug delivery. *Drug Discovery Today* **2005**, *10* (1), 35−43.

(19) Fréchet, J. M. J.; Tomalia, D. A. *Dendrimers and other dendritic polymers*; Wiley: New York, 2001.

(20) Ahmed, N.; Fessi, H.; Elaissari, A. Theranostic applications of nanoparticles in cancer. *Drug Discovery Today* **2012**, *17* (17−18), 928−934.

(21) Jokerst, J. V.; Gambhir, S. S. Molecular imaging with theranostic nanoparticles. *Acc. Chem. Res.* **2011**, *44* (10), 1050−1060.

(22) Ma, X.; Zhao, Y.; Liang, X. J. Theranostic nanoparticles engineered for clinic and pharmaceutics. *Acc. Chem. Res.* **2011**, *44* (10), 1114−1122.

(23) Menjoge, A. R.; Kannan, R. M.; Tomalia, D. A. Dendrimer-based drug and imaging conjugates: design considerations for nanomedical applications. *Drug Discovery Today* **2010**, *15* (5−6), 171−185.

(24) Rudin, M. *Molecular imaging: principles and applications in biomedical research*; Imperial College Press: London, UK, 2005.

(25) Hahn, M. A.; Singh, A. K.; Sharma, P.; Brwon, S. C.; Moudgil, B. M. Nanoparticles as contrast agents for in-vivo bioimaging: current status and future perspectives. *Anal. Bioanal. Chem.* **2011**, *399* (1), 3−27.

(26) Debbage, P.; Jaschke, W. Molecular imaging with nanoparticles: giant roles for dwarf actors. *Histochem. Cell Biol.* **2008**, *130* (5), 845−875.

(27) Jin, M. H. G.; Sun, X.; Chen, W. Nanoparticle-based positron emission tomography and single photon emission computed tomography imaging of cancer. *Rev. Nanosci. Nanotechnol.* **2012**, *1* (19), 3−21.

(28) Kobayashi, H.; Sato, N.; Saga, T.; Nakamoto, Y.; Ishimori, T.; Toyama, S.; Togashi, K.; Konishi, J.; Brechbiel, M. W. Monoclonal antibody-dendrimer conjugates enable radiolabeling of antibody with markedly high specific activity with minimal loss of immunoreactivity. *Eur. J. Nucl. Med.* **2000**, *27* (9), 1334−1339.

(29) Wolinsky, J. B.; Grinstaff, M. W. Therapeutic and diagnostic applications of dendrimers for cancer treatment. *Adv. Drug Delivery Rev.* **2008**, *60* (9), 1037−1055.

(30) Nanjwade, B. K.; Bechra, H. M.; Derkar, G. K.; Manvi, F. V.; Nanjwade, V. K. Dendrimers: emerging polymers for drug-delivery systems. *Eur. J. Pharm. Sci.* **2009**, *38* (3), 185−196.

(31) Fuchs, S.; Kapp, T.; Otto, H.; Schöneberg, T.; Franke, P.; Gust, R.; Schlüter, A. D. A surface-modified dendrimer set for potential application as drug delivery vehicles: synthesis, in vitro toxicity, and intracellular localization. *Chem.—Eur. J.* **2004**, *10* (5), 1167−1192.

(32) Jones, S. P.; Gabrielson, N. P.; Pack, D. W.; Smith, D. K. Synergistic effects in gene delivery-a structure-activity approach to the optimization of hybrid dendritic-lipidic transfection agents. *Chem. Commun.* **2008**, *39*, 4700−4702.

(33) Berna, M.; Dalzoppo, D.; Pasut, G.; Manunta, M.; Izzo, L.; Jones, A. T.; Duncan, R.; Veronese, F. M. Novel monodisperse PEG−dendrons as new tools for targeted drug delivery: synthesis, characterization and cellular uptake. *Biomacromolecules* **2005**, *7* (1), 146−153.

(34) Reul, R.; Renette, T.; Bege, N.; Kissel, T. Nanoparticles for paclitaxel delivery: A comparative study of different types of dendritic polyesters and their degradation behavior. *Int. J. Pharmaceutics* **2011**, *407* (1−2), 190−196.

(35) Langereis, S.; de Lussanet, Q. G.; van Genderen, M. H. P.; Meijer, E. W.; Beets-Tan, R. G. H.; Griffioen, A. W.; van Engelshoven, J. M. A.; Backes, W. H. Evaluation of Gd(III)DTPA-terminated poly(propylene imine) dendrimers as contrast agents for MR imaging. *NMR Biomed.* **2006**, *19* (1), 133−141.

(36) Rolland, O.; Turrin, C.-O.; Caminade, A.-M.; Majoral, J.-P. Dendrimers and nanomedicine: multivalency in action. *New J. Chem.* **2009**, *33* (9), 1809−1824.

(37) Paleos, C. M.; Tsiourvas, D.; Sideratou, Z.; Tziveleka, L.-A. Drug delivery using multifunctional dendrimers and hyperbranched polymers. *Exp. Opin. Drug Delivery* **2010**, *7* (12), 1387−1398.

(38) Chabre, Y. M.; Roy, R. Recent trends in glycodendrimer syntheses and applications. *Curr. Top. Med. Chem.* **2008**, *8* (14), 1237−1285.

(39) Garner, A. L.; Park, J.; Zakhari, J. S.; Lowery, C. A.; Struss, A. K.; Sawada, D.; Kaufmann, G. F.; Janda, K. D. A multivalent probe for AI-2 quorum-sensing receptors. *J. Am. Chem. Soc.* **2011**, *133* (40), 15934−15937.

(40) Schlick, K. H.; Udelhoven, R. A.; Strohniever, G. C.; Cloninger, M. J. Binding of mannose-functionalized dendrimers with pea (Pisum sativum) lectin. *Mol. Pharmaceutics* **2005**, *2* (4), 295−301.

(41) Maheshwari, G.; Brown, G.; Lauffenburger, D. A.; Wells, A.; Griffith, L. G. Cell adhesion and motility depend on nanoscale RGD clustering. *J. Cell Sci.* **2000**, *113* (10), 1677−1686.

(42) Fuki, I. V.; Kuhn, K. M.; Lomazov, I. R.; Rothman, V. L.; Tuszynski, G. P.; Iozzo, R. V.; Swenson, T. L.; Fisher, E. A.; Williams, K. J. The syndecan family of proteoglycans - Novel receptors mediating internalization of atherogenic lipoproteins in vitro. *J. Clin. Invest.* **1997**, *100* (6), 1611−1622.

(43) Schlick, K. H.; Morgan, J. R.; Weiel, J. J.; Kelsey, M. S.; Cloninger, M. J. Clusters of ligands on dendrimer surfaces. *Bioorg. Med. Chem. Lett.* **2011**, *21* (17), 5078−5083.

(44) Venkataraman, S.; Hedrick, J. L.; Ong, Z. Y.; Yang, C.; Ee, P. L. R.; Hammond, P. T.; Yang, Y. Y. The effects of polymeric nanostructure shape on drug delivery. *Adv. Drug Delivery Rev.* **2011**, *63* (14−15), 1228−1246.

(45) Jansen, J. F. G. A.; de Brabander-van den Berg, E. M. M.; Meijer, E. W. Encapsulation of guest molecules into a dendritic box. *Science* **1994**, *266* (5188), 1226−1229.

(46) van Hest, J. C. M.; Delnoye, D. A. P.; Baars, M. W. P. L.; van Genderen, M. H. P.; Meijer, E. W. Polystyrene-dendrimer amphiphilic block copolymers with a generation-dependent aggregation. *Science* **1995**, *268* (5217), 1592−1595.

(47) Kirkpatrick, G. J.; Plumb, J. A.; Sutcliffe, O. B.; Flint, D. J.; Wheate, N. J. Evaluation of anionic half generation 3.5−6.5 poly(amidoamine) dendrimers as delivery vehicles for the active component of the anticancer drug cisplatin. *J. Inorg. Biochem.* **2011**, *105* (9), 1115−1122.

(48) Tziveleka, L.-A.; Kontoyianni, C.; Sideratou, Z.; Tsiourvas, D.; Paleos, C. M. Novel Functional Hyperbranched Polyether Polyols as Prospective Drug Delivery Systems. *Macromol. Biosci.* **2006**, *6* (2), 161−169.

(49) Paleos, C. M.; Tsiourvas, D.; Sideratou, Z.; Tziveleka, L. Acid- and salt-triggered multifunctional poly(propylene imine) dendrimer as a prospective drug delivery system. *Biomacromolecules* **2004**, *5* (2), 524−529.

(50) Sideratou, Z.; Sterioti, N.; Tsiourvas, D.; Tziveleka, L.-A.; Thanassoulas, A.; Nounesis, G.; Paleos, C. M. Arginine end-functionalized poly(l-lysine) dendrigrafts for the stabilization and controlled release of insulin. *J. Colloid Interface Sci.* **2010**, *351* (2), 433−441.

(51) Kono, K.; Kojima, C.; Hayashi, N.; Nishisaka, E.; Kiura, K.; Wataral, S.; Harada, A. Preparation and cytotoxic activity of poly(ethylene glycol)-modified poly(amidoamine) dendrimers bearing adriamycin. *Biomaterials* **2008**, *29* (11), 1664−1675.

(52) Kurtoglu, Y. E.; Mishra, M. K.; Kannan, S.; Kannan, R. M. Drug release characteristics of PAMAM dendrimer-drug conjugates with different linkers. *Int. J. Pharmaceutics* **2010**, *384* (1−2), 189−194.

(53) Chang, Y. L.; Liu, N. A.; Chen, L.; Meng, X. L.; Liu, Y. J.; Li, Y. P.; Wang, J. Y. Synthesis and characterization of DOX-conjugated dendrimer-modified magnetic iron oxide conjugates for magnetic resonance imaging, targeting, and drug delivery. *J. Mater. Chem.* **2012**, *22* (19), 9594−9601.

(54) Agarwal, A.; Gupta, U.; Asthana, A.; Jain, N. K. Dextran conjugated dendritic nanoconstructs as potential vectors for anti-cancer agent. *Biomaterials* **2009**, *30* (21), 3588–3596.

(55) Lee, C. C.; Gillies, E. R.; Fox, M. E.; Guillaudeu, S. J.; Fréchet, J. M. J.; Dy, E. E.; Szoka, F. C. A single dose of doxorubicin-functionalized bow-tie dendrimer cures mice bearing C-26 colon carcinomas. *Proc. Natl. Acad. Sci. U.S.A.* **2006**, *103* (45), 16649–16654.

(56) Lim, J.; Chouai, A.; Lo, S. T.; Liu, W.; Sun, X.; Simanek, E. E. Design, synthesis, characterization, and biological evaluation of triazine dendrimers bearing paclitaxel using ester and ester/disulfide linkages. *Bioconjugate Chem.* **2009**, *20* (11), 2154–2161.

(57) Roller, S.; Zhou, H.; Haag, R. High-loading polyglycerol supported reagents for Mitsunobu- and acylation-reactions and other useful polyglycerol derivatives. *Mol. Divers.* **2005**, *9* (4), 305–316.

(58) Seebach, D.; Herrmann, G. F.; Lengweiler, U. D.; Bachmann, B. M.; Amrein, W. Synthesis and Enzymatic Degradation of Dendrimers from (R)-3-Hydroxybutanoic Acid and Trimesic Acid. *Angew. Chem., Int. Ed. Engl.* **1996**, *35* (23–24), 2795–2797.

(59) Kolhe, P.; Khandare, J.; Pillai, O.; Kannan, S.; Lieh-Lal, M.; Kannan, R. M. Preparation, cellular transport, and activity of polyamidoamine-based dendritic nanodevices with a high drug payload. *Biomaterials* **2006**, *27* (4), 660–669.

(60) Najlah, M.; Freeman, S.; Attwood, D.; D'Emanuele, A. In vitro evaluation of dendrimer prodrugs for oral drug delivery. *Int. J. Pharmaceutics* **2007**, *336* (1), 183–190.

(61) Quintana, A.; Raczka, E.; Piehler, L.; Lee, I.; Myc, A.; Majoros, I.; Patri, A. K.; Thomas, T.; Mule, J.; Baker, J. R. Design and function of a dendrimer-based therapeutic nanodevice targeted to tumor cells through the folate receptor. *Pharm. Res.* **2002**, *19* (9), 1310–1316.

(62) Thomas, T. P.; Majoros, I. J.; Kotlyar, A.; Kukowska-Latallo, J. F.; Bielinska, A.; Myc, A.; Baker, J. R. Targeting and inhibition of cell growth by an engineered dendritic nanodevice. *J. Med. Chem.* **2005**, *48* (11), 3729–3735.

(63) Kale, A. A.; Torchilin, V. P. Design, synthesis, and characterization of pH-sensitive PEG-PE conjugates for stimuli-sensitive pharmaceutical nanocarriers: the effect of substitutes at the hydrazone linkage on the ph stability of PEG-PE conjugates. *Bioconjugate Chem.* **2007**, *18* (2), 363–370.

(64) Shen, W. C.; Ryser, H. J. cis-Aconityl spacer between daunomycin and macromolecular carriers: a model of pH-sensitive linkage releasing drug from a lysosomotropic conjugate. *Biochem. Biophys. Res. Commun.* **1981**, *102* (3), 1048–1054.

(65) Zhu, S.; Hong, M.; Tang, G.; Qian, L.; Lin, J.; Jiang, Y.; Pei, Y. Partly PEGylated polyamidoamine dendrimer for tumor-selective targeting of doxorubicin: The effects of PEGylation degree and drug conjugation style. *Biomaterials* **2010**, *31* (6), 1360–1371.

(66) Gilbert, H. F. Thiol/disulfide exchange equilibria and disulfidebond stability. In *Methods in Enzymology*; Lester, P., Ed.; Academic Press: New York, 1995; Vol. *251*, pp 8–28.

(67) Meister, A.; Anderson, M. E. Glutathione. *Annu. Rev. Biochem.* **1983**, *52* (1), 711–760.

(68) Russo, A.; DeGraff, W.; Friedman, N.; Mitchell, J. B. Selective modulation of glutathione levels in human normal versus tumor cells and subsequent differential response to chemotherapy drugs. *Cancer Res.* **1986**, *46* (6), 2845–2848.

(69) Navath, R. S.; Kurtoglu, Y. E.; Wang, B.; Kannan, S.; Romero, R.; Kannan, R. M. Dendrimer-drug conjugates for tailored intracellular drug release based on glutathione levels. *Bioconjugate Chem.* **2008**, *19* (12), 2446–2455.

(70) Wang, B.; Navath, R. S.; Romero, R.; Kannan, S.; Kannan, R. Anti-inflammatory and anti-oxidant activity of anionic dendrimer-N-acetyl cysteine conjugates in activated microglial cells. *Int. J. Pharmaceutics* **2009**, *377* (1–2), 159–168.

(71) Kurtoglu, Y. E.; Navath, R. S.; Wang, B.; Kannan, S.; Romero, R.; Kannan, R. M. Poly(amidoamine) dendrimer-drug conjugates with disulfide linkages for intracellular drug delivery. *Biomaterials* **2009**, *30* (11), 2112–2121.

(72) Navath, R. S.; Wang, B.; Kannan, S.; Romero, R.; Kannan, R. M. Stimuli-responsive star poly(ethylene glycol) drug conjugates for improved intracellular delivery of the drug in neuroinflammation. *J. Controlled Release* **2010**, *142* (3), 447–456.

(73) Lim, J.; Lo, S. T.; Hill, S.; Pavan, G. M.; Sun, X.; Simanek, E. E. Antitumor activity and molecular dynamics simulations of paclitaxel-laden triazine dendrimers. *Mol. Pharmaceutics* **2012**, *9* (3), 404–412.

(74) Lo, S. T.; Stern, S.; Clogston, J. D.; Zheng, J.; Adiseshaiah, P. P.; Dobrovolskaia, M.; Lim, J.; Patri, A. K.; Sun, X.; Simanek, E. E. Biological assessment of triazine dendrimer: toxicological profiles, solution behavior, biodistribution, drug release and efficacy in a PEGylated, paclitaxel construct. *Mol. Pharmaceutics* **2010**, *7* (4), 993–1006.

(75) Mullen, D. G.; Fang, M.; Desai, A.; Baker, J. R.; Orr, B. G.; Banaszak Holl, M. M. A Quantitative assessment of nanoparticle–ligand distributions: implications for targeted drug and imaging delivery in dendrimer conjugates. *ACS Nano* **2010**, *4* (2), 657–670.

(76) Mullen, D. G.; Borgmeier, E. L.; Desai, A. M.; van Dongen, M. A.; Barash, M.; Cheng, X. M.; Baker, J. R.; Holl, M. M. B. Isolation and characterization of dendrimers with precise numbers of functional groups. *Chem.—Eur. J.* **2010**, *16* (35), 10675–10678.

(77) Hakem, I. F.; Leech, A. M.; Johnson, J. D.; Donahue, S. J.; Walker, J. P.; Bockstaller, M. R. Understanding ligand distributions in modified particle and particlelike systems. *J. Am. Chem. Soc.* **2010**, *132* (46), 16593–16598.

(78) Ornelas, C.; Pennell, R.; Liebes, L. F.; Weck, M. Construction of a well-defined multifunctional dendrimer for theranostics. *Org. Lett.* **2011**, *13* (5), 976–979.

(79) Sapsford, K. E.; Tyner, K. M.; Dair, B. J.; Deschamps, J. R.; Medintz, I. L. Analyzing nanomaterial bioconjugates: a review of current and emerging purification and characterization techniques. *Anal. Chem.* **2011**, *83* (12), 4453–4488.

(80) Mullen, D. G.; Holl, M. M. B. Heterogeneous ligand-nanoparticle distributions: a major obstacle to scientific understanding and commercial translation. *Acc. Chem. Res.* **2011**, *44* (11), 1135–1145.

(81) Zong, H.; Thomas, T. P.; Lee, K. H.; Desai, A. M.; Li, M. H.; Kotlyar, A.; Zhang, Y. H.; Leroueil, P. R.; Gam, J. J.; Holl, M. M. B.; Baker, J. R. Bifunctional PAMAM dendrimer conjugates of folic acid and methotrexate with defined ratio. *Biomacromolecules* **2012**, *13* (4), 982–991.

(82) Mullen, D. G.; Desai, A.; van Dongen, M. A.; Barash, M.; Baker, J. R.; Banaszak Holl, M. M. Best practices for purification and characterization of PAMAM dendrimer. *Macromolecules* **2012**, *45* (12), 5316–5320.

(83) Thomas, T. P.; Huang, B.; Choi, S. K.; Silpe, J. E.; Kotlyar, A.; Desai, A. M.; Zong, H.; Gam, J.; Joice, M.; Baker, J. R. Polyvalent dendrimer-methotrexate as a folate receptor-targeted cancer therapeutic. *Mol. Pharmaceutics* **2012**, *9* (9), 2669–2676.

(84) Karthikeyan, B. K. P. V. Prednisolone conjugated polypropylene imine dendritic architecture confers. reducing hemolytic toxicity- a comparative study. *Int. J. Drug Dev. Res.* **2012**, *4* (2), 188–194.

(85) Roberts, J. C.; Bhalgat, M. K.; Zera, R. T. Preliminary biological evaluation of polyamidoamine (PAMAM) Starburst dendrimers. *J. Biomed. Mater. Res.* **1996**, *30* (1), 53–65.

(86) Malik, N.; Wiwattanapatapee, R.; Klopsch, R.; Lorenz, K.; Frey, H.; Weener, J. W.; Meijer, E. W.; Paulus, W.; Duncan, R. Dendrimers: relationship between structure and biocompatibility in vitro, and preliminary studies on the biodistribution of ^{125}I-labelled polyamidoamine dendrimers in vivo. *J. Controlled Release* **2000**, *65* (1–2), 133–148.

(87) Najlah, M.; Freeman, S.; Attwood, D.; D'Emanuele, A. In vitro evaluation of dendrimer prodrugs for oral drug delivery. *Int. J. Pharmaceutics* **2007**, *336* (1), 183–190.

(88) Kolhatkar, R. B.; Kitchens, K. M.; Swaan, P. W.; Ghandehari, H. Surface acetylation of polyamidoamine (PAMAM) dendrimers decreases cytotoxicity while maintaining membrane permeability. *Bioconjugate Chem.* **2007**, *18* (6), 2054–2060.

(89) Sadekar, S.; Ghandehari, H. Transepithelial transport and toxicity of PAMAM dendrimers: implications for oral drug delivery. *Adv. Drug Delivery Rev.* **2012**, *64* (6), 571–588.

(90) Yang, H.; Lopina, S. T.; DiPersio, L. P.; Schmidt, S. P. Stealth dendrimers for drug delivery: correlation between PEGylation, cytocompatibility, and drug payload. *J. Mater. Sci. Mater. Med.* **2008**, *19* (5), 1991−1997.

(91) Tang, Y.; Li, Y. B.; Wang, B.; Lin, R. Y.; van Dongen, M.; Zurcher, D. M.; Gu, X. Y.; Banaszak Holl, M. M.; Liu, G.; Qi, R. Efficient in vitro siRNA delivery and intramuscular gene silencing using PEG-modified PAMAM dendrimers. *Mol. Pharmaceutics* **2012**, *9* (6), 1812−1821.

(92) Aungst, B. J. Intestinal permeation enhancers. *J. Pharm. Sci.* **2000**, *89* (4), 429−442.

(93) Jevprasesphant, R.; Penny, J.; Jalal, R.; Attwood, D.; McKeown, N. B.; D'Emanuele, A. The influence of surface modification on the cytotoxicity of PAMAM dendrimers. *Int. J. Pharmaceutics* **2003**, *252* (1−2), 263−266.

(94) Thanou, M.; Duncan, R. Polymer-protein and polymer-drug conjugates in cancer therapy. *Curr. Opin. Invest. Drugs* **2003**, *4* (6), 701−709.

(95) Duncan, R. The dawning era of polymer therapeutics. *Nat. Rev. Drug Discovery* **2003**, *2* (5), 347−360.

(96) Matsumura, Y.; Maeda, H. A new concept for macromolecular therapeutics in cancer chemotherapy: mechanism of tumoritropic accumulation of proteins and the antitumor agent smancs. *Cancer Res.* **1986**, *46* (12 Pt 1), 6387−6392.

(97) Munn, L. L. Aberrant vascular architecture in tumors and its importance in drug-based therapies. *Drug Discovery Today* **2003**, *8* (9), 396−403.

(98) Hobbs, S. K.; Monsky, W. L.; Yuan, F.; Roberts, W. G.; Griffith, L.; Torchilin, V. P.; Jain, R. K. Regulation of transport pathways in tumor vessels: role of tumor type and microenvironment. *Proc. Natl. Acad. Sci. U.S.A.* **1998**, *95* (8), 4607−4612.

(99) Padera, T. P.; Kadambi, A.; di Tomaso, E.; Carreira, C. M.; Brown, E. B.; Boucher, Y.; Choi, N. C.; Mathisen, D.; Wain, J.; Mark, E. J.; Munn, L. L.; Jain, R. K. Lymphatic metastasis in the absence of functional intratumor lymphatics. *Science* **2002**, *296* (5574), 1883−1886.

(100) Brannon-Peppas, L.; Blanchette, J. O. Nanoparticle and targeted systems for cancer therapy. *Adv. Drug Delivery Rev.* **2004**, *56* (11), 1649−1659.

(101) Brigger, I.; Dubernet, C.; Couvreur, P. Nanoparticles in cancer therapy and diagnosis. *Adv. Drug Delivery Rev.* **2002**, *54* (5), 631−651.

(102) Rossin, R.; Pan, D.; Qi, K.; Turner, J. L.; Sun, X.; Wooley, K. L.; Welch, M. J. ^{64}Cu-labeled folate-conjugated shell cross-linked nanoparticles for tumor imaging and radiotherapy: synthesis, radiolabeling, and biologic evaluation. *J. Nucl. Med.* **2005**, *46* (7), 1210−1218.

(103) Dubey, P. K.; Mishra, V.; Jain, S.; Mahor, S.; Vyas, S. P. Liposomes modified with cyclic RGD peptide for tumor targeting. *J. Drug Target.* **2004**, *12* (5), 257−264.

(104) Guccione, S.; Li, K. C.; Bednarski, M. D. Vascular-targeted nanoparticles for molecular imaging and therapy. *Methods Enzymol.* **2004**, *386*, 219−236.

(105) Hood, J. D.; Bednarski, M.; Frausto, R.; Guccione, S.; Reisfeld, R. A.; Xiang, R.; Cheresh, D. A. Tumor regression by targeted gene delivery to the neovasculature. *Science* **2002**, *296* (5577), 2404−2407.

(106) Li, Y.; Tseng, Y. D.; Kwon, S. Y.; d'Espaux, L.; Bunch, J. S.; McEuen, P. L.; Luo, D. Controlled assembly of dendrimer-like DNA. *Nat. Mater.* **2004**, *3* (1), 38−42.

(107) Winter, P. M.; Caruthers, S. D.; Kassner, A.; Harris, T. D.; Chinen, L. K.; Allen, J. S.; Lacy, E. K.; Zhang, H.; Robertson, J. D.; Wickline, S. A.; Lanza, G. M. Molecular imaging of angiogenesis in nascent Vx-2 rabbit tumors using a novel $\alpha_v\beta_3$-targeted nanoparticle and 1.5 T magnetic resonance imaging. *Cancer Res.* **2003**, *63* (18), 5838−5843.

(108) Israeli, R. S.; Powell, C. T.; Corr, J. G.; Fair, W. R.; Heston, W. D. Expression of the prostate-specific membrane antigen. *Cancer Res.* **1994**, *54* (7), 1807−1811.

(109) Bostwick, D. G.; Pacelli, A.; Blute, M.; Roche, P.; Murphy, G. P. Prostate specific membrane antigen expression in prostatic intraepithelial neoplasia and adenocarcinoma: a study of 184 cases. *Cancer* **1998**, *82* (11), 2256−2261.

(110) Ghosh, A.; Heston, W. D. Tumor target prostate specific membrane antigen (PSMA) and its regulation in prostate cancer. *J. Cell. Biochem.* **2004**, *91* (3), 528−539.

(111) Huang, X.; Bennett, M.; Thorpe, P. E. Anti-tumor effects and lack of side effects in mice of an immunotoxin directed against human and mouse prostate-specific membrane antigen. *Prostate* **2004**, *61* (1), 1−11.

(112) Lamb, H. M.; Faulds, D. Capromab pendetide. A review of its use as an imaging agent in prostate cancer. *Drug Aging* **1998**, *12* (4), 293−304.

(113) Gong, M. C.; Chang, S. S.; Watt, F.; O'Keefe, D. S.; Bacich, D. J.; Uchida, A.; Bander, N. H.; Reuter, V. E.; Gaudin, P. B.; Molloy, P. L.; Sadelian, M.; Heston, W. D. Overview of evolving strategies incorporating prostate-specific membrane antigen as target for therapy. *Mol. Urol.* **2000**, *4* (3), 217−222.

(114) Chang, S. S. Monoclonal antibodies and prostate-specific membrane antigen. *Curr. Opin. Invest. Drugs* **2004**, *5* (6), 611−615.

(115) Chang, S. S.; Reuter, V. E.; Heston, W. D.; Bander, N. H.; Grauer, L. S.; Gaudin, P. B. Five different anti-prostate-specific membrane antigen (PSMA) antibodies confirm PSMA expression in tumor-associated neovasculature. *Cancer Res.* **1999**, *59* (13), 3192−3198.

(116) Liu, H.; Moy, P.; Kim, S.; Xia, Y.; Rajasekaran, A.; Navarro, V.; Knudsen, B.; Bander, N. H. Monoclonal antibodies to the extracellular domain of prostate-specific membrane antigen also react with tumor vascular endothelium. *Cancer Res.* **1997**, *57* (17), 3629−3634.

(117) Murphy, G. P.; Greene, T. G.; Tino, W. T.; Boynton, A. L.; Holmes, E. H. Isolation and characterization of monoclonal antibodies specific for the extracellular domain of prostate specific membrane antigen. *J. Urol.* **1998**, *160* (6 Pt 2), 2396−2401.

(118) Smith-Jones, P. M.; Vallabhajosula, S.; Navarro, V.; Bastidas, D.; Goldsmith, S. J.; Bander, N. H. Radiolabeled monoclonal antibodies specific to the extracellular domain of prostate-specific membrane antigen: preclinical studies in nude mice bearing LNCaP human prostate tumor. *J. Nucl. Med.* **2003**, *44* (4), 610−617.

(119) Patri, A. K.; Myc, A.; Beals, J.; Thomas, T. P.; Bander, N. H.; Baker, J. R. Synthesis and in vitro testing of J591 antibody-dendrimer conjugates for targeted prostate cancer therapy. *Bioconjugate Chem.* **2004**, *15* (6), 1174−1181.

(120) Brody, E. N.; Gold, L. Aptamers as therapeutic and diagnostic agents. *J. Biotechnol.* **2000**, *74* (1), 5−13.

(121) Brody, E. N.; Willis, M. C.; Smith, J. D.; Jayasena, S.; Zichi, D.; Gold, L. The use of aptamers in large arrays for molecular diagnostics. *Mol. Diagn.* **1999**, *4* (4), 381−388.

(122) Ellington, A. D.; Szostak, J. W. In vitro selection of RNA molecules that bind specific ligands. *Nature* **1990**, *346* (6287), 818−822.

(123) Ellington, A. D.; Szostak, J. W. Selection in vitro of single-stranded DNA molecules that fold into specific ligand-binding structures. *Nature* **1992**, *355* (6363), 850−852.

(124) Gander, T. R.; Brody, E. N.; Mehler, R. E.; Heilig, J. S.; Singer, B. S.; Gold, L. Driving forces in cancer diagnostics. *Med. Lab. Obs.* **2003**, *35* (1), 10−16.

(125) Gold, L.; Singer, B.; He, Y. Y.; Brody, E. SELEX and the evolution of genomes. *Curr. Opin. Genet. Dev.* **1997**, *7* (6), 848−851.

(126) Irvine, D.; Tuerk, C.; Gold, L. SELEXION. Systematic evolution of ligands by exponential enrichment with integrated optimization by non-linear analysis. *J. Mol. Biol.* **1991**, *222* (3), 739−761.

(127) Tuerk, C.; Gold, L. Systematic evolution of ligands by exponential enrichment: RNA ligands to bacteriophage T4 DNA polymerase. *Science* **1990**, *249* (4968), 505−510.

(128) Farokhzad, O. C.; Jon, S.; Khademhosseini, A.; Tran, T. N.; Lavan, D. A.; Langer, R. Nanoparticle-aptamer bioconjugates: a new approach for targeting prostate cancer cells. *Cancer Res.* **2004**, *64* (21), 7668−7672.

(129) Lee, I. H.; An, S.; Yu, M. K.; Kwon, H. K.; Im, S. H.; Jon, S. Targeted chemoimmunotherapy using drug-loaded aptamer-dendrimer bioconjugates. *J. Controlled Release* **2011**, *155* (3), 435−441.

(130) Wu, X.; Ding, B.; Gao, J.; Wang, H.; Fan, W.; Wang, X.; Zhang, W.; Wang, X.; Ye, L.; Zhang, M.; Ding, X.; Liu, J.; Zhu, Q.; Gao, S. Second-generation aptamer-conjugated PSMA-targeted delivery system for prostate cancer therapy. *Int. J. Nanomed.* **2011**, *6*, 1747−1756.

(131) Almushayt, A.; Narayanan, K.; Zaki, A. E.; George, A. Dentin matrix protein 1 induces cytodifferentiation of dental pulp stem cells into odontoblasts. *Gene Ther.* **2006**, *13* (7), 611−620.

(132) Brooks, P. C.; Montgomery, A. M.; Rosenfeld, M.; Reisfeld, R. A.; Hu, T.; Klier, G.; Cheresh, D. A. Integrin $\alpha_v\beta_3$ antagonists promote tumor regression by inducing apoptosis of angiogenic blood vessels. *Cell* **1994**, *79* (7), 1157−1164.

(133) Brakebusch, C.; Bouvard, D.; Stanchi, F.; Sakai, T.; Fassler, R. Integrins in invasive growth. *J. Clin. Invest.* **2002**, *109* (8), 999−1006.

(134) Brooks, P. C.; Clark, R. A.; Cheresh, D. A. Requirement of vascular integrin $\alpha_v\beta_3$ for angiogenesis. *Science* **1994**, *264* (5158), 569−571.

(135) O'Reilly, M. S.; Boehm, T.; Shing, Y.; Fukai, N.; Vasios, G.; Lane, W. S.; Flynn, E.; Birkhead, J. R.; Olsen, B. R.; Folkman, J. Endostatin: an endogenous inhibitor of angiogenesis and tumor growth. *Cell* **1997**, *88* (2), 277−85.

(136) Storgard, C. M.; Stupack, D. G.; Jonczyk, A.; Goodman, S. L.; Fox, R. I.; Cheresh, D. A. Decreased angiogenesis and arthritic disease in rabbits treated with an $\alpha v\beta 3$ antagonist. *J. Clin. Invest.* **1999**, *103* (1), 47−54.

(137) Weidner, N.; Semple, J. P.; Welch, W. R.; Folkman, J. Tumor angiogenesis and metastasis—correlation in invasive breast carcinoma. *N. Engl. J. Med.* **1991**, *324* (1), 1−8.

(138) Bogdanowich-Knipp, S. J.; Chakrabarti, S.; Williams, T. D.; Dillman, R. K.; Siahaan, T. J. Solution stability of linear vs. cyclic RGD peptides. *J. Pept. Res.* **1999**, *53* (5), 530−541.

(139) Bogdanowich-Knipp, S. J.; Jois, D. S.; Siahaan, T. J. The effect of conformation on the solution stability of linear vs. cyclic RGD peptides. *J. Pept. Res.* **1999**, *53* (5), 523−529.

(140) Bogdanowich-Knipp, S. J.; Jois, S. D.; Siahaan, T. J. Effect of conformation on the conversion of cyclo-(1,7)-Gly-Arg-Gly-Asp-Ser-Pro-Asp-Gly-OH to its cyclic imide degradation product. *J. Pept. Res.* **1999**, *54* (1), 43−53.

(141) Hill, E.; Shukla, R.; Park, S. S.; Baker, J. R., Jr. Synthetic PAMAM-RGD conjugates target and bind to odontoblast-like MDPC 23 cells and the predentin in tooth organ cultures. *Bioconjugate Chem.* **2007**, *18* (6), 1756−1762.

(142) Shukla, R.; Thomas, T. P.; Peters, J.; Kotlyar, A.; Myc, A.; Baker, J. R., Jr. Tumor angiogenic vasculature targeting with PAMAM dendrimer-RGD conjugates. *Chem. Commun. (Cambridge)* **2005**, *46*, 5739−5741.

(143) Wen, X.; Jackson, E. F.; Price, R. E.; Kim, E. E.; Wu, Q.; Wallace, S.; Charnsangavej, C.; Gelovani, J. G.; Li, C. Synthesis and characterization of poly(L-glutamic acid) gadolinium chelate: a new biodegradable MRI contrast agent. *Bioconjugate Chem.* **2004**, *15* (6), 1408−1415.

(144) Jaszberenyi, Z.; Moriggi, L.; Schmidt, P.; Weidensteiner, C.; Kneuer, R.; Merbach, A. E.; Helm, L.; Toth, E. Physicochemical and MRI characterization of Gd^{3+}-loaded polyamidoamine and hyperbranched dendrimers. *J. Biol. Inorg. Chem.* **2007**, *12* (3), 406−420.

(145) Kobayashi, H.; Kawamoto, S.; Saga, T.; Sato, N.; Hiraga, A.; Ishimori, T.; Konishi, J.; Togashi, K.; Brechbiel, M. W. Positive effects of polyethylene glycol conjugation to generation-4 polyamidoamine dendrimers as macromolecular MR contrast agents. *Magn. Reson. Med.* **2001**, *46* (4), 781−788.

(146) Kiessling, F.; Morgenstern, B.; Zhang, C. Contrast agents and applications to assess tumor angiogenesis in vivo by magnetic resonance imaging. *Curr. Med. Chem.* **2007**, *14* (1), 77−91.

(147) Bulte, J. W.; Douglas, T.; Witwer, B.; Zhang, S. C.; Strable, E.; Lewis, B. K.; Zywicke, H.; Miller, B.; van Gelderen, P.; Moskowitz, B. M.; Duncan, I. D.; Frank, J. A. Magnetodendrimers allow endosomal magnetic labeling and in vivo tracking of stem cells. *Nat. Biotechnol.* **2001**, *19* (12), 1141−1147.

(148) Scherer, F.; Anton, M.; Schillinger, U.; Henke, J.; Bergemann, C.; Kruger, A.; Gansbacher, B.; Plank, C. Magnetofection: enhancing and targeting gene delivery by magnetic force in vitro and in vivo. *Gene Ther.* **2002**, *9* (2), 102−109.

(149) Liu, W. M.; Xue, Y. N.; He, W. T.; Zhuo, R. X.; Huang, S. W. Dendrimer modified magnetic iron oxide nanoparticle/DNA/PEI ternary complexes: a novel strategy for magnetofection. *J. Controlled Release* **2011**, *152* (Suppl. 1), e159−160.

(150) Xu, R.; Wang, Y.; Wang, X.; Jeong, E. K.; Parker, D. L.; Lu, Z. R. In vivo evaluation of a PAMAM-cystamine-(Gd-DO3A) conjugate as a biodegradable macromolecular MRI contrast agent. *Exp. Biol. Med. (Maywood)* **2007**, *232* (8), 1081−1089.

(151) Kobayashi, H.; Shirakawa, K.; Kawamoto, S.; Saga, T.; Sato, N.; Hiraga, A.; Watanabe, I.; Heike, Y.; Togashi, K.; Konishi, J.; Brechbiel, M. W.; Wakasugi, H. Rapid accumulation and internalization of radiolabeled herceptin in an inflammatory breast cancer xenograft with vasculogenic mimicry predicted by the contrast-enhanced dynamic MRI with the macromolecular contrast agent G6-(1B4M-Gd)(256). *Cancer Res.* **2002**, *62* (3), 860−866.

(152) Talanov, V. S.; Regino, C. A.; Kobayashi, H.; Bernardo, M.; Choyke, P. L.; Brechbiel, M. W. Dendrimer-based nanoprobe for dual modality magnetic resonance and fluorescence imaging. *Nano Lett.* **2006**, *6* (7), 1459−1463.

(153) Kobayashi, H.; Kawamoto, S.; Sakai, Y.; Choyke, P. L.; Star, R. A.; Brechbiel, M. W.; Sato, N.; Tagaya, Y.; Morris, J. C.; Waldmann, T. A. Lymphatic drainage imaging of breast cancer in mice by micro-magnetic resonance lymphangiography using a nano-size paramagnetic contrast agent. *J. Natl. Cancer Inst.* **2004**, *96* (9), 703−708.

(154) Fu, Y.; Nitecki, D. E.; Maltby, D.; Simon, G. H.; Berejnoi, K.; Raatschen, H. J.; Yeh, B. M.; Shames, D. M.; Brasch, R. C. Dendritic iodinated contrast agents with PEG-cores for CT imaging: synthesis and preliminary characterization. *Bioconjugate Chem.* **2006**, *17* (4), 1043−1056.

(155) Ntziachristos, V.; Ripoll, J.; Wang, L. H. V.; Weissleder, R. Looking and listening to light: the evolution of whole-body photonic imaging. *Nat. Biotechnol.* **2005**, *23* (3), 313−320.

(156) Arridge, S. R. Optical tomography in medical imaging. *Inverse Probl.* **1999**, *15* (2), R41−R93.

(157) Konig, K. Multiphoton microscopy in life sciences. *J. Microsc. (Oxford)* **2000**, *200*, 83−104.

(158) Villringer, A.; Chance, B. Non-invasive optical spectroscopy and imaging of human brain function. *Trends Neurosci.* **1997**, *20* (10), 435−442.

(159) Efimov, I. R.; Nikolski, V. P.; Salama, G. Optical imaging of the heart. *Circ. Res.* **2004**, *95* (1), 21−33.

(160) Ballou, B.; Ernst, L. A.; Waggoner, A. S. Fluorescence imaging of tumors in vivo. *Curr. Med. Chem.* **2005**, *12* (7), 795−805.

(161) Citrin, D.; Camphausen, K. Optical imaging of mice in oncologic research. *Exp. Rev. Anticancer Ther.* **2004**, *4* (5), 857−864.

(162) Kosaka, N.; Ogawa, M.; Choyke, P. L.; Kobayashi, H. Clinical implications of near-infrared fluorescence imaging in cancer. *Future Oncol.* **2009**, *5* (9), 1501−1511.

(163) Licha, K.; Olbrich, C. Optical imaging in drug discovery and diagnostic applications. *Adv. Drug Delivery Rev.* **2005**, *57* (8), 1087−1108.

(164) McDonald, D. M.; Choyke, P. L. Imaging of angiogenesis: from microscope to clinic. *Nat. Med.* **2003**, *9* (6), 713−725.

(165) Rao, J.; Dragulescu-Andrasi, A.; Yao, H. Fluorescence imaging in vivo: recent advances. *Curr. Opin. Biotechnol.* **2007**, *18* (1), 17−25.

(166) Koyama, Y.; Talanov, V. S.; Bernardo, M.; Hama, Y.; Regino, C. A. S.; Brechbiel, M. W.; Choyke, P. L.; Kobayashi, H. A dendrimer-based nanosized contrast agent, dual-labeled for magnetic resonance and optical fluorescence imaging to localize the sentinel lymph node in mice. *J. Magn. Reson. Imaging* **2007**, *25* (4), 866−871.

(167) Kobayashi, H.; Koyama, Y.; Barrett, T.; Hama, Y.; Regino, C. A. S.; Shin, I. S.; Jang, B.-S.; Le, N.; Paik, C. H.; Choyke, P. L.; Urano,

Y. Multimodal nanoprobes for radionuclide and five-color near-infrared optical lymphatic imaging. *ACS Nano* **2007**, *1* (4), 258−264.

(168) Yan, H.; Wang, J.; Yi, P.; Lei, H.; Zhan, C.; Xie, C.; Feng, L.; Qian, J.; Zhu, J.; Lu, W.; Li, C. Imaging brain tumor by dendrimer-based optical/paramagnetic nanoprobe across the blood-brain barrier. *Chem. Commun. (Cambridge)* **2011**, *47* (28), 8130−8132.

(169) Phelps, M. E. PET: The merging of biology and imaging into molecular imaging. *J. Nucl. Med.* **2000**, *41* (4), 661−681.

(170) Massoud, T. F.; Gambhir, S. S. Molecular imaging in living subjects: seeing fundamental biological processes in a new light. *Gene. Dev.* **2003**, *17* (5), 545−580.

(171) Boswell, C. A.; Sun, X. K.; Niu, W. J.; Weisman, G. R.; Wong, E. H.; Rheingold, A. L.; Anderson, C. J. Comparative in vivo stability of copper-64-labeled cross-bridged and conventional tetraazamacrocyclic complexes. *J. Med. Chem.* **2004**, *47* (6), 1465−1474.

(172) Jones-Wilson, T. M.; Deal, K. A.; Anderson, C. J.; McCarthy, D. W.; Kovacs, Z.; Motekaitis, R. J.; Sherry, A. D.; Martell, A. E.; Welch, M. J. The in vivo behavior of copper-64-labeled azamacrocyclic complexes. *Nucl. Med. Biol.* **1998**, *25* (6), 523−530.

(173) Wu, C. C.; Jagoda, E.; Brechbiel, M.; Webber, K. O.; Pastan, I.; Gansow, O.; Eckelman, W. C. Biodistribution and catabolism of Ga-67-labeled anti-Tac dsFv fragment. *Bioconjugate Chem.* **1997**, *8* (3), 365−369.

(174) Prata, M. I. M.; Santos, A. C.; Geraldes, C.; de Lima, J. J. P. Structural and in vivo studies of metal chelates of Ga(III) relevant to biomedical imaging. *J. Inorg. Biochem.* **2000**, *79* (1−4), 359−363.

(175) Li, Z. B.; Chen, K.; Chen, X. Ga-68-labeled multimeric RGD peptides for microPET imaging of integrin α(v)β(3) expression. *Eur. J. Nucl. Med. Mol. Imaging* **2008**, *35* (6), 1100−1108.

(176) Jamar, F.; Barone, R.; Mathieu, I.; Walrand, S.; Labar, D.; Carlier, P.; de Camps, J.; Schran, H.; Chen, T.; Smith, M. C.; Bouterfa, H.; Valkema, R.; Krenning, E. P.; Kvols, L. K.; Pauwels, S. Y-86-DOTA(0)-D-Phe(1)-Tyr(3)-octreotide (SMT487) - a phase 1 clinical study: pharmacokinetics, biodistribution and renal protective effect of different regimens of amino acid co-infusion. *Eur. J. Nucl. Med. Mol. Imaging* **2003**, *30* (4), 510−518.

(177) Rosch, F.; Herzog, H.; Stolz, B.; Brockmann, J.; Kohle, M.; Muhlensiepen, H.; Marbach, P.; Muller-Gartner, H. W. Uptake kinetics of the somatostatin receptor ligand Y-86 DOTA-DPhe(1)-Tyr(3)-octreotide (Y-86 SMT487) using positron emission tomography in non-human primates and calculation of radiation doses of the Y-90-labelled analogue. *Eur. J. Nucl. Med.* **1999**, *26* (4), 358−366.

(178) Boerman, O. C.; van Schaijk, F. G.; Oyen, W. J. G.; Corstens, F. H. M. Pretargeted radioimmunotherapy of cancer: Progress step by step. *J. Nucl. Med.* **2003**, *44* (3), 400−411.

(179) Knox, S. J.; Goris, M. L.; Tempero, M.; Weiden, P. L.; Gentner, L.; Breitz, H.; Adams, G. P.; Axworthy, D.; Gaffigan, S.; Bryan, K.; Fisher, D. R.; Colcher, D.; Horak, I. D.; Weiner, L. M. Phase II trial of yttrium-90-DOTA-biotin pretargeted by NR-LU-10 antibody/streptavidin in patients with metastatic colon cancer. *Clin. Cancer Res.* **2000**, *6* (2), 406−414.

(180) Kang, C. S.; Sun, X.; Jia, F.; Song, H. A.; Chen, Y.; Lewis, M.; Chong, H. S. Synthesis and preclinical evaluation of bifunctional ligands for improved chelation chemistry of ^{90}Y and ^{177}Lu for targeted radioimmunotherapy. *Bioconjugate Chem.* **2012**, *23* (9), 1775−1782.

(181) Miao, Y.; Gallazzi, F.; Guo, H.; Quinn, T. P. In-111-labeled lactam bridge-cyclized α-melanocyte stimulating hormone peptide analogues for melanoma imaging. *Bioconjugate Chem.* **2008**, *19* (2), 539−547.

(182) Kwekkeboom, D. J.; Bakker, W. H.; Kooij, P. P. M.; Konijnenberg, M. W.; Srinivasan, A.; Erion, J. L.; Schmidt, M. A.; Bugaj, J. L.; de Jong, M.; Krenning, E. P. Lu-177-DOTA(0),Tyr(3) octreotate: comparison with In-111-DTPA(0) octreotide in patients. *Eur. J. Nucl. Med.* **2001**, *28* (9), 1319−1325.

(183) Perols, A.; Honarvar, H.; Strand, J.; Selvaraju, R.; Orlova, A.; Karlstrom, A. E.; Tolmachev, V. Influence of DOTA chelator position on biodistribution and targeting properties of (111)In-labeled synthetic anti-HER2 affibody molecules. *Bioconjugate Chem.* **2012**, *23* (8), 1661−1670.

(184) Brucke, T.; Podreka, I.; Angelberger, P.; Wenger, S.; Topitz, A.; Kufferle, B.; Muller, C.; Deecke, L. Dopamine-D2 receptor imaging with SPECT- Studies in different neuropsychiatric disorders. *J. Cereb. Blood Flow Metab.* **1991**, *11* (2), 220−228.

(185) Sundaresan, G.; Yazaki, P. J.; Shively, J. E.; Finn, R. D.; Larson, S. M.; Raubitschek, A. A.; Williams, L. E.; Chatziioannou, A. F.; Gambhir, S. S.; Wu, A. M. I-124-labeled engineered Anti-CEA minibodies and diabodies allow high-contrast, antigen-specific small-animal PET imaging of xenografts in athymic mice. *J. Nucl. Med.* **2003**, *44* (12), 1962−1969.

(186) Wang, Y. M.; Klunk, W. E.; Debnath, M. L.; Huang, G. F.; Holt, D. P.; Shao, L.; Mathis, C. A. Development of a PET/SPECT agent for amyloid imaging in Alzheimer's disease. *J. Mol. Neurosci.* **2004**, *24* (1), 55−62.

(187) Menges, M.; Uder, M.; Kuwert, T.; Schmidt, D. I-131 SPECT/CT in the follow-up of patients with differentiated thyroid carcinoma. *Clin. Nucl. Med.* **2012**, *37* (6), 555−560.

(188) Soundararajan, A.; Bao, A.; Phillips, W. T.; Perez, R., III; Goins, B. A. [(186)Re]Liposomal doxorubicin (Doxil): in vitro stability, pharmacokinetics, imaging and biodistribution in a head and neck squamous cell carcinoma xenograft model. *Nucl. Med. Biol.* **2009**, *36* (5), 515−524.

(189) Bayly, S. R.; Fisher, C. L.; Storr, T.; Adam, M. J.; Orvig, C. Carbohydrate conjugates for molecular imaging and radiotherapy: Tc-99m(I) and Re-186(I) tricarbonyl complexes of N-(2′-hydroxybenzyl)-2-amino-2-deoxy-D-glucose. *Bioconjugate Chem.* **2004**, *15* (4), 923−926.

(190) Hashimoto, K.; Yoshihara, K. Rhenium complexes labeled with Re-186,Re-188 for nuclear medicine. *Technetium Rhenium* **1996**, *176*, 275−291.

(191) Chen, L. C.; Chang, C. H.; Yu, C. Y.; Chang, Y. J.; Hsu, W. C.; Ho, C. L.; Yeh, C. H.; Luo, T. Y.; Lee, T. W.; Ting, G. Biodistribution, pharmacokinetics and imaging of Re-188-BMEDA-labeled pegylated liposomes after intraperitoneal injection in a C26 colon carcinoma ascites mouse model. *Nucl. Med. Biol.* **2007**, *34* (4), 415−423.

(192) Cao, J. Q.; Wang, Y. X.; Yu, J. F.; Xia, J. Y.; Zhang, C. F.; Yin, D. Z.; Hafeli, U. O. Preparation and radiolabeling of surface-modified magnetic nanoparticles with rhenium-188 for magnetic targeted radiotherapy. *J. Magn. Magn. Mater.* **2004**, *277* (1−2), 165−174.

(193) Knapp, F. F. Rhenium-188—A generator-derived radioisotope for cancer therapy. *Cancer Biother. Radiopharm.* **1998**, *13* (5), 337−349.

(194) Matsuura, N.; Rowlands, J. A. Towards new functional nanostructures for medical imaging. *Med. Phys.* **2008**, *35* (10), 4474−4487.

(195) Notni, J.; Pohle, K.; Wester, H. J. Comparative gallium-68 labeling of TRAP-, NOTA-, and DOTA-peptides: practical consequences for the future of gallium-68-PET. *EJNMMI Res.* **2012**, *2* (1), 28.

(196) Cooper, M. S.; Ma, M. T.; Sunassee, K.; Shaw, K. P.; Williams, J. D.; Paul, R. L.; Donnelly, P. S.; Blower, P. J. Comparison of (64)Cu-complexing bifunctional chelators for radioimmunoconjugation: labeling efficiency, specific activity, and in vitro/in vivo stability. *Bioconjugate Chem.* **2012**, *23* (5), 1029−1039.

(197) Biddlecombe, G. B.; Rogers, B. E.; de Visser, M.; Parry, J. J.; de Jong, M.; Erion, J. L.; Lewis, J. S. Molecular imaging of gastrin-releasing peptide receptor-positive tumors in mice using 64Cu- and 86Y-DOTA-(Pro1,Tyr4)-bombesin(1−14). *Bioconjugate Chem.* **2007**, *18* (3), 724−730.

(198) Cherry, S. R. Multimodality in vivo imaging systems: Twice the power or double the trouble? *Annu. Rev. Biomed. Eng.* **2006**, *8*, 35−62.

(199) Pichler, B. J.; Wehrl, H. F.; Judenhofer, M. S. Latest advances in molecular imaging instrumentation. *J. Nucl. Med.* **2008**, *49* (Suppl. 2), 5S−23S.

(200) Judenhofer, M. S.; Wehrl, H. F.; Newport, D. F.; Catana, C.; Siegel, S. B.; Becker, M.; Thielscher, A.; Kneilling, M.; Lichy, M. P.; Eichner, M.; Klingel, K.; Reischl, G.; Widmaier, S.; Rocken, M.; Nutt, R. E.; Machulla, H. J.; Uludag, K.; Cherry, S. R.; Claussen, C. D.;

Pichler, B. J. Simultaneous PET-MRI: a new approach for functional and morphological imaging. *Nat. Med.* **2008**, *14* (4), 459−465.

(201) Frullano, L.; Catana, C.; Benner, T.; Sherry, A. D.; Caravan, P. Bimodal MR-PET agent for quantitative pH imaging. *Angew. Chem., Int. Ed. Engl.* **2010**, *49* (13), 2382−2384.

(202) Mukhopadhyay, A.; Bueso-Ramos, C.; Chatterjee, D.; Pantazis, P.; Aggarwal, B. B. Curcumin downregulates cell survival mechanisms in human prostate cancer cell lines. *Oncogene* **2001**, *20* (52), 7597−7609.

(203) Dorai, T.; Cao, Y. C.; Dorai, B.; Buttyan, R.; Katz, A. E. Therapeutic potential of curcumin in human prostate cancer. III. Curcumin inhibits proliferation, induces apoptosis, and inhibits angiogenesis of LNCaP prostate cancer cells in vivo. *Prostate* **2001**, *47* (4), 293−303.

(204) Dorai, T.; Gehani, N.; Katz, A. Therapeutic potential of curcumin in human prostate cancer-I. curcumin induces apoptosis in both androgen-dependent and androgen-independent prostate cancer cells. *Prostate Cancer Prostat. Dis.* **2000**, *3* (2), 84−93.

(205) Dorai, T.; Gehani, N.; Katz, A. Therapeutic potential of curcumin in human prostate cancer. II. Curcumin inhibits tyrosine kinase activity of epidermal growth factor receptor and depletes the protein. *Mol. Urol.* **2000**, *4* (1), 1−6.

(206) Davis, J. N.; Muqim, N.; Bhuiyan, M.; Kucuk, O.; Pienta, K. J.; Sarkar, F. H. Inhibition of prostate specific antigen expression by genistein in prostate cancer cells. *Int. J. Oncol.* **2000**, *16* (6), 1091−1097.

(207) Hsieh, T. C.; Huang, Y. C.; Wu, J. M. Control of prostate cell growth, DNA damage and repair and gene expression by resveratrol analogues, in vitro. *Carcinogenesis* **2011**, *32* (1), 93−101.

(208) Abderrezak, A.; Bourassa, P.; Mandeville, J. S.; Sedaghat-Herati, R.; Tajmir-Riahi, H. A. Dendrimers bind antioxidant polyphenols and cisplatin drug. *PLoS One* **2012**, *7* (3), e33102.

(209) Morgan, M. T.; Carnahan, M. A.; Immoos, C. E.; Ribeiro, A. A.; Finkelstein, S.; Lee, S. J.; Grinstaff, M. W. Dendritic Molecular Capsules for Hydrophobic Compounds. *J. Am. Chem. Soc.* **2003**, *125* (50), 15485−15489.

(210) Morgan, M. T.; Nakanishi, Y.; Kroll, D. J.; Griset, A. P.; Carnahan, M. A.; Wathier, M.; Oberlies, N. H.; Manikumar, G.; Wani, M. C.; Grinstaff, M. W. Dendrimer-encapsulated camptothecins: increased solubility, cellular uptake, and cellular retention affords enhanced anticancer activity in vitro. *Cancer Res.* **2006**, *66* (24), 11913−11921.

(211) Gurdag, S.; Khandare, J.; Stapels, S.; Matherly, L. H.; Kannan, R. M. Activity of dendrimer-methotrexate conjugates on methotrexate-sensitive and -resistant cell lines. *Bioconjugate Chem.* **2006**, *17* (2), 275−283.

(212) Malik, N.; Evagorou, E. G.; Duncan, R. Dendrimer-platinate: a novel approach to cancer chemotherapy. *Anticancer Drugs* **1999**, *10* (8), 767−776.

(213) Chauhan, A. S.; Sridevi, S.; Chalasani, K. B.; Jain, A. K.; Jain, S. K.; Jain, N. K.; Diwan, P. V. Dendrimer-mediated transdermal delivery: enhanced bioavailability of indomethacin. *J. Controlled Release* **2003**, *90* (3), 335−343.

(214) Khandare, J. J.; Jayant, S.; Singh, A.; Chandna, P.; Wang, Y.; Vorsa, N.; Minko, T. Dendrimer versus linear conjugate: Influence of polymeric architecture on the delivery and anticancer effect of paclitaxel. *Bioconjugate Chem.* **2006**, *17* (6), 1464−72.

(215) Kochanek, S.; Gansbacher, B. Prostate cancer gene therapy: attempts to innovate. *Human Gene Ther.* **2010**, *21* (7), 791.

(216) Kay, M. A.; Glorioso, J. C.; Naldini, L. Viral vectors for gene therapy: the art of turning infectious agents into vehicles of therapeutics. *Nat. Med.* **2001**, *7* (1), 33−40.

(217) Merdan, T.; Kopecek, J.; Kissel, T. Prospects for cationic polymers in gene and oligonucleotide therapy against cancer. *Adv. Drug Delivery Rev.* **2002**, *54* (5), 715−758.

(218) Chen, Y.; Wang, G.; Kong, D.; Zhang, Z.; Yang, K.; Liu, R.; Zhao, W.; Xu, Y. Double-targeted and double-enhanced suicide gene therapy mediated by generation 5 polyamidoamine dendrimers for prostate cancer. *Mol. Carcinog.* **2011**, DOI: 10.1002/mc.21850.

(219) Arima, H.; Yoshimatsu, A.; Ikeda, H.; Ohyama, A.; Motoyama, K.; Higashi, T.; Tsuchiya, A.; Niidome, T.; Katayama, Y.; Hattori, K.; Takeuchi, T. Folate-PEG-appended dendrimer conjugate with α-cyclodextrin as a novel cancer cell-Selective siRNA delivery carrier. *Mol. Pharmaceutics* **2012**, *9* (9), 2591−2604.

(220) Zhang, Y.; Zhou, C.; Kwak, K. J.; Wang, X.; Yung, B.; Lee, L. J.; Wang, Y.; Wang, P. G.; Lee, R. J. Efficient siRNA delivery using a polyamidoamine dendrimer with a modified pentaerythritol core. *Pharm. Res.* **2012**, *29* (6), 1627−1636.

(221) Liu, X.; Liu, C.; Laurini, E.; Posocco, P.; Pricl, S.; Qu, F.; Rocchi, P.; Peng, L. Efficient delivery of sticky siRNA and potent gene silencing in a prostate cancer model using a generation 5 triethanolamine-core PAMAM dendrimer. *Mol. Pharmaceutics* **2012**, *9* (3), 470−481.

(222) Jensen, L. B.; Pavan, G. M.; Kasimova, M. R.; Rutherford, S.; Danani, A.; Nielsen, H. M.; Foged, C. Elucidating the molecular mechanism of PAMAM-siRNA dendriplex self-assembly: effect of dendrimer charge density. *Int. J. Pharmaceutics* **2011**, *416* (2), 410−418.

(223) Lupold, S. E.; Hicke, B. J.; Lin, Y.; Coffey, D. S. Identification and characterization of nuclease-stabilized RNA molecules that bind human prostate cancer cells via the prostate-specific membrane antigen. *Cancer Res.* **2002**, *62* (14), 4029−4033.

(224) Liu, X. X.; Rocchi, P.; Qu, F. Q.; Zheng, S. Q.; Liang, Z. C.; Gleave, M.; Iovanna, J.; Peng, L. PAMAM dendrimers mediate siRNA delivery to target Hsp27 and produce potent antiproliferative effects on prostate cancer cells. *ChemMedChem* **2009**, *4* (8), 1302−1310.

(225) Rocchi, P.; So, A.; Kojima, S.; Signaevsky, M.; Beraldi, E.; Fazli, L.; Hurtado-Coll, A.; Yamanaka, K.; Gleave, M. Heat shock protein 27 increases after androgen ablation and plays a cytoprotective role in hormone-refractory prostate cancer. *Cancer Res.* **2004**, *64* (18), 6595−6602.

(226) Rocchi, P.; Beraldi, E.; Ettinger, S.; Fazli, L.; Vessella, R. L.; Nelson, C.; Gleave, M. Increased Hsp27 after androgen ablation facilitates androgen-independent progression in prostate cancer via signal transducers and activators of transcription 3-mediated suppression of apoptosis. *Cancer Res.* **2005**, *65* (23), 11083−11093.

(227) Chen, K.; Rajewsky, N. The evolution of gene regulation by transcription factors and microRNAs. *Nat. Rev. Genet.* **2007**, *8* (2), 93−103.

(228) Bartel, D. P. MicroRNAs: genomics, biogenesis, mechanism, and function. *Cell* **2004**, *116* (2), 281−297.

(229) Bonci, D.; Coppola, V.; Musumeci, M.; Addario, A.; Giuffrida, R.; Memeo, L.; D'Urso, L.; Pagliuca, A.; Biffoni, M.; Labbaye, C.; Bartucci, M.; Muto, G.; Peschle, C.; De Maria, R. The miR-15a-miR-16-1 cluster controls prostate cancer by targeting multiple oncogenic activities. *Nat. Med.* **2008**, *14* (11), 1271−1277.

(230) Toi, M.; Horiguchi, K.; Bando, H.; Saji, S.; Chow, L. W. Trastuzumab: updates and future issues. *Cancer Chemother. Pharmacol.* **2005**, *56* (Suppl.1), 94−99.

(231) Vieweg, J.; Jackson, A. Antigenic targets for renal cell carcinoma immunotherapy. *Exp. Opin. Biol. Ther.* **2004**, *4* (11), 1791−1801.

(232) Vieweg, J.; Dannull, J. Technology Insight: vaccine therapy for prostate cancer. *Nat. Clin. Pract. Urol.* **2005**, *2* (1), 44−51.

(233) Drake, C. G.; Doody, A. D.; Mihalyo, M. A.; Huang, C. T.; Kelleher, E.; Ravi, S.; Hipkiss, E. L.; Flies, D. B.; Kennedy, E. P.; Long, M.; McGary, P. W.; Coryell, L.; Nelson, W. G.; Pardoll, D. M.; Adler, A. J. Androgen ablation mitigates tolerance to a prostate/prostate cancer-restricted antigen. *Cancer Cell* **2005**, *7* (3), 239−249.

(234) Heegaard, P. M.; Boas, U.; Sorensen, N. S. Dendrimers for vaccine and immunostimulatory uses. A review. *Bioconjugate Chem.* **2010**, *21* (3), 405−418.

(235) Pan, M. H.; Gao, D. W.; Feng, J.; He, J.; Seo, Y.; Tedesco, J.; Wolodzko, J. G.; Hasegawa, B. H.; Franc, B. L. Biodistributions of 177Lu- and 111In-labeled 7E11 antibodies to prostate-specific membrane antigen in xenograft model of prostate cancer and potential use of 111In-7E11 as a pre-therapeutic agent for 177Lu-7E11 radioimmunotherapy. *Mol. Imaging Biol.* **2009**, *11* (3), 159−166.

(236) Vallabhajosula, S.; Kuji, I.; Hamacher, K. A.; Konishi, S.; Kostakoglu, L.; Kothari, P. A.; Milowski, M. I.; Nanus, D. M.; Bander, N. H.; Goldsmith, S. J. Pharmacokinetics and biodistribution of 111In- and 177Lu-labeled J591 antibody specific for prostate-specific membrane antigen: prediction of 90Y-J591 radiation dosimetry based on 111In or 177Lu? *J. Nucl. Med.* **2005**, *46* (4), 634−641.

(237) Davies, A. J. Radioimmunotherapy for B-cell lymphoma: Y90 ibritumomab tiuxetan and I(131) tositumomab. *Oncogene* **2007**, *26* (25), 3614−3628.

(238) Phillips, W. T.; Goins, B.; Bao, A.; Vargas, D.; Guttierez, J. E.; Trevino, A.; Miller, J. R.; Henry, J.; Zuniga, R.; Vecil, G.; Brenner, A. J. Rhenium-186 liposomes as convection-enhanced nanoparticle brachytherapy for treatment of glioblastoma. *Neuro-Oncology* **2012**, *14* (4), 416−425.

(239) Liang, S.; Wang, Y.; Yu, J.; Zhang, C.; Xia, J.; Yin, D. Surface modified superparamagnetic iron oxide nanoparticles: as a new carrier for bio-magnetically targeted therapy. *J. Mater. Sci.: Mater. Med.* **2007**, *18* (12), 2297−2302.

(240) Liang, S.; Wang, Y.; Zhang, C.; Liu, X.; Liu, Z.; Xu, R.; Yin, D. Synthesis of amino-modified magnetite nanoparticles coated with Hepama-1 and radiolabeled with Re-188 for bio-magnetically targeted radiotherapy. *J. Radioanal. Nucl. Chem.* **2006**, *269* (1), 3−7.

(241) Chen, L. C.; Chang, C. H.; Yu, C. Y.; Chang, Y. J.; Hsu, W. C.; Ho, C. L.; Yeh, C. H.; Luo, T. Y.; Lee, T. W.; Ting, G. Biodistribution, pharmacokinetics and imaging of (188)Re-BMEDA-labeled pegylated liposomes after intraperitoneal injection in a C26 colon carcinoma ascites mouse model. *Nucl. Med. Biol.* **2007**, *34* (4), 415−423.

(242) Chen, L. C.; Chang, C. H.; Yu, C. Y.; Chang, Y. J.; Wu, Y. H.; Lee, W. C.; Yeh, C. H.; Lee, T. W.; Ting, G. Pharmacokinetics, micro-SPECT/CT imaging and therapeutic efficacy of (188)Re-DXR-liposome in C26 colon carcinoma ascites mice model. *Nucl. Med. Biol.* **2008**, *35* (8), 883−893.

(243) Chen, M. H.; Chang, C. H.; Chang, Y. J.; Chen, L. C.; Yu, C. Y.; Wu, Y. H.; Lee, W. C.; Yeh, C. H.; Lin, F. H.; Lee, T. W.; Yang, C. S.; Ting, G. MicroSPECT/CT imaging and pharmacokinetics of ^{188}Re-(DXR)-liposome in human colorectal adenocarcinoma-bearing mice. *Anticancer Res.* **2010**, *30* (1), 65−72.

(244) Chang, C. H.; Stabin, M. G.; Chang, Y. J.; Chen, L. C.; Chen, M. H.; Chang, T. J.; Lee, T. W.; Ting, G. Comparative dosimetric evaluation of nanotargeted (188)Re-(DXR)-liposome for internal radiotherapy. *Cancer Biother. Radiopharm.* **2008**, *23* (6), 749−758.

(245) Chang, Y. J.; Chang, C. H.; Chang, T. J.; Yu, C. Y.; Chen, L. C.; Jan, M. L.; Luo, T. Y.; Lee, T. W.; Ting, G. Biodistribution, pharmacokinetics and microSPECT/CT imaging of ^{188}Re-bMEDA-liposome in a C26 murine colon carcinoma solid tumor animal model. *Anticancer Res.* **2007**, *27* (4B), 2217−2225.

(246) Chang, Y. J.; Chang, C. H.; Yu, C. Y.; Chang, T. J.; Chen, L. C.; Chen, M. H.; Lee, T. W.; Ting, G. Therapeutic efficacy and microSPECT/CT imaging of ^{188}Re-DXR-liposome in a C26 murine colon carcinoma solid tumor model. *Nucl. Med. Biol.* **2010**, *37* (1), 95−104.

(247) Wilson, J. D.; Broaddus, W. C.; Dorn, H. C.; Fatouros, P. P.; Chalfant, C. E.; Shultz, M. D. Metallofullerene-Nanoplatform-Delivered Interstitial Brachytherapy Improved Survival in a Murine Model of Glioblastoma Multiforme. *Bioconjugate Chem.* **2012**, *23* (9), 1873−1880.

(248) Zhou, C.; Hao, G.; Thomas, P.; Liu, J.; Yu, M.; Sun, S.; Oz, O. K.; Sun, X.; Zheng, J. Near-infrared emitting radioactive gold nanoparticles with molecular pharmacokinetics. *Angew. Chem., Int. Ed. Engl.* **2012**, *51* (40), 10118−10122.

(249) Zhou, C.; Long, M.; Qin, Y.; Sun, X.; Zheng, J. Luminescent gold nanoparticles with efficient renal clearance. *Angew. Chem., Int. Ed. Engl.* **2011**, *50* (14), 3168−3172.

(250) Kang, C. S.; Sun, X.; Jia, F.; Song, H. A.; Chen, Y.; Lewis, M.; Chong, H. S. Synthesis and preclinical evaluation of bifunctional ligands for improved chelation chemistry of ^{90}Y and ^{177}Lu for targeted radioimmunotherapy. *Bioconjugate Chem.* **2012**, *23* (9), 1775−1782.

(251) Perols, A.; Honarvar, H.; Strand, J.; Selvaraju, R.; Orlova, A.; Eriksson Karlstrom, A.; Tolmachev, V. Influence of DOTA chelator position on biodistribution and targeting properties of (111)In-labeled synthetic anti-HER2 affibody molecules. *Bioconjugate Chem.* **2012**, *23* (8), 1661−1670.

(252) Guo, H.; Yang, J.; Shenoy, N.; Miao, Y. Gallium-67-labeled lactam bridge-cyclized α-melanocyte stimulating hormone peptide for primary and metastatic melanoma imaging. *Bioconjugate Chem.* **2009**, *20* (12), 2356−2363.

(253) Dhar, S.; Gu, F. X.; Langer, R.; Farokhzad, O. C.; Lippard, S. J. Targeted delivery of cisplatin to prostate cancer cells by aptamer functionalized Pt(IV) prodrug-PLGA-PEG nanoparticles. *Proc. Natl. Acad. Sci. U.S.A.* **2008**, *105* (45), 17356−17361.

molecular pharmaceutics
Article
pubs.acs.org/molecularpharmaceutics

A Multivalent Approach of Imaging Probe Design To Overcome an Endogenous Anion Binding Competition for Noninvasive Assessment of Prostate Specific Membrane Antigen

Guiyang Hao,[†] Amit Kumar,[†] Timothy Dobin,[‡] Orhan K. Öz,[†] Jer-Tsong Hsieh,[‡] and Xiankai Sun*,[†,§]

[†]Department of Radiology, [‡]Department of Urology, and [§]Advanced Imaging Research Center, The University of Texas Southwestern Medical Center, Dallas, Texas 75390, United States

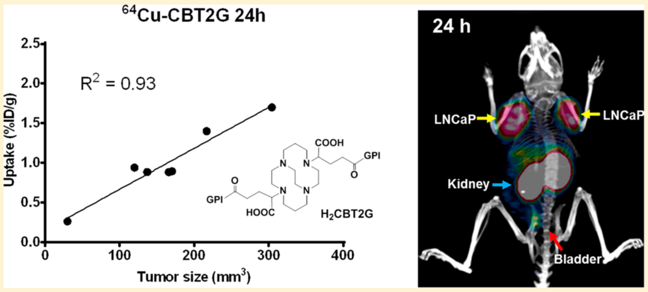

ABSTRACT: 2[(3-Amino-3-carboxypropyl)(hydroxy)(phosphinyl)methyl]pentane-1,5-dioic acid) (GPI) is a highly potent inhibitor of prostate specific membrane antigen (PSMA) with a rapid *in vivo* clearance profile from nontarget organs including kidneys, but its use for imaging of PSMA is impeded by an endogenous anion (serum phosphate) competition, which compromises its specific binding to the antigen. Multipresentation of a targeting molecule on a single entity has been recognized as a practical way for imaging sensitivity enhancement. Herein, we demonstrate a multivalent approach based on a ^{64}Cu-specific bifunctional chelator scaffold to overcome the endogenous phosphate competition thus enabling the utility of GPI conjugates for *in vivo* detection of PSMA and imaging quantification. Both monomeric (H_2CBT1G) and dimeric (H_2CBT2G) conjugates were synthesized and labeled with ^{64}Cu for *in vitro* and *in vivo* evaluations. A 4-fold enhancement of PSMA binding affinity was observed for H_2CBT2G as compared to H_2CBT1G from the PSMA competitive binding assays performed on LNCaP cells. *In vivo* PET imaging studies were conducted on mouse xenograft models established with a PSMA$^+$ cell line, LNCaP, and PSMA$^-$ PC3 and H2009 cell lines. ^{64}Cu-CBT2G showed significantly higher LNCaP tumor uptake than ^{64}Cu-CBT1G at 1, 4, and 24 h postinjection (p.i.) ($p < 0.05$). In addition, tumor uptake of ^{64}Cu-CBT2G remained steady out to 24 h p.i. (1.46 ± 0.54, 1.12 ± 0.56, and 1.00 ± 0.50% ID/g at 1, 4, and 24 h p.i., respectively), while ^{64}Cu-CBT1G showed a great decrease from 1 to 4 h p.i. The PSMA imaging specificity of both H_2CBT1G and H_2CBT2G was demonstrated by their low uptake in PSMA$^-$ tumors (PC3 and H2009) and further confirmed by a significant signal reduction in PSMA$^+$ LNCaP tumors in the blockade study. In addition, the LNCaP tumor uptake (% ID/g) of ^{64}Cu-CBT2G was found to be in a positive linear correlation with the tumor size (R^2 = 0.92, 0.94, and 0.93 for 1 h, 4 h, and 24 h p.i.). This may render the probe with potential application in the management of patients with prostate cancer.

KEYWORDS: *PSMA, prostate cancer, PET, ^{64}Cu, multivalency*

INTRODUCTION

Prostate cancer is the second leading cause of cancer death behind only lung cancer in American men. Noninvasive imaging techniques, such as ultrasound, X-ray, computed tomography (CT), magnetic resonance imaging (MRI), single-photon emission computed tomography (SPECT), and positron emission tomography (PET), have been used for the diagnosis of prostate cancer along with conventional methods. Despite the great success of FDG-PET scan (^{18}F-FDG: 2-deoxy-2-(^{18}F)fluoro-D-glucose) in other cancer types, its role in prostate cancer is limited by the fact that prostate cancer at early stages is not substantially upregulating glucose metabolism and the prostate glands are in close proximity of the bladder, from which most of FDG activity is cleared.[1] To date, various PET radiotracers have been introduced for prostate cancer imaging.[1] For example, ^{11}C or ^{18}F-labeled choline showed promising results for detecting primary and metastatic prostate cancer but was inconsistent in finding densely sclerotic bone lesions;[2,3] ^{11}C-labeled acetate was reported with potential to detect local recurrences and regional lymph node metastases but still remains investigative;[4,5] radiolabeled peptides have been exploited for prostate cancer imaging by specifically targeting prostate cancer cell surface biomarkers or receptors.[6,7] However, noninvasive PET assessment of prostate cancer, local disease or distal metastasis, still remains a challenge.[1,8]

Prostate specific membrane antigen (PSMA) is a type II transmembrane glycoprotein that is overexpressed in prostate cancer but not in the vasculature of normal tissues.[9] Moreover, upregulation of PSMA expression is seen after androgen treatment and found in a positive correlation with lymph node metastases and prostate cancer grade.[10,11] Therefore, PSMA has been utilized as an effective target to develop imaging agents or therapeutics for prostate cancer. Indeed, a U.S. Food and Drug

Received: February 14, 2013
Revised: May 3, 2013
Accepted: June 14, 2013
Published: June 14, 2013

dx.doi.org/10.1021/mp4000844 | *Mol. Pharmaceutics* 2013, 10, 2975−2985

Administration (US FDA) approved prostate cancer imaging agent is an ^{111}In-labeled anti-PSMA monoclonal antibody (^{111}In-capromab pendetide). However, the application of ^{111}In-capromab pendetide is limited because it only reacts with the intracellular epitope of PSMA. Other anti-PSMA antibodies (e.g., J591) that recognize the extracellular PSMA domain have become available, but antibody-mediated imaging suffers from the inherently slow pharmacokinetics and retarded washout rates of antibodies.[12,13] Therefore, while monoclonal antibodies such as J591 are more intended for PSMA-based radioimmunotherapy,[14] small organic molecules have been developed for PSMA-targeted imaging and encouraging results have been seen with glutamate-urea-based and phosphoramidate-based PSMA-targeting ligands.[15−19] A few years ago, 2[(3-amino-3-carboxypropyl)(hydroxy)(phosphinyl)methyl]-pentane-1,5-dioic acid) (GPI) was reported as a potent inhibitor of PSMA with a high binding affinity to prostate cancer cells.[20] Impressively, GPI was found with a rapid *in vivo* clearance profile from nontarget organs including kidneys, which can be regarded as a rather favorable property as compared to the glutamate-urea-based ligands.[20] However, it was also found that the PSMA binding of GPI conjugates was compromised by the serum phosphate anions. To overcome this endogenous competition,[21] a multivalency approach was reported by presenting three copies of GPI on an adamantane scaffold. The adamantane-trimerized GPI conjugate was labeled with ^{99m}Tc, which showed significantly enhanced *in vitro* binding affinity to PSMA but lacking a follow-up *in vivo* evaluation.[22,23]

The role of multivalency has also been recognized in the design of molecular imaging probes for detection sensitivity enhancement. A multivalent imaging probe can be constructed by either attaching a multimeric targeting vector to an imaging platform[24] or imparting the desired multivalency through multipresentation of a target vector on the platform.[25,26] Indeed, the first multimeric PSMA-targeted imaging agent was synthesized by the former approach through coupling a PSMA binding glutamate-urea motif with a bifunctional chelator (DOTA: 1,4,7,10-tetraazacyclododecane-1,4,7,10-tetraacetic acid) in order to enhance the specific binding affinity.[27] However, the complicated synthetic method involved use of solid phase and click chemistry procedures. In the past decade, ^{64}Cu has garnered its popularity in both PET imaging and radiotherapy mainly due to its decay characteristics ($t_{1/2}$ = 12.7 h, 17.4% β^+, $E_{\beta+\max}$ = 0.656 MeV) and its availability in large-scale quantities with high specific activity.[28] In this work, we used the latter approach to construct a dimeric PET imaging probe for PSMA detection by presenting two copies of GPI on a bifunctional chelator scaffold[25] derived from CB-TE2A (2,2′-(1,4,8,11-tetraazabicyclo[6.6.2]hexadecane-4,11-diyl)diacetic acid), an ideal Cu(II) chelator for PET imaging. *In vivo* evaluations of the resulted ^{64}Cu radiotracers were performed in mice bearing LNCaP (PSMA$^+$) and other PSMA$^-$ tumor xenografts.

■ EXPERIMENTAL SECTION

General Methods and Materials. All chemicals, solvents, and reagents were purchased from Sigma-Aldrich and Fisher Chemical unless otherwise noted. All aqueous solutions were prepared in Milli-Q water. Mass spectrum characterization was performed by matrix-assisted laser desorption/ionization time-of-flight (MALDI-TOF) using Voyager-DE PRO Biospectrometry Workstation from Applied Biosystems. The ^{64}CuCl$_2$ solution was purchased from University of Wisconsin. The Na^{125}I solution was purchased from Perkin-Elmer. High performance liquid chromatography (HPLC) was performed on a Waters Xterra Shield RP18 Prep column (250 × 10 mm, 10 μm) and read by a Waters 2996 photodiode array detector and an in-line Shell Jr. 2000 radio-detector. The mobile phase was H_2O with 0.1% TFA (solvent A) and acetonitrile with 0.1% TFA (solvent B). The gradient consisted of 0% B to 80% B in 0−40 min at 4.0 mL/min flow rate. Radio-TLC analysis was performed on a Rita Star Radioisotope TLC Analyzer (Straubenhardt, Germany) to monitor the radiolabeling reaction using C18 reverse phase silica gel plate and 10% NH_4OAc:CH_3OH = 1:1 (v/v) as the mobile phase. GPI was synthesized by following the published procedures with minor modifications, and it remained as a racemic mixture upon the chiral center at the α position of the glutamic acid moiety.[29−32] Both ^{t}Bu-protected CB-TE2A-1DA (2-(11-(carboxymethyl)-1,4,8,11-tetraazabicyclo[6.6.2]hexadecan-4-yl)pentanedioic acid) and CB-TE2A-2DA (2,2′-(1,4,8,11-tetraazabicyclo[6.6.2]-hexadecane-4,11-diyl)dipentanedioic acid) were prepared as previously reported.[25]

Cell Culture and Animal Model. LNCaP, PC3, and H2009 cell lines were obtained from the American Type Culture Collection (ATCC, Manassas, VA). The PC3 cell line was cultured in T-media (Invitrogen Corporation, CA) supplemented with 5% fetal bovine serum (FBS) and 1× penicillin/streptomycin (PS). LNCaP cells were cultured in RPMI 1640 media (HyClone, Thermo Scientific, IL), with 2.05 mM L-glutamine supplemented with 10% FBS. H2009 cell line was cultured in DMEM medium (Invitrogen Corporation, CA) supplemented with 5% FBS. All cells were cultured at 37 °C in an atmosphere of 5% CO_2 and passaged at 75−90% confluency. Male SCID mice (6−8 weeks of age) were purchased from the Wakeland Colony at UT Southwestern. All animal studies were approved by UT Southwestern IACUC. For LNCaP subcutaneous tumor model, LNCaP cell suspension was injected subcutaneously (2.5 × 10^6 cells per injection with 75% BD Matrigel, injection volume 100 μL) into the right and left shoulders of mice. For the PC3 and H2009 dual-tumor model, PC3 cell suspension was injected subcutaneously (2.0 × 10^6 cells per injection with 50% BD Matrigel, injection volume 100 μL) into the right shoulder and H2009 cell suspension was injected subcutaneously (1.0 × 10^6 cells per injection, injection volume 100 μL) into the left shoulder on the same mouse. After injection, animals were monitored twice a week by general observations. Tumor volume (mm^3) was calculated using the ellipsoid formula (π/6 × length × width × depth).

Preparation of H$_2$CBT1G. To a solution of ^{t}Bu$_2$-CB-TE2A-1DA (0.025 g, 47.5 μmol) in anhydrous acetonitrile (0.7 mL) were added *N*-hydroxysuccinimide (NHS, 0.010 g, 82.8 μmol) and 1-ethyl-3-(3-dimethylaminopropyl)carbodiimide hydrochloride (EDC, 0.016 g, 82.8 μmol). The resulting solution was stirred overnight at room temperature (rt). The solvent was then removed under vacuum to afford a crude product, which was purified by HPLC (elution time: 26.7 min), and the resulting fractions were lyophilized to give ^{t}Bu$_2$-CB-TE2A-1NHS (0.013 g, 21.4 μmol, 45%) as a white solid. MALDI-TOF/MS *m*/*z* calculated for $C_{31}H_{53}N_5O_8$: 623.4. Found: 624.6 $[M + H]^+$.

To a solution of the activated acid ^{t}Bu$_2$-CB-TE2A-1NHS (0.005 g, 8.03 μmol) in anhydrous acetonitrile (0.5 mL) was added the solution of GPI (0.003 g, 9.64 μmol) in anhydrous acetonitrile (0.2 mL). To the resulting mixture was added a solution of triethylamine (0.001 g, 10.0 μmol) dissolved in anhydrous acetonitrile (0.2 mL). The resulting mixture was stirred overnight at rt. The solvent was subsequently removed under vacuum to afford a crude product, which was purified by HPLC (elution time: 16.1 min), and the resulting fractions were lyophilized to give ${}^{t}Bu_2$-CB-TE2A-GPI_1 (0.004 g, 5.21 μmol, 65%) as a white solid. MALDI-TOF/MS *m*/*z* calculated for $C_{37}H_{66}N_5O_{13}P$: 819.4. Found: 820.8 $[M + H]^+$. To a solution of ${}^{t}Bu_2$-CB-TE2A-GPI_1 (0.004 g, 5.21 μmol) was added trifluoroacetic acid (0.4 mL). The resulting solution was stirred overnight at rt. The solvent was then removed under vacuum to afford a crude product, which was purified by HPLC (elution time: 9.1 min). The resulting fractions were lyophilized to give the free acid CB-TE2A-GPI_1 (H_2CBT1G) (0.003 mg, 1.22 μmol, 97%) as a white solid. MALDI-TOF/MS *m*/*z* calculated for $C_{29}H_{50}N_5O_{13}P$: 707.3. Found: 708.8 $[M + H]^+$.

Preparation of H_2CBT2G. To a solution of the acid ^{t}Bu-CB-TE2A-2DA (0.035 g, 58.5 μmol) in anhydrous acetonitrile (1.0 mL) were added NHS (0.020 g, 165 μmol) and EDC (0.032 g, 165 μmol). The resulting solution was stirred overnight at rt. The solvent was then removed under vacuum to afford a crude product, which was purified by HPLC (elution time: 28.4 min), and the resulting fractions were lyophilized to give ^{t}Bu-CB-TE2A-2NHS (0.012 g, 14.6 μmol, 25%) as a white solid. MALDI-TOF/MS *m*/*z* calculated for $C_{38}H_{60}N_6O_{12}$: 792.4. Found: 793.6 $[M + H]^+$.

To a solution of the activated acid ${}^{t}Bu_2$-CB-TE2A-2NHS (0.002 g, 2.43 μmol) in anhydrous acetonitrile (0.2 mL) was added the solution of GPI (0.003 g, 9.64 μmol) dissolved in anhydrous acetonitrile (0.2 mL). To the resulting mixture was added a solution of triethylamine (0.001 g, 10.0 μmol) dissolved in anhydrous acetonitrile (0.1 mL). The resulting solution was stirred overnight at rt. The solvent was subsequently removed under vacuum to afford a crude product, which was purified by HPLC (elution time: 16.8 min) and the resulting fraction lyophilized to give ${}^{t}Bu_2$-CB-TE2A-GPI_2 (0.002 g, 1.09 μmol, 45%) as a white solid. MALDI-TOF/MS *m*/*z* calculated for $C_{50}H_{86}N_6O_{22}P_2$: 1184.5. Found: 1186.0 ($[M + H]^+$). To a solution of protected acid ${}^{t}Bu_2$-CB-TE2A-GPI_2 (0.002 g, 1.09 μmol) was added trifluoroacetic acid (0.4 mL). The resulting solution was stirred overnight at rt. The solvent was then removed under vacuum to afford a crude product, which was purified by HPLC (elution time: 10.4 min). The resulting fractions were lyophilized to give the free acid CB-TE2A-GPI_2 (H_2CBT2G) (0.001 mg, 0.76 μmol, 97%) as a white solid. MALDI-TOF/MS *m*/*z* calculated for $C_{42}H_{70}N_6O_{22}P_2$: 1072.4. Found: 1074.0 $[M + H]^+$.

Preparation of ^{64}Cu-CBT1G and ^{64}Cu-CBT2G. To a 1.5 mL vial containing 0.5−1 μg of H_2CBT1G or H_2CBT2G in 50 μL of 0.4 M NH_4OAc (pH = 6.5) solution, 37−74 MBq of ${}^{64}Cu^{2+}$ in 0.1 M HCl was added. The reaction mixture was incubated at 75 °C for 30 min. The radiolabeling yields were determined by radio-TLC. The unreacted ${}^{64}Cu^{2+}$ stayed at the bottom of the TLC plate, while ^{64}Cu-CBT1G or ^{64}Cu-CBT2G moved to the solvent front.

***In Vitro* and *In Vivo* Stability.** The *in vitro* stability test was performed in rat serum. Briefly, ^{64}Cu-CBT1G or ^{64}Cu-CBT2G (0.74 MBq, 5 μL) was added into 100 μL of rat serum (*n* = 3). A 50 μL of sample was taken out and mixed with 200 μL of ethanol, after 4 and 24 h incubation at 37 °C, respectively. The solution was vortexed and centrifuged for 5 min at 21000*g*. The supernatant was then analyzed by radio-TLC. For *in vivo* stability evaluation, male SCID mice were injected with 3.7 MBq of ^{64}Cu-CBT1G or ^{64}Cu-CBT2G in 100 μL of saline via the tail vein. Urine samples were collected within 1 and 24 h p.i., and then analyzed by radio-TLC.

1-Octanol/Water Distribution Coefficient. PBS (phosphate buffered saline, 1×, pH 7.4) and 1-octanol were premixed a day before the experiment. Approximately 0.111 MBq (10 μL) of ^{64}Cu-CBT1G or ^{64}Cu-CBT2G was added to the premixed PBS (490 μL) and 1-octanol (500 μL). The mixture was vigorously vortexed for 1 min at rt. After centrifugation at 21000*g* for 5 min, 100 μL aliquots of both layers were measured using a γ-counter. Then log $D_{\text{oct/water}}$ values were calculated. The experiment was performed in quintuplicate.

Preparation of ^{125}I-GPI. To a solution of *N*-sulfosuccinimidyl-3-(4-hydroxyphenyl)proprionate (Sulfo-SHPP, water-soluble Bonton−Hunter reagent: 7 mg, 19.3 μmol) in 0.2 mL of phosphate buffer (0.1 M, pH 8.0) was added the solution of GPI (3 mg, 9.64 μmol, 0.01 mL of H_2O). The resulting solution was stirred overnight at rt. The product was purified by HPLC, and the collected fractions were lyophilized to give GPI modified with a Bolton−Hunter moiety (BH-GPI: 1.8 mg, 3.86 μmol, 40%) as a white solid. MALDI-TOF/MS *m*/*z* calculated for $C_{19}H_{26}NO_{10}P$: 459.4. Found: 460.2 $[M + H]^+$. A Pierce precoated iodination tube was wetted with 1 mL of Tris buffer (pH 7.5). To the prewetted tube was added 100 μL of Tris buffer, followed by 5 μL (37 MBq) of $Na^{125}I$ (Perkin-Elmer). The iodide was activated for 6 min at rt and then added to the BH-GPI solution (0.5 μg in 0.025 mL of H_2O). After 9 min at rt, the mixture was directly applied to semipreparative HPLC. HPLC fractions of ^{125}I-GPI were collected between 20 and 21 min and then concentrated by a Sep-Pak Light C18 cartridge.

***In Vitro* Cell Binding Assay.** The PSMA binding affinities of H_2CBT1G and H_2CBT2G were determined by a competitive cell-binding assay using ^{125}I-GPI as the radioligand. Suspended LNCaP cells in Tris-buffered saline (TBS) were seeded on multiwell DV plates (Millipore) with 5×10^4 cells per well, and then incubated with ^{125}I-GPI (33,000 cpm/well) in the presence of increasing concentrations (0−10,000 nM) of GPI, H_2CBT1G, and H_2CBT2G at rt for 2 h (*n* = 4). The final volume in each well was maintained at 200 μL. At the end of incubation, unbound ^{125}I-GPI was removed by filtration followed by five-time rinses with cold TBS buffer. The filters were collected, and their radioactivity was measured. The best-fit IC_{50} values (inhibitory concentration where 50% of the ^{125}I-GPI bound on LNCaP cells were displaced) of GPI, H_2CBT1G, and H_2CBT2G were calculated by fitting the data with nonlinear regression using GraphPad Prism 5.0. The same experiments were performed in triplicate.

Cell Uptake and Internalization. Cell uptake and internalization of ^{64}Cu-CBT1G and ^{64}Cu-CBT2G were measured according to ref 33. Briefly, LNCaP cells were seeded into 48-well plates (BD BioCoat, poly-D-lysine) at a density of 2.5×10^5 cells/well and incubated at 37 °C, 5% CO_2 overnight. After washing the cells once with 0.5 mL of TBS buffer at 37 °C, approximately 150,000 cpm of ^{64}Cu-CBT1G or ^{64}Cu-CBT2G was added to cells in 0.2 mL of TBS buffer and incubated at 37 °C, 5% CO_2 for 1, 10, 30, 60, and 120 min (*n* = 6). There were three additional wells coincubating ^{64}Cu-CBT1G or ^{64}Cu-CBT2G with 2 μg of GPI for nonspecific binding assay. The unbound radioligands were removed by rinsing with 0.5 mL of ice-cold TBS buffer per well. The surface bound radioligands were removed by incubating with 0.5 mL of ice-cold low-pH stripping buffer (50 mM glycine and 0.15 M NaCl, pH 3.0) for 10 min at 4 °C. Then the stripping buffer

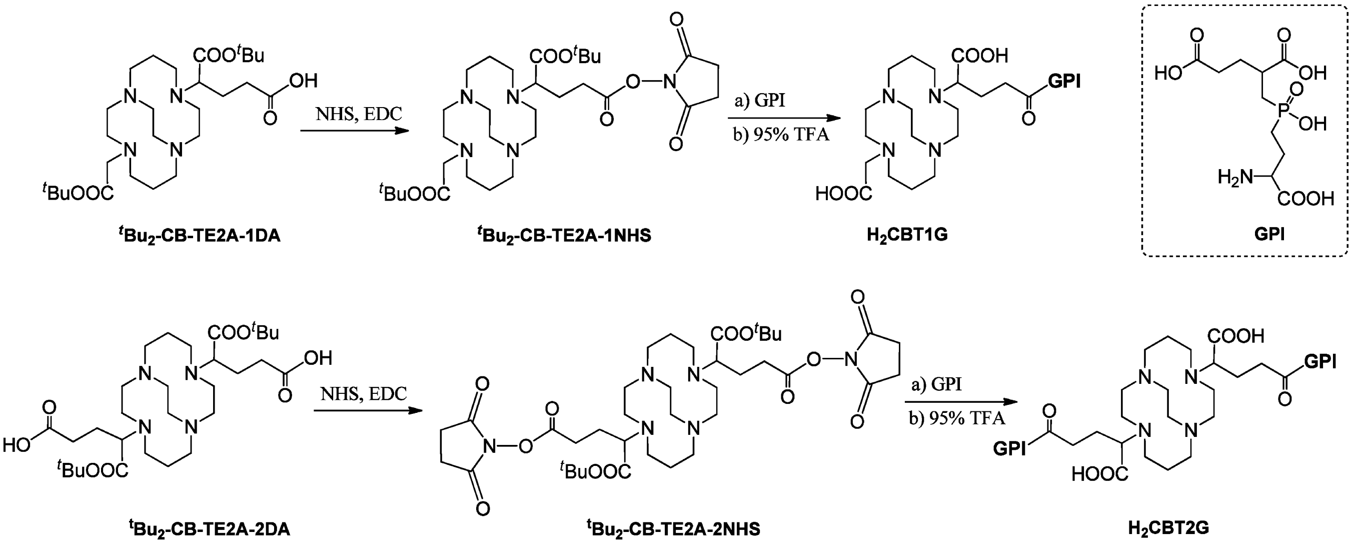

Figure 1. Synthetic routes to H_2CBT1G and H_2CBT2G conjugates.

media were collected and counted with a γ-counter to determine the surface bound radioligand level. At last, 0.5 mL of 1 M NaOH was added to each well to solubilize cells. The activity was counted to quantify the internalized radioligand.

Anion Competition Assay in Different Solutions. LNCaP cells were seeded into 48-well plates (BD BioCoat, poly-D-lysine) at a density of 2.5 × 10^5 cells/well and incubated at 37 °C, 5% CO_2 overnight. After washing the cells with 0.5 mL of TBS buffer, PBS buffer, or LNCaP cell culture medium, approximately 150,000 cpm of ^{64}Cu-CBT1G or ^{64}Cu-CBT2G was added to the cells in different buffers or media and incubated at 37 °C, 5% CO_2 for 2 h ($n = 3$). The unbound radioligand was removed from cells by washing with 0.5 mL of ice-cold corresponding buffer per well. The cells were then solubilized in 1 M NaOH for radioactivity measurement by γ-counter. To measure the nonspecific binding, 2 μg of GPI was coloaded with ^{64}Cu-CBT1G or ^{64}Cu-CBT2G in the TBS buffer condition ($n = 3$).

Small Animal PET/CT Imaging. Small animal PET/CT imaging was performed with a Siemens Inveon PET/CT Multimodality System on tumor-bearing SCID mice that had intravenously received ca. 3.7 MBq of ^{64}Cu-CBT1G or ^{64}Cu-CBT2G in 100 μL via the tail vein. Prior to imaging, the mouse was sedated on the imaging bed under 2% isoflurane anesthesia for the duration of imaging. Immediately after the CT data acquisition that was performed at 80 kV and 500 μA with a focal spot of 58 μm, static PET scans were conducted at the given time points postinjection (p.i.) (1 h, 4 h, and 24 h) for 15 min. For the blockade study, the radiotracer was coadministrated with 2-(phosphonomethyl)pentanedioic acid (2-PMPA) at the dose of 30 mg/kg of mouse body weight. Both CT and PET images were reconstructed with manufacturer's software. Reconstructed CT and PET images were fused for quantitative data analysis; regions of interest (ROIs) were drawn as guided by CT and quantitatively expressed as percent injected dose per gram of tissue (% ID/g).

Statistical Analysis. Statistical analyses were performed using GraphPad Prism. A p value less than 0.05 (unpaired t test) was considered statistically significant. All results are presented as mean ± standard deviation.

■ RESULTS

Preparation of H_2CBT1G and H_2CBT2G. CB-TE2A-1DA and CB-TE2A-2DA were prepared according to our previously reported procedures[25] (Figure 1). The inner and outer carboxylate groups of CB-TE2A-1DA and CB-TE2A-2DA were orthogonally protected. In this work, their outer carboxylate groups were deprotected for the conjugation with GPI while the inner carboxylate groups remained protected with ^{t}Bu group. The GPI conjugation was carried out by a typical NHS/EDC procedure. The NHS esters, ^{t}Bu$_2$-CB-TE2A-1NHS and ^{t}Bu$_2$-CB-TE2A-2NHS, were synthesized and subsequently treated with amine containing GPI under basic conditions. The synthesis of these NHS-activated esters was reported in our previous work, in which the ester purification was performed by extraction.[25] However, the use of extracted ^{t}Bu$_2$-CB-TE2A-1NHS and ^{t}Bu$_2$-CB-TE2A-2NHS led to poor yields and difficult purification in this present work. The problem was especially evident when using ^{t}Bu$_2$-CB-TE2A-2NHS. To address this unexpected issue, we performed the ester purification via HPLC so that the impurities and side products could be efficiently removed. The relevant fraction from HPLC were collected and immediately lyophilized. Each time only freshly prepared −NHS ester intermediates were used for GPI conjugation. The conjugation of ^{t}Bu$_2$-CB-TE2A-1NHS and ^{t}Bu$_2$-CB-TE2A-2NHS with 1 and 4 equiv of GPI in the presence of triethylamine provided ^{t}Bu-protected conjugates in 45−65% yields. Finally, the α-carboxylate group was deprotected using 95% TFA to provide H_2CBT1G and H_2CBT2G, each containing two internal α-carboxylic acids for ^{64}Cu chelating.

Radiochemistry. Both H_2CBT1G and H_2CBT2G were efficiently labeled by ^{64}Cu at 75 °C in 0.4 M NH_4OAc buffer within 30 min as monitored by radio-TLC. For *in vitro* and *in vivo* evaluations, the radiochemical purities of ^{64}Cu-CBT1G and ^{64}Cu-CBT2G were maintained at over 99% as determined by radio-HPLC. Their specific activities were in the range of 50−80 GBq/μmol. Both ^{64}Cu-CBT1G and ^{64}Cu-CBT2G are highly hydrophilic, as indicated by their low log D values (^{64}Cu-CBT1G, −3.25 ± 0.15; ^{64}Cu-CBT2G, −2.70 ± 0.03). The serum stability test and the urine sample analysis showed that both ^{64}Cu-CBT1G and ^{64}Cu-CBT2G remained intact within 24

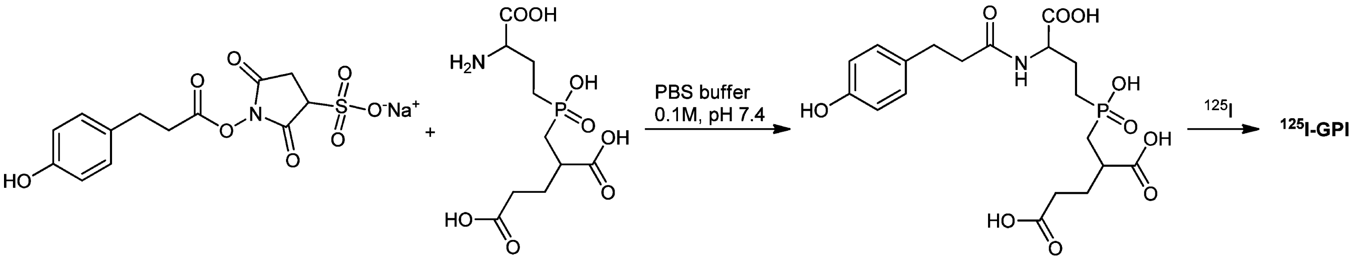

Figure 2. Preparation of ^{125}I-GPI.

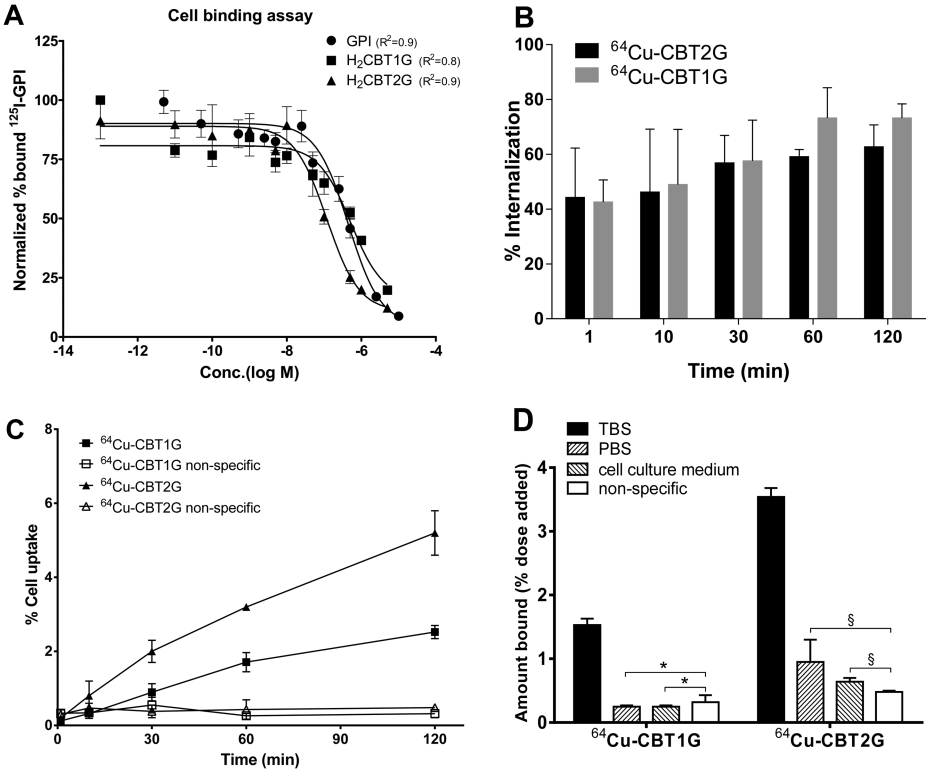

Figure 3. *In vitro* cell binding assay. (A) The PSMA binding affinities of GPI, H_2CBT1G, and H_2CBT2G were measured by a competitive cell-binding assay using LNCaP cells (PSMA positive) where ^{125}I-GPI was employed as the PSMA-specific radioligand. The IC_{50} values of GPI, H_2CBT1G, and H_2CBT2G were determined to be 460 ± 13, 578 ± 81, and 129 ± 17 nM, respectively ($n = 3$). (B) Cell internalization of ^{64}Cu-CBT1G and ^{64}Cu-CBT2G. (C) Cell uptake kinetics in LNCaP cells with ^{64}Cu-CBT1G and ^{64}Cu-CBT2G ($n = 6$) and their nonspecific internalization levels by coincubating with 2 μg of GPI per well ($n = 3$). (D) LNCaP cell binding assay in TBS buffer, PBS buffer, and cell culture medium. Nonspecific binding assay was performed by coincubating with 2 μg of GPI in TBS buffer. $^*p > 0.05$; $^{\S}p < 0.05$.

h without detectable demetallization, which is a great advantage of using our CB-TE2A derived chelator scaffold for ^{64}Cu-labeling.

***In Vitro* Cell Study.** The high PSMA binding affinity ($K_i = 9$ nM) of GPI reported in the literature was measured by using ^{99m}Tc-labeled GPI as the PSMA specific radioligand.[20,22] In this work, we designed and synthesized an ^{125}I-labeled GPI analogue (Figure 2) as the radioligand for the competitive cell binding assay of GPI, H_2CBT1G, and H_2CBT2G. Because GPI has no available functional group for direct radioiodination, a Bolton–Hunter moiety was introduced. To obtain the highest achievable specific activity of ^{125}I-GPI, an HPLC purification method was applied. The *in vitro* PSMA binding affinities of GPI, H_2CBT1G, and H_2CBT2G were measured by the required concentration to displace 50% of LNCaP cell bound ^{125}I-GPI ($n = 3$), where GPI served as the positive control. All three compounds inhibited the binding of ^{125}I-GPI to LNCaP cells in a dose-dependent manner (Figure 3A). The calculated IC_{50} values were 460 ± 13 nM (GPI), 578 ± 81 nM (H_2CBT1G), and 129 ± 17 nM (H_2CBT2G). No significant difference was observed between GPI and H_2CBT1G, indicating the conjugation had negligible effect on the PSMA binding affinity of GPI. The significant increase of H_2CBT2G's PSMA binding affinity reflects the anticipated multivalent effect.

The PSMA-mediated uptake and internalization of ^{64}Cu-CBT1G and ^{64}Cu-CBT2G were evaluated using LNCaP cells with and without presence of excess GPI in TBS buffer. Both ^{64}Cu-CBT1G and ^{64}Cu-CBT2G displayed a similar and appreciable level of internalization in a time-dependent manner in the absence of GPI (Figure 3B), while the cell uptake amount of ^{64}Cu-CBT2G was about two times higher than that of ^{64}Cu-CBT1G starting from 10 min (Figure 3C). The presence of GPI at the saturating concentration nearly abolished cell uptake (down to <0.5%), indicating that cell uptake was mediated by PSMA.

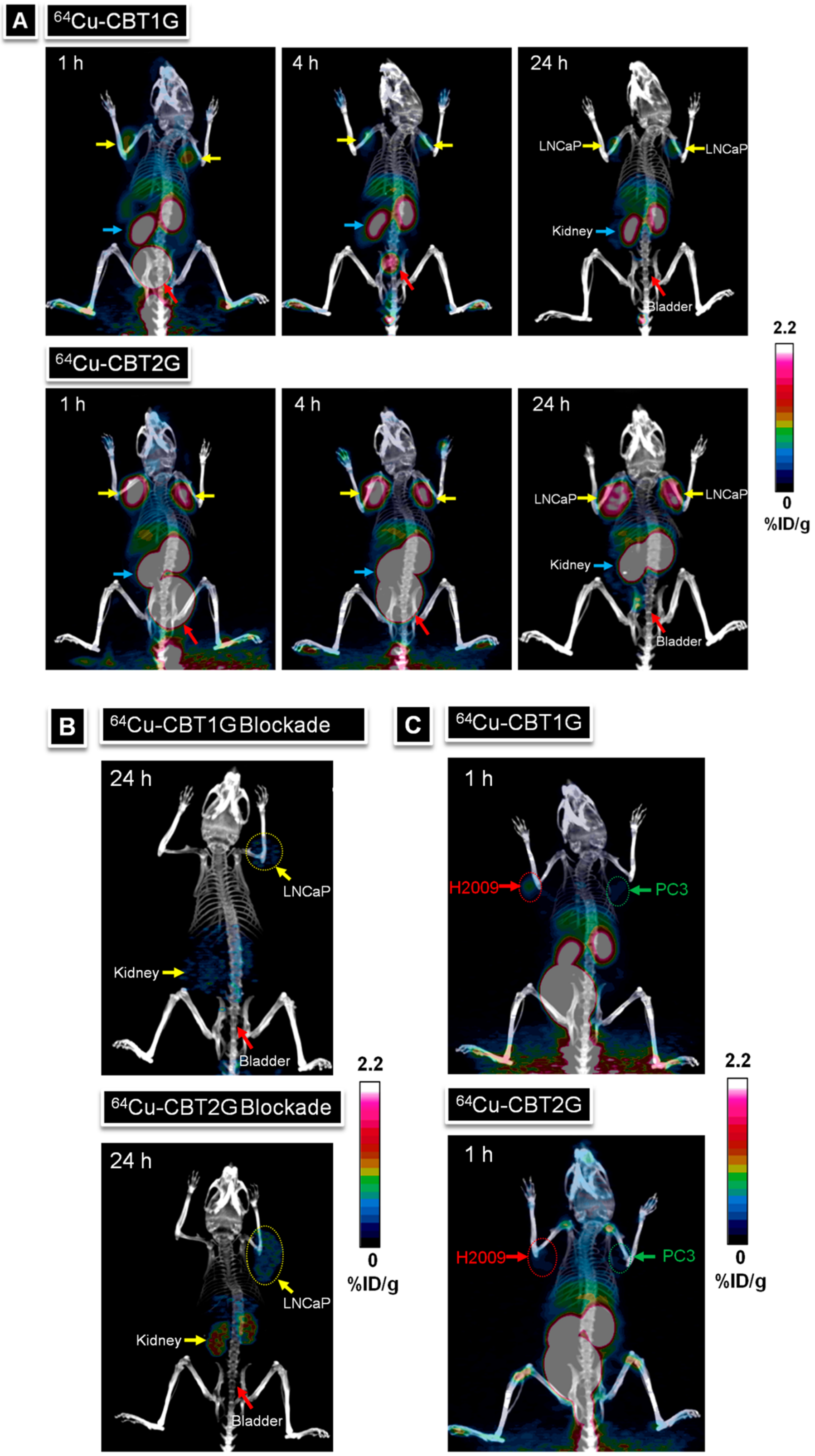

Figure 4. Representative whole-body coronal PET/CT images of ^{64}Cu-CBT1G and ^{64}Cu-CBT2G in (A) LNCaP tumor bearing mice at 1, 4, and 24 h p.i.; (B) LNCaP tumor bearing mice at 24 h p.i. with blockade (coadministration with 30 mg/kg of 2-PMPA); and (C) PC3 and H2009 tumor bearing mice at 1 h p.i. All the images are presented at the same signal intensity scale (0–2.2% ID/g).

The multimeric design of ^{64}Cu-CBT2G was intended to address the binding competition of GPI with the endogenous phosphate anions in serum.[22] In order to evaluate the multivalent effect on this competition,[21] both ^{64}Cu-CBT1G and ^{64}Cu-CBT2G were tested to bind with LNCaP cells in no phosphate-containing TBS buffer and phosphate-containing PBS buffer and LNCaP cell culture medium. Shown in Figure 3D, both phosphate-containing buffers, PBS and cell culture

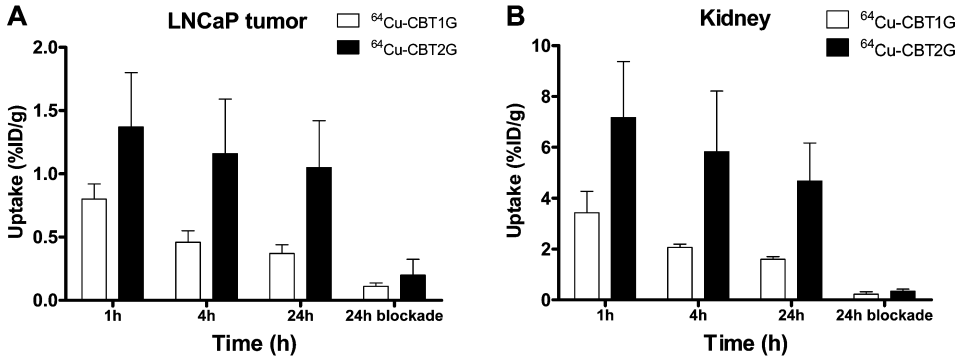

Figure 5. Comparative uptake of ^{64}Cu-CBT1G and ^{64}Cu-CBT2G at 1 h, 4 h, 24 h, and 24 h blockade in LNCaP tumors (A) and kidneys (B) obtained from quantitative imaging analysis. Data are presented as % ID/g ± SD ($n = 3$).

medium, significantly inhibited the PSMA binding of ^{64}Cu-CBT1G and ^{64}Cu-CBT2G as compared to TBS. However, while the monomeric ^{64}Cu-CBT1G's PMSA binding was reduced to the nonspecific binding level when exposed to phosphate anions, the dimeric ^{64}Cu-CBT2G showed a significant improvement of its PSMA binding in competing with phosphates ($p < 0.05$).

Small Animal PET/CT Imaging. Small animal PET/CT imaging studies were conducted in SCID mice bearing LNCaP (PSMA$^+$) or PC3 and H2009 (PSMA$^-$) tumors. To increase the sample size for statistics, LNCaP tumors were implanted on both sides of shoulder. Representative coronal PET/CT images are presented in Figure 4. LNCaP tumors were clearly visualized by ^{64}Cu-CBT2G at 1, 4, and 24 h p.i., and their intensity maintained steady throughout the 24 h period (Figure 4A). LNCaP tumors were also visible by ^{64}Cu-CBT1G but with much lower contrast than ^{64}Cu-CBT2G at all time points. Both ^{64}Cu-CBT1G and ^{64}Cu-CBT2G exhibited a rapid clearance profile through the urinary route, which is desirable for good tumor to background contrast. Besides PSMA$^+$ tumors, kidneys and bladder (urine) were other major organs showing significant activity accumulation at 1 and 4 h p.i. Once urine was out of the body, the bladder was nearly invisible especially at 24 h p.i.

The quantitative imaging analysis is shown in Figure 5. The LNCaP tumor accumulation of ^{64}Cu-CBT2G remained rather stable within 24 h (1.46 ± 0.54, 1.12 ± 0.56, and 1.00 ± 0.50% ID/g at 1, 4, and 24 h p.i., respectively). In contrast, ^{64}Cu-CBT1G showed much lower LNCaP tumor uptake (0.81 ± 0.12, 0.46 ± 0.10, and 0.35 ± 0.11% ID/g at 1, 4, and 24 h p.i., respectively) than ^{64}Cu-CBT2G (one tailed $p < 0.05$ at each time point) and a significant tumor uptake drop from 1 to 4 h p.i. (43%, one tailed $p < 0.05$). The significantly enhanced tumor uptake and imaging signal retention of the dimeric ^{64}Cu-CBT2G can be attributed to the multivalent effect. Due to their negatively charged and highly hydrophilic nature, both ^{64}Cu-CBT1G and ^{64}Cu-CBT2G showed low liver uptake (<1.0% ID/g). However, relatively high kidney uptake was observed for both GPI conjugates. This is consistent with the previous report of PSMA expression in proximal renal tubules[34,35] (Figure 5B). Of note, ^{64}Cu-CBT1G and ^{64}Cu-CBT2G displayed a similar uptake difference in PMSA$^+$ tumors and kidneys, indicative of their imaging specificity of PSMA that was verified by a blockade study using a known PSMA inhibitor, 2-PMPA. In the blockade study, LNCaP tumor uptake of both ^{64}Cu-CBT1G and ^{64}Cu-CBT2G at 24 h p.i. was reduced by approximately five times (Figure 5A). A similar magnitude of uptake decrease was also observed in kidneys at 24 h p.i. The PSMA imaging specificity was further confirmed by using two PMSA$^-$ tumor models, PC3 and H2009. At the time point as early as 1 h p.i., PC3 and H2009 tumors were barely visible by either ^{64}Cu-CBT1G or ^{64}Cu-CBT2G.

■ DISCUSSION

The cell membrane bound PSMA is a valuable biomarker that has drawn considerable interest in the development of diagnostics and therapeutics of prostate and other cancer types, given the well recognized fact that its upregulation in primary prostate cancer and metastases and its expression level has positive correlations with prostatic cancer stages, especially in castration resistance prostate cells.[10,11,34,36] In addition to antibody-based imaging agents (i.e., US FDA approved capromab pendetide), a different class of urea based small organic compounds, initially developed for the inhibition of PSMA activities, has been extensively utilized for PET and SPECT imaging probe development for noninvasive assessment of PSMA expression in prostate cancer. For instance, ^{123}I-MIP-1072 ((*S*)-2-(3-((*S*)-1-carboxy-5-((4-^{123}I-iodobenzyl)-amino)pentyl)ureido)pentanedioic acid) has been in clinical trials.[37] Reported with a high binding affinity (9 nM) to PSMA, GPI chemically resembles the glutamate-urea compounds and the phosphoramidate ligands as well, due to the similar binding pentanedioic acid moiety. A major obstacle that impedes the use of GPI for *in vivo* PSMA imaging is the endogenous binding competition caused by phosphate anions in serum. Based on the assumption that multivalency can enhance the desired specific binding affinity and decrease the off-rate of the specific ligand, indeed a multivalency strategy was reported to overcome the hurdle by presenting three copies of GPI on an adamantine. Although the *in vitro* data demonstrated a great success as indicated by the significantly enhanced PSMA binding affinity and tolerance to the endogenous binding competition,[22] the *in vivo* performance of such multivalent GPI radiolabeled agents has not been reported.

Among nonstandard PET nuclides, ^{64}Cu is of great clinical potential owing to its low positron range, commercial availability, and reasonably long decay half-life.[28] Recently we have reported a bifunctional chelator scaffold, CB-TE2A-2DA, for multivalent PET probe design aimed for the use of ^{64}Cu.[25] As compared to the commonly used chelator as DOTA, this chelator scaffold features an intact CB-TE2A core to form a stable and neutral complex with ^{64}Cu and two peripheral functional groups for anchoring of targeting molecules.[25] In this work, we presented two copies of GPI on CB-TE2A-2DA for

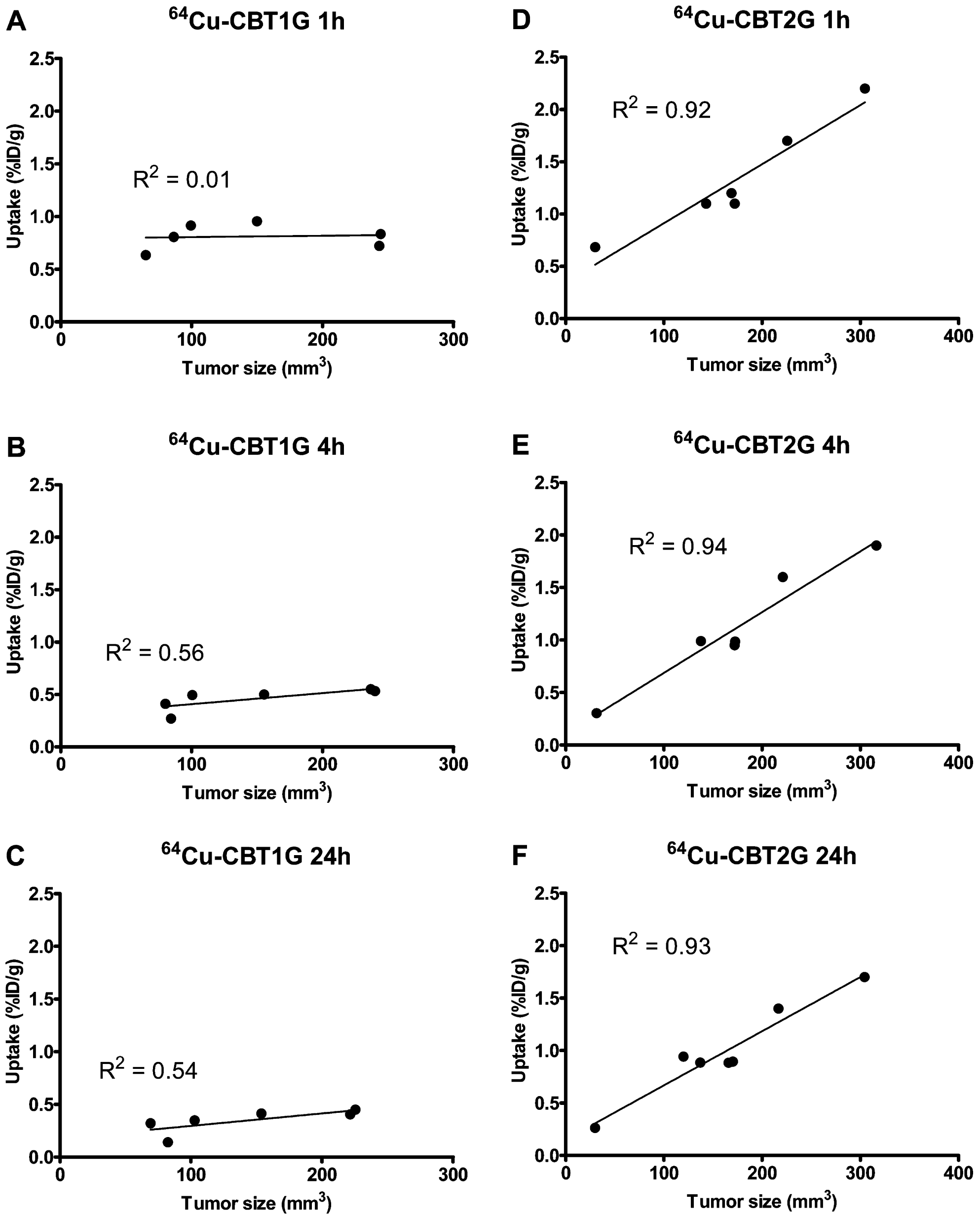

Figure 6. Correlations between LNCaP tumor uptake and tumor size (mm^3) at 1 h, 4 h, and 24 h p.i. A−C: ^{64}Cu-CBT1G. D−F: ^{64}Cu-CBT2G.

^{64}Cu PET probe design with the goal of developing a practical approach for noninvasive imaging of PSMA.

Measured by an *in vitro* competitive cell binding assay, the dimeric GPI conjugate, H_2CBT2G, indeed showed the anticipated enhancement of PSMA binding affinity. The multivalent enhancement ratios calculated by dividing IC_{50} values were 3.6 (GPI/H_2CBT2G) and 4.5 (H_2CBT1G/H_2CBT2G), consistent with the multivalent effect. As mentioned above, increased PSMA binding affinities can be attributed to the multivalent effect, which might be explained by the structure of PSMA. It was reported that PSMA exists in both noncovalently dimeric and monomeric forms; and the homodimerization occurs in the extracellular domain of PSMA.[38] Interestingly, it is the PSMA dimer that maintains the native conformation and possesses a higher level enzymatic activity than monomeric PSMA.[38] These findings provide further rationales in support of multivalent imaging probe design for PSMA detection.

In the absence of antibody binding, PSMA is constitutively internalized at a fairly consistent rate of ∼60%.[39] Therefore, it is critically important for GPI-based imaging probes to reach the target for imaging signal buildup. In other words, they must be able to out-compete endogenous phosphate anions for PSMA binding. Not surprisingly, phosphate anions showed a strong effect on PSMA binding of both monomeric ^{64}Cu-CBT1G and dimeric ^{64}Cu-CBT2G (Figure 3C), whereas the dimeric one displayed a significant improvement of PSMA binding when in competition with phosphate anions. This improvement might be attributed to the decreased off-rate of ^{64}Cu-CBT2G from PSMA targets.

Given the structural similarities between GPI and other PSMA inhibitors of phosphoramidate peptidomimetics, ^{64}Cu-CBT2G observed similar internalization profiles as reported,[40] which can be characterized by two features: time dependence before reaching the steady retention state (Figure 3B) and no obvious effect on PSMA internalization.[41] In contrast, anti-

PSMA antibodies, such as J591, are capable of accelerating PSMA internalization up to 3-fold in a dose dependent manner.[39] Upon the mode of PSMA inhibition ^{64}Cu-CBT2G likely exhibited rapidly reversible profiles as 2-PMPA due to the lack of a phosphoramidate P−N linkage in GPI.[42] This reversible profile has been suggested to be less favorable for *in vivo* PSMA targeting,[43] which might be another reason for relatively low PSMA$^+$ tumor uptake for ^{64}Cu-CBT2G.

The imaging signal amplification resulting from the dimeric presentation in ^{64}Cu-CBT2G was evaluated in a PSMA$^+$ mouse xenograft model established by LNCaP cell line. As shown in Figure 4A, the visual contrast of LNCaP tumors was strikingly enhanced by ^{64}Cu-CBT2G as compared to ^{64}Cu-CBT1G during the period of study. The corresponding imaging quantification revealed the signal amplification was approximately 2-fold at all three imaging time points (Figure 5A). The PSMA imaging specificity was verified by two different methods. One used the conventional blocking approach by coadministering the radiotracer with a blocking dose of a known PSMA inhibitor (Figure 4B); and the other employed two PSMA$^-$ tumor xenografts, PC3 and H2009 (Figure 4C). The significant imaging signal reduction as shown in both methods clearly demonstrated the PSMA imaging specificity for both ^{64}Cu-CBT1G and ^{64}Cu-CBT2G. It is noteworthy that no bone uptake was observed for ^{64}Cu-CBT1G or ^{64}Cu-CBT2G, indicating that the GPI-based PSMA imaging probes may find potential application for detection of prostate cancer metastases, which are preferentially found in bone. In addition, it was found that the bladder radioactivity was voided at 24 h p.i., while the tumor imaging intensity was maintained with ^{64}Cu-CBT2G. This late time point imaging, which was made possible by the reasonably long decay half-life of ^{64}Cu, provides an opportunity of imaging localized prostate cancer with ^{64}Cu-CBT2G. Both ^{64}Cu-CBT1G and ^{64}Cu-CBT2G showed an appreciable level of renal uptake. This is not a surprise because the proximal renal tubules express PSMA.[17] Of note, the renal uptake level of ^{64}Cu-CBT2G was much lower at all three time points compared to the reported Glu-urea based imaging agents[15−18,27] (Figure 5B). This is obviously a desirable feature for PSMA targeted agents.

High sensitivity aside, PET is capable of imaging quantification. Therefore, an ideal PET imaging probe is expected to enable both detection and quantification of a target biomarker. This is of great clinical significance because it offers a noninvasive approach for molecular profiling of disease status, which can potentiate personalized treatment of disease by stratifying patients for tailored therapy. Indeed, endeavors to quantify the PSMA expression with noninvasive imaging approaches have been seen in the literature[18,44] as represented by ^{64}Cu-J591 enabled PET[44] and ^{123}I-MIP-1072 enabled SPECT.[18] Given the PSMA detection capability proved for ^{64}Cu-CBT2G, we further evaluated its potential to quantitatively delineate the expression level of PSMA in tumors at various stages. In our evaluation, PSMA$^+$ LNCaP tumors were allowed to grow to different sizes (weights). Both ^{64}Cu-CBT1G and ^{64}Cu-CBT2G were used to image tumors. As shown in Figure 6, ^{64}Cu-CBT2G displayed a much better linear correlation ($R^2 \geq 0.92$ at all three time points) between the tumor uptake (% ID/g) and the tumor size than ^{64}Cu-CBT1G ($R^2 = 0.01$, 0.56, and 0.54 at 1 h, 4 h, and 24 h, respectively). Of note, the unit of % ID/g in Figure 6 is a standardized radiotracer uptake value obtained from the quantitative PET imaging analysis on the assumption that 1 cm^3 of tumor tissue equals 1 g. Given that the target of GPI is PMSA, we believe that the radiotracer concentration (% ID/g) found in LNCaP tumors reflects the PMSA density expressed by the tumors during the course of tumor growth. Of course, this must be further verified by immunohistochemistry. Interestingly, the slope of the linear correlation, which represents the detection sensitivity and accuracy of PSMA level change, was much greater for ^{64}Cu-CBT2G than for ^{64}Cu-CBT1G. This observation clearly indicates the imaging quantification potential of PSMA in prostate cancer when ^{64}Cu-CBT2G is used.

CONCLUSION

A promising PSMA targeted imaging probe, ^{64}Cu-CBT2G, was successfully designed and synthesized by presenting two copies of GPI on a bifunctional chelator scaffold. Our results indicate that the multivalent approach of imaging probe design was able to minimize the endogenous serum phosphate competition that hampers the PSMA binding of GPI and thus afforded the desired imaging sensitivity for *in vivo* detection of PSMA. Given the positive linear relationship observed between the tumor uptake of ^{64}Cu-CBT2G and the tumor size, ^{64}Cu-CBT2G is expected to potentiate the quantitative assessment of PSMA expression in prostate cancer noninvasively.

AUTHOR INFORMATION

Corresponding Author

*Department of Radiology & Advanced Imaging Research Center, The University of Texas Southwestern Medical Center, Dallas, Texas 75390, United States. Phone: 214-645-5978. Fax: 214-645-2885. E-mail: Xiankai.Sun@UTSouthwestern.edu.

Notes

The authors declare no competing financial interest.

ACKNOWLEDGMENTS

This work was partially supported by grants from the National Institutes of Health (UL1 RR024982, U24 CA126608, and R01CA159144) and the Prostate Cancer Research Program of the United States Army Medical Research and Materiel Command (W81XWH-12-1-0336 and W81XWH-08-1-0305). The authors acknowledge the generous support of a private donor that allowed the purchase of the Inveon PET/CT system.

ABBREVIATIONS USED

PSMA, prostate specific membrane antigen; CT, computed tomography; MRI, magnetic resonance imaging; SPECT, single-photon emission computed tomography; PET, positron emission tomography; ^{18}F-FDG, 2-deoxy-2-(^{18}F)fluoro-D-glucose; FDA, food and drug administration; GPI, 2[(3-amino-3-carboxypropyl)(hydroxy)(phosphinyl)-methyl]pentane-1,5-dioic acid); DOTA, 1,4,7,10-tetraazacyclododecane-1,4,7,10-tetraacetic acid; CB-TE2A, 2,2′-(1,4,8,11-tetraazabicyclo[6.6.2]-hexadecane-4,11-diyl)diacetic acid; % ID/g, percentage of the injected dose per gram of tissue; MALDI-TOF, matrix-assisted laser desorption/ionization time-of-flight; HPLC, high performance liquid chromatography; TLC, thin layer chromatography; CB-TE2A-1DA, 2-(11-(carboxymethyl)-1,4,8,11-tetraazabicyclo[6.6.2]hexadecan-4-yl)pentanedioic acid; CB-TE2A-2DA, 2,2′-(1,4,8,11-tetraazabicyclo[6.6.2]hexadecane-4,11-diyl)dipentanedioic acid; FBS, fetal bovine serum; IACUC, Institutional Animal Care and Use Committee;

NHS, *N*-hydroxysuccinimide; EDC, 1-ethyl-3-(3-dimethylaminopropyl)carbodiimide; TBS, Tris-buffered saline; ROI, regions of interest; 2-PMPA, 2-(phosphonomethyl)-pentanedioic acid

■ REFERENCES

(1) Emonds, K. M.; Swinnen, J. V.; Mortelmans, L.; Mottaghy, F. M. Molecular imaging of prostate cancer. *Methods* **2009**, *48* (2), 193–9.

(2) Vees, H.; Buchegger, F.; Albrecht, S.; Khan, H.; Husarik, D.; Zaidi, H.; Soloviev, D.; Hany, T. F.; Miralbell, R. F-18-choline and/or C-11-acetate positron emission tomography: detection of residual or progressive subclinical disease at very low prostate-specific antigen values (< 1 ng/mL) after radical prostatectomy. *BJU Int.* **2007**, *99* (6), 1415–1420.

(3) Giovacchini, G.; Gajate, A. M.; Messa, C.; Fazio, F. Increased C-11 choline uptake in pagetic bone in a patient with coexisting skeletal metastases from prostate cancer. *Clin. Nucl. Med.* **2008**, *33* (11), 797–8.

(4) Albrecht, S.; Buchegger, F.; Soloviev, D.; Zaidi, H.; Vees, H.; Khan, H. G.; Keller, A.; Bischof Delaloye, A.; Ratib, O.; Miralbell, R. (11)C-acetate PET in the early evaluation of prostate cancer recurrence. *Eur. J. Nucl. Med. Mol. Imaging* **2007**, *34* (2), 185–96.

(5) Ponde, D. E.; Dence, C. S.; Oyama, N.; Kim, J.; Tai, Y. C.; Laforest, R.; Siegel, B. A.; Welch, M. J. 18F-fluoroacetate: a potential acetate analog for prostate tumor imaging—in vivo evaluation of 18F-fluoroacetate versus 11C-acetate. *J. Nucl. Med.* **2007**, *48* (3), 420–8.

(6) Rogers, B. E.; Bigott, H. M.; McCarthy, D. W.; Della Manna, D.; Kim, J.; Sharp, T. L.; Welch, M. J. MicroPET imaging of a gastrin-releasing peptide receptor-positive tumor in a mouse model of human prostate cancer using a Cu-64-labeled bombesin analogue. *Bioconjugate Chem.* **2003**, *14* (4), 756–763.

(7) Zhang, X.; Cai, W.; Cao, F.; Schreibmann, E.; Wu, Y.; Wu, J. C.; Xing, L.; Chen, X. 18F-labeled bombesin analogs for targeting GRP receptor-expressing prostate cancer. *J. Nucl. Med.* **2006**, *47* (3), 492–501.

(8) Bouchelouche, K.; Capala, J.; Oehr, P. Positron emission tomography/computed tomography and radioimmunotherapy of prostate cancer. *Curr. Opin. Oncol.* **2009**, *21* (5), 469–74.

(9) Bander, N. H. Technology insight: monoclonal antibody imaging of prostate cancer. *Nat. Clin. Pract. Urol.* **2006**, *3* (4), 216–25.

(10) Wright, G. L., Jr.; Grob, B. M.; Haley, C.; Grossman, K.; Newhall, K.; Petrylak, D.; Troyer, J.; Konchuba, A.; Schellhammer, P. F.; Moriarty, R. Upregulation of prostate-specific membrane antigen after androgen-deprivation therapy. *Urology* **1996**, *48* (2), 326–34.

(11) Sweat, S. D.; Pacelli, A.; Murphy, G. P.; Bostwick, D. G. Prostate-specific membrane antigen expression is greatest in prostate adenocarcinoma and lymph node metastases. *Urology* **1998**, *52* (4), 637–40.

(12) Jain, R. K. Transport of molecules, particles, and cells in solid tumors. *Annu. Rev. Biomed. Eng.* **1999**, *1*, 241–63.

(13) Holland, J. P.; Divilov, V.; Bander, N. H.; Smith-Jones, P. M.; Larson, S. M.; Lewis, J. S. 89Zr-DFO-J591 for immunoPET of prostate-specific membrane antigen expression in vivo. *J. Nucl. Med.* **2010**, *51* (8), 1293–300.

(14) Akhtar, N. H.; Pail, O.; Saran, A.; Tyrell, L.; Tagawa, S. T. Prostate-specific membrane antigen-based therapeutics. *Adv. Urol.* **2012**, *2012*, 973820.

(15) Banerjee, S. R.; Foss, C. A.; Castanares, M.; Mease, R. C.; Byun, Y.; Fox, J. J.; Hilton, J.; Lupold, S. E.; Kozikowski, A. P.; Pomper, M. G. Synthesis and evaluation of technetium-99m- and rhenium-labeled inhibitors of the prostate-specific membrane antigen (PSMA). *J. Med. Chem.* **2008**, *51* (15), 4504–17.

(16) Kularatne, S. A.; Wang, K.; Santhapuram, H. K.; Low, P. S. Prostate-specific membrane antigen targeted imaging and therapy of prostate cancer using a PSMA inhibitor as a homing ligand. *Mol. Pharmaceutics* **2009**, *6* (3), 780–9.

(17) Banerjee, S. R.; Pullambhatla, M.; Byun, Y.; Nimmagadda, S.; Green, G.; Fox, J. J.; Horti, A.; Mease, R. C.; Pomper, M. G. 68Ga-labeled inhibitors of prostate-specific membrane antigen (PSMA) for imaging prostate cancer. *J. Med. Chem.* **2010**, *53* (14), 5333–41.

(18) Hillier, S. M.; Kern, A. M.; Maresca, K. P.; Marquis, J. C.; Eckelman, W. C.; Joyal, J. L.; Babich, J. W. 123I-MIP-1072, a small-molecule inhibitor of prostate-specific membrane antigen, is effective at monitoring tumor response to taxane therapy. *J. Nucl. Med.* **2011**, *52* (7), 1087–93.

(19) Nedrow-Byers, J. R.; Jabbes, M.; Jewett, C.; Ganguly, T.; He, H.; Liu, T.; Benny, P.; Bryan, J. N.; Berkman, C. E. A phosphoramidate-based prostate-specific membrane antigen-targeted SPECT agent. *Prostate* **2012**, *72* (8), 904–12.

(20) Humblet, V.; Lapidus, R.; Williams, L. R.; Tsukamoto, T.; Rojas, C.; Majer, P.; Hin, B.; Ohnishi, S.; De Grand, A. M.; Zaheer, A.; Renze, J. T.; Nakayama, A.; Slusher, B. S.; Frangioni, J. V. High-affinity near-infrared fluorescent small-molecule contrast agents for in vivo imaging of prostate-specific membrane antigen. *Mol. Imaging* **2005**, *4* (4), 448–62.

(21) Robinson, M. B.; Blakely, R. D.; Couto, R.; Coyle, J. T. Hydrolysis of the brain dipeptide N-acetyl-L-aspartyl-L-glutamate. Identification and characterization of a novel N-acetylated alpha-linked acidic dipeptidase activity from rat brain. *J. Biol. Chem.* **1987**, *262* (30), 14498–506.

(22) Misra, P.; Humblet, V.; Pannier, N.; Maison, W.; Frangioni, J. V. Production of multimeric prostate-specific membrane antigen small-molecule radiotracers using a solid-phase 99mTc preloading strategy. *J. Nucl. Med.* **2007**, *48* (8), 1379–89.

(23) Humblet, V.; Misra, P.; Bhushan, K. R.; Nasr, K.; Ko, Y. S.; Tsukamoto, T.; Pannier, N.; Frangioni, J. V.; Maison, W. Multivalent Scaffolds for Affinity Maturation of Small Molecule Cell Surface Binders and Their Application to Prostate Tumor Targeting. *J. Med. Chem.* **2009**, *52* (2), 544–50.

(24) Zhou, Y.; Chakraborty, S.; Liu, S. Radiolabeled Cyclic RGD Peptides as Radiotracers for Imaging Tumors and Thrombosis by SPECT. *Theranostics* **2011**, *1*, 58–82.

(25) Liu, W.; Hao, G. Y.; Long, M. A.; Anthony, T.; Hsieh, J. T.; Sun, X. K. Imparting Multivalency to a Bifunctional Chelator: A Scaffold Design for Targeted PET Imaging Probes. *Angew. Chem., Int. Ed.* **2009**, *48* (40), 7346–9.

(26) Singh, A. N.; Liu, W.; Hao, G.; Kumar, A.; Gupta, A.; Oz, O. K.; Hsieh, J. T.; Sun, X. Multivalent bifunctional chelator scaffolds for gallium-68 based positron emission tomography imaging probe design: signal amplification via multivalency. *Bioconjugate Chem.* **2011**, *22* (8), 1650–62.

(27) Banerjee, S. R.; Pullambhatla, M.; Shallal, H.; Lisok, A.; Mease, R. C.; Pomper, M. G. A modular strategy to prepare multivalent inhibitors of prostate-specific membrane antigen (PSMA). *Oncotarget* **2011**, *2* (12), 1244–53.

(28) Hao, G.; Singh, A. N.; Oz, O. K.; Sun, X. Recent advances in copper radiopharmaceuticals. *Curr. Radiopharm.* **2011**, *4* (2), 109–21.

(29) Jackson, P. F.; Tays, K. L.; Maclin, K. M.; Ko, Y. S.; Li, W.; Vitharana, D.; Tsukamoto, T.; Stoermer, D.; Lu, X. C.; Wozniak, K.; Slusher, B. S. Design and pharmacological activity of phosphinic acid based NAALADase inhibitors. *J. Med. Chem.* **2001**, *44* (24), 4170–5.

(30) Selvam, C.; Oueslati, N.; Lemasson, I. A.; Brabet, I.; Rigault, D.; Courtiol, T.; Cesarini, S.; Triballeau, N.; Bertrand, H. O.; Goudet, C.; Pin, J. P.; Acher, F. C. A virtual screening hit reveals new possibilities for developing group III metabotropic glutamate receptor agonists. *J. Med. Chem.* **2010**, *53* (7), 2797–813.

(31) Zeng, B. Q.; Wong, K. K.; Pompliano, D. L.; Reddy, S.; Tanner, M. E. A phosphinate inhibitor of the meso-diaminopimelic acid-adding enzyme (MurE) of peptidoglycan biosynthesis. *J. Org. Chem.* **1998**, *63* (26), 10081–5.

(32) Feng, Y.; Coward, J. K. Prodrug forms of N-[(4-deoxy-4-amino-10-methyl)pteroyl]glutamate-gamma-[psiP(O)(OH)]-glutar ate, a potent inhibitor of folylpoly-gamma-glutamate synthetase: synthesis and hydrolytic stability. *J. Med. Chem.* **2006**, *49* (2), 770–88.

(33) Hausner, S. H.; Abbey, C. K.; Bold, R. J.; Gagnon, M. K.; Marik, J.; Marshall, J. F.; Stanecki, C. E.; Sutcliffe, J. L. Targeted in vivo imaging of integrin alphavbeta6 with an improved radiotracer and its

relevance in a pancreatic tumor model. *Cancer Res.* **2009**, *69* (14), 5843−50.

(34) Silver, D. A.; Pellicer, I.; Fair, W. R.; Heston, W. D.; Cordon-Cardo, C. Prostate-specific membrane antigen expression in normal and malignant human tissues. *Clin. Cancer Res.* **1997**, *3* (1), 81−5.

(35) Kinoshita, Y.; Kuratsukuri, K.; Landas, S.; Imaida, K.; Rovito, P. M., Jr.; Wang, C. Y.; Haas, G. P. Expression of prostate-specific membrane antigen in normal and malignant human tissues. *World J. Surg.* **2006**, *30* (4), 628−36.

(36) Rajasekaran, S. A.; Anilkumar, G.; Oshima, E.; Bowie, J. U.; Liu, H.; Heston, W.; Bander, N. H.; Rajasekaran, A. K. A novel cytoplasmic tail MXXXL motif mediates the internalization of prostate-specific membrane antigen. *Mol. Biol. Cell* **2003**, *14* (12), 4835−45.

(37) Barrett, J.; LaFrance, N.; Coleman, R. E.; Goldsmith, S.; Stubbs, J.; Petry, N.; Vallabhajosula, S.; Maresca, K.; Femia, F.; Babich, J. Targeting metastatic prostate cancer [PCa] in patients with 123I-MIP1072 & 123I-MIP1095. *J. Nucl. Med.* **2009**, *50* (Suppl.), 522.

(38) Schulke, N.; Varlamova, O. A.; Donovan, G. P.; Ma, D. S.; Gardner, J. P.; Morrissey, D. M.; Arrigale, R. R.; Zhan, C. C.; Chodera, A. J.; Surowitz, K. G.; Maddon, P. J.; Heston, W. D. W.; Olson, W. C. The homodimer of prostate-specific membrane antigen is a functional target for cancer therapy. *Proc. Natl. Acad. Sci. U.S.A.* **2003**, *100* (22), 12590−5.

(39) Liu, H.; Rajasekaran, A. K.; Moy, P.; Xia, Y.; Kim, S.; Navarro, V.; Rahmati, R.; Bander, N. H. Constitutive and antibody-induced internalization of prostate-specific membrane antigen. *Cancer Res.* **1998**, *58* (18), 4055−60.

(40) Liu, T.; Wu, L. Y.; Kazak, M.; Berkman, C. E. Cell-Surface labeling and internalization by a fluorescent inhibitor of prostate-specific membrane antigen. *Prostate* **2008**, *68* (9), 955−64.

(41) Rajasekaran, A. K.; Anilkumar, G.; Christiansen, J. J. Is prostate-specific membrane antigen a multifunctional protein? *Am. J. Physiol.* **2005**, *288* (5), C975−C981.

(42) Liu, T.; Toriyabe, Y.; Kazak, M.; Berkman, C. E. Pseudoirreversible inhibition of prostate-specific membrane antigen by phosphoramidate peptidomimetics. *Biochemistry* **2008**, *47* (48), 12658−60.

(43) Liu, T.; Wu, L. Y.; Hopkins, M. R.; Choi, J. K.; Berkman, C. E. A targeted low molecular weight near-infrared fluorescent probe for prostate cancer. *Bioorg. Med. Chem. Lett.* **2010**, *20* (23), 7124−6.

(44) Evans, M. J.; Smith-Jones, P. M.; Wongvipat, J.; Navarro, V.; Kim, S.; Bander, N. H.; Larson, S. M.; Sawyers, C. L. Noninvasive measurement of androgen receptor signaling with a positron-emitting radiopharmaceutical that targets prostate-specific membrane antigen. *Proc. Natl. Acad. Sci. U.S.A.* **2011**, *108* (23), 9578−82.

European Journal of Medicinal Chemistry 80 (2014) 308–315

Contents lists available at ScienceDirect

European Journal of Medicinal Chemistry

journal homepage: http://www.elsevier.com/locate/ejmech

Original article

Enantiopure bifunctional chelators for copper radiopharmaceuticals – Does chirality matter in radiotracer design?[☆]

Ajay N. Singh [a,b,1], Marianna Dakanali [a,1], Guiyang Hao [a], Saleh Ramezani [a], Amit Kumar [a], Xiankai Sun [a,c,*]

[a] *Department of Radiology, The University of Texas Southwestern Medical Center, Dallas, TX, USA*
[b] *Department of Basic Science, Appalachian College of Pharmacy, Oakwood, VA, USA*
[c] *Department of Advanced Imaging Research Center, The University of Texas Southwestern Medical Center, Dallas, TX, USA*

ARTICLE INFO

Article history:
Received 18 January 2014
Received in revised form
22 April 2014
Accepted 23 April 2014
Available online 25 April 2014

Keywords:
Molecular imaging
Positron emission tomography
Integrin $\alpha_v\beta_3$
Copper-64
Bifunctional chelator (BFC)
Imaging
Diagnosis
Prognosis

ABSTRACT

It is well recognized that carbon chirality plays a critical role in the design of drug molecules. However, very little information is available regarding the effect of stereoisomerism of macrocyclic bifunctional chelators (BFC) on biological behaviors of the corresponding radiopharmaceuticals. To evaluate such effects, three enantiopure stereoisomers of a copper radiopharmaceutical BFC bearing two chiral carbon atoms were synthesized in forms of R,R-, S,S-, and R,S-. Their corresponding peptide conjugates were prepared by coupling with a model peptide sequence, c(RGDyK), which targets the $\alpha_v\beta_3$ integrin for *in vitro* and *in vivo* evaluation of their biological behaviors as compared to the racemic conjugate. Despite the chirality differences, all the conjugates showed a similar *in vitro* binding affinity profile to the $\alpha_v\beta_3$ integrin (106, 108, 85 and 100 nM for rac-H_2-**1**, RR-H_2-**1**, SS-H_2-**1**, and RS-H_2-**1** respectively with all *p* values > 0.05) and a similar level of *in vivo* tumor uptake (2.72 ± 0.45, 2.60 ± 0.52, 2.45 ± 0.48 and 2.88 ± 0.59 for rac-^{64}Cu-**1**, RR-^{64}Cu-**1**, SS-^{64}Cu-**1**, and RS-^{64}Cu-**1** at 1 h p.i. respectively). Furthermore, they demonstrated a nearly identical biodistribution pattern in major organs (e.g. 2.07 ± 0.21, 2.13 ± 0.58, 1.70 ± 0.20 and 1.90 ± 0.46 %ID/g at 24 h p.i. in liver for rac-^{64}Cu-**1**, RR-^{64}Cu-**1**, SS-^{64}Cu-**1**, and RS-^{64}Cu-**1** respectively; 1.80 ± 0.46, 2.30 ± 1.49, 1.73 ± 0.31 and 2.23 ± 0.71 at 24 h p.i. in kidneys for rac-^{64}Cu-**1**, RR-^{64}Cu-**1**, SS-^{64}Cu-**1**, and RS-^{64}Cu-**1** respectively). Therefore we conclude that the chirality of BFC plays a negligible role in $\alpha_v\beta_3$-targeted copper radiopharmaceuticals. However, we believe it is still worthwhile to consider the chirality effects of BFCs on other targeted imaging or therapeutic agents.

1. Introduction

Positron emission tomography (PET) is routinely used in clinical and preclinical settings for diagnostic or prognostic imaging of cancer or other diseases [1–5]. The success of PET lies in its high sensitivity and specificity to detect physiological changes at cellular or molecular level. Combined with computed tomography (CT), dual-modal PET/CT imaging provides both molecular changes and detailed anatomical information for a better diagnosis. Currently, ^{18}F ($t_{1/2} = 109$ min) and ^{11}C ($t_{1/2} = 20.3$ min) are the most commonly used PET radionuclides for the development of PET imaging probes. However, their short half-lives limit their applications mainly in small organic or biological molecules. Recently, ^{64}Cu ($t_{1/2} = 12.7$ h; $E_{\beta+\,\max} = 0.653$ MeV, 17.4%), a non-standard PET radionuclide, has drawn considerable attention in the community of PET due to its low positron energy, commercial availability, and reasonably long decay half-life [6,7]. More importantly, the well-established coordination chemistry of copper potentially enables a rapid translation from bench-top science to clinical practice of copper radiopharmaceuticals with a variety of imaging or radiotherapeutic applications involving peptides, antibodies or their fragments, and nanoparticles [8–10].

The stability of the metal complex moiety is of critical importance in the design of a metal radiopharmaceutical. In the past decade, we and other groups had research focused on a cross-

---

[☆] Grant support: This work was partially supported by the Prostate Cancer Research Program of the United States Army Medical Research and Materiel Command (W81XWH-08-1-0305 and W81XWH-12-1-0336). The authors acknowledge the generous support of a private donor that allowed the purchase of the Siemens Inveon PET-CT Multi-modality System.

[*] Corresponding author. University of Texas Southwestern Medical Center, 5323 Harry Hines Blvd, Dallas, TX 75390-8542, USA.

E-mail address: Xiankai.Sun@UTSouthwestern.edu (X. Sun).

[1] Authors contributed to this work equally.

http://dx.doi.org/10.1016/j.ejmech.2014.04.071
0223-5234/

bridged tetraazamacrocyclic chelator, CB-TE2A [4,11-bis-(carbo-*tert*-butoxymethyl)-1,4,8,11-tetraazabicyclo[6.6.2]hexadecane] for the development of novel copper radiopharmaceuticals because CB-TE2A forms one of the most stable complexes with Cu(II), which is more resistant to reductive metal loss than are other tetraazamacrocyclic complexes [11,12]. The high *in vivo* stability of Cu(II)-CB-TE2A complex arises from the perfect match of Cu(II) and the cavity size formed by the pre-organized CB-cyclam ligand [11,13]. In this hexa coordinated complex, Cu(II) is completely encapsulated in the CB-cyclam cavity by four coordinating nitrogen atoms and two carboxylate oxygen atoms. However, once a pendent carboxylate arm of the CB-TE2A is converted to amide during vector conjugation, the stability of the Cu(II)-CB-TE2A will be compromised and the metal moiety become positively charged, which could be detrimental to the biological behavior of the copper radiopharmaceuticals. To avoid this problem, we have recently reported a novel bifunctional chelating (BFC) scaffold based on the CB-TE2A core [10]. The designed BFC scaffold, CB-TE2GA (Fig. 1), utilizes an orthogonally protected glutaric heterodiester as the coordinating side arm. The choice of this side arm allows selective deprotection of the peripheral carboxylates for conjugation with targeting molecules, while the inner carboxylates can be preserved for ^{64}Cu complexation. We reported that the imaging probe so designed (rac-^{64}Cu-**1**) indeed showed high *in vivo* stability and enhanced tumor uptake due to the multivalent effect [10].

However, our reported BFC scaffold, CB-TE2GA, bears two chiral carbon atoms in the glutaric acid side arm, which can give rise to three potential stereoisomers [14,15]. When targeting molecules are attached to the side arms, the chirality difference may lead to different spatial dispositions of the targeting moieties depending on the chirality of the side arms, which can potentially impact their binding affinities to the target receptors.

To evaluate the role of chiral BFC in the properties of copper radiopharmaceuticals, we synthesized CB-TE2GA in three enantiopure forms (RR-**8**, SS-**8**, RS-**8**) starting from the enantiopure side arm precursors, namely R- and S-5-benzyl 1-(*tert*-butyl) 2-((methylsulfonyl)oxy)pentadioate (R-**6**, S-**6**). The synthesized BFCs, RR-**8**, SS-**8**, and RS-**8**, were conjugated with an $\alpha_v\beta_3$ integrin specific peptide, c(RGDyK), to provide enantiopure peptide conjugates (RR-H$_2$-**1**, SS-H$_2$-**1**, RS-H$_2$-**1**), respectively. When labeled with ^{64}Cu, the peptide conjugates were evaluated by *in vitro* binding assay, PET/CT imaging, and imaging-derived biodistribution profiles in tumor-bearing mice. The racemic conjugate was used as the control for comparative evaluation.

2. Results

2.1. Synthesis

The synthesis of enantiopure RR-H$_2$-**1**, SS-H$_2$-**1**, and RS-H$_2$-**1** was achieved in three steps; i) synthesis of the chiral side arms, S-**6** and R-**6** ii) synthesis of the BFC scaffolds, RR-**8**, SS-**8**, and RS-**8**, and iii) conjugation of two molecules of c(RGDyK) on to the BFCs (Schemes 1–3). The synthesis of the chiral side arms, S-**6** and R-**6**, started from L- and D-glutamic acid, respectively. Following a reported procedure [16,17], L- or D-glutamic acid was converted to S- or R-**2** respectively, via diazotization using sodium nitrite (NaNO$_2$) in the presence of excess HCl in 78% yield. The stereoselectivity of the conversion of L-glutamic acid to **S-2** depends critically on both the rate of the addition of the aqueous NaNO$_2$ solution to the acidic L-glutamic acid solution and on the reaction temperature that must be maintained between 0 and 5 °C during the addition [17]. The synthesis of S-**2** uses the stereoselectivity of the deamination reaction, which is known to proceed with complete retention of the configuration [16]. The *t*Bu-protected ester S-**3** was synthesized in 55% yield using a standard esterification procedure, namely 4-dimethylaminopyridine (DMAP) and *N*, *N*′-dicyclohexylcarbodiimide (DCC) in tetrahydrofuran (THF). Unlike the reported procedure where S-**3** was synthesized from the acid chloride of S-**2**, the DMAP/DCC directed esterification was easy to handle and the product, lactone S-**3,** could be purified and obtained at gram scale. The obtained S-**3** was then hydrolyzed using one equivalent of 1 N KOH to provide the potassium salt of S-**4**. A small sample of the above synthesized salt was treated with 3 N HCl to yield the corresponding acid in 60% yield for purification and characterization purposes. The carboxylate salt of S-**4** was alkylated with benzyl bromide (BnBr) in dimethylformamide (DMF) to afford the crude S-**5,** an orthogonally protected diester. Purification of crude S-**5** using column chromatography yielded the pure product in 52% yield. The secondary alcohol of S-**5** was then converted to the corresponding mesylate as a leaving group to provide S-**6** in quantitative yield. Mesylate was chosen as the leaving group based on the fact that it is stable in aqueous workup at room temperature and the controlled alkylation of CB-cyclam by S$_N$2 reaction affords the complete inversion of stereochemistry of the product. Dialkylation of CB-cyclam was carried out by adding the mesylated S-**6** or R-**6**, to a suspension of a half equivalent of CB-cyclam in acetonitrile preheated to 50 °C in the presence of potassium carbonate. The orthogonally protected diester, RR-**7** or SS-**7**, was obtained in 52%

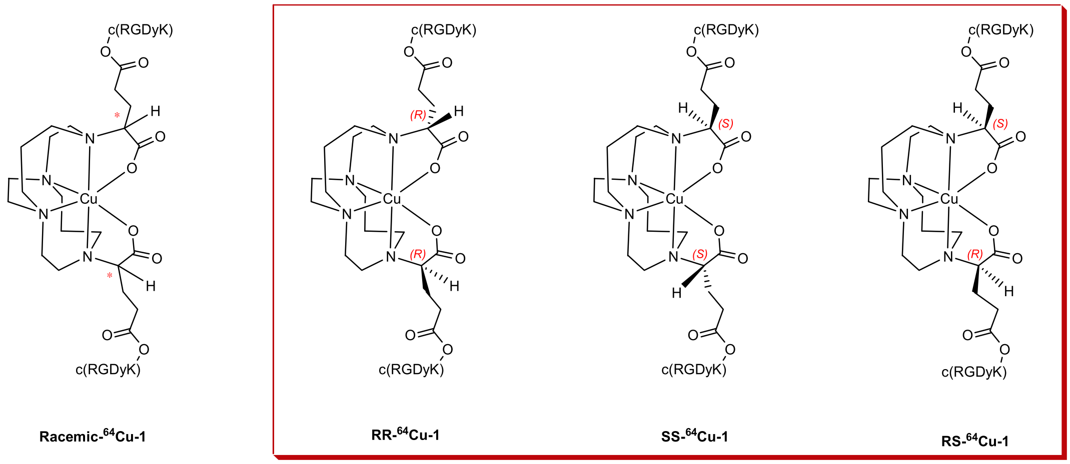

Racemic-^{64}Cu-1 **RR-^{64}Cu-1** **SS-^{64}Cu-1** **RS-^{64}Cu-1**

Fig. 1. Structures of peptide conjugates: rac-^{64}Cu-**1**, RR-^{64}Cu-**1**, SS-^{64}Cu-**1** and RS-^{64}Cu-**1**.

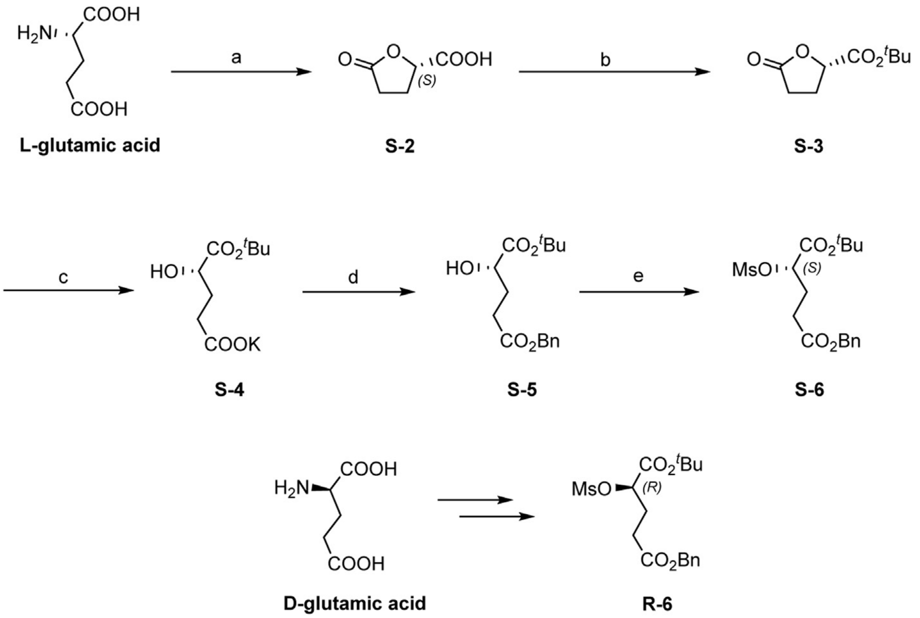

Scheme 1. Synthesis of 5-benzyl 1-(*tert*-butyl) 2-((methylsulfonyl)oxy)pentadioate (S-**6**) and (R-**6**). Reagents and conditions: a) L-glutamic acid (1 equiv), HCl_{conc}, $NaNO_2$ (1.5 equiv), H_2O/dioxane, 0 °C then r.t., 20 h; b) *t*-BuOH (1.1 equiv), DMAP (0.4 equiv), DCC (1.1 equiv), CH_2Cl_2, r.t., 18 h; c) 1 N KOH (2 equiv), THF, 0 °C then r.t., 4 h; d) BnBr (1 equiv), DMF, r.t. 8 h; e) MsCl (1.01 equiv), Et_3N (1.4 equiv), CH_2Cl_2, 0 °C then r.t., 2 h.

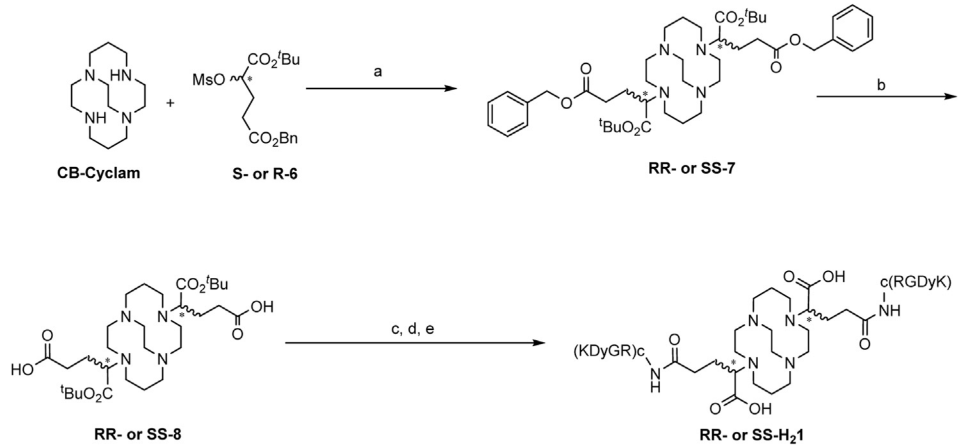

Scheme 2. Synthesis of RR-H_2-**1** and SS-H_2-**1**. Reagents and conditions: a) K_2CO_3 (1.2 equiv), CH_3CN, r.t. 24 h then 50 °C 24 h; b) 10% Pd/C (catalytic), H_2, 2-propanol, r.t. 12 h; c) NHS (4 equiv), EDC HCl (4 equiv), CH_3CN, r.t. 18 h; d) c(RGDyK) (4 equiv), DIPEA, DMF, r.t 24 h; e) TFA, r.t. 12 h.

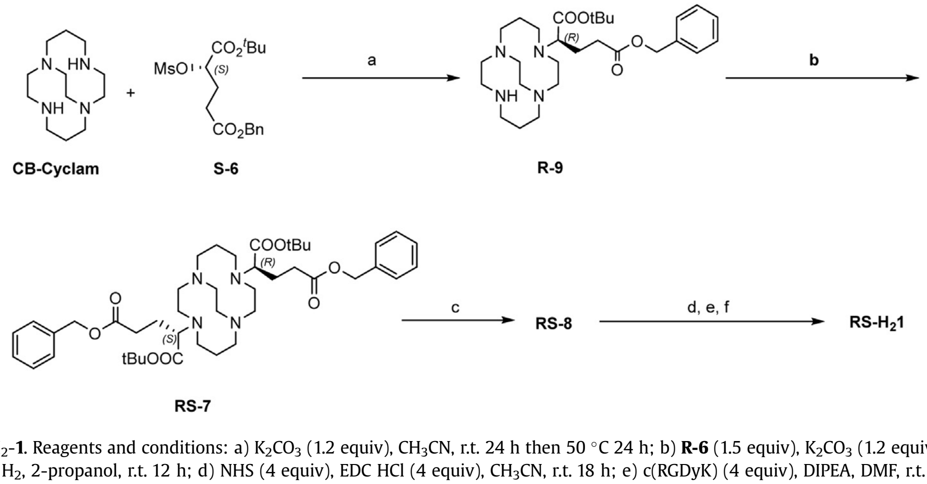

Scheme 3. Synthesis of RS-H_2-**1**. Reagents and conditions: a) K_2CO_3 (1.2 equiv), CH_3CN, r.t. 24 h then 50 °C 24 h; b) **R-6** (1.5 equiv), K_2CO_3 (1.2 equiv), CH_3CN, r.t. 24 h then 50 °C 24 h; c) 10% Pd/C (catalytic), H_2, 2-propanol, r.t. 12 h; d) NHS (4 equiv), EDC HCl (4 equiv), CH_3CN, r.t. 18 h; e) c(RGDyK) (4 equiv), DIPEA, DMF, r.t. 24 h; f) TFA, r.t. 12 h.

yield. Addition of the chiral side arms, S-**6** and R-**6**, provided the BFC scaffolds RR-**7** and SS-**7**, respectively, with the complete inversion of configuration. The BFC scaffold RS-**7** was synthesized in two steps: reaction of CB-cylam with S-**6**, to yield scaffold R-**9**, followed by alkylation with R-**6** to provide RS-**7** in 40% yield.

The synthesized BFC scaffolds RR-**7**, SS-**7**, and RS-**7** contain two protected carboxylate groups at α and γ positions of the side arms. The benzyl protected γ-carboxylate groups were selectively deprotected and the resulting acids were conjugated with the c(RGDyK) peptide. Catalytic debenzylation of RR-**7**, SS-**7**, and RS-**7** was achieved using 10% Pd/C in 2-propanol under hydrogen atmosphere to afford RR-**8**, SS-**8**, and RS-**8** in quantitative yield. The obtained γ-carboxylic acids were activated by N-hydroxysuccinimide (NHS) for acid-amine conjugation chemistry. The conjugation of NHS-activated RR-**8**, SS-**8**, and RS-**8** with two equivalents of c(RGDyK) in the presence of N, N-diisopropylethylamine (DIPEA) provided the *t*-butyl protected conjugates in quantitative yield. Finally, the α-carboxylate groups were deprotected using 95% trifluoroacetic acid to provide RR-H_2-**1**, SS-H_2-**1**, and RS-H_2-**1**, each of which contains two free carboxylic acids for radiolabeling with ^{64}Cu.

Compounds, S- or R-**2** to S- or R-**6** were characterized by ^{1}H and ^{13}C NMR and found to be identical to those reported in the literature [17]. Compounds, S- or R-**2** to S- or R-**6**, showed no differences in ^{1}H and ^{13}C NMR spectra as expected for enantiomers. The peptide conjugates were characterized by their molecular ion peak shown on MALDI-mass spectra, and the purity of the conjugates was verified by HPLC. Optical rotation $[\alpha]_D$ for compounds RR-**7** and SS-**7** was recorded to be +34.594 and −36.594 respectively, verifying that these compounds are enantiomers. Furthermore, the circular dichroism (CD) spectra measured in CH_3CN:H_2O (1:5) solution, further confirm the enantiomeric nature of the optically active BFC scaffolds, RR-**8** and SS-**8**. The CD spectrum of RR-**8** shows a positive Cotton effect in the 230–280 nm region, while SS-**8** exhibits the opposite sign of the effect in the same range (Fig. 2).

2.2. Radiochemistry

All peptide conjugates (rac-H_2-**1**, RR-H_2-**1**, SS-H_2-**1**, and RS-H_2-**1**) were successfully labeled (>90% RCY) with ^{64}Cu within 30 min at 75 °C in 0.4 mM NH_4OAc buffer to provide rac-^{64}Cu-**1**, RR-^{64}Cu-**1**, SS-^{64}Cu-**1**, and RS-^{64}Cu-**1**, respectively. A series of radiolabeling conditions by decreasing the amount of peptide conjugates while the radioactivity of ^{64}Cu was fixed were tested to reach around 20 GBq/mmol specific activity. The ^{64}Cu-labeled conjugates were purified in one step using a pre-conditioned C-18 Sep-Pak light cartridge with a >90% recovery rate. The radiochemical purity of the ^{64}Cu-labeled conjugates after cartridge purification was >97% as determined by radio-HPLC. The overall radiochemical procedure including the synthesis and purification steps took less than 45 min.

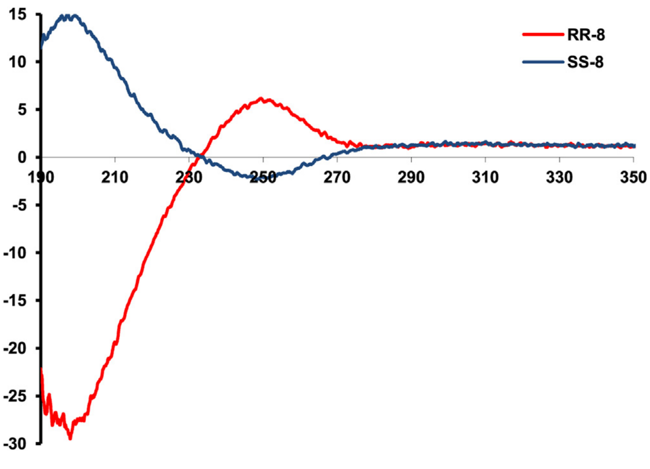

Fig. 2. Measured CD spectra of RR-**8** and SS-**8** in CH_3CN:H_2O 1:5.

2.3. Binding assay

The $\alpha_v\beta_3$ binding affinities of rac-H_2-**1**, RR-H_2-**1**, SS-H_2-**1**, and RS-H_2-**1** were measured by a competitive cell-binding assay using U87MG cells in which ^{125}I-echistatin was employed as $\alpha_v\beta_3$-specific radioligand for competitive displacement. The U87MG cell line was chosen because the $\alpha_v\beta_3$ integrin density on the cell surface is the highest among the solid tumor cell lines that have been assessed [18]. The IC_{50} values of rac-H_2-**1**, RR-H_2-**1**, SS-H_2-**1**, and RS-H_2-**1** which represent their concentrations required to displace 50% of the ^{125}I-echistation bound on the U87MG cells, were determined to be 106, 108, 85 and 100 nM, respectively ($n = 4$) with all p values >0.05 (see Fig. 3).

2.4. Small animal PET-CT imaging

To evaluate the effect of the chirality of BFC on the *in vivo* properties of the $\alpha_v\beta_3$-targeted imaging agents, a comparative PET/CT imaging study was performed in SCID mice bearing integrin $\alpha_v\beta_3$-positive PC-3 prostate cancer xenografts on a Siemens Inveon PET/CT Multimodality System. Representative trans-axial PET/CT images at 1, 4, and 24 h p.i. are displayed in Fig. 4. The PC-3 tumors were clearly visualized by all four probes up to 24 h p.i. The four agents showed nearly identical tumor uptake at the three time points, namely 2.72 ± 0.45, 2.60 ± 0.52, 2.45 ± 0.48 and 2.88 ± 0.59 for rac-^{64}Cu-**1**, RR-^{64}Cu-**1**, SS-^{64}Cu-**1**, and RS-^{64}Cu-**1** respectively at 1 h p.i., 2.32 ± 0.37, 2.13 ± 0.49, 1.58 ± 0.32 and 1.73 ± 0.36 at 4 h p.i. and 1.77 ± 0.32, 1.92 ± 0.51, 1.16 ± 0.20 and 1.22 ± 0.31 at 24 h p.i. with all p values > 0.05 except for SS-^{64}Cu-**1** that showed significantly lower uptake than other conjugates at 4 and 24 h p.i. due to its lower specific activity at the injection time. In addition, we compared their *in vivo* distribution profiles in major organs and

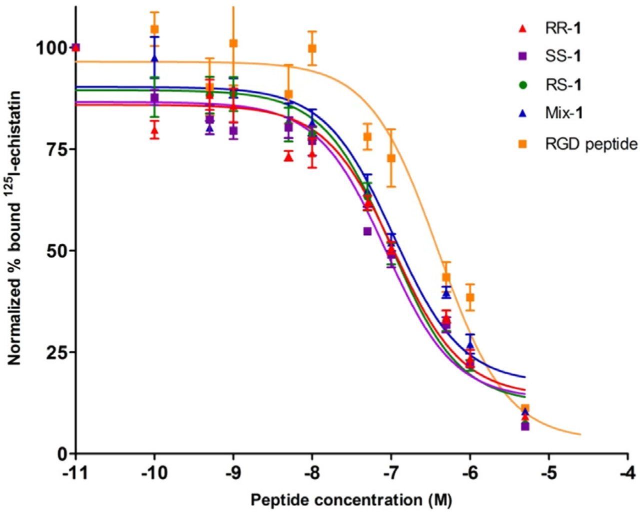

Fig. 3. The integrin $\alpha_v\beta_3$ binding affinities of cRGDyK peptide, RR-**1**, SS-**1**, RS-**1** and rac-**1** measured by a competitive cell-binding assay using ^{125}I-echistatin as the radioligand. The IC_{50} values were calculated to be 396 nM (cRGDyK), 108 nM (RR-**1**), 85 nM (SS-**1**), 100 nM (RS-**1**) and 106 nM (rac-**1**) (R^2: 0.91–0.94).

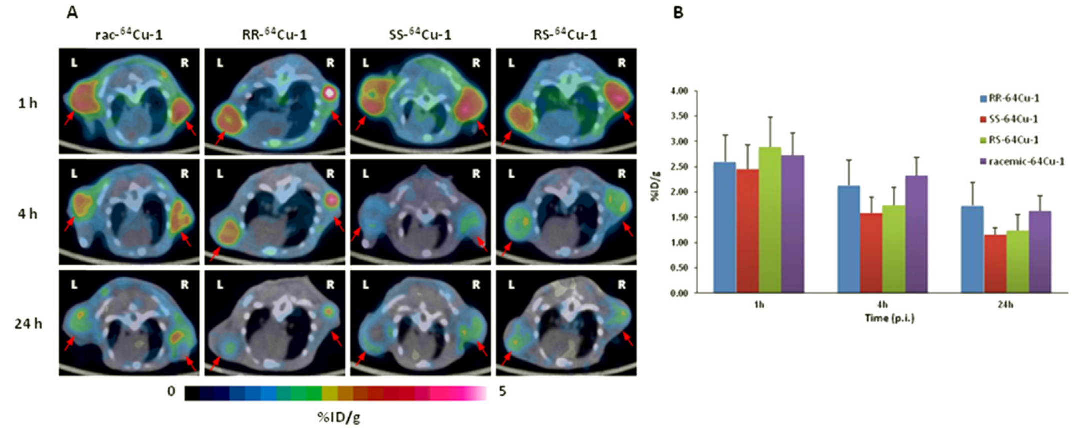

Fig. 4. (A) Comparative transaxial PET/CT images of PC-3 tumors in SCID mice intravenously injected with rac-^{64}Cu-**1**, RR-^{64}Cu-**1**, SS-^{64}Cu-**1**, and RS-^{64}Cu-**1** at 1 h, 4 h, and 24 h p.i. (B) Quantitative tumor uptake analysis of the four ^{64}Cu-labled peptide conjugates ($n = 6$).

found that the stereoisomers shared a similar biodistribution pattern in the mouse tumor model.

3. Discussion

Copper has several radioisotopes of interest for the development of radiopharmaceuticals, which can be used for PET imaging (^{61}Cu, ^{62}Cu, and ^{64}Cu) and radiotherapy (^{64}Cu and ^{67}Cu). Most copper radiopharmaceuticals are designed and prepared by incorporation of copper radioisotope into a biological substrate through the linkage often provided by a tetraazamacrocyclic BFC [6,7,19,20]. The BFCs usually consist of a Cu(II) chelating moiety and a pendent linker for the attachment to a biomolecule of interest. As such, the carbon atoms in the pendent linker may become chiral depending on the chemical modification as in our reported design of CB-TE2GA. In the case of drugs, these subtle stereo chemical differences may lead to one form of the chiral molecule being therapeutically beneficial, while the other form may be physiologically neutral or even harmful [21,22]. However, very little information is available on stereoisomerism of the radiolabeled macrocyclic BFC-conjugate at tracer level [23–25].

The role of linker chirality on ligand-receptor interaction partially depends upon the application of the linker. In case of monovalent BFC, where linker is solely used as the attachment point, the linker chirality is not supposed to play significant role in ligand-receptor interaction. This is clearly exemplified by ^{99m}Tc-(HYNIC-K(NIC)-3G-RGD$_2$) (tricine) monovalent conjugates, where no significant differences in biological behavior or properties were observed for its separable enantiomers or diastereomers [23]. The results for the monovalent conjugates are not surprising given the fact that one radioligand binds to one receptor site, which perhaps is the main reason that the commercial available BFCs, such as DOTA-SCN and NOTA-SCN, are provided as racemates. In the case of multivalent BFC, multiple linkers provide multiple attachment points as well as different spatial orientations for the multi-presentation of a biologically active molecule, where the linker chirality may play a significant role in multi-valent or multiplexing ligand-receptor interactions.

In our reported multivalent BFC scaffold design for ^{64}Cu-based PET imaging probe, the BFC scaffold provides multiple peripheral functional points for multi-presentation of targeting vectors. Bearing two chiral carbon atoms in the glutaric acid side arm, the BFC scaffold can have three potential stereoisomers RR-**8**, SS-**8**, and RS-**8** [14,15]. Attachment of c(RGDyK) to the chiral side arms leads to different spatial dispositions of the c(RGDyK) depending on the chirality of the side arms, which can potentially impact their binding affinities to the target receptors. Indeed it was reported that, when two binding motifs of gonadotropin-releasing hormone (GnRH) peptide (intact peptide: pEHWSYGLRPG-NH$_2$, binding motifs: pEHW and RPG) were connected by D-Lys or L-Lys, a difference of more than two orders of magnitude was observed in their binding to GnRH receptor [25]. Therefore we reasoned that the enantiopure peptide conjugates (RR-H$_2$-**1**, SS-H$_2$-**1**, RS-H$_2$-**1**) might yield different ligand-receptor affinity and hence *in vivo* properties of the corresponding copper radiopharmaceuticals.

Synthesis of the enantiopure side arms was the key step towards the success of this work. Enantiopure side arms, R-**6** and S-**6**, were synthesized in gram quantity from D/L-glutaric acid, respectively [16]. The enantio-selective synthesis relied on the use of an enantio-specific deamination reaction to form the lactone (Scheme 1). Further functionalization of the lactone, as well as the ring opening reaction does not affect the conformation of the molecule. The synthesis of BFC scaffolds, RR-**7**, and SS-**7**, was achieved in one step by dialkylation of CB-cyclam using enantiopure side arm, S-**6**, and R-**6**, respectively. On the other hand, for the synthesis of RS-**7**, stepwise alkylation was required using different enantiomer in each step. The alkylation of CB-cyclam proceeded via an S$_N$2 type reaction to provide the product with inversion of configuration. Finally, RR-H$_2$-**1**, SS-H$_2$-**1**, and RS-H$_2$-**1** were synthesized by conjugating the c(RGDyK) peptide with the outer carboxylate groups, followed by deprotection of the inner carboxylate groups using 95% TFA for radiolabeling with copper radioisotopes.

The designed imaging agents, enantiopure (RR-^{64}Cu-**1**, SS-^{64}Cu-**1**) and the meso (RS-^{64}Cu-**1**) contain two c(RGDyK) units for multivalent interactions. The distance between the two RGD motifs in the conjugates is greater than 25 bonds (including the lysine spacers), the minimum spacing length required to realize multivalent binding of RGD motifs to the $\alpha_v\beta_3$ integrin [26]. The spatial orientations of the c(RGDyK) units are expected to be different in each stereoisomeric conjugate. To evaluate the chirality effect of BFC on the imaging properties of the agents, we performed PET/CT imaging in PC-3 tumor bearing mice. To our surprise, all the agents showed similar bio-distribution and tumor uptake at all-time points. This observation suggests that the spatial orientation difference of the two c(RGDyK) units presented on the chiral BFC scaffold has negligible effects on the bio-distribution profile of the $\alpha_v\beta_3$-targeted imaging agents in the mouse tumor model. This may indicate that the multivalent ligand–receptor interaction is likely a stepwise mechanism. Since the multivalent binding can be a concerted process, binding of one RGD unit to integrin $\alpha_v\beta_3$ enables the second RGD unit to reorient itself towards a second $\alpha_v\beta_3$ binding site as long as the spacer between them including the chelator moiety is flexible. However, given the fact that ligand–receptor interaction is receptor specific, what we have observed with the chiral BFC scaffolds for integrin $\alpha_v\beta_3$ in this work may not be necessarily conserved for other receptors. Judicious selection of BFC scaffolds with regards to their chirality should still be consider so as to achieve the optimal imaging properties for noninvasive assessment of the expression status of specific biomarkers towards personalized disease stratification.

4. Conclusions

Three enantiopure BFC scaffolds for copper radiopharmaceuticals were designed and synthesized. Using well-validated integrin $\alpha_v\beta_3$ ligand, c(RGDyK), peptide conjugates of the enantiopure BFC scaffolds were prepared to evaluate the effect of BFC chirality on ligand-receptor binding and the implications on the *in vivo* behavior of so-designed agents. Our work suggests that the chirality of BFC scaffolds plays an insignificant role in integrin $\alpha_v\beta_3$ targeted copper radiopharmaceuticals. Although this observation does not support our design rationale, the importance of BFC chirality in radiopharmaceutical agents cannot be undervalued without discretion when it is applied to other biological targets.

5. Experimental section

5.1. General methods and materials

All reactions were carried out under N_2 atmosphere in degassed dried solvents. Commercially available starting materials were purchased from vendors and used directly without further purification unless otherwise stated. Milli-Q water (18 MΩ cm) was obtained from a Millipore Gradient Milli-Q water system (Billerica, MA). All aqueous solutions were prepared with Milli-Q water. Silica gel 60 (70–230 mesh, Merck) was used for column chromatography. Analytical thin-layer chromatography (TLC) was performed using F254 silica gel (precoated sheets, 0.2 mm thick) (Lawrence, KS). ^{1}H and ^{13}C NMR spectra were recorded on a Varian 400 spectrometer; chemical shifts are expressed in ppm relative to TMS (0.0 ppm). Matrix-assisted laser desorption/ionization (MALDI) mass spectra were acquired on an Applied Biosystems Voyager-6115 mass spectrometer. Optical rotation data were collected on a APIV-6W Rudolph Research automatic polarimeter. Radiolabeled conjugates were purified by Light C-18 Sep-Pak cartridges (Waters, Milford, MA).

Bulk solvents were removed by rotary evaporator under reduced pressure, and trace solvents were removed by vacuum pump. 1,4,8,11-tetraazabicyclo[6.6.2]hexadecane (CB-cyclam) was synthesized according to a published procedure [27]. ^{64}Cu(II) in 0.1 M HCl was purchased from either Washington University School of Medicine in St. Louis or the University of Wisconsin at Madison.

5.2. High performance liquid chromatography (HPLC) methods

HPLC separation was performed on a Waters 600 Multisolvent Delivery System equipped with a Waters 2996 Photodiode Array detector. The mobile phase consisted of H_2O with 0.1% TFA (solvent A) and acetonitrile with 0.1% TFA (solvent B). The analytical HPLC was performed on an XTerra RP18 column (150 × 4.6 mm) with a gradient of 0% B to 100% B in 50 min at the flow rate of 1.0 mL/min. The HPLC separation was performed on a semi-preparative XTerra RP18 Column (250 × 10 mm) with a gradient of 0% B to 100% B in 50 min at the flow rate of 4.0 mL/min.

5.3. Integrin $\alpha_v\beta_3$ binding assay

The binding affinities of c(RGDyK), rac-H_2-**1**, RR-H_2-**1**, RS-H_2-**1**, and SS-H_2-**1** to integrin $\alpha_v\beta_3$ were determined by a competitive cell-binding assay using ^{125}I-echistatin (PerkinElmer) as the $\alpha_v\beta_3$-specific radioligand. The experiments were performed on U87MG human glioblastoma cells following our previously reported method [10]. Briefly, U87MG cells were grown in RPMI 1640 medium supplemented with penicillin, streptomycin, and 10% (v/v) fetal bovine serum (FBS) at 37 °C under 5% CO_2. Suspended U87MG cells in binding buffer (20 mM Tris, pH 7.4, 150 mM NaCl, 2 mM $CaCl_2$, 1 mM $MgCl_2$, 1 mM $MnCl_2$, 0.1% bovine serum albumin) were seeded on multi-well DV plates (Millipore) with 5×10^4 cells per well and then incubated with ^{125}I-echistatin (10,000 cpm/well) in the presence of increasing concentrations (0–5000 nM) of c(RGDyK) peptide conjugates for 2 h. The final volume in each well was maintained at 250 μL. At the end of incubation, unbound ^{125}I-echistatin was removed by filtration followed by five rinses with cold binding buffer. The retentive was collected and the radioactivity was measured using a γ-counter. The best-fit IC_{50} values (inhibitory concentration where 50% of the ^{125}I-echistatin bound on U87MG cells are displaced) of c(RGDyK), rac-H_2-**1**, RR-H_2-**1**, SS-H_2-**1**, and RS-H_2-**1** were calculated by fitting the data with nonlinear regression using GraphPad Prism (GraphPadSoftware, Inc.). Experiments were duplicated with quintuplicate samples.

5.4. Tissue culture and animal model

All animal studies were performed in compliance with guidelines set by the UT Southwestern Institutional Animal Care and Use Committee (IACUC). The PC-3 cell line was obtained from the American Type Culture Collection (ATCC, Manassas, VA), and was cultured in T-media (Invitrogen, Carlsbad, CA) at 37 °C in an atmosphere of 5% CO_2 and were passaged at 75% confluence in P150 plates. T-media was supplemented with 5% Fetal Bovine Serum (FBS) and 1× Penicillin/Streptomycin. PC-3 cells were harvested from monolayer using PBS and trypsin/EDTA, and suspended in T-media with 5% FBS. The cell suspension was then injected subcutaneously (5×10^5 cells in 100 μL media) into the front flanks of male SCID (Severe combined immunodeficiency) mice. After injection, animals were monitored three times a week by general observations. The tumor was allowed to grow three weeks to reach a palpable size (50–150 mm^3) for microPET/CT imaging studies.

5.5. Mouse PET/CT imaging

The imaging studies were performed on a Siemens Inveon Multimodality PET/CT system once the tumor size reached the range of 50–150 mm^3 (tumor volume = ½ (length × width^2)). One hour prior to imaging, each mouse bearing PC-3 tumor was injected with 100–125 μCi of a ^{64}Cu labeled conjugate in 100 μL of saline via the tail vein. Ten minutes prior to imaging, the animals were anesthetized using 3% isofluorane at room temperature until stable vitals were established. Once the animal was sedated, it was placed onto the imaging bed under 2% isofluorane anesthesia for the duration of imaging data requisition. At each time point (1 h, 4 h, and 24 h) post-injection (p.i.), a CT scan was performed (8 min), followed immediately by a static PET scan (15 min). The CT imaging was acquired at 80 kV and 500 μA with a focal spot of 58 μm. The total rotation of the gantry was 360° with 360 rotation steps obtained at an exposure time of approximately 180 ms/frame. The images were attained using CCD readout of 4096 × 3098 with a binning factor of four and an average frame of one. Under low magnification the effective pixel size was 103.03 μm. The CT images were reconstructed with a down sample factor of two using Cobra

Reconstruction Software. PET images were reconstructed using Fourier Rebinning and Ordered Subsets Expectation Maximization 3D (OSEM3D) algorithm. Reconstructed CT and PET images were fused and analyzed using the manufacturer's software. For quantification, regions of interest were placed in the areas expressing the highest ^{64}Cu-labeled conjugate activity as determined by PET and visually guided by CT images. The tissues examined include the tumor, heart, liver, lung, kidney, and muscle. The resulting quantitative data were expressed in percentage of the injected dose in per gram of the tissue (%ID/g) on the assumption that the density of the tissue is 1 g/cm^3.

5.6. Synthesis

5.6.1. Synthesis of (S)-5-oxotetrahydrofuran-2-carboxylic acid (***S-2***)

L-glutamic acid (30.0 g, 200 mmol) was suspended in a water/dioxane mixture (75/25 mL) and stirred at 0 °C for 30 min. The white slurry became clear after 40 mL of concentrated HCl (37%) was added, followed by drop-wise addition of a solution of $NaNO_2$ (21.0 g, 300 mmol) in 50 mL of water. The reaction temperature was maintained around 0 °C during the 4 h of addition. The reaction mixture was then left stirring at room temperature for 20 h. Upon completion, the solvent was evaporated under reduced pressure to provide a white solid, which was then treated with EtOAc (300 mL) and Na_2SO_4 for 30 min. The solution was filtered and the solvent was evaporated to yield **S-2** as a white solid (21.50 g, 78%). ^{1}H NMR (400 MHz, $CDCl_3$) δ 11.08 (bs, 1H), 5.01 (m, 1H), 2.71–2.55 (m, 3H), 2.45–2.37 (m, 1H); ^{13}C NMR (100 MHz, $CDCl_3$) δ 176.8, 174.5, 75.4, 26.8, 25.7.

5.6.2. Synthesis of tert-butyl (S)-5-oxotetrahydrofuran-2-carboxylate (***S-3***)

In a solution of S-**2** (10.0 g, 77 mmol) in CH_2Cl_2 (240 mL), *t*-butanol (8 mL, 84 mmol) and 4-dimethylaminopyridine (DMAP, 3.75 g, 31 mmol) were added and the reaction mixture was cooled to 0 °C. To this solution, N, N-dicyclohexylcarbodiimide (DCC, 16.2 g, 84.5 mmol) in CH_2Cl_2 (80 mL) was added dropwise. The reaction was stirred at room temperature overnight and upon completion the solvent was removed under reduced pressure. The residue was purified by column chromatography (silica gel, gravity) using hexane (250 mL) and EtOAc:hexane (1:4) to give S-**3** as white solid (7.0 g, 55%) : ^{1}H NMR (400 MHz, $CDCl_3$) δ 4.79 (m, 1H), 2.65–2.44 (m, 3H), 2.24 (m, 1H), 1.48 (s, 9H) ppm; ^{13}C NMR (100 MHz, $CDCl_3$) δ 176.2, 169.0, 83.1, 76.2, 27.9, 26.8, 25.8 ppm.

5.6.3. Synthesis of potassium (S)-5-(tert-butoxy)-4-hydroxy-5-oxopentanoate (***S-4***)

Compound S-**3** (5.0 g, 30 mmol) was dissolved in THF (60 mL), and cooled to 0 °C. To this mixture, 1 N KOH (aqueous, 66 mL) was added dropwise. The resulting mixture was stirred at room temperature over 4 h and upon completion the solvent was evaporated to give S-**4** as white solid. Compound S-**4** was directly used for the synthesis of S-**5**. However, for characterization of the compound, a sample of S-**4** was converted to its acid using 3 N hydrochloric acid. The acidified aqueous layer was then extracted with EtOAc (3 × 30 mL). The organic layers were combined and dried over anhydrous $MgSO_4$ and concentrated. The residue was purified by column chromatography (silica gel, gravity) using hexane (100 mL) and EtOAc:hexane (1:3) to yield the acid form of S-**4** as a white solid (3.0 g, 60%) : ^{1}H NMR (400 MHz, $CDCl_3$) δ 4.10 (m, 1H), 2.57–2.41 (m, 2H), 2.16–2.07 (m, 1H), 1.92–1.83 (m, 1H), 1.47 (s, 9H); ^{13}C NMR (100 MHz, $CDCl_3$) δ 178.6, 173.9, 82.8, 69.5, 29.4, 29.0, 27.8.

5.6.4. Synthesis of 5-benzyl 1-(tert-butyl) (S)-2-hydroxypentanedioate (***S-5***)

S-**4** (2.0 g, 9.8 mmol) was suspended in DMF (15 mL), to which was added benzyl bromide (1.67 g, 9.8 mmol). After stirred for 8 h, the mixture was poured into ice water (20 mL) and extracted with EtOAc (3 × 25 mL). The combined organic layer was dried over Na_2SO_4 and concentrated under reduced pressure. The residue was purified by column chromatography (silica gel, gravity) using hexane and EtOAc:hexanes (1:4) to give S-**5** as a white solid (1.5 g, 52%) . ^{1}H NMR (400 MHz, $CDCl_3$) δ 7.35 (m, 5H), 5.13 (s, 2H), 4.08 (bs, 1H), 2.88 (bs, 1H), 2.59–2.44 (m, 2H),2.17 (m, 2H), 1.91 (m, 1H), 1.48 (s, 9H). ^{13}C NMR (100 MHz, $CDCl_3$) δ 173.9, 173.0, 135.9, 128.5, 128.2, 128.1, 82.8, 69.6, 66.3, 29.7, 29.4, 28.0.

5.6.5. Synthesis of 5-benzyl 1-(tert-butyl) (S)-2-((methylsulfonyl) oxy)pentadioate (***S-6***)

Methanesulfonyl chloride (0.42 g, 3.7 mmol) was added to a mixture of S-**5** (1.0 g, 3.4 mmol) and Et_3N (0.47 g, 4.7 mmol) in CH_2Cl_2 (25 mL) at 0–5 °C. After the addition was completed, the mixture was warmed to room temperature and stirred for 2 h. Upon completion, water (10 mL) was added, the organic phase was separated and washed with brine (3 × 10 mL), dried over Na_2SO_4 and concentrated to give S-**6** (0.7 g, 60%). ^{1}H NMR (400 MHz, $CDCl_3$) δ 7.36 (m, 5H), 5.14 (s, 2H), 4.98 (m, 1H), 3.11 (s, 3H), 2.55 (m, 2H), 2.30 (m, 1H), 1.49 (s, 9H). ^{13}C NMR (100 MHz, $CDCl_3$) δ 171.8, 167.4, 135.5, 128.5, 128.2, 128.2, 83.5, 76.6, 66.5, 38.9, 29.3, 27.8, 27.0.

The synthesis of 5-benzyl 1-(*tert*-butyl) (*R*)-2-((methylsulfonyl) oxy)pentadioate (R-**6**) was accomplished in the same way as above from D-glutamic acid.

5.6.6. Synthesis of compound RR-7

Compound S-**6** (500 mg, 1.3 mmol) was added to a suspension of cross-bridge cyclam (150 mg, 0.6 mmol) and K_2CO_3 (0.10 g) in anhydrous acetonitrile (50 mL). The reaction was stirred at room temperature for 24 h and then for another 24 h at 50 °C. The reaction mixture was filtered and the solid was washed twice with chloroform (2 × 20 mL). The combined filtrates were concentrated under reduced pressure and purified by column chromatography (silica gel, 60–230 mesh) using 10:1 $CHCl_3$/MeOH to 9:1 EtOAc/isopropylamine to yield RR-**7** as viscous oil (250 mg; Yield: 52%): MALDI-TOF/MS [M^+]: calc': 778.49; found: 778.59.

5.6.7. Synthesis of compound RR-$H_2$1

To a solution of RR-**7** (13 mg, 16.7 μmol) in 0.5 mL of 2-propanol was added portion wise 10 mg of 10% Pd/C. The suspension was shaken in a hydrogenator (Parr, Moline, Illionis) at room temperature for 12 h under an H_2 atmosphere (60 psi). After removal of the solids, evaporation of the solvent afforded compound RR-**8** as a white foam in nearly quantitative yield. A mixture of compound RR-**8** (10.0 mg, 16.7 μmol), *N*-hydroxysuccinimide (7.6 mg, 66.8 μmol) and EDC·HCl (12.8 mg, 66.8 μmol) in 500 μL of dry acetonitrile (MeCN) was stirred under N_2 for overnight. The solvent was removed under reduced pressure and the residue was redissolved in $CHCl_3$ (1 mL) and then washed with water promptly three times (3 × 2 mL). $CHCl_3$ was evaporated under reduced pressure, the residue was frozen by liquid nitrogen and the remaining water was removed by a freeze dryer to give a pale yellow solid in quantitative yield. The activated ester was used directly for the next reaction without further purification. Cyclic Arg-Gly-Asp-D-Tyr-Lys [c(RGDyK)] (10 mg, 16 μmol) was mixed with the activated ester (2.4 mg, 4 μmol) in 200 μL of anhydrous DMF. To this solution, 30 μL of N, N-diisopropylethylamine (DIPEA) were added. The mixture was stirred at room temperature for 24 h under N_2. Upon completion, the solvent was evaporated under reduced pressure and the crude product was purified by HPLC. The collected fractions were combined and lyophilized to yield the *t*-butyl protected product, which was then dissolved in 95% TFA and stirred at room temperature for 12 h. After evaporation of the solvent, the residue was purified by semi-preparative reverse-phase HPLC. The collected fractions from multiple runs were collected and lyophilized to afford RR-H_2**1** as white solid at quantitative yield. MALDI-TOF/MS [M+H$^+$]: calc'd: 1689.87; found: 1690.67.

5.6.8. Synthesis of compound SS-$H_2$1

Compound SS-H_2**1** was synthesized in a similar manner starting from CB-Cyclam and R-**6**. MALDI-TOF/MS [M+H$^+$]: calc'd: 1689.87; found: 1690.67.

5.7. Radiolabeling of rac-H_2-1, RR-H_2-1, RS-H_2-1, and SS-H_2-1 with ^{64}Cu

To a 1.5 mL vial containing 5 μg of respective conjugate in 200 μL of 0.4 M NH_4OAc (pH = 6.5) solution, 2–3 mCi of ^{64}Cu(II) in 0.1 M HCl were added. The reaction mixture was shaken and incubated at 75 °C for 0.5 h. Then, 5 μL of 5 mM diethylenetriaminepentaacetic acid (DTPA) was added into the reaction mixture and allowed to incubate for another 5 min. After incubation, purification of ^{64}Cu-labeled conjugate was carried out by passing the mixture through a preconditioned Sep-Pak C-18 light cartridge. After thorough rinsing (3 × 3 mL water) of the cartridge, the ^{64}Cu-labeled conjugate was eluted by an ethanol-water mixture (70:30). Radio-TLC analysis was performed on a Rita Star Radioisotope TLC Analyzer (Straubenhardt, Germany) to monitor the radiolabeling efficiency via ITLC paper, developed by 10 mM PBS. High performance liquid chromatography (HPLC) analysis was conducted to determine radiochemical purity of the products on a Waters 600 Multisolvent Delivery System equipped with a Waters 2996 Photodiode Array (PDA) detector and an in-line Shell Jr. 2000 radio-detector (Fredericksburg, VA) on a Waters Xtera column (150 × 4.6 mm, 5 μm). The gradient mobile phase started with 100% A (0.1% TFA in H_2O) to 50% B (0.1% TFA in MeCN) and 50% A at 25 min with a flow rate of 1 mL/min.

5.8. Statistical analysis

Quantitative data were expressed as the mean ± SD. Unpaired *t* test (two-tailed, confidence intervals: 95%) was performed using GraphPad Prism. *P* values of <0.05 were considered statistically significant.

Conflict of interests

The authors declare no conflicts of interest.

Appendix A. Supplementary data

Supplementary data related to this article can be found at http://dx.doi.org/10.1016/j.ejmech.2014.04.071.

References

[1] R.T.M. de Rosales, E. Arstad, P.J. Blower, Nuclear imaging of molecular processes in cancer, Targeted Oncology 4 (2009) 183–197.
[2] S.S. Gambhir, Molecular imaging of cancer with positron emission tomography, Nature Reviews. Cancer 2 (2002) 683–693.
[3] V.N. Harry, S.I. Semple, D.E. Parkin, F.J. Gilbert, Use of new imaging techniques to predict tumour response to therapy, The Lancet Oncology 11 (2010) 92–102.
[4] G. Kelloff, J.M. Hoffman, B. Johnson, H.I. Scher, B.A. Siegel, E.Y. Cheng, B.D. Cheson, J. O'Shaughnessy, K.Z. Guyton, D.A. Mankoff, L. Shankar, S.M. Larson, C.C. Sigman, R.L. Schilsky, D.C. Sullivan, Progress and promise of FDG-PET imaging for cancer patient management and oncologic drug development, Clinical Cancer Research 11 (2005) 2785–2808.
[5] G.K. von Schulthess, H.C. Steinert, T.F. Hany, Integrated PET/CT-3: current applications and future directions, Radiology 238 (2006) 405–422.
[6] G. Hao, A.N. Singh, W. Liu, X. Sun, PET with non-standard nuclides, Current Topics in Medicinal Chemistry 10 (2010) 1096–1112.
[7] G. Hao, A.N. Singh, O.K. Oz, X. Sun, Recent advances in copper radiopharmaceuticals, Current Radiopharmaceuticals 4 (2011) 109–121.
[8] R. Haubner, H.R. Wester, Radiolabeled tracers for imaging of tumor angiogenesis and evaluation of anti-angiogenic therapies, Current Pharmaceutical Design 10 (2004) 1439–1455.
[9] R. Rossin, S. Muro, M.J. Welch, V.R. Muzykantov, D.P. Schuster, In vivo imaging of Cu-64-labeled polymer nanoparticles targeted to the lung endothelium, Journal of Nuclear Medicine 49 (2008) 103–111.
[10] W. Liu, G.Y. Hao, M.A. Long, T. Anthony, J.T. Hsieh, X.K. Sun, Imparting multivalency to a bifunctional chelator: a scaffold design for targeted PET imaging probes, Angewandte Chemie International Edition 48 (2009) 7346–7349.
[11] X.K. Sun, M. Wuest, G.R. Weisman, E.H. Wong, D.P. Reed, C.A. Boswell, R. Motekaitis, A.E. Martell, M.J. Welch, C.J. Anderson, Radiolabeling and in vivo behavior of copper-64-labeled cross-bridged cyclam ligands, Journal of Medicinal Chemistry 45 (2002) 469–477.
[12] K.S. Woodin, K.J. Heroux, C.A. Boswell, E.H. Wong, G.R. Weisman, W.J. Niu, S.A. Tomellini, C.J. Anderson, L.N. Zakharov, A.L. Rheingold, Kinetic inertness and electrochemical behavior of copper(II) tetraazamacrocyclic complexes: possible implications for in vivo stability, European Journal of Inorganic Chemistry (2005) 4829–4833.
[13] C.A. Boswell, X.K. Sun, W.J. Niu, G.R. Weisman, E.H. Wong, A.L. Rheingold, C.J. Anderson, Comparative in vivo stability of copper-64-labeled cross-bridged and conventional tetraazamacrocyclic complexes, Journal of Medicinal Chemistry 47 (2004) 1465–1474.
[14] J. Notni, J. Simecek, P. Hermann, H.J. Wester, TRAP, a powerful and versatile framework for gallium-68 radiopharmaceuticals, Chemistry: A European Journal 17 (2011) 14718–14722.
[15] A.N. Singh, W. Liu, G.Y. Hao, A. Kumar, A. Gupta, O.K. Oz, J.T. Hsieh, X.K. Sun, Multivalent bifunctional chelator scaffolds for gallium-68 based positron emission tomography imaging probe design: signal amplification via multivalency, Bioconjugate Chemistry 22 (2011) 1650–1662.
[16] R.C. Cooke, K.A. van Leeuwen, D.L. Capone, R. Gawel, G.M. Elsey, M.A. Sefton, Odor detection thresholds and enantiomeric distributions of several 4-alkyl substituted γ-lactones in Australian red wine, Journal of Agricultural and Food Chemistry 57 (2009) 2462–2467.
[17] S.G. Levy, V. Jacques, K.L. Zhou, S. Kalogeropoulos, K. Schumacher, J.C. Amedio, J.E. Scherer, S.R. Witowski, R. Lombardy, K. Koppetsch, Development of a multigram asymmetric synthesis of 2-(R)-2-(4,7,10-Tris tert-Butylcarboxymethyl-1,4,7,10-tetraazacyclododec-1-yl)-pentanedioic acid, 1-tert-butyl esterg (R)-tert-Bu-4-DOTAGA, Organic Process Research & Development 13 (2009) 535–542.
[18] X.Z. Zhang, Z.M. Xiong, Y. Wu, W.B. Cai, J.R. Tseng, S.S. Gambhir, X.Y. Chen, Quantitative PET imaging of tumor integrin alpha(v)beta(3) expression with F-18-FRGD2, Journal of Nuclear Medicine 47 (2006) 113–121.
[19] C.J. Anderson, R. Ferdani, Copper-64 radiopharmaceuticals for PET imaging of cancer: advances in preclinical and clinical research, Cancer Biotherapy and Radiopharmaceuticals 24 (2009) 379–393.
[20] M. Shokeen, C.J. Anderson, Molecular imaging of cancer with copper-64 radiopharmaceuticals and Positron Emission Tomography (PET), Accounts of Chemical Research 42 (2009) 832–841.
[21] N.M. Davies, X.W. Teng, Importance of chirality in drug therapy and pharmacy practice: implications for psychiatry, Advances in Pharmacy 1 (2003) 242–252.
[22] S.J. Gardiner, E.J. Begg, Pharmacogenetics, drug-metabolizing enzymes, and clinical practice, Pharmacological Reviews 58 (2006) 521–590.
[23] Y. Zhou, Y.-S. Kim, X. Lu, S. Liu, Evaluation of ^{99m}Tc-labeled cyclic RGD Dimers: impact of cyclic RGD peptides and ^{99m}Tc chelates on biological properties, Bioconjugate Chemistry 23 (2012) 586–595.
[24] F.L.G. Gomez, T. Uehara, T. Rokugawa, Y. Higaki, H. Suzuki, H. Hanaoka, H. Akizawa, Y. Arano, Synthesis and evaluation of diastereoisomers of 1,4,7-triazacyclononane-1,4,7-tris-(glutaric acid) (NOTGA) for multimeric radiopharmaceuticals of gallium, Bioconjugate Chemistry 23 (2012) 2229–2238.
[25] H.X. Guo, J. Lu, H. Hathaway, M.E. Royce, E.R. Prossnitz, Y.B. Miao, Synthesis and evaluation of novel gonadotropin-releasing hormone receptor-targeting peptides, Bioconjugate Chemistry 22 (2011) 1682–1689.
[26] Z.B. Li, W.B. Cai, Q.Z. Cao, K. Chen, Z.H. Wu, L.N. He, X.Y. Chen, ^{64}Cu-Labeled tetrameric and octameric RGD peptides for small-animal PET of tumor alpha(v)beta(3) integrin expression, Journal of Nuclear Medicine 48 (2007) 1162–1171.
[27] E.H. Wong, G.R. Weisman, D.C. Hill, D.P. Reed, M.E. Rogers, J.S. Condon, M.A. Fagan, J.C. Calabrese, K.-C. Lam, I.A. Guzei, A.L. Rheingold, Synthesis and characterization of cross-bridged cyclams and pendant-armed derivatives and structural studies of their copper(II) complexes, Journal of the American Chemical Society 122 (2000) 10561–10572.

About the Authors

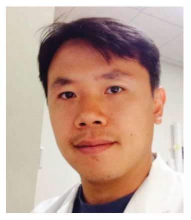

Su-Tang Lo

Su-Tang Lo obtained his BSc in 2001 from National Central University (Taiwan) in Chemistry, MSc in 2004 from National Taiwan University (Taiwan) in Biochemistry and PhD in 2013 from the University of Texas Southwestern Medical Center (Dallas, TX, USA) in Radiological Sciences. Currently, he is working as a postdoctoral fellow in Xiankai Sun's laboratory with research interest in the development of theranostic agents for cancer and multimodality imaging techniques for noninvasive assessment of pancreatic β-cell.

Amit Kumar

Amit Kumar obtained his BSc in 2001 from Banaras Hindu University (India) in Chemistry, MSc in 2003 from Indian Institute of Technology, Bombay (India) in Inorganic Chemistry and PhD in 2010 from University of Houston (TX, USA) in Chemistry. Currently, he is working as a postdoctoral fellow at the University of Texas Southwestern Medical Center (Dallas, TX, USA) in Xiankai Sun's laboratory with research projects focused on developing multimodality imaging probes for early detection of diabetes and cancer.

Xiankai Sun

Xiankai Sun obtained his PhD in Chemistry in 2000 from University of New Hampshire (Durhan, NH, USA). After three years of postdoctoral training and a short junior faculty stay at Washington University School of Medicine in St. Louis (MO, USA), he joined the faculty of the University of Texas Southwestern Medical Center (Dallas, TX, USA), where he is currently an Associate Professor in the Department of Radiology and the Advanced Imaging Research Center. Research interests of his laboratory include: development of biocompatible nanoscale scaffolds to enable multipresentation of functionalities for detection and intervention of disease states; design and synthesis of bifunctional chelator scaffolds for imaging signal amplification and preparation of targeted imaging probes for noninvasive assessment of pancreatic β-cell mass and function.

For reprint orders, please contact reprints@future-science.com

Chapter 10

Delivery and controlled release of therapeutics via dendrimer scaffolds

doi:10.4155/fseb2013.13.123

Su-Tang Lo, Amit Kumar & Xiankai Sun

Dendrimers are highly symmetric synthetic polymers branched out from a central core, which have shown great potential as carriers for drug delivery. Given the chemistries that have been developed for the synthesis of dendrimers, the size and chemical composition of a dendrimer scaffold can be controlled to meet the specific needs of an application with desirable pharmacokinetics and biocompatibility. This chapter is intended to outline the drug loading and release mechanisms of dendrimer scaffolds that have been commonly used for controlled delivery of chemotherapeutics. In addition, it briefly covers the newly emerged applications of using dendrimers as nonviral vectors for gene therapy and delivery vehicles for radioisotope-based therapy.

Figure 10.1 Basic components of a dendrimer system: a central core, repeating dendrons & peripheral functional groups.

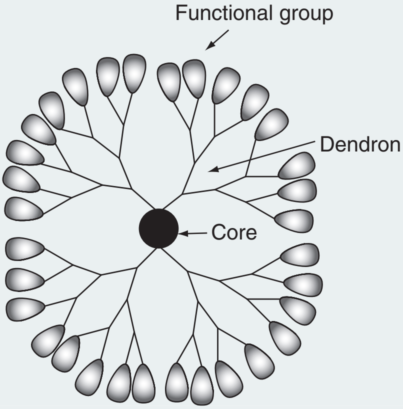

Background

The dendrimer chemistry was first introduced by Vögtle *et al.* in 1978 with the development of '*cascade molecular*'. The term of '*dendrimer*' was not seen until 1985. It is a combination of two Greek words, *dendron* and *meros*, which mean *tree* and *part*, respectively [1]. With three major components representing a central core, repeating dendrons and peripheral functional groups (**Figure 10.1**), dendrimers are often characterized as highly symmetric spheres featuring monodispersity and well-defined three-dimensional structures as compared with their polymeric counterparts, and thus possessing definable multivalent functionality [2], which makes dendrimers an appealing drug delivery system. The development of dendrimers to the current stage can be mainly attributed to the original work from the groups of Denkewalter, Tomalia, Newkome and Fréchet [1].

Dendrimers are synthesized in a stepwise sequence leading to a higher 'generation'. Each progressing generation of dendrimer exponentially adds the functional groups to the previous generation and progressively shields the interior functionalities. This progression bestows each generation of the dendrimer molecules with different pharmacokinetic properties (**Figure 10.2**). As such, the generation number can be judiciously controlled so as to provide an ideal drug delivery platform. For example, different generations of the same dendrimer system can be selected to achieve the desired *in vivo* pharmacokinetic requirements; shielded interior for drug loading and peripheral functional groups, often in the form of amine or carboxylate, for conjugation with functional molecules in a multivalent format for targeting or therapeutic efficacy enhancement. However, dendrimers such

Figure 10.2 A tuneable dendrimer system for different pharmacokinetic behaviors.

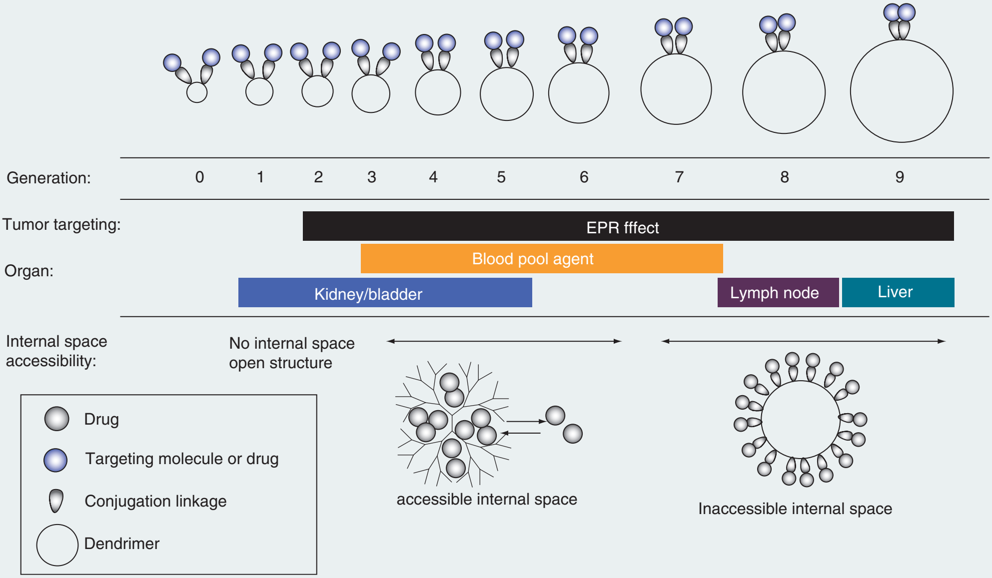

This unique feature is represented by a well-developed PAMAM—DTPA (Gd) system (G0—G9) MRI contrast agents.
EPR: Enhanced permeability and retention; PAMAM: Poly(amidoamine) dendrimer; G: Generation; DTPA: Diethylenetriaminepentaacetic acid; Gd: Gadolinium.
Reproduced from [4] ⓒ American Chemical Society (2013).

as polypropylenimine (PPI), Poly(amidoamine) (PAMAM) and poly-L-lysine may induce cytotoxicity particularly due to the positive-charged or cationic surfaces. Therefore, surface modifications such as PEGylation, acetylation, carbohydrate and peptide conjugation have been used to improve the biocompatibility of positively charged dendrimers [3]. To enhance the specificity in drug delivery, the peripheral functional groups have been extensively exploited for the attachment of a variety of targeting vectors. In this eBook chapter, we describe the potential of dendrimer systems for therapeutic drug delivery with focus on the mechanisms of drug loading and releasing and applications in gene therapy and boron neutron capture therapy (BNCT).

Advantages of using dendrimer scaffolds for drug delivery

A large number of highly potent pharmaceutics are limited in their clinical applications due to their poor water solubility. In general, to solve this problem, these drugs are delivered in their intact forms by large volumes of aqueous vehicle or in conjunction with surfactants (e.g., Cremophor EL), or in a

Table 10.1. **Dendrimer scaffolds for delivery & controlled release of therapeutics.**

Chemotherapeutic delivery				
Drug molecule	**Dendrimer scaffold**	**Interaction**	**Drug release**	**Ref.**
5-FU	PDEA modified G3 PAMAM	EN	pH sensitive (PDEA coating)	[13]
Cisplatin	G3.5 PAMAM	C.C.	-	[34]
	Biotinylated PAMAM	EN	-	[35]
DOX	PEG modified G4 PAMAM	C.C.	pH sensitive (cis-aconityl linkage)	[36]
	PEG modified G4 PAMAM	C.C.	pH sensitive (amide and hydrazone bonds)	[37]
Famotidine	G5 PPI	EN	pH sensitive (protonation)	[10]
MTX	FA conjugated G5 PAMAM	C.C.	-	[9]
Nifedipine	G3 PAMAM with EDA core	EN	pH sensitive (protonation)	[11]
PTX	PEG modified G2 triazine	C.C.	pH sensitive (ester bond), redox sensitive (disulfide bond)	[38]
Gene delivery				
IL-10	G5 PAMAM with EDA core	I.C.		[23]
Boron neutron capture therapy (BNCT)				
Boron	EGF-conjugated PAMAM	C.C.		[39]

5-FU: 5-Fluorouracil; C.C.: Covalent conjugation; DOX: Doxorubicin; EDA: Ethylenediamine; EGF: Epidermal growth factor; EN: Encapsulation; FA: Folic acid; I.C.: Ionic coordination; MTX: Methotrexate; PDEA: Poly(2-(N,N-diethylamino)ethyl methacrylate); PPI: Polypropylenimine dendrimer; PTX: Paclitaxel.

modified form by attaching to prodrug platforms or water-soluble polymers. However, these approaches may result in side effects, reduced therapeutic efficacy or undesirable polydispersity [5]. With the availability of versatile surface modification chemistries, dendrimer platforms have the potential to enhance the water solubility and drug payload of these pharmaceutics by a single dendrimer-drug construct. **Table 10.1** summarizes chemotherapeutics that have been reported with dendrimer-facilitated delivery: Cisplatin, 5-Fluorouracil (5-FU), indomethacin (IND), Methotrexate (MTX), Paclitaxel (PTX), Camptothecin (CPT), 10-hydroxycamptothecin (10HCPT), Primaquine phosphate, Doxorubicin (DOX), Difunisal, Flurbiprofen, Ibuprofen and Ketoprofen.

Drug-loading on a dendrimer platform

There are two mechanisms to load the pharmaceutics onto dendrimer platforms: noncovalently encapsulation in its internal space (**Figure 10.3**A) and

Figure 10.3 Two common methods for loading pharmaceutics onto dendrimer scaffolds: (A) noncovalently encapsulation in internal space & (B) ionic coordination or covalently conjugation with outer functional groups.

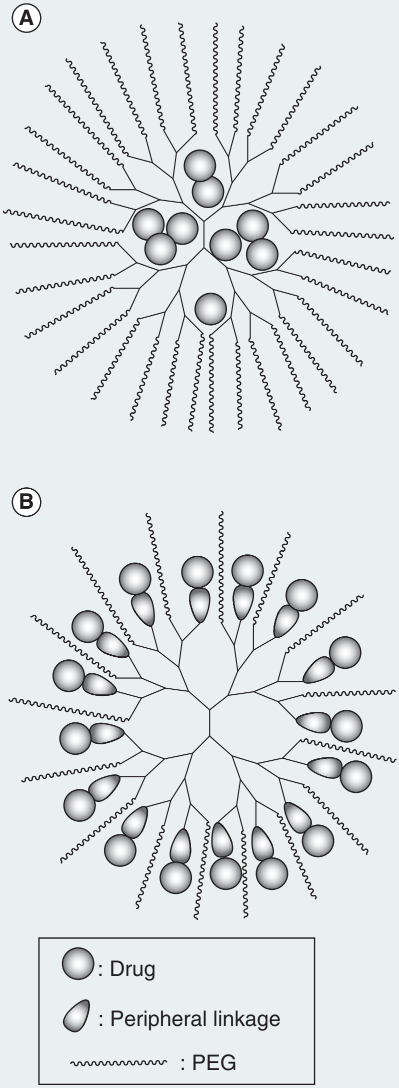

coordinated interaction or covalent conjugation with peripheral functional groups (**Figure 10.3**B). Noncovalent encapsulation is driven by the dielectric gradient across the dendrimer. For example, the surface molecules of a PAMAM dendrimer can be adjusted by the final amidation reaction, through which the reactive groups such as amines or carboxylic acids, or less reactive groups such as hydroxyls and hydrocarbon chains can be positioned on the dendrimer surface. Consequently, a dielectric gradient is developed by the tertiary amine in the internal space along with the tuneable peripheral functional groups. This property can be used to concentrate hydrophilic, hydrophobic or even amphiphilic compounds in the internal space [6]. Also, the drug molecules can also interact with nitrogen or oxygen atoms inside of the dendrimer through 'secondary interactions' (e.g., hydrogen bonding, electrostatic interaction, dipole—dipole interaction and hydrophobic interaction) [7,8]. In contrast to the encapsulation, the ionic coordination and covalent conjugation strategies are more feasible within higher generation dendrimer. In this method, multiple copies of the same or different therapeutics are attached to the peripheral functional groups (amine, carboxylate or hydroxyl) of each dendrimer molecule by corresponding conjugation reactions.

As shown in **Figure 10.2**, the size of the dendrimer affects the option for drug loading. Based on the available data of PAMAM dendrimers, dendrimers between G3 to G6 are better choices for drug loading by encapsulation, while higher generations (>G6) are better suitable for the covalent drug-loading. Without targeting vectors, dendrimer-drug constructs have a tendency to accumulate in solid tumors through the so-called enhanced permeation and retention effect. With targeting molecules, the pharmaceutics-loaded dendrimers can exhibit enhanced therapeutic efficacy [9]

Drug-releasing mechanism

Although dendrimer scaffolds can be used to significantly improve the solubility of native drugs and carry a large payload, their therapeutic potential cannot be unleashed without an efficient drug-release mechanism. In this regard, dendrimer scaffolds can be advantageous due to the versatile structural features of dendrimer. For the release of encapsulated drugs, the controllability is largely dependent on the protonation/deprotonation kinetic profiles of the functional groups associated with the drug packing. For instance, the acidic tumor microenvironment can be utilized to facilitate the desired drug release. For the chemically bound drugs, it is determined by the kinetic stability of the chemical linkages to which the pharmaceutics are coupled. To date, studies have shown that the chemical linkage design can be tuned to controlled release under different *in vivo* conditions, such as the acidic tumor microenvironment, site-specific enzymatic reactivity or disease-specific metabolic alternation [4].

Figure 10.4 Schematic pH-sensitive release mechanism of encapsulated drug via protonation of functional groups of a PEGylated dendrimer platform.

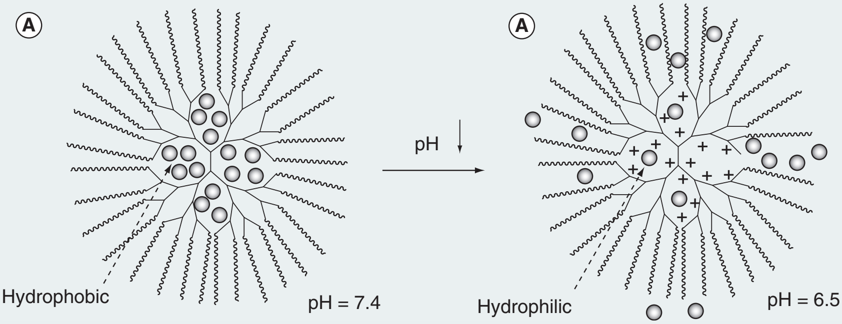

pH-sensitive release of encapsulated drugs

With different or mixed peripheral functional groups such as tertiary amino and/or carboxyl groups, the controlled release of encapsulated drugs can be realized by alternation of the protonation and deprotonation kinetics under different pH conditions (**Figure 10.4**). This has been documented with the controlled release of famotidine [10] encapsulated in PEGylated PPI and nifedipine [11] encapsulated in PEGylated PAMAM.

In addition, the incorporation of poly(2-(N,N-diethylamino)ethyl methacrylate) (PDEA) into a dendrimer scaffold has been reported as an efficient method to render the delivery vehicle with capability of releasing its encapsulated drugs upon pH change [12]. Shown in **Figure 10.5**, PDEA presents in a folded form (red coils) inside the dendrimer scaffold because of its limited solubility under the physiological condition. When pH decreases, PDEA becomes more water soluble and thus stretches out to release the encapsulated drug. This controlled release mechanism has been applied to 5-FU (Fluorouracil) encapsulated in PEGylated G3 PAMAM [13].

pH-sensitive release of drugs from chemical linkages

Another strategy of pH-sensitive drug release is through chemical linkages, which can be cleaved under reduced pH conditions (**Figure 10.6**). To date, ester bonds have been shown their effectiveness on controlled release of therapeutic drugs. In addition, cis-aconityl and hydrazone linkages have also been used to achieve pH-sensitive drug release from dendrimer scaffolds. For instance, dendrimer conjugates of doxorubicin (DOX) constructed via both cis-aconityl and hydrazone linkages displayed an acid triggered DOX release.

Figure 10.5 Incorporation of poly(2-(N,N-diethylamino)ethyl methacrylate) polymer molecules into a G3 poly(amidoamine) dendrimer system for pH-sensitive release of encapsulated 5-fluorouracil [13].

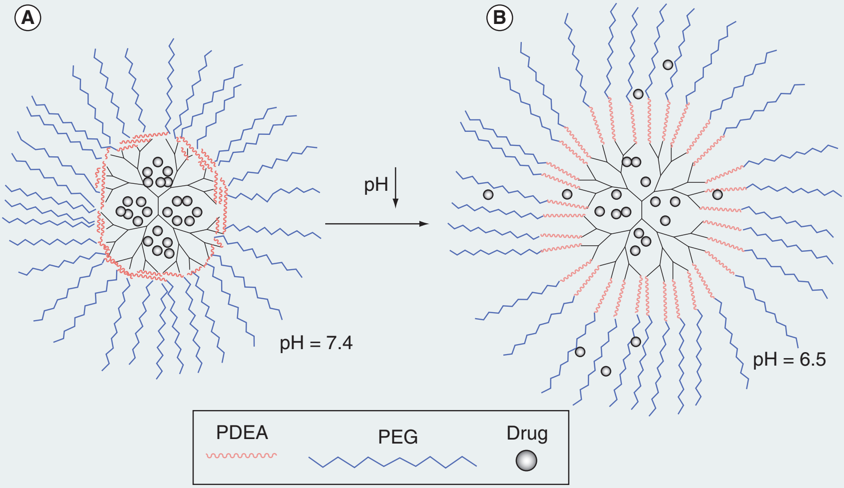

Redox-sensitive release of drugs from chemical linkages

The disulfide linkage (-S-S-) has been extensively used to achieve the desired controlled release of therapeutic drugs from delivery vehicles under reductive conditions. Disulfide bond is formed through the oxidation of two thiols and remains stable under mild oxidative conditions (e.g., atmospheric oxygen or the blood stream). When exposed to a reducing agent, the disulfide linkage can be cleaved to form two thiols. For instance, in tumor cells under hypoxic conditions, a high concentration of reduced glutathione (GSH) is able to break the disulfide linkage thus releasing drugs. Such strategy has been applied to construct dendrimer-drug conjugates toward controlled drug release [14].

Despite the success of the methods mentioned above, it must be noted that conjugating different classes of functional molecules to the surface of the dendrimer scaffolds often results in a heterogeneous distribution of the functionalization and thus hinders the interpretation of biological and clinical results as the structure–activity relationship is compromised. To address this problem, efforts have been seen through the implementation of new synthetic strategies and scalable purification techniques [15].

Figure 10.6 Schematic acid-assisted drug release via pH-sensitive linkages incorporated to dendrimer platforms.

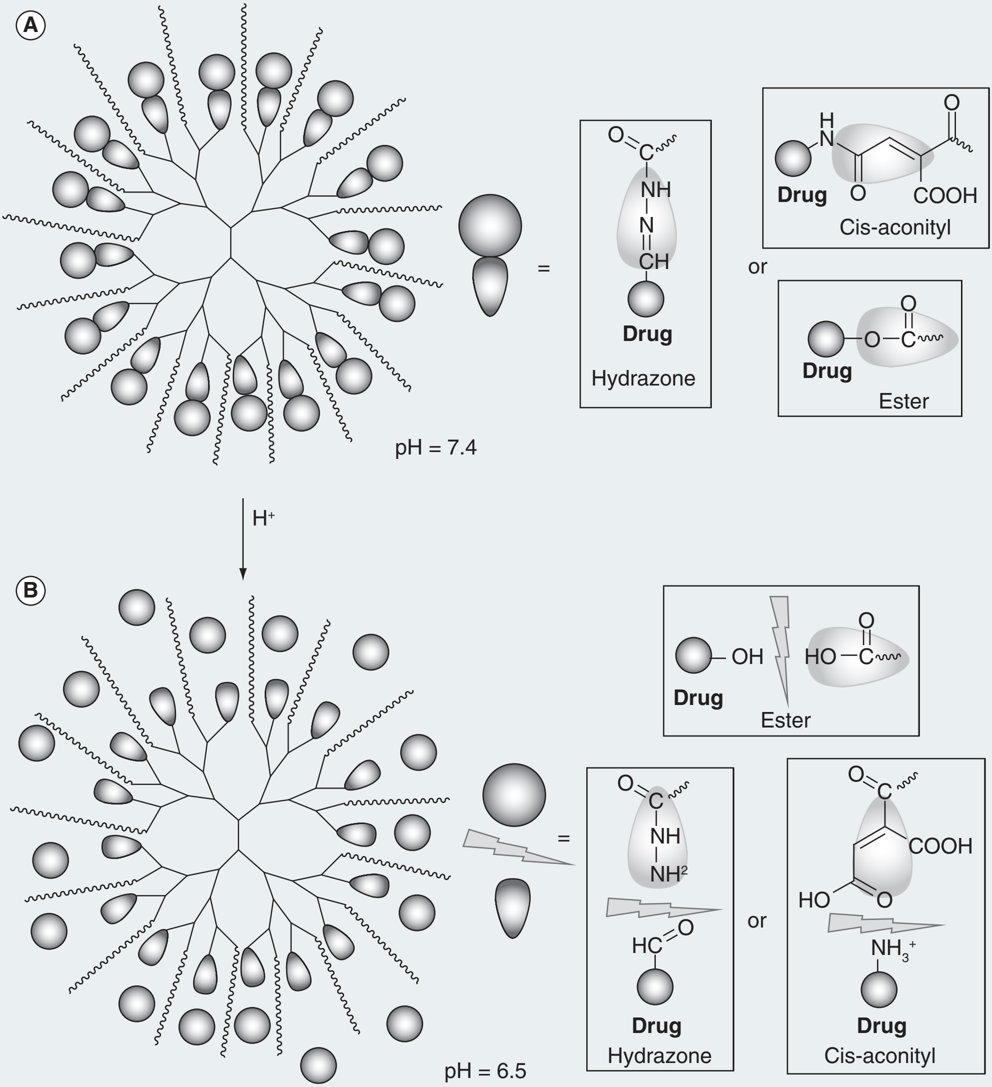

Newly emerged applications of dendrimer scaffolds

Dendrimer scaffolds as nonviral vectors for gene therapy

Gene therapy is a biomedical technique, in which an exogenous genetic material is transferred to the host with the goal to upregulate or down-regulate the targeted genes. This technique has shown great promise and potential in the treatment of various diseases [4] such as Parkinson's disease, cystic fibrosis, severe combined immunodeficiency and cancer. The effectiveness of gene therapy mainly depends on the delivery efficiency of the genetic material to the targeted cells without inducing nonspecific pathogenic effects [16]. Currently, viral vectors are the most efficient vehicles for gene delivery. However, the risks of using viral vectors, such as unwanted toxicity, potential oncogenicity and immunogenicity limit the scope of gene therapy in both basic research and clinical applications [17]. Recently, the development of nonviral delivery systems has drawn considerable interest for gene therapy. With the unique structural features, dendrimer scaffolds are one of the nonviral delivery systems which have shown promise in gene therapy. For instance, cationic dendrimers such as amino-terminated PAMAM or PPI dendrimers are capable of carrying payloads crossing the membranes (plasma and nuclear), which is prerequisite for gene therapy. However, the toxicity of unmodified cationic dendrimer cannot be neglected and often it is mitigated by surface modification with PEGylation [18] or introduction of histidine to cationic dendrimers [19]. The transfection efficiency of this delivery system can be improved by conjugating with alkyl chains, cell permeation peptides or carbohydrates [20]. Interestingly, it was reported that the transfection efficiency can also be improved by stabilizing the dendrimer structure by entrapping gold nanoparticles [21]. Partially degraded (or fragmented) dendrimers have been shown being able to afford a more flexible structure (fewer amide bonds), which can form a more compact complex with gene materials that allows gene delivery through endocytotic pathway [22]. As compared with viral vectors, dendrimer scaffolds can deliver more genetic material with less safety concern. For instance, after complexed with viral interleukin-10 gene, the hybrid of G5 PAMAM with ethylenediamine core showed low *in vitro* and *in vivo* cytotoxicity while dramatically increasing the gene transfer efficacy by 1000-fold in a murine cardiac graft model [23].

Dendrimer scaffolds as delivery vehicles of radioisotopes for radiation therapy

Dendrimer scaffolds conjugated with bifunctional chelators have been widely used for radioisotope-based imaging and therapy. Radioisotopes of therapeutic use include ^{64}Cu, ^{90}Y, ^{177}Lu and $^{186/188}$Re [24–26]. However, there are concerns associated with such radioisotope-based therapy, such as radiation exposure, public fear of radiation and unwanted internal radiation after the therapy administration due to the relatively long blood circulation half-life of dendrimer conjugates [27]. Moreover, the inevitable passive accumulation in the reticuloendothelial system (RES) organs imposes unnecessary radiation exposure burden to the liver, spleen and bone marrow. Besides the applications of radioisotope delivery, dendrimer scaffolds have also been reported for boron neutron capture therapy (BNCT) [28]. The concept of BNCT is based on the nuclear capture and fission reactions that occur when stable boron isotope (^{10}B) is irradiated with low energy neutrons, which emit high energy α particles and lithium-7 (^{7}Li) nuclei. The α particles and ^{7}Li nuclei deliver short range ionization ($5-9$ μm) to ablate the abnormal cell mass [29]. To sustain an effective lethal $^{10}B(n, \alpha)^{7}Li$ reaction, it has been estimated that a dose of 35–50 μg of ^{10}B per gram of tumor needs to be delivered to the target [30]. In order to have a high boron loading and specific targeting, an antibody-conjugated boronated poly-lysine construct containing greater than 1700 boron atoms has been developed [31]. However, the inhomogeneity of the linear polymer resulted in the loss of its *in vivo* targeting property [32]. On the other hand, with the uniform and tuneable structure of G4 PAMAM dendrimer, the antibody-conjugated boronated dendrimer maintains its *in vivo* immunoreactivity [33] and the PEGylation on dendrimer further reduces the accumulation in the RES [72]. However, the BNCT application is limited due to the accessibility of low energy neutrons.

Conclusion & future perspective

Dendrimers are highly symmetric spheres featuring monodispersity and well-defined three-dimensional structures, which are highly desirable for therapeutic drug delivery. In addition, the biological behavior of dendrimers or dendrimer scaffolds can be tuned to meet specific applications as they can be tailored or modified to afford control over their architecture, size, shape, branching length density and surface functionality without compromising the desired loading capacity. In general, the loading of therapeutic agents to dendrimer scaffolds can be achieved by encapsulation, chemical attachment, or physically adsorption. Moreover, the dense presentation of functional groups on the dendrimer surface also allows the attachment of targeting vectors for specific applications. Controlled release of therapeutic drugs from the dendrimer scaffolds has received considerable attention recently and the approaches have been evolving. Promising work has been done as represented by incorporation of pH-sensitive or redox-sensitive linkages into dendrimer—drug conjugates. However, most advances if not all still remain at preclinical stages due to the complexity and lack of reproducibility of the chemical procedures, which leads to the difficulties in the synthesis of large quantities of the delivery system with pharmaceutical-grade purity. Nevertheless, new methods and strategies for the synthesis, modification and derivatization of dendrimers are continuously being developed. We believe that the challenges standing in the course of clinical transition will be surmounted in a decade to come.

Financial & competing interests disclosure

The authors acknowledge the funding supports to their work on developing theranostic agents for prostate cancer by the National Institutes of Health (R01CA159144) and the Prostate Cancer Research Program of the United States Army Medical Research and Materiel Command (W81XWH-12–1–0336). The authors have no other relevant affiliations or financial involvement with any organization or entity with a financial interest in or financial conflict with the subject matter or materials discussed in the manuscript apart from those disclosed.

No writing assistance was utilized in the production of this manuscript.

Summary

- With tunable size and chemical composition, highly symmetrical dendrimers are capable of meeting the desired pharmacokinetics and biocompatibility for drug delivery.
- Two main drug-loading methods to explore a dendrimer scaffold for drug delivery: noncovalent encapsulation and covalent conjugation.
- Mechanisms most exploited for controlled drug-release: acidic and/or reductive *in vivo* microenvironments.
- Dendrimer scaffolds may find potential application in gene therapy as nonviral vectors and in the development of theranostics as multivalent and multiplexed carriers.

Key terms

Dendrimers:	synthetic macromolecules with a well-defined and symmetrical structure that encompasses a central core, repetitive branching units and terminal functionalities.
Therapeutics:	in this chapter, refers to therapeutic agents, synthetic or natural chemical substances, with proven healing or preventive effects on diseases, which they are intended to treat or prevent.
Drug delivery:	systematic approaches of formulation, administration and transportation of a therapeutic agent to the diseased sites so that the desired therapeutic effect can be achieved without causing severe side effects or damages to normal organs or tissues. In this chapter, drug delivery deals with specifically designed chemical carriers to control or manage the dosage and duration of the presence of a therapeutic agent in the body.

References

1. Tomalia DA, Frechet JM. Discovery of dendrimers and dendritic polymers: a brief historical perspective. *J. Polym. Sci.* 40(16), 10 (2002).

2. Tomalia DA. Dendrimer research. *Science* 252(5010), 1231 (1991).
3. Jain K, Kesharwani P, Gupta U, Jain NK. Dendrimer toxicity: let's meet the challenge. *Inte. J. Pharm.* 394(1–2), 122–142 (2010).
4. Lo ST, Kumar A, Hsieh JT, Sun X. Dendrimer nanoscaffolds for potential theranostics of prostate cancer with a focus on radiochemistry. *Mol. Pharm.* 10(3), 793–812 (2013).
5. Driver RW, Yang LX. Synthesis and pharmacology of new camptothecin drugs. *Mini Rev. Med. Chem.* 5(5), 425–439 (2005).
6. Jansen JF, de Brabander-van den Berg EM, Meijer EW. Encapsulation of guest molecules into a dendritic box. *Science* 266(5188), 1226–1229 (1994).
7. Sampathkumar S, Yarema KJ. Dendrimers in cancer treatment and diagnosis. *Nanotechnol. Life Sci.* 7, 43 (2007).
8. Cheng Y, Tomalia DA. *Dendrimer-Based Drug Delivery Systems: From Theory to Practice.* Wiley, New York, USA (2012).
9. Majoros IJ, Thomas TP, Mehta CB, Baker JR, Jr. Poly(amidoamine) dendrimer-based multifunctional engineered nanodevice for cancer therapy. *J. Med. Chem.* 48(19), 5892–5899 (2005).
10. Gajbhiye V, Vijayaraj Kumar P, Tekade RK, Jain NK. PEGylated PPI dendritic architectures for sustained delivery of H2 receptor antagonist. *Eur. J. Med. Chem.* 44(3), 1155–1166 (2009).
11. Devarakonda B, Hill RA, de Villiers MM. The effect of PAMAM dendrimer generation size and surface functional group on the aqueous solubility of nifedipine. *Int. J. Pharm.* 284(1–2), 133–140 (2004).
12. Jin Y, Ren X, Wang W *et al.* A 5-fluorouracil-loaded pH-responsive dendrimer nanocarrier for tumor targeting. *Int. J. Pharm.* 420(2), 378–384 (2011).
13. Du L, Jin Y, Yang J, Wang S, Wang X. A functionalized poly(amidoamine) nanocarrier-loading 5-fluorouracil: pH-responsive drug release and enhanced anticancer effect. *Anticancer Drugs* 24(2), 172–180 (2013).
14. Wang B, Navath RS, Romero R, Kannan S, Kannan R. Anti-inflammatory and anti-oxidant activity of anionic dendrimer-N-acetyl cysteine conjugates in activated microglial cells. *Int. J. Pharm.* 377(1–2), 159–168 (2009).
15. Mullen DG, Banaszak Holl MM. Heterogeneous ligand-nanoparticle distributions: a major obstacle to scientific understanding and commercial translation. *Acc. Chem. Res.* 44(11), 1135–1145 (2011).
16. Li S, Huang L. Nonviral gene therapy: promises and challenges. *Gene Ther.* 7(1), 31–34 (2000).
17. Liu YP, Berkhout B. miRNA cassettes in viral vectors: problems and solutions. *Biochim. Biophys. Acta* 1809(11–12), 732–745 (2011).
18. Wang W, Xiong W, Wan J, Sun X, Xu H, Yang X. The decrease of PAMAM dendrimer-induced cytotoxicity by PEGylation via attenuation of oxidative stress. *Nanotechnology* 20(10), 105103 (2009).
19. Yu GS, Bae YM, Choi H, Kong B, Choi IS, Choi JS. Synthesis of PAMAM dendrimer derivatives with enhanced buffering capacity and remarkable gene transfection efficiency. *Bioconjug. Chem.* 22(6), 1046–1055 (2011).
20. Lakshminarayanan A, Ravi VK, Tatineni R *et al.* Efficient dendrimer-DNA complexation and gene delivery vector properties of nitrogen-core poly(propyl ether imine) dendrimer in mammalian cells. *Bioconjug. Chem.* 24(9), 1612–1623 (2013).
21. Xiao T, Cao X, Shi X. Dendrimer-entrapped gold nanoparticles modified with folic acid for targeted gene delivery applications. *J. Control. Release* 172(1), e114–e115 (2013).
22. Dennig J, Duncan E. Gene transfer into eukaryotic cells using activated polyamidoamine dendrimers. *J. Biotechnol.* 90(3–4), 339–347 (2002).
23. Qin L, Pahud DR, Ding Y *et al.* Efficient transfer of genes into murine cardiac grafts by Starburst polyamidoamine dendrimers. *Hum. Gene Ther.* 9(4), 553–560 (1998).
24. Seregni E, Maccauro M, Coliva A *et al.* Treatment with tandem [(90)Y]DOTA-TATE and [(177)Lu] DOTA-TATE of neuroendocrine tumors refractory to conventional therapy: preliminary results. *Q. J. Nucl. Med. Mol. Imag.* 54(1), 84–91 (2010).
25. Yuan J, You Y, Lu X, Muzik O, Oupicky D, Peng F. Synthesis of poly[APMA]-DOTA-64Cu conjugates for interventional radionuclide therapy of

prostate cancer: assessment of intratumoral retention by micro-positron emission tomography. *Mol. Imag.* 6(1), 10–17 (2007).

26. Chen LC, Chang CH, Yu CY *et al.* Pharmacokinetics, micro-SPECT/CT imaging and therapeutic efficacy of (188)Re-DXR-liposome in C26 colon carcinoma ascites mice model. *Nucl. Med. Biol.* 35(8), 883–893 (2008).
27. Lee CC, MacKay JA, Frechet JM, Szoka FC. Designing dendrimers for biological applications. *Nat. Biotechnol.* 23(12), 1517–1526 (2005).
28. Shukla S, Wu G, Chatterjee M *et al.* Synthesis and biological evaluation of folate receptor-targeted boronated PAMAM dendrimers as potential agents for neutron capture therapy. *Bioconjug. Chem.* 14(1), 158–167 (2003).
29. Barth RF, Coderre JA, Vicente MG, Blue TE. Boron neutron capture therapy of cancer: current status and future prospects. *Clin. Cancer Res.* 11(11), 3987–4002 (2005).
30. Javid M, Brownell, GL, Sweet WH. The possible use of neutron capture isotope such as boron-10 in the treatment of neoplasms: II. Computation of the radiation energy and estimates of effects in normal and neoplastic brain. *J. Clin. Invest.* 31, 603–610 (1952).
31. Alam F, Soloway AH, Barth RF, Mafune N, Adams DM, Knoth WH. Boron neutron capture therapy: linkage of a boronated macromolecule to monoclonal antibodies directed against tumor-associated antigens. *J. Med. Chem.* 32(10), 2326–2330 (1989).
32. Barth RF, Mafune N, Alam F *et al.* Conjugation, purification and characterization of boronated monoclonal antibodies for use in neutron capture therapy. *Strahlenther. Onkol.* 165(2–3), 142–145 (1989).
33. Barth RF, Adams DM, Soloway AH, Alam F, Darby MV. Boronated starburst dendrimer-monoclonal antibody immunoconjugates: evaluation as a potential delivery system for neutron capture therapy. *Bioconjug. Chem.* 5(1), 58–66 (1994).
34. Malik N, Evagorou EG, Duncan R. Dendrimer-platinate: a novel approach to cancer chemotherapy. *Anti-cancer Drugs* 10(8), 767–776 (1999).
35. Yellepeddi VK, Kumar A, Maher DM, Chauhan SC, Vangara KK, Palakurthi S. Biotinylated PAMAM dendrimers for intracellular delivery of cisplatin to ovarian cancer: role of SMVT. *Anticancer Res.* 31(3), 897–906 (2011).
36. Zhu S, Hong M, Zhang L, Tang G, Jiang Y, Pei Y. PEGylated PAMAM dendrimer-doxorubicin conjugates: in vitro evaluation and in vivo tumor accumulation. *Pharm. Res.* 27(1), 161–174 (2010).
37. Kono K, Kojima C, Hayashi N *et al.* Preparation and cytotoxic activity of poly(ethylene glycol)-modified poly(amidoamine) dendrimers bearing adriamycin. *Biomaterials* 29(11), 1664–1675 (2008).
38. Lim J, Lo ST, Hill S, Pavan GM, Sun X, Simanek EE. Antitumor activity and molecular dynamics simulations of paclitaxel-laden triazine dendrimers. *Mol. Pharmaceut.* 9(3), 404–412 (2012).
39. Yang W, Barth RF, Wu G *et al.* Convection enhanced delivery of boronated EGF as a molecular targeting agent for neutron capture therapy of brain tumors. *J. Neuro. Oncol.* 95(3), 355–365 (2009).

Bioconjugate Chemistry

Article

pubs.acs.org/bc

Molecular Platform for Design and Synthesis of Targeted Dual-Modality Imaging Probes

Amit Kumar,[†] Shanrong Zhang,[‡] Guiyang Hao,[†] Gedaa Hassan,[†] Saleh Ramezani,[†] Koji Sagiyama,[‡] Su-Tang Lo,[†] Masaya Takahashi,[‡] A. Dean Sherry,[‡] Orhan K. Öz,[†] Zoltan Kovacs,[‡] and Xiankai Sun*[,†,‡]

[†]Department of Radiology, [‡]Advanced Imaging Research Center, University of Texas Southwestern Medical Center, Dallas, Texas 75390, United States

Supporting Information

ABSTRACT: We report a versatile dendritic structure based platform for construction of targeted dual-modality imaging probes. The platform contains multiple copies of 1,4,7,10-tetraazacyclododecane-1,4,7,10-tetraacetic acid (DOTA) branching out from a 1,4,7-triazacyclononane-*N*,*N*′,*N*″-triacetic acid (NOTA) core. The specific coordination chemistries of the NOTA and DOTA moieties offer specific loading of $^{68/67}Ga^{3+}$ and Gd^{3+}, respectively, into a common molecular scaffold. The platform also contains three amino groups which can potentiate targeted dual-modality imaging of PET/MRI or SPECT/MRI (PET: positron emission tomography; SPECT: single photon emission computed tomography; MRI: magnetic resonance imaging) when further functionalized by targeting vectors of interest. To validate this design concept, a bimetallic complex was synthesized with six peripheral Gd-DOTA units and one Ga-NOTA core at the center, whose ion T_1 relaxivity per gadolinium atom was measured to be 15.99 mM^{-1} s^{-1} at 20 MHz. Further, the bimetallic agent demonstrated its anticipated in vivo stability, tissue distribution, and pharmacokinetic profile when labeled with ^{67}Ga. When conjugated with a model targeting peptide sequence, the trivalent construct was able to visualize tumors in a mouse xenograft model by both PET and MRI via a single dose injection.

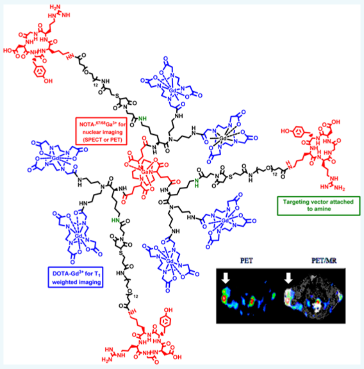

INTRODUCTION

Molecular imaging is gaining importance for noninvasive assessment of biological events in animal and human subjects. Through in vivo real-time visualization and imaging quantification of biological targets of interest, a better understanding of the biological processes underlining the initiation and progression of diseases can be obtained for more efficacious diagnosis and treatment.[1,2] However, a single imaging technique is often unable to deliver all the necessary information required for a definitive clinical decision. To date, successful attempts have been seen to combine two or more imaging modalities in order to overcome the shortcomings of single modality systems for optimal visualization and better quantitative delineation of targets of interest. Consequently, multimodal imaging techniques have become the norm in both clinical practice and preclinical research as evidenced by the implementation of PET/CT (PET: positron emission tomography; CT: computed tomography) and PET/MRI (MRI: magnetic resonance imaging) procedures to patient care and the increasing use of a variety of combinations of the currently available imaging techniques in translational or basic biomedical research, such as MRI/optical and PET/NIRF (NIRF: near-infrared fluorescence).[3−8] The fusion of PET and MRI is especially desirable because technically their physical features are complementary. While radionuclide-based imaging techniques, either PET or SPECT (single photon emission computed tomography), are extremely sensitive and quantitative, which allows the studies of biological events or processes at the molecular and cellular level, their spatial resolution is limited (>1 cm for current clinical scanners).[9−11] On the other hand, while MRI is able to provide high spatial resolution (<0.1 cm) with exquisite soft tissue contrast even without exogenous contrast agents, contrast agents are often required to highlight specific biological or physiological processes in an amount a few orders of magnitude higher than PET or SPECT.[12−14]

Given that more and more PET/MRI systems will likely be used in the practice of diagnostic radiology, it becomes important to develop dual modality imaging probes that can realize the full potential of both modalities.

To take advantage of the strengths of PET and MRI, our approach is to design and synthesize a dual-modality agent scaffold offering a "single pharmacological behavior" for both imaging acquisitions. The merging of PET and MRI probe moieties to a single molecular platform would facilitate colocation and cross-validation of each modality in targeted regions of interest (two measures of one event). While MRI can provide the exact location of the probe, motion artifact correction, and PET partial volume correction, PET can afford better imaging quantification for higher detection sensitivity. Further, given that the proton MRI contrast actually reflects the

Received: January 13, 2015
Revised: January 23, 2015

DOI: 10.1021/acs.bioconjchem.5b00028

map of the proton density, a colocalized PET signal distinct from the proton background could make the MRI contrast more identifiable, which further improves the MRI sensitivity.

Indeed several nanoparticle-based PET/MRI agents have been reported with enhanced magnetic relaxivities and considerable promise as dual-modality imaging agents.[15−17] However, a nanoparticle platform for PET/MRI probe development presents challenges. First, the nanoparticle-based PET/MRI probes are not single molecular entities and often have questionable in vivo stability or molecular integrity. Second, to serve the purpose of diagnostic imaging, contrast agents are desired to have a reasonable blood circulation half-life for efficient accumulation in targets and minimal non-specific deposition in the mononuclear phagocyte system (MPS) organs after systemic administration. However, it is well-known that most nanoparticles if not all possess suboptimal in vivo distribution as shown by rapid sequestration into MPS organs and thereafter slow clearance. These properties present potential health hazards[18−20] which could impede their translation toward clinical applications. Third, the majority of nanoparticle-based PET/MRI agents provide T_2 contrast; only a handful are T_1-based agents, which are preferred in the cases of low proton density in the target tissues. To date, a wide range of macromolecules, such as perfluorocarbon emulsions,[15] silica nanoparticles,[16,21,22] liposomal vesicles,[17,23−25] dendrimers,[26−32] and polymers,[33] have been explored for the development of gadolinium-based T_1 contrast agents. Of the macromolecular systems, dendrimers, which possess definitive molecular structures and formula, have shown a promising role. For instance, the dendrimer systems of poly(amido amine) (PAMAM) have been used as blood pool,[34] liver,[35] renal,[36] lymphatic,[37] and tumor-specific[38] contrast agents. However, the Gd-PAMAM complexes rarely afford an ionic relaxivity greater than 11 mM^{-1} s^{-1} per gadolinium ion.[39,40] When such dendrimer platforms are used to develop PET/MRI or SPECT/MRI agents, it is challenging to achieve precise control of radioisotope loading into specific chelating moieties. Herein, we present a dual-modality molecular probe design (Figure 1) carrying six 1,4,7,10-tetraazacyclododecane-1,4,7,10-tetraacetic acid (DOTA) moieties branched out from a single 1,4,7-triazacyclononane-*N*,*N*′,*N*″-triacetic acid (NOTA) core structure. In this work, we demonstrate an exclusive loading of Gd^{3+} into the DOTA units affording a T_1 ion relaxivity of 15.99 mM^{-1} s^{-1} at 20 MHz, while the NOTA core remains available to form a chelate with $^{67/68}Ga^{3+}$ for nuclear imaging. If the targeted accumulation event is rapid, ^{68}Ga ($t_{1/2}$ = 68 min; β^+ = 89%, $E_{\beta+\max}$ = 1.92 MeV; EC = 11%) will be used for PET imaging; otherwise, ^{67}Ga ($t_{1/2}$ = 3.26 d; γ = 184 keV) will be used for SPECT imaging.

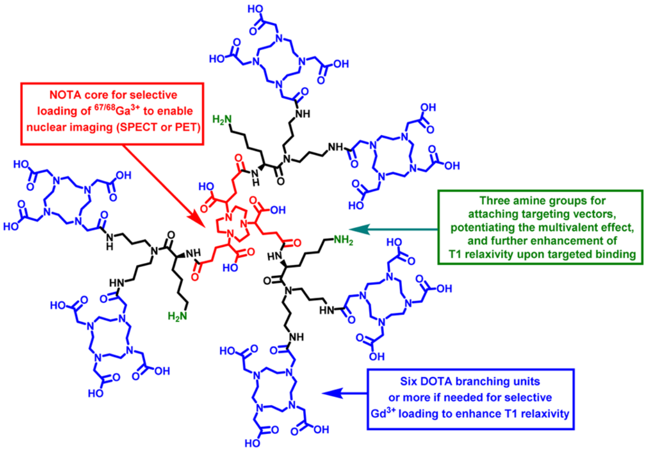

H_{21}**L**

Figure 1. Dual-modality molecular probe design.

RESULTS AND DISCUSSION

The dual-modality molecular probe design also possesses three amino groups for potential conjugation with multiple copies of targeting molecules, thereby providing multivalent effect to the construct for better specific binding to the biological target of interest. Of note, the strong interaction between the targeting molecule tethered probe and the corresponding target, triggered by multivalent effect, is expected to further enhance the relaxivity of the probe. For proof of concept, we conjugated each amine with a model integrin $\alpha_v\beta_3$ targeting peptide, c(RGDyK). The main features of this molecular dual-modality imaging probe design include the apparent in vivo stability (due to the inertness of the Gd-DOTA and Ga-NOTA complexes) and the defined molecular formula with selective loading of two metal ions.

Synthesis. The desired ligand H_{21}**L** was synthesized in 7 steps with an overall yield of approximately 15%. The structure of each intermediate was verified by ^{1}H NMR and ^{13}C NMR as well as mass spectroscopy. The synthesis route to compound H_{21}**L** is outlined in Scheme 1 and its functionalization is depicted in Scheme 2. Compound **2** was obtained from bis(3-aminopropyl)amine and carbobenzyloxy (Cbz) protected lysine in three steps (see Supporting Information). The free primary amine of **2** was coupled to the carboxylic acid bearing side arms of NOTA-(OH)$_3$ (Scheme 1) via carbodiimide chemistry to form **3**. The *N*-phthaloyl protected amino groups of **3** were freed by deprotection via hydrazine to afford **4**, which contains six amino groups serving as points of attachment for the DOTA units.

Scheme 1. Synthetic Route to Ligand H_{21}L

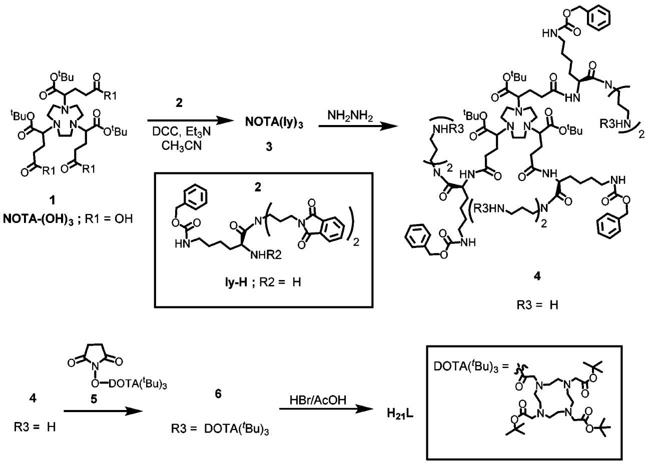

The *N*-hydroxy succinamide activated DOTA ester, **5**, was reacted to the six amino groups forming **6**. Attempts to deprotect the Boc groups of compound **6** led to partial deprotection of the Cbz groups. To overcome this problem, the ligand was fully deprotected by 30% HBr in an acetic acid solution. The synthesized ligand, H_{21}**L**, was fully characterized. The ligand carries six DOTA units intended for chelating Gd^{3+}

Scheme 2. Synthesis of Integrin $\alpha_v\beta_3$ Targeted Ligand Scaffolds

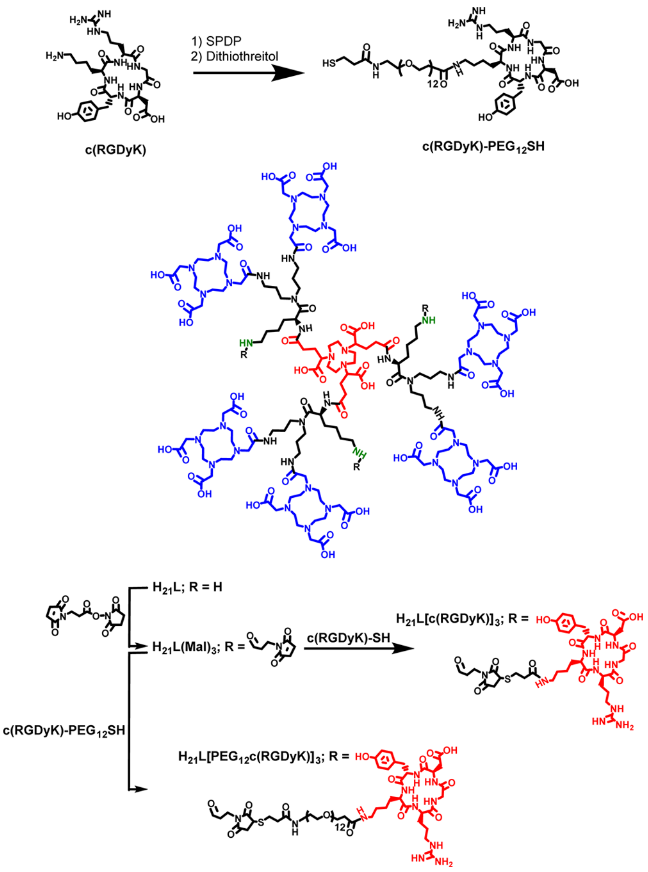

and one NOTA unit intended for chelating Ga^{3+}. Since Gd^{3+} and Ga^{3+} can be specifically loaded into the DOTA and NOTA moieties, respectively, based on their ion-size preference, the bimetallic molecular complex is expected to carry the two metal ions in a specified ratio so as to facilitate PET imaging based quantification.

Functionalization of ligand H_{21}**L** was performed by utilizing the previously mentioned amino groups. Maleimido groups were tethered to amines using the commercially available reagent of *N*-succinimidyl 3-maleimidopropionate (Scheme 2). The model targeting peptide, c(RGDyK), was tethered to the maleimido carrying ligand H_{21}**L** via thiol−maleimide coupling. Given that targeting molecules attached to the bimetallic complex may not be able to stretch out for specific binding because of the steric hindrance from the construct, additionally we introduced a PEG_{12} linker between the complex and targeting vector.

The thiol group without a spacer (zero) or with a PEG_{12} linker was introduced to c(RGDyK) using the commercially available reagent: 2-pyridyldithiol-tetraoxaoctatriacontane-*N*-hydroxysuccinimide (SPDP). The thiol terminated c(RGDyK) peptides with zero and PEG_{12} linker were subsequently added to H_{21}**L**$(Mal)_3$ to afford Gd_6H_3**L**$[c(RGDyK)]_3$ and Gd_6H_3**L**$[PEG_{12}c(RGDyK)]_3$, respectively.

Complexation with Gd^{3+} and Ga^{3+} to form Gd_6LGa. The thermodynamic stability constants of Gd-DOTA (log $K_{Gd\text{-}DOTA}$ = 24.7), Gd-NOTA (log $K_{Gd\text{-}NOTA}$ = 14.3), and Ga-NOTA (log $K_{Ga\text{-}NOTA}$ = 31.0)[41,42] suggest that when ligand H_{21}**L** is treated with 6 equiv of Gd^{3+}, its complex can be formed exclusively with the DOTA units. The bimetallic complex of H_{21}**L**, Gd_6**L**Ga, can then be formed by incorporation of Ga^{3+} into the NOTA core. However, considering that the reaction of **L** with the stoichiometric amount of Gd^{3+} may be slow and could lead to partial complexation of the DOTA units, the first complexation was performed with excess of Gd^{3+} to give complete chelation of both the DOTA and NOTA units forming Gd_7**L**. This was confirmed with mass spectroscopy (see Supporting Information) as well as ^1H NMR spectra using Eu^{3+} instead of Gd^{3+}. Later, Gd^{3+} was efficiently removed from the NOTA core by treating the complex with excess diethylene triamine pentaacetic acid (DTPA) (the log K of Gd-DTPA[42] is approximately 8 orders of magnitude higher than that of Gd-NOTA). The incorporation of either cold Ga^{3+} or $^{68}Ga^{3+}$ into the NOTA core of complex of Gd_6H_3**L** was then carried out at pH 3−5 in an HEPES buffer. The cold Gd_6**L**Ga complex was purified and characterized by HPLC and mass spectrometry. Various concentration of Gd_6**L**Ga were injected to inductively coupled plasma mass spectrometry (ICP-mass) and the ratio of Gd:Ga was calculated to be 6:1 (see Supporting Information). The Gd_6**L**^{68}Ga was purified and characterized by radio-HPLC using the cold complex as reference.

Coordination Chemistry of the NOTA Core of H_{21}L. To prove the efficient removal of Gd^{3+} from the NOTA core during the complexation procedure, the same complexation procedure was followed using Eu^{3+} instead of Gd^{3+}. Chemically, Eu^{3+} and Gd^{3+} have similar reactivities toward NOTA and DOTA. Since Eu^{3+} is only weakly paramagnetic, the ^1H NMR signals of its complexes are relatively sharp and also paramagnetically shifted. This facilitates relatively straightforward structural characterization by NMR spectroscopy. To accomplish this, the Eu^{3+} complex of H_{21}**L**, were synthesized via two procedures, i.e., with and without a challenge by excess DTPA, followed by HPLC purification. Both complexes were characterized by ^1H NMR spectroscopy (400 MHz). Figure 2a,b shows the ^1H NMR spectra of Eu^{3+} complexes of H_{21}**L** with and without the DTPA challenge, respectively. The DTPA treated Eu^{3+} complex (Figure 2a) showed sharp peaks in the NOTA region (around 3−4 ppm) suggesting a metal free NOTA core as opposed to the untreated complex (Figure 2b), which showed broad peaks indicating the interaction of metal with the NOTA core. This characterization along with the mass

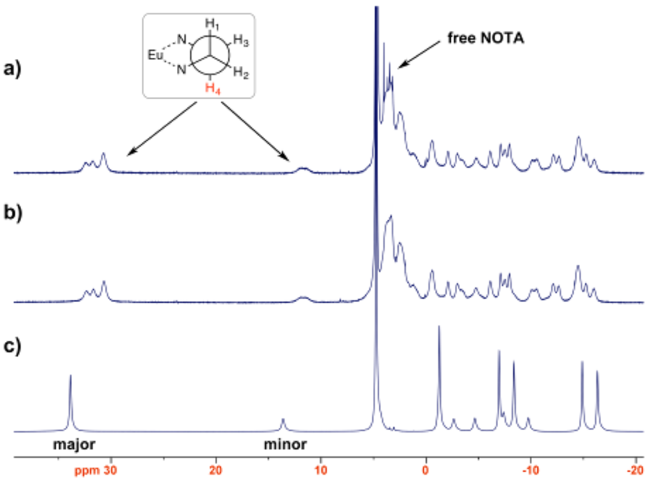

Figure 2. 400 MHz ^1H NMR spectra of (a) Eu^{3+} complex of H_{21}**L** treated with excess DTPA, (b) untreated Eu^{3+} complex of H_{21}**L**, and (c) Eu-DOTA complex.

DOI: 10.1021/acs.bioconjchem.5b00028

spectroscopy results of $Gd_7\mathbf{L}$ and $Gd_6H_3\mathbf{L}$ indicates the exclusive Gd^{3+} coordination with the six DOTA moieties of $H_{21}\mathbf{L}$. Further, the formation of $Gd_6\mathbf{L}Ga$ was confirmed by the molar ratio of Gd:Ga determined by ICP-mass (Supporting Information). These results demonstrate that Gd^{3+} and Ga^{3+} have been exclusively loaded to the DOTA and NOTA moieties as designed, respectively, for the preparation of the desired dual-modality molecular imaging probe.

Relaxometric Measurements. The T_1 relaxivity of $Gd_6\mathbf{L}Ga$ was measured at 20 MHz, 25 °C, to be 95.98 mM^{-1} s^{-1} with R^2 value greater than 0.99 (each Gd^{3+} in the complex accounted for 15.99 mM^{-1} s^{-1} (ion relaxivity)). Under the same conditions, the relaxivity of Magnavist was found to be 4.1 mM^{-1} s^{-1}. Impressively, the T_1 relaxivity of $Gd_6H_3\mathbf{L}$ was approximately 4 times higher than that of the Gd-DOTA complex and comparable to the Gd-PAMAM complexes, which have been reported with the ion relaxivity up to 11 mM^{-1} s^{-1}.[39,40] It is noteworthy that a similar relaxivity was also reported for a polylysine-based contrast agent (MW 17 453) with 24 Gd-DOTA units.[43,44] At the physiological temperature of 37 °C, the relaxivity of $Gd_6\mathbf{L}Ga$ was unchanged while its relaxivity in rat serum at 25 °C increased to 153.1 mM^{-1} s^{-1}. These observations suggest two things: first, the lack of temperature dependence between 25 and 37 °C suggests that the water exchange rate in the appended Gd-DO3A-monoamide complexes limits the relaxivity somewhat at 25 °C. Given that water exchange is faster at 37 °C, the expected decline in relaxivity with increasing temperatures is offset by faster water exchange and a more favorable relaxivity at 37 °C. This was an unanticipated yet welcomed added advantage for this probe platform design. The higher relaxivity in serum indicates that $Gd_6\mathbf{L}Ga$ does interact with one or more serum proteins.

MR Imaging and Relaxivity Measurements of $Gd_6\mathbf{L}Ga$ at 1.0 T. The MR imaging potential of $Gd_6\mathbf{L}Ga$ was evaluated at magnetic field of 1.0 T. Figure 3 shows the T_1 weighted imaging of $Gd_6\mathbf{L}Ga$ in comparison with Magnevist at a series of decreasing concentrations (0.4–0.02 mM determined by ICP-mass). The images of $Gd_6\mathbf{L}Ga$ were obviously brighter than those of Magnevist (4.1 mM^{-1} s^{-1}) at each equivalent concentration. The T_1 relaxivity of $Gd_6\mathbf{L}Ga$ was measured at 113.36 mM^{-1} s^{-1} (T_1 ion relaxivity: 18.89 mM^{-1} s^{-1}) at 1.0 T (25 °C). Since the agent is intended for conjugation to a targeting moiety for receptor-based imaging, such interactions could further enhance the relaxivity of the agent in vivo.

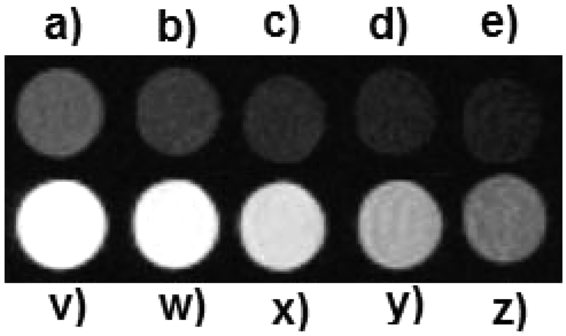

Figure 3. T_1-weighted MR images of samples recorded at 1.0 T at 25 °C. Samples of Magnevist (a → e) and Gd_6H_3L (v → z) containing a series of decreasing concentrations from 0.4 mM, 0.2 mM, 0.1 mM, 0.04 mM, to 0.02 mM.

In Vivo Tissue Distribution, Pharmacokinetics, and Stability of $Gd_6\mathbf{L}Ga$. As compared to other nanoparticle-based dual modality imaging platforms, our molecular probe design is expected to have a reasonable blood circulation half-life and an efficient clearance profile from the organs. To evaluate the in vivo behavior of this probe design, $Gd_6\mathbf{L}H_3$ was radiolabeled with ^{67}Ga ($t_{1/2}$ = 3.26 d) so that the tissue biodistribution could be evaluated over an extended period. As shown in Table 1, the bimetallic complex, $Gd_6\mathbf{L}^{67}Ga$, indeed displayed a rapid and efficient clearance profile from all major organs except kidneys in normal mice. The high renal uptake can be attributed to the net positive charge on the probe due to the presence of amine groups.[45] However, an efficient renal clearance is obvious after the initial high uptake as seen from the decrease of the kidney uptake level from 101.0 ± 4.3%ID/g at 1 h p.i. to 43.0 ± 5.1%ID/g at 24 h p.i. One would anticipate that kidney clearance would be even faster once the positively charged amino groups are removed from the agent through conjugation with a targeting vector. Indeed, when the amine groups of the agent were capped with c(RGDyK), the kidney uptake was impressively reduced to ca. 3%ID/g at 2 h p.i.

Table 1. Tissue Distribution Data and Pharmacokinetic Parameters of $Gd_6\mathbf{L}^{67}Ga$ in Normal Balb/C Mice (n = 4)[a]

	%ID/g		
Organ	1 h	4 h	24 h
Blood	3.51 ± 0.22	2.63 ± 0.84	0.21 ± 0.06
Heart	1.21 ± 0.13	0.94 ± 0.40	0.21 ± 0.02
Lung	2.59 ± 0.5	1.78 ± 0.87	0.38 ± 0.09
Liver	1.39 ± 0.11	2.13 ± 0.81	1.39 ± 0.24
Kidney	101.32 ± 4.32	57.42 ± 17.29	43.90 ± 5.12
Spleen	0.73 ± 0.19	0.69 ± 0.07	0.42 ± 0.12
Muscle	0.27 ± 0.09	0.38 ± 0.13	0.08 ± 0.02
Fat	0.27 ± 0.10	0.27 ± 0.10	0.06 ± 0.02
Brain	0.08 ± 0.01	0.07 ± 0.02	0.02 ± 0.00
Two-Compartment Clearance Profile (min)			
$t_{1/2\alpha}$	11.33 ± 1.31	$t_{1/2\beta}$	438.37 ± 15.11

[a] Data are presented as mean ± standard deviation.

The pharmacokinetics of $Gd_6\mathbf{L}^{67}Ga$ showed a two-compartment profile with $t_{1/2\alpha}$ = 11.3 min and $t_{1/2\beta}$ = 7.3 h, quite different compared to nanoparticle-based imaging agents which can be described by one-compartment models.[46,47] The $t_{1/2\alpha}$ reveals that the tissue distribution of $Gd_6\mathbf{L}^{67}Ga$ was relatively rapid while the reasonably long $t_{1/2\beta}$ enables the probe to accumulate in its targeted tissues without incurring high background uptake. This indicates that the probe behaves similarly to other clinically available small molecule contrast agents.[48] The presence of amine groups on the ligand provides the ease of incorporation of polyethylene glycol (PEG) chains into the probe for optimization of the in vivo kinetics if necessary.

The in vitro and in vivo stabilities of $Gd_6\mathbf{L}^{67}Ga$ were evaluated through incubation in rat serum and by mouse urine metabolite analysis, respectively. The bimetallic complex remained intact during the entire course of study, which further validates this molecular probe platform design.

Receptor-Binding Assay of Targeted $Gd_6\mathbf{L}Ga$ Complexes. Two integrin $\alpha_v\beta_3$ targeted $Gd_6\mathbf{L}Ga$ complexes $Gd_6H_3\mathbf{L}[c(RGDyK)]_3$ and $Gd_6H_3\mathbf{L}[PEG_{12}c(RGDyK)]_3$) were prepared to validate that our molecular construct design can be utilized for specific imaging of cancer biomarkers. The $\alpha_v\beta_3$-binding affinities were determined by a competitive cell-binding assay using ^{125}I-echistatin (PerkinElmer) as the $\alpha_v\beta_3$-specific radioligand. The best-fit IC_{50} values (inhibitory concentration where 50% of the ^{125}I-echistatin bound on U87MG cells are displaced) of c(RGDyK), Gd_6H_3**L**[c(RGDyK)]$_3$, and Gd_6H_3**L**[PEG$_{12}$c(RGDyK)]$_3$) were measured to be 199 nM, 489 nM, and 37 nM (Supporting Information), respectively. The significantly improved $\alpha_v\beta_3$ binding affinity of Gd_6H_3**L**[PEG$_{12}$c(RGDyK)]$_3$) clearly indicates the critical role of the PEG$_{12}$ linker in the desired targeting property of our molecular scaffold design.

PET/MR Imaging Using Gd$_6$L[PEG$_{12}$c(RGDyK)]$_3$^{68}Ga. To overcome the sensitivity difference between PET and MR, the radioactivity of ^{68}Ga was controlled in the labeling of Gd_6H_3**L**[PEG$_{12}$c(RGDyK)]$_3$. The final dose injected into each animal carried about 6.0 mg of the final compound with an activity of 100−150 μCi (Gd: ca. 0.027 mmol/kg; c(RGDyK): 2.0 μmol). Figure 4 shows in vivo dual PET/MR images of integrin $\alpha_v\beta_3$ positive U87MG tumor enabled by a single dose injection of Gd_6**L**[PEG$_{12}$c(RGDyK)]$_3$^{68}Ga. The average tumor uptake measured by PET was 0.88%ID/g. It should be noted that the tumor uptake value was reduced by roughly 3 times when the injected amount of the agent increased from 0.1 mg to 6.0 mg. This decrease also indicates the integrin $\alpha_v\beta_3$ imaging specificity. The observed MR contrast enhancement in the tumor was 3.06 ($n = 3$) when compared to the contrast before injection.

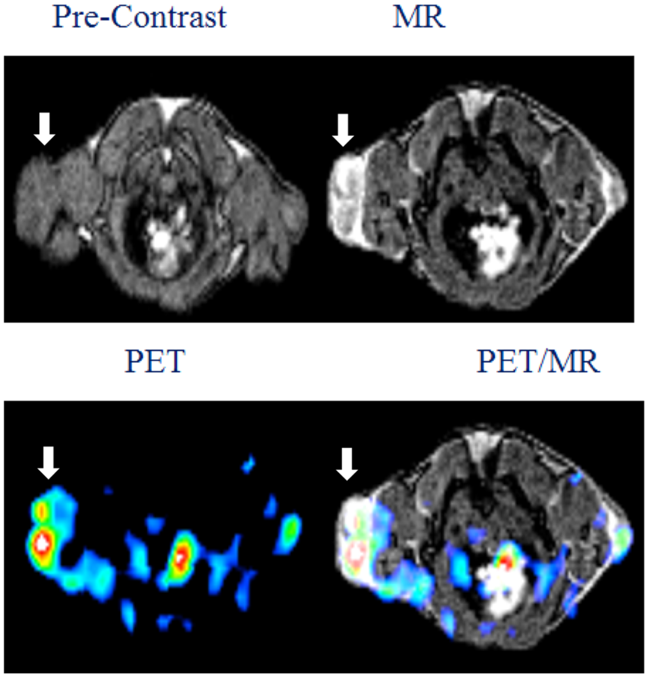

Figure 4. Representative MRI (upper panel), PET (lower panel: left), and fused PET/MR (lower panel: right) images of U87MG tumor xenograft in SCID mice at 1 h post injection of Gd_6**L**[PEG$_{12}$c-(RGDyK)]$_3$^{68}Ga. The white arrow indicates the tumor site.

To date, few PET/MRI or SPECT/MRI agents with a defined structure have been reported. In vivo pH monitoring PET/MRI agents carrying one Gd-DOTA unit along with ^{18}F or ^{68}Ga as PET contrast have been reported.[49] Bimetallic complexes carrying one Gd-DOTA conjugated to ^{68}Ga-NOTA and one Gd-DOTA conjugated to cold Cu or In-DOTA do exist.[50,51] However, they were not designed to serve the goal of providing targeted contrast to both imaging techniques. To provide proof of concept, the probe design in this work consists of only six gadolinium chelatable DOTA units. While the anticipated T_1 relaxivity enhancement was achieved, we recognize that further amplification of MRI sensitivity is necessary in order to realize the practical application of the molecular probe design as dual-modality imaging agents. Given the versatility of the design concept, we believe that it can be readily modified or adapted to reach the desired MRI sensitivity.

In conclusion, we have successfully demonstrated a molecular platform intended for targeted dual-modality imaging of PET/MRI or SPECT/MRI, which carries quantifiable numbers of $^{67/68}Ga^{3+}$ and Gd^{3+} ions in their specific chelation moieties. This probe design displays a very favorable high T_1 relaxivity for MRI contrast enhancement. With the current rapid growth of hybrid PET/MRI systems in diagnostic radiology, our molecular design of dual-modality agents possessing a "single pharmacological behavior" offers a versatile platform for the development of multimodality imaging agents with potential applications for noninvasive molecular profiling of various diseases.

■ EXPERIMENTAL PROCEDURES

General Materials and Methods. All reactions were carried out under N_2 atmosphere in degassed dried solvents. Commercially available starting materials were purchased from commercial vendors and used directly without further purification unless otherwise stated. All aqueous solutions were prepared with Milli-Q water. Bulk solvents were removed using rotary evaporator under reduced pressure at 40 °C. Trace solvents were removed under high vacuum. Matrix-assisted laser desorption/ionization (MALDI) mass spectra were acquired on an Applied Biosystems Voyager-6115 mass spectrometer. Radiolabeled conjugates were purified by Light C-18 Sep-Pak cartridges (Waters, Milford, MA). High performance liquid chromatography (HPLC) was performed on a Waters Xterra Shield RP C-18 semiprep column (250 × 10 mm, 10 μm) and read by a Waters 2996 photodiode array detector and an in-line Shell Jr. 2000 radio-detector. The mobile phase was H_2O with 0.1% trifluoroacetic acid (TFA) (solvent A) and acetonitrile with 0.1% TFA (solvent B). The gradient consisted of 0% B to 80% B in 0−40 min at 4.0 mL/min flow rate. The radioactivity of excised tissue samples and radioactive standards were counted by a Wizard2 300 automatic γ-counter (PerkinElmer).

Synthesis Procedures. ***Compound 3.*** To a solution of the protected acid **1** (0.10 g, 0.15 mmol) in CH_3CN (1.0 mL) were added the deprotected amine **2** (0.40 g, 0.60 mmol), dicyclohexylcarbodiimide (0.15 g, 0.83 mmol), and triethylamine (0.30 g, 0.27 mmol). The resultant solution was stirred for 12 h, filtered, and the solvent evaporated. The crude product was purified by flash chromatography (ethyl acetate) to give **3**, a NOTA derivative, as a white solid (0.26 g, 0.10 mmol, 67%). ^{1}H NMR (400 MHz, $CDCl_3$): δ 8.73 (bs, 6H), 7.71 (m, 12H), 7.61 (m, 12H), 7.23 (m, 15H), 5.56 (bs, 2H), 4.99 (m, 5H), 4.74 (m, 3H), 3.79−3.27 (m, 24H), 3.25−2.77 (m, 13H), 2.60−2.17 (m, 4H), 2.15−1.71 (m, 12H), 160 (m, 4H), 1.38 (m, 43H). ^{13}C NMR (100 MHz, $CDCl_3$): δ 172.5, 168.3, 156.8, 136.5, 134.1, 133.9, 131.8, 128.4, 127.9, 123.3, 123.2, 79.0, 69.8, 66.5, 64.8, 49.3, 45.9, 44.3, 40.5, 35.5, 35.3, 325, 32.2, 29.3, 28.3, 27.9, 26.8, 22.6. MS (MALDI) *m/z* calcd for $C_{141}H_{168}N_{18}O_{30}$: 2594.2; found: 2595.9 ($[M + H]^+$).

Compound ***4***. To a solution of **3** (0.26 g, 0.11 mmol) in ethanol (1.0 mL) was added hydrazine monohydrate (0.1 mL, 2.0 mM) and the mixture was stirred for 12 h at room temperature. After the reaction, the precipitate was removed by filtration. The filtrate was evaporated and extracted with CH_2Cl_2 (3 × 10 mL). The combined organic layers were evaporated to give **4** as light yellow oil (0.15 g, 0.08 mmol, 80%). This compound was used for the next step without further purification. ^1H NMR (400 MHz, CD_3OD): δ 7.31 (s, 15H), 4.99 (m, 6H), 4.66 (m, 3H), 3.68−3.39 (m, 10H), 3.38−3.31 (m, 6H), 3.20−2.94 (m, 17H), 2.93−2.72 (m, 9H), 2.65−2.30 (m, 7H), 1.95−1.81 (m, 6H), 1.78−1.57 (m, 6H), 1.55−1.20 (m, 44H). ^{13}C NMR (100 MHz, CD_3OD): δ 173.7, 173.1, 157.6, 136.9, 128.9, 127.3, 126.8, 126.5, 82.6, 77.3, 65.9, 64.5, 50.2, 48.8, 45.9, 44.5, 42.3, 38.5, 38.1, 36.7, 30.3, 29.1, 27.8, 26.6, 25.2. MS (MALDI) *m/z* calcd for $C_{93}H_{156}N_{18}O_{18}$: 1814.1; found: 1816.3 ($[M + H]^+$).

Compound ***6***. To a solution of **4** (0.15 g, 0.08 mmol) in DMF (1 mL) were added **5** (0.53 g, 0.80 mM), an *N*-hydroxysuccinimide ester of DOTA, and the mixture was stirred for 24 h at room temperature. The solvent was evaporated and the product purified by reverse phase HPLC using water and acetonitrile solvent mixture to give **6** as a white solid (0.29 g, 0.06 mmol, 70%). ^1H NMR (400 MHz, $CDCl_3$): δ 7.40−7.18 (s, 15H), 5.15−4.99 (m, 6H), 4.71 (m, 6H), 4.38−4.83 (m, 26H), 3.82−3.36 (m, 61H), 3.30−2.62 (m, 17H), 2.60−2.30 (m, 12H), 2.23−1.98 (m, 10H), 1.99−1.80 (m, 10H), 1.79−0.96 (m, 174H). ^{13}C NMR (100 MHz, CD_3OD): δ 172.8, 172.6, 170.8, 170.6, 157.3, 137.2, 128.2, 127.6, 127.2, 84.5, 81.5, 65.8, 64.7, 53.6, 51.6, 49.2, 48.5, 45.3, 43.6, 42.0, 40.1, 36.5, 31.9, 27.2, 28.5, 27.2, 27.1, 22.7. MS (MALDI) *m/z* calcd for $C_{261}H_{456}N_{42}O_{60}$: 5139.4; found: 5138.7 ($[M + H]^+$).

Ligand H_{21}***L***. To a solution of **6** (0.10 g, 0.02 mmol) was added 30% HBr in AcOH (2 mL) and the solution was allowed to stir for 4 h. The solvent was evaporated, and the product neutralized and purified by reverse phase HPLC using water and acetonitrile solvent mixture to give H_{21}**L** as a white solid (0.06 g, 0.02 mmol, 75%). ^1H NMR (400 MHz, CD_3OD): δ 4.42−3.62 (m, 89H), 3.59−3.32 (m, 67H), 3.24−2.85 (m, 48H), 2.80−2.30 (m, 22H), 2.34−2.03 (m, 17H), 2.06−1.85 (m, 14H), 1.88−1.65 (m, 20H), 1.65−1.39 (m, 11H), 1.31 (m, 6H). MS (MALDI) *m/z* calcd for $C_{153}H_{270}N_{42}O_{54}$: 3561.9; found: 3563.0 ($[M + H]^+$).

Compound H_{21}***L****(Mal)*$_3$. To the free ligand H_{21}**L** (0.200 g, 0.056 mmol) dissolved in DMF (1 mL) was added triethyl amine (0.022 g, 0.224 mmol) and *N*-(γ-maleimidobutyryloxy)-succinimide and the solution was allowed to stir for 24 h. The solvent was evaporated, the product neutralized and purified by reverse phase HPLC using water and acetonitrile solvent mixture to give H_{21}**L**(Mal)$_3$ as a white solid. (0.102 g, 0.052 mmol, 45.1%). MS (MALDI) *m/z* calcd for $C_{174}H_{285}N_{45}O_{63}$: 4015.0; found: 4016.3 ($[M + H]^+$).

Compound c(RGDyK)-SH. To the DMF solution (1 mL) of the commercially available integrin $\alpha_v\beta_3$ targeting peptide c(RGDyK) (0.030 g, 0.048 mmol) (Peptides International Inc., Kentucky) was added *N*-succinimidyl 3-(2-pyridyldithio)-propionate (0.020 g, 0.064 mmol) (Thermo Scientific, IL) and the solution was allowed to stir for 6 h. The solvent was evaporated, the product neutralized and purified by reverse phase HPLC using water and acetonitrile solvent mixture and lyophilized. The resultant white solid was dissolved in DMF (1.0 mL) and dithiothreitol (0.010 g, 0.065 mmol) was then added. The solution was allowed to stir for 3 h. The solvent was evaporated and the product neutralized and purified by reverse phase HPLC using water and acetonitrile solvent mixture to give c(RGDyK)-SH as a white solid (0.103 g, 0.014 mmol, 29.5%). MS (MALDI) *m/z* calcd for $C_{30}H_{45}N_9O_9S$: 707.3; found: 708.3 ($[M + H]^+$).

Compound H_{21}***L****[c(RGDyK)]*$_3$. To the malemide carrying ligand, H_{21}**L**(Mal)$_3$, (0.020 g, 0.005 mmol) dissolved in PBS (1×) was added the thiol carrying c(RGDyK)-SH (0.014 g, 0.029 mmol), and the solution was allowed to stir for 18 h. The solution was purified by reverse phase HPLC using water and acetonitrile solvent mixture to give H_{21}**L**[c(RGDyK)]$_3$ as a white solid. (0.010 g, 0.002 mmol, 33.3%). MS (MALDI) *m/z* calcd for $C_{264}H_{420}N_{72}O_{90}S_3$: 6136.9; found: 6139.1 ($[M + H]^+$).

Compound c(RGDyK)PEG$_{12}$*SH*. To the DMF solution (1 mL) of the integrin $\alpha_v\beta_3$ targeting peptide c(RGDyK) (0.040 g, 0.064 mmol) (Peptides International Inc., Kentucky) dissolved in DMF (1.0 mL) was added *N*-2-pyridyldithiol-tetraoxaoctatriacontane-*N*-hydroxysuccinimide (0.060 g, 0.065 mmol) (Thermo Scientific, IL) and the solution was allowed to stir for 6 h. The solvent was evaporated and the product neutralized and purified by reverse phase HPLC using water and acetonitrile solvent mixture and lyophilized. The resultant white solid was dissolved in DMF (1 mL) and dithiothreitol (0.010 g, 0.065 mmol) was then added and the solution was allowed to stir for 3 h. The solvent was evaporated and the product neutralized and purified by reverse phase HPLC using water and acetonitrile solvent mixture to give c(RGDyK)-PEG$_{12}$SH as a colorless viscous liquid. (0.025 g, 0.019 mmol, 30.2%). MS (MALDI) *m/z* calcd for $C_{57}H_{98}N_{10}O_{22}S$: 1306.6; found: 1307.5 ($[M + H]^+$).

Compound H_{21}***L****[PEG*$_{12}$*c(RGDyK)]*$_3$. To the malemide carrying ligand, H_{21}**L**(Mal)$_3$ (0.030 g, 0.007 mmol), dissolved in PBS (1×) was added the thiol carrying peptide c(RGDyK)-SH (0.038 g, 0.028 mmol) and the solution was allowed to stir for 18 h. The solution was purified by reverse phase HPLC using water and acetonitrile solvent mixture to give H_{21}**L**[PEG$_{12}$c(RGDyK)]$_3$ as a white solid (0.019 g, 0.002 mmol, 35.3%). MS (MALDI) *m/z* calcd for $C_{345}H_{579}N_{75}O_{129}S_3$: 7936.0; found: 7936.7 ($[M + H]^+$).

Compound Gd$_7$***L***. The free ligand H_{21}**L** (0.060 g, 0.013 mmol) was dissolved in water (1 mL) and the pH was adjusted to 7.0 with NaOH (0.1 M). To this solution was added an excess amount of $GdCl_3 \cdot 6H_2O$ and the pH was readjusted to 6.5 and allowed to stir at room temperature overnight. The pH of the resultant solution was raised above 8 using 1 M aqueous NaOH, causing the excess Gd^{3+} to precipitate as $Gd(OH)_3$. The solution was filtered and the pH was readjusted to 7.0 using 1 N HCl. The solution was purified using HPLC and the fractions pooled together and lyophilized to give a white solid (0.051 g, 0.011 mmol, 84.6%). MS (MALDI) *m/z* calcd for $C_{153}H_{261}Gd_7N_{42}O_{60}$: 4644.2; found: 4645.1 ($[M + H]^+$).

Compound Gd$_6$*H*$_3$***L***. To the solution of Gd$_7$**L** (0.05 g, 0.011 mmol), DTPA (0.1 mM, 1 mL) was added. The solution was stirred at room temperature for 2 h and then purified using HPLC. The desired fractions were pooled together and lyophilized to give Gd$_6$H$_3$**L** as a white solid (0.04 g, 0.01 mmol, 81%). MS (MALDI) *m/z* calcd for $C_{153}H_{264}Gd_6N_{42}O_{60}$: 4489.3; found: 4634.9 ($[M + K+ 6H_2O]^+$).

Compound Eu$_6$*H*$_3$***L***. The free ligand H_{21}**L** (0.030 g, 0.008 mmol) was dissolved in water (1 mL) and the pH was adjusted to 7.0 with NaOH (0.1 M). To this solution was added an excess amount of $EuCl_3 \cdot 6H_2O$ and the pH was readjusted to 6.5 and allowed to stir at room temperature overnight. The pH was raised above 8.0 using 1.0 N aqueous NaOH, which caused the excess Eu^{3+} to precipitate as $Eu(OH)_3$. The solution was filtered and the pH was readjusted to 7.0 using 1.0 N HCl. To the resulting solution, DTPA (0.1 mM, 1 mL) was added and the solution was purified using HPLC to give the desired complex. The desired fractions were pooled together and lyophilized to give Eu_6**L**H_3 as a white solid. (0.042 g, 0.009 mmol, 54%). MS (MALDI) *m*/*z* calcd for $C_{153}H_{252}Eu_6N_{42}O_{54}$: 4453.4; found: 4454.5 ($[M + H]^+$).

*Compound Cold Gd_6**L**Ga.* The gadolinium complex, Gd_6H_3**L** (0.001 g, 0.225 μmol), was dissolved in a solution of 4-(2-hydroxyethyl)-1-piperazineethanesulfonic acid (HEPES, pH = 6.5, 1.0 M, 1.0 mL). To the resulting solution was added a solution of $GaCl_3$ (0.0001 g, 0.567 μmol) in 0.6 N HCl (0.3 mL) and the resulting solution was stirred for 1 h. To the mixture was added 500 μL of 5.0 mM ethylendiaminetetraacetic acid (EDTA) and the mixture was stirred for another 5 min at room temperature (EDTA was used to remove nonspecifically bound or free $GaCl_3$ from the complex). The purification of the bimetallic complex was carried out by passing the mixture through a preconditioned Sep-Pak C-18 heavy cartridge. After thorough rinsing (3 × 5 mL, water) of the cartridge, the bimetallic complex, Gd_6**L**Ga, was eluted by an ethanol−water mixture (70:30). The product was purified with HPLC and characterized by mass spec. MS (MALDI) *m*/*z* calcd for $C_{153}H_{264}GaGd_6N_{42}O_{60}$: 4555.28; found: 4556.9 ($[M + H]^+$).

*Compound Gd_6**L**^{68}Ga.* To a 1.5 mL eppendorf tube containing 30 μg Gd_6H_3**L** complex in 1.0 mL of HEPES (pH = 6.5) solution was added a solution of 8.0 mCi of $^{68}GaCl_3$ in 0.6 N HCl. The reaction mixture was incubated at 75 °C for 0.5 h on a shaker. To this solution was added DTPA (5.0 mM, 5.0 μL) and the reaction mixture was stirred for 5 min at room temperature (DTPA was used to remove nonspecifically bound or free ^{68}Ga from Gd_6**L**^{68}Ga). The Gd_6**L**^{68}Ga complex was purified by passing the mixture through a preconditioned Sep-Pak C-18 light cartridge. After thorough rinsing (3 × 3 mL, water) of the cartridge, Gd_6**L**^{68}Ga was eluted by an ethanol−water mixture (70:30) to give 3.6 mCi of labeled compound. The product was first analyzed by a Rita Star Radioisotope TLC Analyzer (Straubenhardt, Germany) on instant thin-layer chromatography (ITLC-SG) plates (Pall Life Sciences, East Hills, NY) and then by radio-HPLC to determine the radiochemical purity of the product. The compound was determined to have more than 95% purity.

*Compound Gd_6**L**^{67}Ga.* To a 1.5 mL eppendorf tube containing 30 μg Gd_6H_3**L** complex in 1.0 mL of HEPES (pH = 6.5) solution was added a solution of 4.0 mCi of $^{67}GaCl_3$ in 0.6 N HCl. The reaction mixture was shaken and incubated at 75 °C for 0.5 h. To this solution was added DTPA (5.0 mM, 5.0 μL) and the reaction mixture was incubated for 5 min at room temperature. The Gd_6**L**^{67}Ga complex was purified by passing the mixture through a preconditioned Sep-Pak C-18 light cartridge. After thorough rinsing (3 × 3 mL, water) of the cartridge, Gd_6**L**^{67}Ga was eluted by an ethanol−water mixture (70:30) to give 2.1 mCi of the labeled compound. The product was first analyzed by a TLC Analyzer on ITLC-SG plates and then by radio-HPLC to determine the radiochemical purity of the product. The compound was determined to have more than 95% purity.

*Compound Gd_6H_3**L**[c(RGDyK)]$_3$.* The c(RGDyK) modified ligand H_{21}**L**[c(RGDyK)]$_3$ (0.010 g, 0.002 mmol) was dissolved in water (1 mL) and the pH was adjusted to 7 with NaOH (0.1 M). To this solution was added an excess of $GdCl_3 \cdot 6H_2O$ and the pH was again adjusted to 6.5 and allowed to stir at room temperature overnight. The pH was raised above 8.0 using 1.0 N aqueous NaOH, which caused the excess Gd^{3+} to precipitate as $Gd(OH)_3$. The solution was filtered and the pH was readjusted to 7.0 using 1.0 N HCl. To the resulting solution, DTPA (0.1 mM, 1 mL) was added and the solution was purified using HPLC to give the desired complex. The desired fractions were pooled together and lyophilized to give Gd_6H_3**L**[c(RGDyK)]$_3$ as a white solid. (0.005 g, 0.001 mmol, 48%). MS (MALDI) *m*/*z* calcd for $C_{264}H_{402}Gd_6N_{72}O_90S_3$: 7064.4; found: 7085.0 ($[M + Na]^+$).

*Compound Gd_6**L**[c(RGDyK)]$_3$^{68}Ga.* To a 1.5 mL eppendorf tube containing 80 μg Gd_6H_3**L**[c(RGDyK)]$_3$ complex in 1 mL of HEPES (pH = 6.5) solution was added a solution of 15.0 mCi of $^{68}GaCl_3$ in 0.6 N HCl. The reaction mixture was incubated at 75 °C for 0.5 h on a shaker. To this solution was added DTPA (5.0 mM, 5.0 μL) and the reaction mixture was incubated for 5 min at room temperature. The ^{68}Ga-labeled conjugate, Gd_6**L**[c(RGDyK)]$_3$^{68}Ga, was purified by passing the mixture through a preconditioned Sep-Pak C-18 light cartridge. After thorough rinsing (3 × 5 mL, water) of the cartridge, Gd_6**L**[c(RGDyK)]$_3$^{68}Ga was eluted by an ethanol−water mixture (70:30) to give 9.0 mCi of the labeled compound. The product was analyzed by radio-HPLC to determine the radiochemical purity of the product. The radiochemical purity of the compound was determined to be higher than 95%.

*Compound Gd_6H_3**L**[PEG$_{12}$c(RGDyK)]$_3$.* The c(RGDyK) modified ligand H_{21}**L**[PEG$_{12}$c(RGDyK)]$_3$ (0.019 g, 0.002 mmol) was dissolved in water (1.0 mL) and the pH was adjusted to 7.0 with NaOH (0.1 M). To this solution was added an excess of $GdCl_3 \cdot 6H_2O$ and the pH was again adjusted to 6.5 and allowed to stir at room temperature overnight. The pH was raised above 8.0 using 1.0 N aqueous NaOH, which caused the excess Gd^{3+} to precipitate as $Gd(OH)_3$. The solution was filtered and the pH was readjusted to 7.0 using 1.0 N HCl. To the resulting solution DTPA (0.1 mM, 1.0 mL) was added and the solution was purified using HPLC to give the desired complex. The desired fractions were pooled together and lyophilized to give Gd_6H_3**L**[PEG$_{12}$c(RGDyK)]$_3$ as a white solid. (0.006 g, 0.001 mmol, 51%). MS (MALDI) *m*/*z* calcd for $C_{345}H_{561}Gd_6N_{75}O_{129}S_3$: 8864.3; found: 8864.7 ($[M + H]^+$).

*Compound Gd_6**L**[PEG$_{12}$c(RGDyK)]$_3$Ga.* The gadolinium complex, Gd_6H_3**L**[PEG$_{12}$c(RGDyK)]$_3$ (0.001 g, 0.112 μmol), was dissolved in an HEPES solution (pH = 6.5, 1.0 M, 1.0 mL). To the resulting solution was added a solution of $GaCl_3$ (0.001 g, 0.567 μmol) in 0.6 N HCl (0.3 mL) and the resulting solution was stirred for 1 h. To the mixture was added 500 μL of 5.0 mM of EDTA, and the mixture was allowed to incubate for another 5 min at room temperature (EDTA was used to remove nonspecifically bound or free $GaCl_3$). The purification of Gd_6**L**[PEG$_{12}$c(RGDyK)]$_3$Ga was carried out by passing the mixture through a preconditioned Sep-Pak C-18 heavy cartridge. After thorough rinsing (3 × 5 mL, water) of the cartridge, Gd_6**L**[PEG$_{12}$c(RGDyK)]$_3$Ga was eluted by an ethanol−water mixture (70:30). The product was characterized by mass spec. MS (MALDI) *m*/*z* calcd for $C_{345}H_{558}GaGd_6N_{75}O_{129}S_3$: 8930.9; found: 8954.8 ($[M + Na]^+$).

*Compound Gd_6**L**[PEG$_{12}$c(RGDyK)]$_3$^{68}Ga.* For PET/MR imaging, a slightly different labeling procedure was followed. To a 1.5 mL eppendorf tube containing 6.0 mg of Gd_6H_3**L**[PEG$_{12}$c(RGDyK)]$_3$ complex in 1.0 mL of HEPES (pH = 6.5) solution was added a solution of 300 μCi of $^{68}\mathrm{GaCl_3}$ in 0.6 N HCl. The reaction mixture was incubated at 75 °C for 10 min on a shaker. To this solution was added DTPA (5.0 mM, 5.0 μL) and the reaction mixture was incubated for 1 min at room temperature. The ^{68}Ga-labeled conjugate was purified by passing the mixture through a preconditioned Sep-Pak C-18 plus cartridge. After thorough rinsing (3 × 5 mL, water) of the cartridge, $\mathrm{Gd_6}\mathbf{L}[\mathrm{PEG_{12}c(RGDyK)}]_3{}^{68}\mathrm{Ga}$ was eluted by an ethanol−water mixture (70:30) to give 180−200 μCi of the labeled compound. The product was analyzed by radio-HPLC to determine the radiochemical purity of the product. The radiochemical purity of the compound was determined to be higher than 95%.

Biodistribution and Pharmacokinetics Studies of $\mathrm{Gd_6}\mathbf{L}^{67}\mathrm{Ga}$. Male BALB/C mice were injected with 300 μCi of $\mathrm{Gd_6}\mathbf{L}^{67}\mathrm{Ga}$ complex to evaluate the tissue distribution of the tracer in mice. Mice were sacrificed 1, 4, and 24 h post injection (p.i.). The organs of interest (blood, heart, lung, liver, spleen, kidney, stomach, muscle, fat, small intestine, large intestine, and brain) were harvested and weighed, and radioactivity was quantified using a γ-counter. Standards were prepared and counted along with the tissue samples to calculate the percentage-injected dose per gram (%ID/g). To determine the pharmacokinetic parameters, mice injected with the tracer were blood sampled from the retro-orbital sinus at 2, 5, 10, and 30 min, and 1, 2, 24, and 48 h p.i. and quantified using a γ-counter. The pharmacokinetic parameters were calculated based on a two-compartment open model.

In Vitro and Ex Vivo Stability of $\mathrm{Gd_6}\mathbf{L}^{67}\mathrm{Ga}$. The in vitro stability test was performed in rat serum. Briefly, $\mathrm{Gd_6}\mathbf{L}^{67}\mathrm{Ga}$ complex (100 μCi, 5 μL) was added into 100 μL of rat serum (n = 3). The solution was incubated for 1, 4, 24, and 48 h at 37 °C, respectively. The solution was vortexed and centrifuged for 5 min at the speed of 21 000 g. The supernatant was then analyzed by HPLC. For the in vivo stability evaluation, each male mouse was injected with 600 μCi of $\mathrm{Gd_6}\mathbf{L}^{67}\mathrm{Ga}$ complex in 100 μL of saline via the tail vein. The urine samples were collected at 1, 4, 24, and 48 h p.i. and then analyzed by HPLC.

Integrin $\alpha_v\beta_3$ Receptor-Binding Assay. The integrin $\alpha_v\beta_3$ binding affinities of c(RGDyK), $\mathrm{Gd_6H_3}\mathbf{L}[\mathrm{c(RGDyK)}]_3$, and $\mathrm{Gd_6H_3}\mathbf{L}[\mathrm{PEG_{12}c(RGDyK)}]_3$ were determined by a competitive cell-binding assay using ^{125}I-echistatin (PerkinElmer) as the $\alpha_v\beta_3$-specific radioligand. The experiments were performed on U87MG human glioblastoma cells following a previously reported method.[52] Briefly, U87MG cells were grown in RPMI 1640 medium supplemented with penicillin, streptomycin, and 10% (v/v) fetal bovine serum (FBS) at 37 °C under 5% $\mathrm{CO_2}$. Suspended U87MG cells in the binding buffer (20 mM Tris, pH 7.4, 150 mM NaCl, 2.0 mM $\mathrm{CaCl_2}$, 1.0 mM $\mathrm{MgCl_2}$, 1.0 mM $\mathrm{MnCl_2}$, 0.1% bovine serum albumin) were seeded on multiwell DV plates (Millipore) with 5×10^4 cells per well and then incubated with ^{125}I-echistatin (10 000 cpm/well) in the presence of increasing concentrations (0−5000 nM) of each c(RGDyK) peptide conjugate for 2 h. The final volume in each well was maintained at 200 μL. At the end of incubation, unbound ^{125}I-echistatin was removed by filtration followed by three rinses with cold binding buffer. The retentate was collected and the radioactivity was measured using a γ-counter. The best-fit $\mathrm{IC_{50}}$ values (inhibitory concentration where 50% of the ^{125}I-echistatin bound on U87MG cells are displaced) of c(RGDyK), $\mathrm{Gd_6H_3}\mathbf{L}[\mathrm{c(RGDyK)}]_3$, and $\mathrm{Gd_6H_3}\mathbf{L}[\mathrm{PEG_{12}c(RGDyK)}]_3$ were calculated by fitting the data with nonlinear regression using GraphPad Prism (GraphPadSoftware, Inc.). Experiments were repeated with quintuplicate samples.

Relaxivity Measurements at 0.5 T (T). The T_1 values were recorded at 23 MHz (0.5 T) at 25 °C by using a Maran Ultra relaxometer (Oxford Instruments, UK). Longitudinal relaxation times were measured by using the inversion−recovery pulse sequence (180°-t-90°). The T_1 relaxivities were determined by the linear regression analysis of the water proton relaxation rates in solutions ranging in concentration from 0.005 to 12.0 mM, in Millipore water in triplicate.

MRI Imaging and Relaxivity Measurements at 1.0 T. The T_1-weighted MR images of samples in 0.5 mL microfuge tubes were collected using Aspect Imaging M2TM 1.0 T (43.5−45 MHz, 60 mm diameter volume coil) Gradient Echo Spoiled External Averaging (GRE-EXT) sequence. For imaging, the following parameters were used: TR = 14.2 ms; effective echo time (TE) = 2.8 ms; FOV 64 × 100 mm2, data matrix = 256 × 256, averaging = 4, slice = 1 mm. The T_1-maps of the samples at 1.0 T were determined from a series of multi-T_1 (0.01 ms to 5 s) inversion recovery spin echo sequence (IR-SE with minimum TE = 7.0 ms); TR = 10 s; FOV = 64 × 100 mm^2; matrix = 128 × 128; averaging = 1, steady state scans = 10), fitted and calculated using Matlab code. All the fits for T_1 values used to calculate the longitudinal relaxivity, r_1, had fitting coefficients, $R^2 \geq 0.99$. Three trials were performed. The Gd and Ga metal concentrations of samples were determined by inductively coupled plasma mass spectrometry (ICP-MS).

PET/MR Imaging Using $\mathrm{Gd_6}\mathbf{L}[\mathrm{PEG_{12}c(RGDyK)}]_3{}^{68}\mathrm{Ga}$. The MR and PET imaging studies were performed on a 1.0 T MR scanner (Aspect Imaging, Shoham, Israel) using a 35 mm mouse body coil, and a Siemens Inveon Multimodality PET/CT system (Siemens Medical Solutions Inc., Knoxville, TN, USA), respectively. Ten minutes prior to imaging, the animals were anesthetized using 3% isofluorane at room temperature until stable vitals were established. Once the animals were sedated, they were placed onto a custom-made interchangeable bed between the MR and PET scanners under 2% isofluorane anesthesia for the duration of the imaging. A T_1-weighted gradient echo, spoiled sequence (echo time/repetition time [TE/TR] 3/15 ms; field of view [FOV] 80 × 100 mm; slice thickness 0.8 mm; matrix 256 × 256; number of excitations [NEX] = 3; flip angle = 25°) was performed for each mouse. Each mouse was injected with 100−150 μCi (Gd: ca. 0.027 mmol/kg) via the tail-vein. MR scans were obtained precontrast and 1 h after contrast medium injection.

PET imaging was acquired with the mouse mounted on the interchangeable bed directly following the MR acquisition. A 15 min PET static scan was performed and reconstructed using Fourier rebinning and ordered subsets expectation maximization 3D (OSEM3D) algorithm. Reconstructed MR and PET images were fused and analyzed using the VivoQuant software (Invicro LLC, Boston, USA). For quantification, regions of interest were placed on the tumor and muscle. The latter was used for normalization. The resulting quantitative data were expressed in intensity and %ID/g for MR and PET images.

■ ASSOCIATED CONTENT

Ⓢ Supporting Information

Supporting schemes, synthesis of compounds, ICP quantification. This material is available free of charge via the Internet at http://pubs.acs.org.

AUTHOR INFORMATION

Corresponding Author

*E-mail: Xiankai.Sun@UTSouthwestern.edu.

Author Contributions

The manuscript was written through contributions of all authors. All authors have given approval to the final version of the manuscript.

Funding

This work was partially supported by the Prostate Cancer Research Program of the United States Army Medical Research and Materiel Command (W81XWH-12−1−0336), the Dr. Jack Krohmer Professorship Funds, and the National Institutes of Health (CA115531 and EB0158908).

Notes

The authors declare no competing financial interest.

REFERENCES

(1) Weissleder, R. (2006) Molecular imaging in cancer. *Science 312*, 1168−1171.

(2) Cheon, J., and Lee, J.-H. (2008) Synergistically integrated nanoparticles as multimodal probes for nanobiotechnology. *Acc. Chem. Res. 41*, 1630−1640.

(3) Jennings, L. E., and Long, N. J. (2009) 'Two is better than one'-probes for dual-modality molecular imaging. *Chem. Commun. 28*, 3511−3524.

(4) Ntziachristos, V., Yodh, A. G., Schnall, M., and Chance, B. (2000) Concurrent MRI and diffuse optical tomography of breast after indocyanine green enhancement. *Proc. Natl. Acad. Sci. U.S.A. 97*, 2767−2772.

(5) Beyer, T., Townsend, D. W., Brun, T., Kinahan, P. E., Charron, M., Roddy, R., Jerin, J., Young, J., Byars, L., and Nutt, R. (2000) A combined PET/CT scanner for clinical oncology. *J. Nucl. Med. 41*, 1369−1379.

(6) Murray, C. B., Norris, D. J., and Bawendi, M. G. (1993) Synthesis and characterization of nearly monodisperse CdE (E = sulfur, selenium, tellurium) semiconductor nanocrystallites. *J. Am. Chem. Soc. 115*, 8706−8715.

(7) Link, S., and El-Sayed, M. A. (1999) Spectral properties and relaxation dynamics of surface plasmon electronic oscillations in gold and silver nanodots and nanorods. *J. Phys. Chem. B 103*, 8410−8426.

(8) Alivisatos, A. P. (1996) Semiconductor clusters, nanocrystals, and quantum dots. *Science 271*, 933−937.

(9) Catana, C., Wu, Y., Judenhofer, M. S., Qi, J., Pichler, B. J., and Cherry, S. R. (2006) Simultaneous acquisition of multislice PET and MR images: initial results with a MR-compatible PET scanner. *J. Nucl. Med. 47*, 1968−1976.

(10) Cherry, S. R. (2006) The 2006 Henry N. Wagner lecture: of mice and men (and positrons)–advances in PET imaging technology. *J. Nucl. Med. 47*, 1735−1745.

(11) Cherry, S. (2001) Fundamentals of positron emission tomography and applications in preclinical drug development. *J. Clin. Pharmacol. 41*, 482−491.

(12) Caravan, P., Ellison, J. J., McMurry, T. J., and Lauffer, R. B. (1999) Gadolinium(III) chelates as MRI contrast agents: structure, dynamics, and applications. *Chem. Rev. 99*, 2293−2352.

(13) Raymond, K. N., and Pierre, V. r. C. (2004) Next generation, high relaxivity gadolinium MRI agents. *Bioconjugate Chem. 16*, 3−8.

(14) Seo, W. S., Lee, J. H., Sun, X., Suzuki, Y., Mann, D., Liu, Z., Terashima, M., Yang, P. C., McConnell, M. V., Nishimura, D. G., et al. (2006) FeCo/graphitic-shell nanocrystals as advanced magnetic-resonance-imaging and near-infrared agents. *Nat. Mater. 5*, 971−976.

(15) Morawski, A. M., Winter, P. M., Crowder, K. C., Caruthers, S. D., Fuhrhop, R. W., Scott, M. J., Robertson, J. D., Abendschein, D. R., Lanza, G. M., and Wickline, S. A. (2004) Targeted nanoparticles for quantitative imaging of sparse molecular epitopes with MRI. *Magn. Reson. Med. 51*, 480−486.

(16) Santra, S., Bagwe, R. P., Dutta, D., Stanley, J. T., Walter, G. A., Tan, W., Moudgil, B. M., and Mericle, R. A. (2005) Synthesis and characterization of fluorescent, radio-opaque, and paramagnetic silica nanoparticles for multimodal bioimaging applications. *Adv. Mater. 17*, 2165−2169.

(17) Cheng, Z., and Tsourkas, A. (2008) Paramagnetic porous polymersomes. *Langmuir 24*, 8169−8173.

(18) Cheng, L., Yang, K., Li, Y., Chen, J., Wang, C., Shao, M., Lee, S.-T., and Liu, Z. (2011) Facile preparation of multifunctional upconversion nanoprobes for multimodal imaging and dual-targeted photothermal therapy. *Angew. Chem., Int. Ed. 123*, 7523−7528.

(19) Chen, J., Wiley, B., Li, Z. Y., Campbell, D., Saeki, F., Cang, H., Au, L., Lee, J., Li, X., and Xia, Y. (2005) Gold nanocages: engineering their structure for biomedical applications. *Adv. Mater. 17*, 2255−2261.

(20) Gao, X., Cui, Y., Levenson, R. M., Chung, L. W. K., and Nie, S. (2004) In vivo cancer targeting and imaging with semiconductor quantum dots. *Nat. Biotechnol. 22*, 969−976.

(21) Lin, Y.-S., Hung, Y., Su, J.-K., Lee, R., Chang, C., Lin, M.-L., and Mou, C.-Y. (2004) Gadolinium(III)-incorporated nanosized mesoporous silica as potential magnetic resonance imaging contrast agents. *J. Phys. Chem. B 108*, 15608−15611.

(22) Rieter, W. J., Kim, J. S., Taylor, K. M. L., An, H., Lin, W., Tarrant, T., and Lin, W. (2007) Hybrid silica nanoparticles for multimodal imaging. *Angew. Chem., Int. Ed. 119*, 3754−3756.

(23) Hak, S., Sanders, H. M. H. F., Agrawal, P., Langereis, S., Grüll, H., Keizer, H. M., Arena, F., Terreno, E., Strijkers, G. J., and Nicolay, K. (2009) A high relaxivity Gd(III)DOTA-DSPE-based liposomal contrast agent for magnetic resonance imaging. *Eur. J. Pharm. Biopharm. 72*, 397−404.

(24) Terreno, E., Delli Castelli, D., Cabella, C., Dastrù, W., Sanino, A., Stancanello, J., Tei, L., and Aime, S. (2008) Paramagnetic liposomes as innovative contrast agents for magnetic resonance (MR) molecular imaging applications. *Chem. Biodivers. 5*, 1901−1912.

(25) Unger, E. C., MacDougall, P., Cullis, P., and Tilcock, C. (1989) Liposomal Gd-DTPA: Effect of encapsulation on enhancement of hepatoma model by MRI. *Magn. Reson. Imaging 7*, 417−423.

(26) Boswell, C. A., Eck, P. K., Regino, C. A. S., Bernardo, M., Wong, K. J., Milenic, D. E., Choyke, P. L., and Brechbiel, M. W. (2008) Synthesis, characterization, and biological evaluation of integrin $\alpha_v\beta_3$-targeted PAMAM dendrimers. *Mol. Pharmaceutics 5*, 527−539.

(27) Kobayashi, H., and Brechbiel, M. W. (2005) Nano-sized MRI contrast agents with dendrimer cores. *Adv. Drug Delivery Rev. 57*, 2271−2286.

(28) Langereis, S., de Lussanet, Q. G., van Genderen, M. H. P., Meijer, E. W., Beets-Tan, R. G. H., Griffioen, A. W., van Engelshoven, J. M. A., and Backes, W. H. (2006) Evaluation of Gd(III)DTPA-terminated poly(propylene imine) dendrimers as contrast agents for MR imaging. *NMR Biomed. 19*, 133−141.

(29) Langereis, S., Dirksen, A., Hackeng, T. M., van Genderen, M. H. P., and Meijer, E. W. (2007) Dendrimers and magnetic resonance imaging. *New J. Chem. 31*, 1152−1160.

(30) Rudovský, J., Botta, M., Hermann, P., Hardcastle, K. I., Lukeš, I., and Aime, S. (2006) PAMAM dendrimeric conjugates with a Gd−DOTA phosphinate derivative and their adducts with polyaminoacids: the interplay of global motion, internal rotation, and fast water exchange. *Bioconjugate Chem. 17*, 975−987.

(31) Bolskar, R. D. (2008) Gadofullerene MRI contrast agents. *Nanomedicine 3*, 201−213.

(32) Zhu, W., Okollie, B., Bhujwalla, Z. M., and Artemov, D. (2008) PAMAM dendrimer-based contrast agents for MR imaging of Her-2/neu receptors by a three-step pretargeting approach. *Magn. Reson. Med. 59*, 679−685.

(33) Duarte, M. G., Gil, M. H., Peters, J. A., Colet, J. M., Elst, L. V., Muller, R. N., and Geraldes, C. F. G. C. (2001) Synthesis, characterization, and relaxivity of two linear Gd(DTPA)−polymer conjugates. *Bioconjugate Chem. 12*, 170−177.

(34) Brasch, R. C. (1991) Rationale and applications for macromolecular Gd-based contrast agents. *Magn. Reson. Med. 22*, 282−287.

(35) Kobayashi, H., Kawamoto, S., Saga, T., Sato, N., Hiraga, A., Ishimori, T., Akita, Y., Mamede, M. H., Konishi, J., Togashi, K., et al. (2001) Novel liver macromolecular MR contrast agent with a polypropylenimine diaminobutyl dendrimer core: Comparison to the vascular MR contrast agent with the polyamidoamine dendrimer core. *Magn. Reson. Med. 46*, 795−802.

(36) Kobayashi, H., Kawamoto, S., Jo, S. K., Sato, N., Saga, T., Hiraga, A., Konishi, J., Hu, S., Togashi, K., Brechbiel, M. W., et al. (2002) Renal tubular damage detected by dynamic micro-MRI with a dendrimer-based magnetic resonance contrast agent. *Kidney Int. 61*, 1980−1985.

(37) Sugaya, M., Watanabe, T., Yang, A., Starost, M. F., Kobayashi, H., Atkins, A. M., Borris, D. L., Hanan, E. A., Schimel, D., Bryant, M. A., et al. (2005) Lymphatic dysfunction in transgenic mice expressing KSHV k-cyclin under the control of the VEGFR-3 promoter. *Blood 105*, 2356−2363.

(38) Wiener, E. C., Konda, S., Shadron, A., Brechbiel, M., and Gansow, O. (1997) Targeting dendrimer-chelates to tumors and tumor cells expressing the high-affinity folate receptor. *Invest. Radiol. 32*, 748−754.

(39) Kobayashi, H., and Brechbiel, M. W. (2003) Dendrimer-based macromolecular MRI contrast agents: characteristics and application. *Mol. Imaging 2*, 1−10.

(40) Venditto, V. J., Regino, C. A. S., and Brechbiel, M. W. (2005) PAMAM dendrimer based macromolecules as improved contrast agents. *Mol. Pharmaceutics 2*, 302−311.

(41) Kumar, K., Chang, C. A., Francesconi, L. C., Dischino, D. D., Malley, M. F., Gougoutas, J. Z., and Tweedle, M. F. (1994) Synthesis, stability, and structure of gadolinium(III) and yttrium(III) macrocyclic poly(amino carboxylates). *Inorg. Chem. 33*, 3567−3575.

(42) Reichert, D. E., Hancock, R. D., and Welch, M. J. (1996) Molecular mechanics investigation of gadolinium(III) complexes. *Inorg. Chem. 35*, 7013−7020.

(43) Dong, Q., Hurst, D. R., Weinmann, H. J., Chenevert, T. L., Londy, F. J., and Prince, M. R. (1998) Magnetic resonance angiography with gadomer-17: an animal study. *Invest. Radiol. 33*, 699−708.

(44) Nicolle, G. M., Tóth, É., Schmitt-Willich, H., Radüchel, B., and Merbach, A. E. (2002) The impact of rigidity and water exchange on the relaxivity of a dendritic MRI contrast agent. *Chem.—Eur. J. 8*, 1040−1048.

(45) Behr, T. M., Goldenberg, D. M., and Becker, W. (1998) Reducing the renal uptake of radiolabeled antibody fragments and peptides for diagnosis and therapy: present status, future prospects and limitations. *Eur. J. Nucl. Med. 25*, 201−212.

(46) Ma, H. L., Xu, Y. F., Qi, X. R., Maitani, Y., and Nagai, T. (2008) Superparamagnetic iron oxide nanoparticles stabilized by alginate: Pharmacokinetics, tissue distribution, and applications in detecting liver cancers. *Int. J. Pharm. 354*, 217−226.

(47) Lux, F., Mignot, A., Mowat, P., Louis, C., Dufort, S., Bernhard, C., Denat, F., Boschetti, F., Brunet, C., Antoine, R., et al. (2011) Ultrasmall rigid particles as multimodal probes for medical applications. *Angew. Chem., Int. Ed. 123*, 12507−12511.

(48) Iznaga-Escobar, N., Arocha, L. A. T., Morales, A. M., Suzarte, M. R., Mesa, N. R., and Rodríguez, R. P. (1998) Technetium-99m-antiepidermal growth factor-receptor antibody in patients with tumors of epithelial origin: part II. pharmacokinetics and clearances. *J. Nucl. Med. 39*, 1918−1927.

(49) Vologdin, N., Rolla, G. A., Botta, M., and Tei, L. (2013) Orthogonal synthesis of a heterodimeric ligand for the development of the Gd-III-Ga-III ditopic complex as a potential pH-sensitive MRI/PET probe. *Org. Biomol. Chem. 11*, 1683−1690.

(50) Notni, J., Hermann, P., Dregely, I., and Wester, H.-J. (2013) Simultaneous in vivo PET/MRI imaging with a bi-metal bimodal tracer: Towards Ga-68-labeled responsive gadolinium contrast agents. *J. Labelled Comp. Radiopharm. 56*, S62−S62.

(51) Suchy, M., Bartha, R., and Hudson, R. H. E. (2013) "Click" chemistry toward bis(DOTA-derived) heterometallic complexes: potential bimodal MRI/PET(SPECT) molecular imaging probes. *RSC Adv. 3*, 3249−3259.

(52) Liu, W., Hao, G. Y., Long, M. A., Anthony, T., Hsieh, J. T., and Sun, X. K. (2009) Imparting multivalency to a bifunctional chelator: a scaffold design for targeted PET imaging probes. *Angew. Chem., Int. Ed. 48*, 7346−7349.

Bioconjugate Chemistry

Article

pubs.acs.org/bc

Click-Chemistry Strategy for Labeling Antibodies with Copper-64 via a Cross-Bridged Tetraazamacrocyclic Chelator Scaffold

Amit Kumar,[†] Guiyang Hao,[†] Li Liu,[†] Saleh Ramezani,[†] Jer-Tsong Hsieh,[‡] Orhan K. Öz,[†] and Xiankai Sun*,[†,§]

[†]Departments of Radiology and [‡]Urology, and [§]Advanced Imaging Research Center, University of Texas Southwestern Medical Center, Dallas, Texas 75390, United States

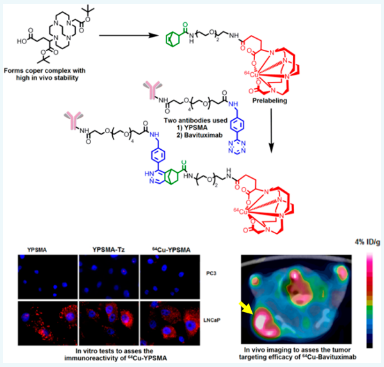

ABSTRACT: We report a click-chemistry based modular strategy for antibody labeling with ^{64}Cu ($t_{1/2}$ = 12.7 h; β^+ 0.656 MeV, 17.4%; β^- 0.573 MeV, 39%; EC 43%) under ambient condition utilizing a cross-bridged tetraazamacrocyclic (CB-TE2A) analogue, which otherwise requires harsh conditions that make the CB-TE2A analogues underutilized for protein labeling despite the fact that they form kinetically inert copper complexes with high in vivo stability. Our strategy involves prelabeling a CB-TE2A based scaffold (CB-TE2A-1C) with ^{64}Cu and its subsequent reaction with an antibody via the tetrazine-norbornene mediated click chemistry. The effectiveness of this strategy was demonstrated by labeling two monoclonal antibodies, an anti-PSMA antibody (YPSMA-1) and a chimeric anti-phosphatidylserine antibody (Bavituximab). The immunoreactivity of the antibodies remained unchanged after the tetrazine modification and click-chemistry ^{64}Cu labeling. To further demonstrate the practicality of the modular ^{64}Cu labeling strategy, we tested positron emission tomography (PET) imaging of tumor with the ^{64}Cu-labeled bavituximab in a mouse xenograft model. The tumor visualization and uptake of the labeled antibody exhibited the versatility of the click-chemistry strategy.

■ INTRODUCTION

Copper-64 ($t_{1/2}$ = 12.7 h; β^+ 0.656 MeV, 17.4%; β^- 0.573 MeV, 39%; EC 43%) has been investigated for use in monoclonal antibodies (mAb) based radiopharmaceuticals[1−4] for both positron emission tomography (PET) imaging and radiotherapy.[2,5−7] The half-life of ^{64}Cu ($t_{1/2}$ = 12.7 h) enables an imaging procedure up to 48 h after administration, which accommodates the in vivo distribution and target localization of mAbs. Recently, the concept of using the same radiopharmaceutical constructs for both imaging and therapy has made ^{64}Cu an attractive radioisotope for the development of theranostic agents.[3,8]

A major step toward the development of ^{64}Cu based radiopharmaceuticals is the identification of bifunctional chelator (BFC) ligands that can stably complex ^{64}Cu^{2+} under physiological conditions.[5,9,10] Most of the currently available BFCs used for this purpose are not ideal because of their poor in vivo stability or the harsh conditions required for efficient incorporation of ^{64}Cu. One of the most widely used bifunctional chelators in radiopharmaceuticals, 1,4,7,10-tetraazacyclododecane-1,4,7,10-tetraacetic acid (DOTA), has been extensively exploited for ^{64}Cu labeling of biomolecules including antibodies and peptides (Figure 1). However, ^{64}Cu labeled DOTA bioconjugates are only moderately stable under in vivo conditions, undergoing demetalation subsequently causing high liver accumulation.[1,11−19] Copper complexes with improved stability have been reported. Hexaazamacrobicyclic cage-type ligands, based upon the sepulchrate or sarcophagine cage motifs, have been efficiently radiolabeled under mild conditions and have been shown to possess high in vivo stability (Figure 1).[4,20,21] However, the yield of antibody conjugation with these chelators is often low because of side reactions including protein cross-linking caused by the use of 1-ethyl-3-(3-(dimethylamino)propyl)carbodiimide (EDC).[22] Moreover, copper complexes of these ligands carry a net positive charge, which leads to high hepatic uptake and slow kidney clearance.[23−25] Derivatives of 1,4,7-triazacyclononane-1,4,7-triacetic acid (NOTA)[26,27] and cross-bridged 4,11-bis-

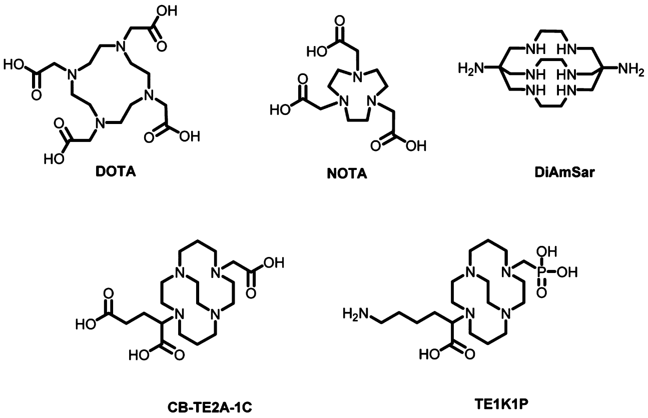

Figure 1. Bifunctional chelators for copper radiopharmaceuticals.

Received: February 17, 2015
Revised: March 7, 2015
Published: March 11, 2015

DOI: 10.1021/acs.bioconjchem.5b00102

(carboxymethyl)-1,4,8,11-tetraaza-bicyclo[6.6.2]hexadecane (CB-TE2A)[19,20] form negative or neutral complexes with Cu(II) and demonstrate high in vivo stability (Figure 1). In fact, the latter forms one of the most stable complexes with ^{64}Cu(II)[28] and the Cu(II)-CB-TE2A complex is more resistant to the reductive metal loss than any other known tetramacrocyclic complexes.[29] However, CB-TE2A and its analogues require harsh reaction conditions such as elevated temperature for ^{64}Cu labeling, which makes them unsuitable for use in antibody labeling (Figure 2). Recently, attempts have been made to develop CB-TE2A based chelators for ^{64}Cu labeling at room temperature. For instance, a CB-TE2A variant with two phosphonate arms, which could be radiolabeled with ^{64}Cu at room temperature, was communicated.[30] However, conjugation of the phosphonate group to primary amine side chains of peptides and antibodies proved challenging. Recently, a new cross-bridged cyclam chelator, CB-TE1K1P (Figure 1), which could be labeled with ^{64}Cu under mild conditions, was reported.[31] In vivo imaging of epidermal growth-factor receptor (EGFR) using the same chelator has also been reported.[32] Though TE1K1P is an excellent chelator for antibody labeling, it carries an extra negative charge under the physiological pH, which may alter the pharmacokinetics of the antibody. More recently, click chemistry via Cu(I)-catalyzed azide−alkyne cycloaddition has been used to conjugate peptides with the cross-bridged tetraazamacrocyclic chelating core for ^{64}Cu labeling.[33,34] However, the chelating core forms a positively charged Cu(II) complex, which is suboptimal for the preservation of in vivo behavior of the targeting molecules.

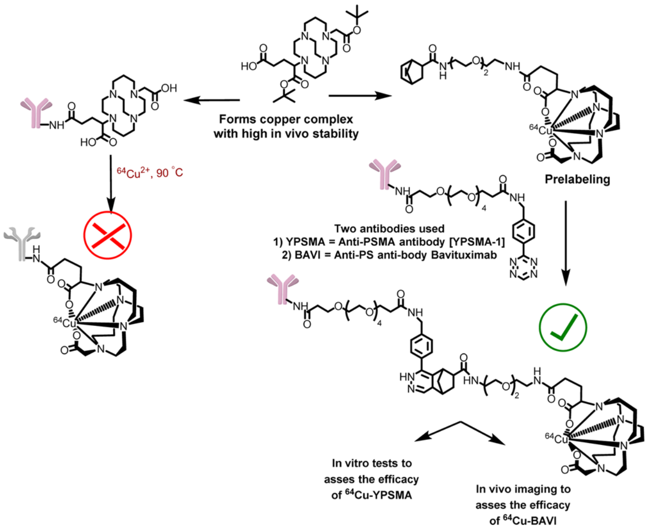

Figure 2. Click chemistry strategy for ^{64}Cu-labeling of antibodies using a cross-bridged tetraazamacrocyclic analogue (CB-TE2A-1C).

In this work, we describe a modular strategy for the construction of ^{64}Cu labeled antibodies utilizing the chemical inertness of Cu(II)-CB-TE2A-1C, a neutral moiety, without exposing antibodies to elevated temperature, thereby better preserving the immunoreactivity of the antibody (Figure 2).

■ RESULTS AND DISCUSSION

This work was to develop a modular synthetic strategy to readily label antibody conjugates with ^{64}Cu through CB-TE2A-1C under mild conditions. To achieve the goal, we employed a "copperless click reaction" variant, which involves the reaction between a tetrazine moiety and a strained alkene dienophile.[35−37] The labeling is accomplished in a two-step procedure in which a tetrazine-modified antibody is reacted with a ^{64}Cu-labeled chelator-modified strained alkene. Depicted in Scheme 1 and Figure 3, the synthetic route to the construction of radiolabeled antibodies involves four steps: (1) preparation of a stock of tetrazine-modified antibody via carbodiimide coupling followed by checking the immunoreactivity of the tetrazine modified antibody by immunohistochemistry; (2) creation of a stock of strained alkene-modified chelator via carbodiimide coupling; (3) radiolabeling of the strained alkene-modified chelator; and (4) construction of the desired radiolabeled antibody by the click reaction between the alkene and tetrazine moieties.

Scheme 1. Derivatization of Tetrazine and Norbornene with Functionalized Spacers

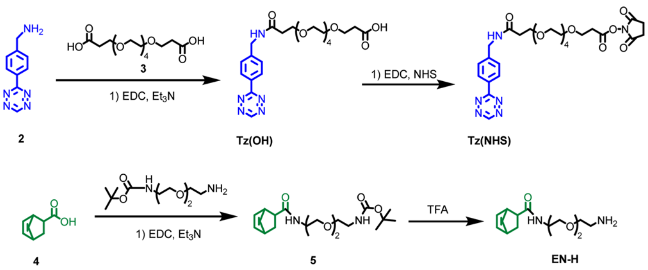

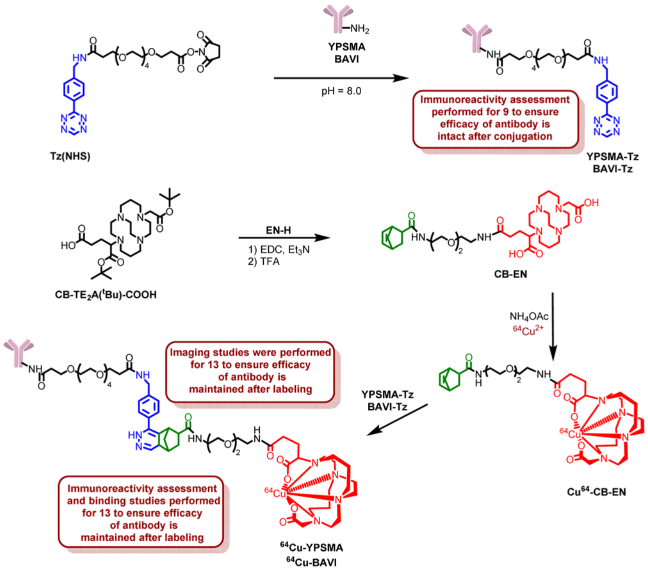

Figure 3. Tetrazine conjugation to antibody and subsequent labeling through click reaction.

Similar prelabeling strategies involving ligations of dienophiles with tetrazines have already been employed with success for radiochemistry with ^{18}F, ^{111}In, and ^{64}Cu.[38−41] It should be noted that copper catalyzed click reaction, though synthetically less challenging, was not employed due to the concern on the possible interference of cold copper (catalyst) with ^{64}Cu labeling.

To test our modular strategy, we chose two antibodies. The first one was anti-PSMA (prostate-specific membrane antigen) antibody YPSMA-1 (YPSMA), which has high binding specificity to PSMA in prostate cancer but little or no cross-reactivity to benign prostate hyperplasia or to normal prostatic tissue. In vitro assays were performed on this antibody conjugate to validate our method. The second one was Bavituximab (BAVI), a phosphatidylserine (PS) targeting antibody. It is currently under clinical trials in cancer patients as an adjuvant to chemotherapy. In vivo PET imaging with ^{64}Cu-labeled BAVI (^{64}Cu-BAVI) was conducted in a tumor xenograft mouse model to further validate the potential use of our click-chemistry startegy.

Chemical Synthesis. The synthetic route was designed considering the stability of tetrazine (**2**) and norbornene (**4**). Since tetrazine is sensitive to high temperature, it was used to modify the antibody. Norbornene being stable at high temperature was conjugated to CB-TE2A(^{t}Bu)-COOH as the cross bridged scaffold requires harsh labeling conditions. Compound **2** was successfully synthesized through the reaction of commercially available reactants, 4-(aminomethyl)-benzonitrile hydrochloride, formamidine acetate, and elemental sulfur. The resultant product, a dihydrotetrazine intermediate ((4-(1,2-dihydro-1,2,4,5-tetrazin-3-yl)phenyl)methanamine) was oxidized with sodium nitrite forming the aromatic tetrazine product. To enable the tethering of the tetrazine moiety to an antibody and to make **2** water-soluble, a tetraethylene glycol (PEG-4) based linker was introduced (Scheme 1). The amino group of **2** was converted to a carboxyl group via a PEG-4 prosthetic arm by conjugating **2** with a dicarboxylate spacer, **3**, via carbodiimide chemistry. To ensure a 1:1 stoichiometric reaction, an excess amount of **3** (5 equiv) was used. The carboxylate group of the resultant compound, Tz(OH), was then activated via the formation of an NHS ester, Tz(NHS). The carboxylic group of 5-norbornene-2-carboxylic acid (**4**) was converted to an amino functionality by tethering it with N-Boc-2,2′-(ethylene-dioxy)diethylamine prosthetic arm. The Boc protection of the resultant compound was removed under the treatment of TFA. The resultant product, EN-H, was conjugated to CB-TE2A(^{t}Bu)-COOH, which was synthesized per our published procedure[42] via the carbodiimde coupling reaction using EDC.

Antibody Modification and Radiolabeling. Prior to modifications, the antibodies, YPSMA and BAVI, were subjected to a buffer exchange through Micro Bio-Spin chromatography columns with a 6000 Da molecular weight cutoff and reconstituted in phosphate-buffered saline (PBS, pH 8.0). This step was necessary, as the antibodies were stored at pH 7.4 mixed with additives such as sodium azide. At pH 7.4, the rate of reaction between the antibody and Tz(NHS) is slow as compared to the hydrolysis of activated acid. Reaction at the slightly basic pH (pH = 8.0) ensures a fast and efficient reaction of Tz(NHS) with the lysine moieties of the antibody. The reaction was incubated at room temperature for 6 h, followed by centrifugal filtration with a 10 000 Da molecular weight cutoff to purify the resultant antibody conjugate. This step removes the unreacted Tz(NHS) and hydrolyzed small molecule reactants. For prelabeling, CB-EN conjugate was used, as norbornene derivatives are stable at high temperatures. Prelabeling was realized by heating a solution of CB-EN and ^{64}Cu(II) in 0.4 M (pH = 6.5) NH_4OAc buffer at 85 °C for 30 min. After labeling, the reaction mixture was purified via Sep-Pak C-18 light cartridge. Since the eluted conjugate, ^{64}Cu-CB-EN, was in 80% ethanol, it was reconstituted in PBS buffer to avoid denaturing the antibody. After reconstitution, the resultant Tz-modified antibody (YPSMA-Tz or BAVI-Tz) was mixed with 44.4 MBq of ^{64}Cu-CB-EN. Since the rate and efficiency of the above reaction heavily relies on the concentration, attention was paid to keep the volume of the reaction to minimal (80−150 μL). The resultant mixture was then incubated for 1−4 h at 37 °C. Of note, the volumes for ^{64}Cu-CB-EN to react with YPSMA-Tz and BAVI-Tz were kept the same but the reaction time was different as the respective radiochemical yields were different. This discrepancy may be attributed to the use of different antibodies, which may have different numbers of functional points for conjugation. As the reaction mixture of labeled antibody contained unreacted ^{64}Cu-CB-EN, it was purified using centrifugal filter units with a 10 000 Da molecular weight cutoff. The radiochemical purity of the final radiolabeled antibody was assayed by size exclusion radio-HPLC (high-performance liquid chromatography) and found to be >99%.

Immunoreactivity Assay of YPSMA-Tz and ^{64}Cu-YPSMA. Our modular click-chemistry strategy of antibody labeling encompasses chemical modification (tethering of antibody with tetrazine) and radiolabeling (reaction of tetrazine tethered antibody with CB-EN). To evaluate the effect of chemical modification and radiolabeling on the immunoreactivity of the antibody, several tests were carried out (Figure 4).

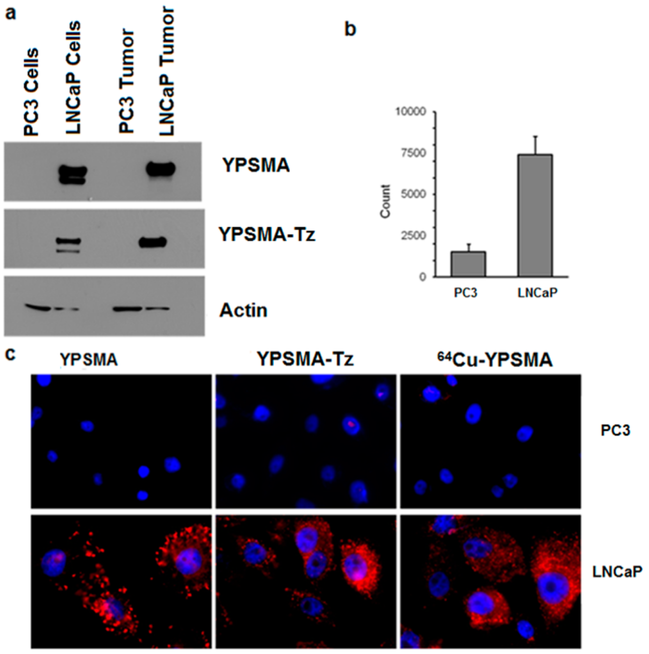

Figure 4. Western blot results of PC3 and LNCaP cell and tumor tissue extracts treated with unmodified YPSMA and tetrazine modified YPSMA-Tz (a). Radioactivity measurement of ^{64}Cu-YPSMA uptaken by PC3 and LNCaP cells (b). Immunochemistry staining of PC3 and LNCaP cell lines using YPSMA, YPSMA-Tz, and ^{64}Cu- YPSMA (c).

Western blot was performed on membrane proteins obtained from LNCaP and PC3 cell line and tumor tissues to see whether the specific binding affinity of YPSMA had been compromised after the tetrazine modification. As shown in Figure 4a, no detectable signal was observed on PC3 lanes confirming the fact that PC3 cells did not have PSMA expression. The LNCaP lanes showed that the immunoreactivity of the Tz-modified antibody was maintained through the chemical modification.

To further assess the effects of chemical modification and radiolabeling on the immunoreactivity of YPSMA, ^{64}Cu-YPSMA was incubated with PC3 and LNCaP cells. The incubated cells were then thoroughly washed with buffer to remove any nonspecific interaction before the cell bound radioactivity was measured using a gamma counter. Shown in Figure 4b, ^{64}Cu-YPSMA displayed significantly higher uptake in the PSMA$^+$ LNCaP cells than in the PSMA$^-$ PC3 cells, further confirming that the immunoreactivity was maintained through the chemical modification and labeling conditions. In addition, we performed immunochemistry staining of PC3 and LNCaP cell lines with unmodified YPSMA, tetrazine modified YPSMA-Tz, and ^{64}Cu-labeled YPSMA. Depicted in Figure 4c, the PSMA expression stained with YPSMA, YPSMA-Tz, and ^{64}Cu-YPSMA is displayed in red and the cell nuclei stained in blue. Both YPSMA-Tz and ^{64}Cu-YPSMA showed the same level of immune-staining of PSMA as YPSMA, while no meaningful red staining occurred with PC3 cells. Taken together, these results demonstrate that our modular click-chemistry strategy of antibody modification and radiolabeling had minimal or negligible effects on the immunoreactivity of the antibody.

It should be noted that YPSMA binds to the intracellular domains of PSMA.[43] Like ProstaScint, YPSMA may not be able to be developed as an optimal imaging agent for noninvasive assessment of PSMA in vivo.[44] In addition, despite the fact that our modular click-chemistry strategy was successfully applied to YPSMA without compromising its immunoreactivity, the overall ^{64}Cu-labeling yield of YPSMA was low. Therefore, we did not pursue further in vivo imaging with ^{64}Cu-YPSMA after we had proven the feasibility of our modular click-chemistry strategy. Instead, we extended the application of our validated strategy to a chimeric antiphosphatidylserine antibody, BAVI, which was developed at our institution and is currently undergoing clinical trials.[45]

Tumor Imaging with ^{64}Cu-BAVI. In order to assess the in vivo imaging profile of ^{64}Cu-BAVI prepared by our click-chemistry strategy, a PET/CT imaging study was performed in a mouse model bearing LNCaP xenografts. As shown in Figure 5, the LNCaP tumor were clearly visualized with ^{64}Cu-BAVI after 2 h p.i. and a steady tumor retention of the radioactivity was observed up to 46 h p.i. The quantitative analysis performed on the images further revealed that the tumor uptake levels were 3.4%, 3.2%, 3.1%, and 3.2% ID/g at 2, 16, 34, and 46 h, respectively. Due to the intrinsic nature of radiolabeled antibodies, a substantial level of liver uptake was also observed. However, the hepatic uptake showed a decreasing trend from 38.4% ID/g at 2 h to 20.6% ID/g at 46 h.

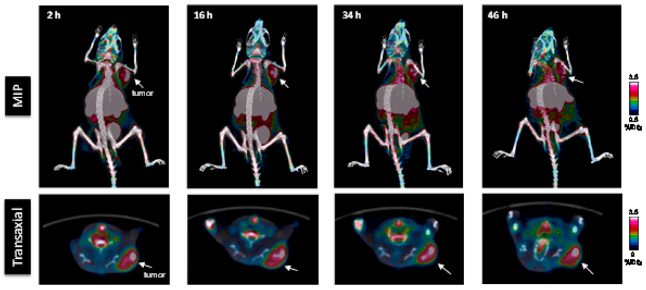

Figure 5. Representative PET/CT images of LNCaP tumor xenografts with ^{64}Cu-BAVI in a mouse model at 2, 16, 34, and 46 h p.i. Images are shown by maximum intensity projection (MIP). The tumors are indicated by white arrow.

Immunohistochemical Staining of PS. To validate the PS-targeted tumor imaging of ^{64}Cu-BAVI, the LNCaP tumor xenografts were sectioned and doubly stained with anti-CD31 (red) and BAVI (green) as shown in Figure 6. LNCaP tumor sections were stained by H&E (left), The merged images (second column from the left) of tumor vasculatures stained by anti-CD31 (red; third column from the left) and PS positive tissues stained by BAVI (green; right) indicates a 29% ± 10% (yellow) of prevalence in the whole tumor.

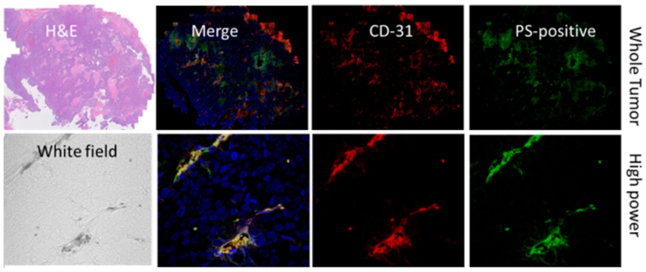

Figure 6. Immunohistochemical staining of phosphatidylserine (PS) expression in LNCaP tumor xenografts.

Although more comprehensive evaluations on the practicality of using ^{64}Cu-BAVI for phosphatidylserine imaging are warranted (e.g., imaging under the condition of chemo-drug or radiation induced apoptosis[46]), our proof of concept PET/CT imaging study with ^{64}Cu-BAVI demonstrated the feasibility of our modular click-chemistry strategy for ^{64}Cu-labeling of antibodies using cross-bridged tetraazamacrocyclic chelators.

MATERIALS AND METHODS

All chemicals, unless otherwise noted, were acquired from Sigma-Aldrich (St. Louis, MO) and used as received without further purification. All water used was ultrapure (Milli-Q, Millipore, Billerica, MA) and passed through a 10 cm column of Chelex resin (Bio-Rad Laboratories, Hercules, CA) before use. DMSO was of molecular biology grade (>99.9%), 5-norbornene-2-carboxylic acid, N-Boc-2,2′-(ethylenedioxy)-diethylamine, 1-ethyl-3-(3-(dimethylamino)propyl) carbodiimide hydrochloride, triethylamine, and all other solvents were of the highest grade commercially available. NMR (nuclear magnetic resonance) spectroscopy was performed on a Bruker 400 MHz NMR. HPLC was performed using a Waters HPLC equipped with a Waters Xterra Shield RP18 semiprep column (250 × 10 mm, 10 μm) and read by a Waters 2996 photodiode array detector and an in-line Shell Jr. 2000 radio-detector, using a gradient of 0:100 MeCN/H_2O (both with 0.1% TFA) to 100:0 MeCN/H_2O within 50 min. The anti-PSMA antibody, YPSMA, was purchased from Abcam (Cambridge, MA). BAVI was obtained from Dr. Philip E. Thorpe's laboratory at the University of Texas Southwestern Medical Center. Copper-64 was purchased from Washington University in St. Louis, MO. For accurate quantification of radioactivity, experimental samples were counted for 1 min on a calibrated PerkinElmer (Waltham, MA) Automatic Wizard2 Gamma Counter. Matrix-assisted laser desorption/ionization (MALDI) mass spectra were acquired on an Applied Biosystems Voyager-6115 mass spectrometer.

Compound 2. The synthesis was performed according to a published procedure with modifications.[36] In brief, 4-(aminomethyl)-benzonitrile hydrochloride (0.84 g, 0.005 mol), formamidine acetate (2.08 g, 0.02 mol), and elemental sulfur (0.16 g, 0.005 mol) were added to a dry, 50 mL round-bottom flask. Anhydrous hydrazine (2.0 mL) was then added to the flask, and the resultant orange reaction mixture was stirred for 20 h. After the allotted time, 1% HCl (aq) (50 mL) was slowly added to the reaction mixture, and the resultant solution was stirred for 10 min and subsequently filtered through a medium glass frit. The remaining orange solution was cooled in an ice bath to 0 °C, and a solution of 1.7 g of $NaNO_2$ in 15 mL of water was then added dropwise to the reaction mixture. While still cooling in an ice bath, acetic acid (50 mL) was added slowly, and the reaction mixture immediately turned bright pink. After allowing this solution to warm up to room temperature over the course of 3 h, the solvent was evaporated at 50 °C and 20 Torr on a rotary evaporator. The resultant red crude solids were purified by flash chromatography using a gradient of MeOH (0.01% TFA)/$CHCl_3$ (0.01% TFA) 30:70 after the removal of solvent, the pure product was obtained in 35% yield (0.33 g, 0. 1.80 mmol). ^{1}H NMR (400 MHz, D_2O): δ = 10.46 (s, 1H), 8.54 (d, 2H), 7.77 (d, 2H), 4.41 (s, 2H). MS (MALDI) *m/z* calcd. for $C_9H_9N_5$: 187.1; found: 188.4 ([M + H]$^+$).

Compound Tz(OH). To a solution of amino terminated tetrazine derivative **2** (0.10 g, 0.53 mmol) in DMF (2.0 mL) was added the dicarboxylic acid derived from tetraethylene glycol (**3**, 0.72 g, 2.13 mmol), 1-ethyl-3-(3-(dimethylamino)-propyl) carbodiimide hydrochloride (101 mg, 0.53 mmol), and triethylamine (0.05 g, 0.53 mmol). The resultant solution was stirred for 12 h, filtered, and the solvent evaporated. The crude product was purified by flash chromatography (ethyl acetate) to give carboxylate carrying PEG-4 tetrazine derivative Tz(OH) (0.08 g, 0.16 mmol, 30%) as a red liquid. ^{1}H NMR (400 MHz, $CDCl_3$): δ = 10.21 (s, 1H), 10.08 (s, 1H), 8.35 (m, 1H), 7.71 (m, 1H), 7.36 (m, 1H), 4.97−4.08 (m, 4H), 4.08−3.00 (m, 16H), 2.84−2.59 (m, 2H), 2.31−2.56 (m, 2H). ^{13}C NMR (100 MHz, $CDCl_3$): δ = 174.1, 173.2, 166.7, 165.9, 157.7, 143.9, 130.33, 128.2, 70.4, 70.2, 70.0, 69.9, 66.9, 66.4, 65.4, 42.9, 36.3, 34.6, 31.9. MS (MALDI) *m/z* calcd. for $C_{23}H_{33}N_5O_8$: 507.2; found: 530.7 ([M + Na]$^+$).

Compound Tz(NHS). To a solution of PEG-4 tetrazine derivative Tz(OH) (0.08 g, 0.16 mmol) in DMF (1.0 mL) was added *N*-hydroxysuccinimide (0.15 g, 0.21 mmol) and 1-ethyl-3-(3-(dimethylamino)propyl) carbodiimide hydrochloride (0.04 g, 0.21 mmol). The resultant solution was stirred for 12 h, filtered, and the solvent evaporated. The crude product was purified by flash chromatography (ethyl acetate) to give NHS activated ester of PEG-4 tetrazine derivative Tz(NHS) (0.04 g, 0.08 mmol, 50%) as a red solid. ^{1}H NMR (400 MHz, $CDCl_3$): δ = 10.17 (s, 1H), 8.50 (m, 2H), 7.50 (m, 2H), 4.54 (m, 2H), 4.98−3.37 (m, 20H), 2.88−2.73 (m, 2H), 2.62 (s, 4H), 2.60−2.43 (m, 2H). ^{13}C NMR (100 MHz, $CDCl_3$): δ = 172.6, 172.2, 169.1, 166.2, 157.7, 144.3, 130.33, 128.4, 128.2, 70.4, 70.4, 70.1, 67.2, 66.5, 65.6, 51.7, 42.9, 36.7, 34.7, 32.06, 25.4. MS (MALDI) *m/z* calcd. for $C_{27}H_{36}N_6O_{10}$: 604.2; found: 627.4 ([M + Na]$^+$).

Compound 5. To a solution of 5-norbornene-2-carboxylic acid (**4**, 0.10 g, 0.72 mmol) in DMF (2.0 mL) was added the N-Boc-2,2′-(ethylenedioxy)diethylamine (0.23 g, 0.92 mmol), 1-ethyl-3-(3-(dimethylamino)propyl) carbodiimide hydrochloride (0.14 g, 0.72 mmol), and triethylamine (0.07 g, 0.72 mmol). The resultant solution was stirred for 12 h, and the solvent evaporated. The crude product was purified by flash chromatography (ethyl acetate) to give a triethylene glycol (PEG-3) modified norbornene derivative **5** (0.19 g, 0.50 mmol, 70%) as a colorless oil. ^{1}H NMR (400 MHz, $CDCl_3$): δ = 6.37 (s, 1H), 5.93 (m, 2H), 5.13 (s, 1H), 3.43 (m, 2H), 3.36 (m, 2H), 3.27 (m, 2H), 3.11 (m, 2H), 2.72 (m, 2H), 1.85 (m, 1H), 1.73 (m, 1H), 1.56 (m, 1H), 1.25 (s, 9H), 1.11 (m, 2H). ^{13}C NMR (100 MHz, $CDCl_3$): δ = 175.7, 155.9, 137.9, 135.9, 78.9, 70.1, 70.0, 69.8, 47.1, 46.1, 41.4, 40.1, 39.1, 28.26. MS (MALDI) *m/z* calcd. for $C_{19}H_{32}N_2O_5$: 368.2; found: 369.3 ([M + H]$^+$).

Compound EN-H. The solution of PEG-3 norbornene derivative (**5**, 0.19 g, 0.50 mmol) was stirred with TFA (2.0 mL) for 4 h. After deprotection, the solvent was evaporated and the product was purified by flash chromatography (ethyl acetate) to give **EN-H** (0.12 g, 0.44 mmol, 88%) as a colorless vicious liquid. ^{1}H NMR (400 MHz, $CDCl_3$): δ = 6.95 (s, 1H), 6.08 (m, 1H), 6.04 (m, 1H), 3.82−3.48 (m, 7H), 3.41 (m, 2H), 3.20 (m, 2H), 2.86 (m, 2H), 2.43 (m, 1H), 2.11 (m, 1H), 1.73 (m, 1H), 1.50 (m, 1H), 1.32 (m, 1H). ^{13}C NMR (100 MHz, $CDCl_3$): δ = 178.8, 137.9, 135.6, 69.9, 69.8, 66.1, 46.7, 44.4, 41.4, 39.9, 39.6, 30.5. MS (MALDI) *m/z* calcd. for $C_{14}H_{24}N_2O_3$: 268.2; found: 269.3 ([M + H]$^+$).

Compound CB-EN. To a solution of PEG-3 norbornene derivative (EN-H, 0.12 g, 0.43 mmol) in DMF (2.0 mL) was added protected cross-bridged chelator (CB-TE2A(^{t}Bu)-COOH, 0.19 g, 0.36 mmol), 1-ethyl-3-(3-(dimethylamino)-propyl) carbodiimide hydrochloride (0.07 g, 0.36 mmol), and triethylamine (0.04 g, 0.36 mmol). The resultant solution was stirred for 12 h, filtered, and the solvent evaporated. The crude protected product was purified by HPLC (0.11 g, 0.14 mmol, 40%) as a white solid. ^{1}H NMR (400 MHz, $CDCl_3$): δ = 9.09 (m, 2H), 6.08 (m, 2H), 3.95−3.45 (m, 10H), 3.48−3.00 (m, 12H), 2.97−2.54 (m, 10H), 2.52−2.19 (m, 4H), 2.15−1.65 (m, 10H), 1.58−1.33 (m, 15H), 1.33−1.05 (m, 4H). ^{13}C NMR (100 MHz, $CDCl_3$): δ 176.1, 175.9, 138.2, 136.1, 82.5, 81.9, 70.3, 70.1, 70.0, 68.7, 62.4, 56.2, 55.9, 51.1, 47.9, 47.2, 46.3, 44.6, 44.4, 41.5, 39.6, 39.2, 32.9, 30.4, 28.1, 25.2. MS (MALDI) *m/z* calcd. for $C_{41}H_{72}N_6O_8$: 776.5; found: 799.5 ([M + Na]$^+$). The protected product was mixed with TFA (2.0 mL) and the solution was stirred for 12 h. After the reaction, the solvent was evaporated and the product was purified by HPLC to give CB-EN (0.08 g, 0.13 mmol, 90%) as a red viscous liquid. ^{1}H NMR (400 MHz, $CDCl_3$): δ = 6.13 (m, 2H), 3.96−3.49 (m, 12H), 3.49−2.97 (m, 13H), 2.97−2.70 (m, 5H), 2.70−2.31 (m, 3H), 2.31−1.91 (m, 5H), 1.91−1.61 (m, 3H), 1.61−1.43 (m, 2H), 1.43−1.25 (m, 2H),1.03 (s 1H). ^{13}C NMR (100 MHz, $CDCl_3$): δ 179.9, 175.4, 141.9, 139.9, 73.9, 73.6, 72.7, 61.3, 54.1, 51.0, 50.0, 48.1, 46.6, 45.4, 43.4, 42.9, 36.3, 34.2, 31.7, 31.2, 26.9. MS (MALDI) *m/z* calcd. for $C_{33}H_{56}N_6O_8$: 664.4; found: 665.8 ([M + H]$^+$).

Modification of YPSMA with Tetrazine (YPSMA-Tz). A 100 μL solution of the antibody (1.0 mg/mL) was subjected to a buffer exchange by using Micro Bio-Spin chromatography columns (Bio-Rad Laboratories) with a 6000 Da molecular weight cutoff. After centrifugation, the antibody was reconstituted with (PBS, 1×, pH 8.0). To the resulting solution was added 50 equiv of the NHS activated tetrazine derivative, Tz(NHS), in 10 μL of PBS, pH 7.4. The reaction was incubated at room temperature for 6 h, followed by centrifugal filtration with a 10 000 Da molecular weight cutoff to purify the resultant antibody conjugate, YPSMA-Tz. The purified antibody conjugate was reconstituted with 100 μL PBS, pH 7.4, and used directly for further reaction.

Modification of BAVI with Tetrazine (BAVI-Tz). A 90 μL solution of the antibody (18.5 mg/mL) was subjected to a buffer exchange by using Micro Bio-Spin chromatography columns (Bio-Rad Laboratories) with a 6000 Da molecular weight cutoff. After centrifugation, the antibody was reconstituted in PBS, pH 8.0. To the resultant antibody was added 50 equiv of the NHS activated tetrazine derivative, Tz(NHS), in 10 μL of PBS, pH 7.4. The reaction was incubated at room temperature for 6 h, followed by centrifugal filtration with a 10 000 Da molecular weight cutoff to purify the resultant antibody conjugate, BAVI-Tz.

Prelabeling of CB-EN with ^{64}Cu (^{64}Cu-CB-EN). To a 0.5 mL eppendorf tube containing 2.2 μg of conjugate CB-EN in 40 μL of 0.6 M NH_4OAc buffer was added 70.3 MBq of $^{64}CuCl_2$ solution. The reaction mixture was shaken and incubated at 85 °C for 30 min. To remove the nonspecifically bound and free $^{64}CuCl_2$ from the ^{64}Cu-labeled conjugate, 2 μL of 5 mM diethylene triamine pentaacetic acid (DTPA) was added to the reaction mixture. The mixture was allowed to incubate for 5 min followed by passing the mixture through a preconditioned Sep-Pak C-18 light cartridge. The cartridge was rinsed thoroughly with water (5 mL) followed by elution of ^{64}Cu-labeled norbornene conjugate (^{64}Cu-CB-EN) by 0.5 mL of ethanol/10 mM PBS mixture (80:20). The elute yielded 48.1 MBq of ^{64}Cu-labeled product. The product was analyzed by radio-HPLC to determine the radiochemical yield and purity. The eluted product was dried under stream of nitrogen at 50 °C and then reconstituted in 10 mM PBS solution (50 μL).

^{64}Cu Labeling of YPSMA (^{64}Cu-YPSMA). To the previously purified antibody tethered with tetrazine (YPSMA-Tz, 100 μL) was added ^{64}Cu-labeled norbornene conjugate (CB-EN, 44.4 MBq). The mixture was incubated at 37 °C for 4 h. The resulting mixture was then purified by centrifugal filtration with a 10 000 molecular weight cutoff to give 2220 KBq of labeled antibody, ^{64}Cu-YPSMA. The radiochemical purity of the final radiolabeled bioconjugate was assayed by radio-HPLC fitted with size exclusion column (BioSuite SEC Column, 125 Å, 10 μm, 7.5 mm × 300 mm) and was found to be >99%.

^{64}Cu Labeling of BAVI (^{64}Cu-BAVI). To the purified antibody tethered with tetrazine (BAVI-Tz, 30 μL) was added ^{64}Cu-labeled norbornene conjugate (CB-EN, 118.4 MBq). The mixture was incubated at 37 °C for 1 h. The resulting mixture was then purified by centrifugal filtration with a 10 000 molecular weight cutoff to give 22.9 MBq of labeled antibody, ^{64}Cu-BAVI. The radiochemical purity of the final radiolabeled bioconjugate was assayed by radio-FPLC fitted with Superdex 200 Increase GL and was found to be >99%.

Small Animal PET/CT Imaging. Small animal PET/CT imaging was performed on a Siemens Inveon PET/CT Multimodality System in LNCaP tumor-bearing SCID mice that had been intravenously injected with 17.2 MBq of ^{64}Cu-BAVI via the tail vein. The mouse was sedated on the imaging bed under 2% isoflurane for the duration of imaging. Immediately after the CT data acquisition that was performed at 80 kV and 500 μA with a focal spot of 58 μm, static PET scans were conducted at the given time points post injection (p.i.) (2, 16, 23, 34, and 46 h) for 15 min. Both CT and PET images were reconstructed with manufacturer's software. Reconstructed CT and PET images were fused for quantitative data analysis; regions of interest (ROIs) were drawn as guided by CT and quantitatively expressed as percent injected dose per gram of tissue (% ID/g).

Immunohistochemistry for YPSMA, YPSMA-Tz, and ^{64}Cu-YPSMA. A volume of 500 μL RPIM 1640 culture media containing approximately 20 000 cells, either PSMA$^+$ LNCaP or PSMA$^-$ PC3, was added to a 24 well plate containing gelatin-coated coverslips. When the cells reached the desired density, the culture media were removed from each well and washed twice with PBS. A volume of 200 μL of 4% formaldehyde fixing solution was added to each well, and incubated for 20 min at room temperature. Each well was washed twice with PBS. The solution of 200 μL of the primary antibody YPSMA, diluted in a ratio of 1:500, 1:250 YPSMA-Tz, or 1:125 ^{64}Cu-YPSMA (^{64}Cu-YPSMA, the labeled antibody was stored for 64 h at 4 °C and tests were performed when the radioactivity was decayed) at 4 °C for 4 h. The goat anti-mouse tagged with Texas red (abcam) was then added to the plate stored at room temperature for 1 h. Each well was then rinsed twice with 400 μL of wash buffer. A diluted solution of (1:200; 200 μL) Alexa Fluor 488 Phalloidin (Invitrogen) was then added to each well, and incubated for 20 min at room temperature. After two rinsings (once with PBS and once with water), the coverslips were removed from the wells and excess water was carefully blotted out. One drop of ProLong Gold antifade reagent (Life Technologies) was then added along with DAPI (4′,6-diamidino-2-phenylindole, Invitrogen) onto the microscope slide per coverslip. The glass coverslip was placed on the slide and the edges sealed with nail polish. The slides were visualized using Zeiss AxioObserver Epifluorescence Microscope using filter sets appropriate for the label used under 63× objective oil lens.

Western Blot Analysis. Protein from PC3 and LNCaP cells and tumor tissue were extracted by standard methods. Western blots were performed with 30 μg of total protein and transferred to PVDF membrane, blocked by 5% skim milk and probed using YPSMA primary antibody (ab19071, Abcam) (1:500) and modified YPSMA-Tz (1:250) and anti-Actin antibody (1:5000, Sigma) 4 °C overnight. Following incubation with HRP-labeled secondary antibody (GE Life Sciences, 1:1000) 1 h, immunoblots were visualized by ECL Plus (Millipore) and the target bands were recorded on X-ray film. Actin protein levels were used as a control to verify equal protein loading.

Cell Uptake Assay. The cell uptake of ^{64}Cu-YPSMA was measured using the PSMA$^+$ LNCaP and PSMA$^-$ PC3 cells. The cells were washed with PBS buffer following by RPMI 1640 medium without FBS, and then resuspended in RPMI 1640 medium without FBS at the concentration of 2×10^6 cells/mL. The cell suspension was then dispensed into 1.5 mL eppendorf tubes (1×10^6 cells per tube), to each of which was added approximately 12 000 cpm of ^{64}Cu-YPSMA in 0.02 mL of PBS buffer. After the cells were incubated at room temperature for 60 min ($n = 5$), the cell suspension was centrifuged and the supernatant from each vial was stored separately. Each pellet was resuspended in 0.5 mL of ice-cold PBS buffer. To remove the unbound ^{64}Cu-YPSMA, the above procedure was repeated five times. The combined supernatant solutions and the remaining cell pellet from each tube were counted with a γ-counter to determine the cell bound ^{64}Cu-YPSMA level.

Phosphatidylserine (PS) Expression in LNCaP Tumors Measured by Immunohistochemical Staining. SCID/Nude male mice bearing LNCaP tumors were injected intravenously (i.v.) with 100 μg of BAVI and allowed to circulate for 2 h. Anesthetized mice were then perfused by transcardial perfusion with heparinized normal saline followed immediately by 4% paraformaldehyde (PFA) in PBS (pH 7.4) at a rate of 90 mL/h using a syringe pump. The tumors were then excised and dissected. All tumor pieces were placed in 4%

PFA at 4 °C overnight with continuous gentle agitation. All tumor tissues were then transferred to PBS and equilibrated overnight at 4 °C. Tissues for cryoembedding were transferred to a 10% sucrose/PBS solution overnight at 4 °C and then transferred to an 18% sucrose/PBS solution. After removed from solution, tissues were blotted and submerged in optimal cutting temperature (OCT) compound. Tissues in OCT were then frozen rapidly by partial immersion in liquid N2 cooled isopentane and stored at −80 °C until sectioning. Vascular endothelium was stained using a rat anti-mouse CD31 antibody (BD Biosciences, San Jose, CA) followed by Cy3-labeled goat anti-rat IgG; BAVI-positive vessels were identified with biotinylated goat anti-human IgG conjugated to Cy2-labeled streptavidin. Fluorescent Images were captured using CarlZeiss Axioscan (Carl Zeiss, Jena, Germany) (whole tumor and low power) and Zeiss confocal microscope (Carl Zeiss, Jena, Germany, high power, 40× oil lens) mounted on Elipse E600 fluorescent microscope (Nikon, Melville, NY) and analyzed with Zen software. Doubly labeled endothelial cells (CD31 positive/PS positive) were identified by yellow fluorescence on merged images. The percentage of doubly positive vessels was calculated as follows: (mean number of yellow vessels per field/mean number of total vessels) × 100.

■ AUTHOR INFORMATION

Corresponding Author

*E-mail: Xiankai.Sun@UTSouthwestern.edu.

Author Contributions

The manuscript was written through contributions of all authors. All authors have given approval to the final version of the manuscript.

Notes

The authors declare no competing financial interest.

■ ACKNOWLEDGMENTS

This work was partially supported by the Prostate Cancer Research Program of the United States Army Medical Research and Materiel Command (W81XWH-12−1−0336), the Dr. Jack Krohmer Professorship Funds, and the National Institutes of Health (CA159144).

■ REFERENCES

(1) Niu, G., Li, Z., Cao, Q., and Chen, X. (2009) Monitoring therapeutic response of human ovarian cancer to 17-DMAG by noninvasive PET imaging with ^{64}Cu-DOTA-trastuzumab. *Eur. J. Nucl. Med. Mol. Imaging 36*, 1510−1519.

(2) Anderson, C. J., Connett, J. M., Schwarz, S. W., Rocque, P. A., Guo, L. W., Philpott, G. W., Zinn, K. R., Meares, C. F., and Welch, M. J. (1992) Copper-64-labeled antibodies for PET imaging. *J. Nucl. Med. 33*, 1685−1691.

(3) Bryan, J. N., Jia, F., Mohsin, H., Sivaguru, G., Miller, W. H., Anderson, C. J., Henry, C. J., and Lewis, M. R. (2005) Comparative uptakes and biodistributions of internalizing vs. noninternalizing copper-64 radioimmunoconjugates in cell and animal models of colon cancer. *Nucl. Med. Biol. 32*, 851−858.

(4) Voss, S. D., Smith, S. V., DiBartolo, N., McIntosh, L. J., Cyr, E. M., Bonab, A. A., Dearling, J. L. J., Carter, E. A., Fischman, A. J., Treves, S. T., et al. (2007) Positron emission tomography (PET) imaging of neuroblastoma and melanoma with ^{64}Cu-SarAr immunoconjugates. *Proc. Natl. Acad. Sci. U.S.A. 104*, 17489−17493.

(5) Smith, S. V. (2004) Molecular imaging with copper-64. *J. Inorg. Biochem. 98*, 1874−1901.

(6) Connett, J. M., Buettner, T. L., and Anderson, C. J. (1999) Maximum tolerated dose and large tumor radioimmunotherapy studies of Cu-64-labeled monoclonal antibody 1A3 in a colon cancer model. *Clin. Cancer Res. 5*, 3207S−3212S.

(7) Wu, A. M., Yazaki, P. J., Tsai, S.-w., Nguyen, K., Anderson, A.-L., McCarthy, D. W., Welch, M. J., Shively, J. E., Williams, L. E., Raubitschek, A. A., et al. (2000) High-resolution microPET imaging of carcinoembryonic antigen-positive xenografts by using a copper-64-labeled engineered antibody fragment. *Proc. Natl. Acad. Sci. U.S.A. 97*, 8495−8500.

(8) Bryan, J. N., Lewis, M. R., Henry, C. J., Owen, N. K., Zhang, J., Mohsin, H., Jia, F., Sivaguru, G., and Anderson, C. J. (2004) Development of a two-antibody model for the evaluation of copper-64 radioimmunotherapy. *Vet. Comp. Oncol. 2*, 82−90.

(9) Bass, L. A., Wang, M., Welch, M. J., and Anderson, C. J. (2000) In vivo transchelation of copper-64 from TETA-octreotide to superoxide dismutase in rat liver. *Bioconjugate Chem. 11*, 527−532.

(10) Jones-Wilson, T. M., Deal, K. A., Anderson, C. J., McCarthy, D. W., Kovacs, Z., Motekaitis, R. J., Sherry, A. D., Martell, A. E., and Welch, M. J. (1998) The in vivo behavior of copper-64-labeled azamacrocyclic complexes. *Nucl. Med. Biol. 25*, 523−530.

(11) Shokeen, M., and Anderson, C. J. (2009) Molecular imaging of cancer with copper-64 radiopharmaceuticals and positron emission tomography (PET). *Acc. Chem. Res. 42*, 832−841.

(12) Chen, X., Liu, S., Hou, Y., Tohme, M., Park, R., Bading, J. R., and Conti, P. S. (2004) MicroPET imaging of breast cancer αv-integrin expression with ^{64}Cu-labeled dimeric RGD peptides. *Mol. Imaging Biol. 6*, 350−359.

(13) Wu, Y., Zhang, X., Xiong, Z., Cheng, Z., Fisher, D. R., Liu, S., Gambhir, S. S., and Chen, X. (2005) MicroPET imaging of glioma integrin $\alpha v\beta 3$ expression using ^{64}Cu-labeled tetrameric RGD peptide. *J. Nucl. Med. 46*, 1707−1718.

(14) Anderson, C. J., Pajeau, T. S., Edwards, W. B., Sherman, E. L. C., Rogers, B. E., and Welch, M. J. (1995) In vitro and in vivo evaluation of copper-64-octreotide conjugates. *J. Nucl. Med. 36*, 2315−2325.

(15) Anderson, C. J., Jones, L. A., Bass, L. A., Sherman, E. L. C., McCarthy, D. W., Cutler, P. D., Lanahan, M. V., Cristel, M. E., Lewis, J. S., and Schwarz, S. W. (1998) Radiotherapy, toxicity and dosimetry of copper-64-TETA-octreotide in tumor-bearing rats. *J. Nucl. Med. 39*, 1944−1951.

(16) McQuade, P., Miao, Y., Yoo, J., Quinn, T. P., Welch, M. J., and Lewis, J. S. (2005) Imaging of melanoma using ^{64}Cu- and ^{86}Y-DOTA-ReCCMSH(Arg11), a cyclized peptide analogue of α-MSH. *J. Med. Chem. 48*, 2985−2992.

(17) Chen, X., Hou, Y., Tohme, M., Park, R., Khankaldyyan, V., Gonzales-Gomez, I., Bading, J. R., Laug, W. E., and Conti, P. S. (2004) Pegylated Arg-Gly-Asp peptide: ^{64}Cu labeling and PET imaging of brain tumor $\alpha v\beta 3$-integrin expression. *J. Nucl. Med. 45*, 1776−1783.

(18) Elsässer-Beile, U., Reischl, G., Wiehr, S., Bühler, P., Wolf, P., Alt, K., Shively, J., Judenhofer, M. S., Machulla, H.-J., and Pichler, B. J. (2009) PET imaging of prostate cancer xenografts with a highly specific antibody against the prostate-specific membrane antigen. *J. Nucl. Med. 50*, 606−611.

(19) Boswell, C. A., Sun, X., Niu, W., Weisman, G. R., Wong, E. H., Rheingold, A. L., and Anderson, C. J. (2004) Comparative in vivo stability of copper-64-labeled cross-bridged and conventional tetraazamacrocyclic complexes. *J. Med. Chem. 47*, 1465−1474.

(20) Sprague, J. E., Peng, Y., Fiamengo, A. L., Woodin, K. S., Southwick, E. A., Weisman, G. R., Wong, E. H., Golen, J. A., Rheingold, A. L., and Anderson, C. J. (2007) Synthesis, characterization and in vivo studies of Cu(II)-64-labeled cross-bridged tetraazamacrocycle-amide complexes as models of peptide conjugate imaging agents. *J. Med. Chem. 50*, 2527−2535.

(21) Di Bartolo, N. M., Sargeson, A. M., Donlevy, T. M., and Smith, S. V. (2001) Synthesis of a new cage ligand, SarAr, and its complexation with selected transition metal ions for potential use in radioimaging. *Dalton Trans.*, 2303−2309.

(22) Di Bartolo, N., Sargeson, A. M., and Smith, S. V. (2006) New ^{64}Cu PET imaging agents for personalised medicine and drug development using the hexa-aza cage, SarAr. *Org. Biomol. Chem. 4*, 3350−3357.

(23) Smith, S. V., Waters, D. J., and DiBartolo, N. (1996) Separation of Cu-64 from Ga-67 waste products using anion exchange and low acid aqueous/organic mixtures. *Radiochim. Acta. 75*, 65−68.

(24) Anderson, C. J., and Ferdani, R. (2009) Copper-64 radiopharmaceuticals for PET imaging of cancer: advances in preclinical and clinical research. *Cancer Biother. Radiopharm. 24*, 379−393.

(25) Dearling, J. L. J., Voss, S. D., Dunning, P., Snay, E., Fahey, F., Smith, S. V., Huston, J. S., Meares, C. F., Treves, S. T., and Packard, A. B. (2011) Imaging cancer using PET — the effect of the bifunctional chelator on the biodistribution of a ^{64}Cu-labeled antibody. *Nucl. Med. Biol. 38*, 29−38.

(26) Chong, H.-S., Mhaske, S., Lin, M., Bhuniya, S., Song, H. A., Brechbiel, M. W., and Sun, X. (2007) Novel synthetic ligands for targeted PET imaging and radiotherapy of copper. *Bioorg. Med. Chem. Lett. 17*, 6107−6110.

(27) Prasanphanich, A. F., Nanda, P. K., Rold, T. L., Ma, L., Lewis, M. R., Garrison, J. C., Hoffman, T. J., Sieckman, G. L., Figueroa, S. D., and Smith, C. J. (2007) [^{64}Cu-NOTA-8-Aoc-BBN(7−14)NH2] targeting vector for positron-emission tomography imaging of gastrin-releasing peptide receptor-expressing tissues. *Proc. Natl. Acad. Sci. U.S.A. 104*, 12462−12467.

(28) Sun, X., Wuest, M., Weisman, G. R., Wong, E. H., Reed, D. P., Boswell, C. A., Motekaitis, R., Martell, A. E., Welch, M. J., and Anderson, C. J. (2001) Radiolabeling and in vivo behavior of copper-64-labeled cross-bridged cyclam ligands. *J. Med. Chem. 45*, 469−477.

(29) Woodin, K. S., Heroux, K. J., Boswell, C. A., Wong, E. H., Weisman, G. R., Niu, W. J., Tomellini, S. A., Anderson, C. J., Zakharov, L. N., and Rheingold, A. L. (2005) Kinetic inertness and electrochemical behavior of copper(II) tetraazamacrocyclic complexes: Possible implications for in vivo stability. *Eur. J. Inorg. Chem.*, 4829−4833.

(30) Stigers, D. J., Ferdani, R., Weisman, G. R., Wong, E. H., Anderson, C. J., Golen, J. A., Moore, C., and Rheingold, A. L. (2010) A new phosphonate pendant-armed cross-bridged tetraamine chelator accelerates copper(II) binding for radiopharmaceutical applications. *Dalton Trans. 39*, 1699−1701.

(31) Zeng, D., Ouyang, Q., Cai, Z., Xie, X.-Q., and Anderson, C. J. (2014) New cross-bridged cyclam derivative CB-TE1K1P, an improved bifunctional chelator for copper radionuclides. *Chem. Commun. 50*, 43−45.

(32) Zeng, D., Guo, Y., White, A. G., Cai, Z., Modi, J., Ferdani, R., and Anderson, C. J. (2014) Comparison of conjugation strategies of cross-bridged macrocyclic chelators with cetuximab for copper-64 radiolabeling and PET imaging of EGFR in colorectal tumor-bearing mice. *Mol. Pharm. 11*, 3980−3987.

(33) Lebedev, A. Y., Holland, J. P., and Lewis, J. S. (2010) Clickable bifunctional radiometal chelates for peptide labeling. *Chem. Commun. 46*, 1706−1708.

(34) Cai, Z., Li, B. T. Y., Wong, E. H., Weisman, G. R., and Anderson, C. J. (2015) Cu(i)-assisted click chemistry strategy for conjugation of non-protected cross-bridged macrocyclic chelators to tumour-targeting peptides. *Dalton Trans. 44*, 3945−3948.

(35) Devaraj, N. K., Upadhyay, R., Haun, J. B., Hilderbrand, S. A., and Weissleder, R. (2009) Fast and sensitive pretargeted labeling of cancer cells through a tetrazine/trans-cyclooctene cycloaddition. *Angew. Chem., Int. Ed. 48*, 7013−7016.

(36) Devaraj, N. K., Weissleder, R., and Hilderbrand, S. A. (2008) Tetrazine-based cycloadditions: application to pretargeted live cell imaging. *Bioconjugate Chem. 19*, 2297−2299.

(37) Blackman, M. L., Royzen, M., and Fox, J. M. (2008) Tetrazine ligation: fast bioconjugation based on inverse-electron-demand Diels−Alder reactivity. *J. Am. Chem. Soc. 130*, 13518−13519.

(38) Rossin, R., Renart Verkerk, P., van den Bosch, S. M., Vulders, R. C. M., Verel, I., Lub, J., and Robillard, M. S. (2010) In vivo chemistry for pretargeted tumor imaging in live mice. *Angew. Chem., Int. Ed. 49*, 3375−3378.

(39) Reiner, T., Keliher, E. J., Earley, S., Marinelli, B., and Weissleder, R. (2011) Synthesis and in vivo imaging of a 18F-labeled PARP1 inhibitor using a chemically orthogonal scavenger-assisted high-performance method. *Angew. Chem., Int. Ed. 50*, 1922−1925.

(40) Zeglis, B. M., Mohindra, P., Weissmann, G. I., Divilov, V., Hilderbrand, S. A., Weissleder, R., and Lewis, J. S. (2011) Modular strategy for the construction of radiometalated antibodies for positron emission tomography based on inverse electron demand Diels−Alder click chemistry. *Bioconjugate Chem. 22*, 2048−2059.

(41) Zeglis, B. M., Sevak, K. K., Reiner, T., Mohindra, P., Carlin, S. D., Zanzonico, P., Weissleder, R., and Lewis, J. S. (2013) A pretargeted PET imaging strategy based on bioorthogonal diels−alder click chemistry. *J. Nucl. Med. 54*, 1389−1396.

(42) Liu, W., Hao, G. Y., Long, M. A., Anthony, T., Hsieh, J. T., and Sun, X. K. (2009) Imparting multivalency to a bifunctional chelator: A scaffold design for targeted PET imaging probes. *Angew. Chem., Int. Ed. 48*, 7346−7349.

(43) Rybalov, M., Ananias, H. J. K., Hoving, H. D., van der Poel, H. G., Rosati, S., and de Jong, I. J. (2014) PSMA, EpCAM, VEGF and GRPR as imaging targets in locally recurrent Prostate cancer after radiotherapy. *Int. J. Mol. Sci. 15*, 6046−6061.

(44) Taneja, S. S. (2004) ProstaScint® scan: Contemporary use in clinical practice. *Rev. Urol. 6*, S19−S28.

(45) Stafford, J. H.; Hao, G.; Best, A. M.; Sun, X.; Thorpe, P. E. (2013) Highly specific PET imaging of prostate tumors in mice with an Iodine-124-labeled antibody fragment that targets phosphatidylserine. *PLoS One 8*; DOI: 10.1371/journal.pone.0084864.

(46) Ogasawara, A., Tinianow, J. N., Vanderbilt, A. N., Gill, H. S., Yee, S., Flores, J. E., Williams, S. P., Ashkenazi, A., and Marik, J. (2013) ImmunoPET imaging of phosphatidylserine in pro-apoptotic therapy treated tumor models. *Nucl. Med. Biol. 40*, 15−22.

Bioconjugate Chemistry

Article

pubs.acs.org/bc

Design of a Small-Molecule Drug Conjugate for Prostate Cancer Targeted Theranostics

Amit Kumar,[†] Tara Mastren,[†] Bin Wang,[‡,§] Jer-Tsong Hsieh,[‡] Guiyang Hao,*[,†] and Xiankai Sun*[,†,∥]

[†]Department of Radiology, [‡]Department of Urology, and [∥]Advanced Imaging Research Center, University of Texas Southwestern Medical Center, Dallas, Texas 75390, United States

[§]Department of Urology, the First Affiliated Hospital, Medical School of Xi'An Jiaotong University, Xi'An, Shaanxi 710061, P. R. China

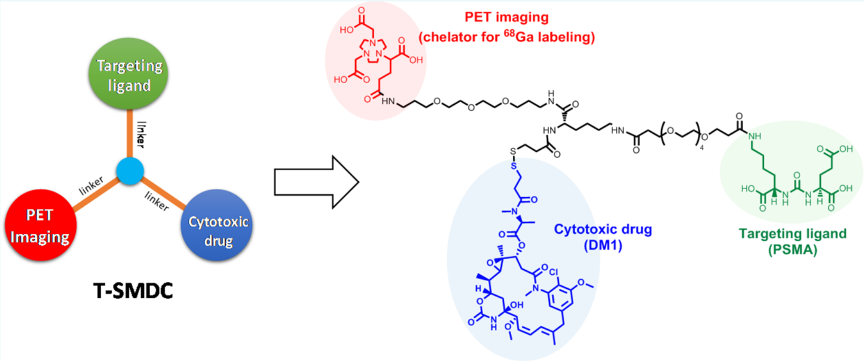

ABSTRACT: Targeted therapy has become an effective strategy of precision medicine for cancer treatment. Based on the success of antibody-drug conjugates (ADCs), here we report a theranostic design of small-molecule drug conjugates (T-SMDCs) for targeted imaging and chemotherapy of prostate cancer. The structure of T-SMDCs built upon a polyethylene glycol (PEG) scaffold consists of (i) a chelating moiety for positron emission tomography (PET) imaging when labeled with ^{68}Ga, a positron-emitting radioisotope; (ii) a prostate specific membrane antigen (PSMA) specific ligand for prostate cancer targeting; and (iii) a cytotoxic drug (DM1) for chemotherapy. For proof-of-concept, such a T-SMDC, NO3A-DM1-Lys-Urea-Glu, was synthesized and evaluated. The chemical modification of Lys-Urea-Glu for the construction of the conjugate did not compromise its specific binding affinity to PSMA. The PSMA-mediated internalization of ^{68}Ga-labeled NO3A-DM1-Lys-Urea-Glu displayed a time-dependent manner, allowing the desired drug delivery and release within tumor cells. The antiproliferative activity of the T-SMDC showed a positive correlation with the PSMA expression level. Small animal PET imaging with ^{68}Ga-labeled NO3A-DM1-Lys-Urea-Glu exhibited significantly higher uptake ($p < 0.01$) in the PSMA positive PC3-PIP tumors (4.30 ± 0.20%ID/g) at 1 h postinjection than in the PSMA negative PC3-Flu tumors (1.12 ± 0.42%ID/g). Taken together, we have successfully designed and synthesized a T-SMDC system for prostate cancer targeted imaging and therapy.

■ INTRODUCTION

Prostate cancer remains the second leading cause of death in American men, with an estimated 26 120 deaths in 2016[1] primarily as a result of the complications from castration-resistant prostate cancer (CRPC). Chemotherapy was not effective in the treatment of CRPC until 2004 when a combination of docetaxel and prednisone was reported with an overall survival gain.[2,3] Further advances have been seen as the United States Food and Drug Administration (US-FDA) approved cabazitaxel in 2010 as a second-line treatment of metastatic CRPC patients. However, due to the multidrug resistance and safety concerns of cytotoxic drugs, chemotherapy of prostate cancer is still deemed less favorable.[4,5]

To date, the strategy of targeted therapy has demonstrated its effectiveness when treating lymphoma and breast cancer as represented by several US-FDA approved antibody drug conjugates (ADCs).[6,7] Despite the promising outcome, the limitations of ADCs are obvious in their suboptimal in vivo distribution and kinetics owing to their large size,[8] which precludes efficient penetration into solid tumors.[9] In addition, antibodies elicit immunogenic responses[10] and are slowly cleared from nontarget organs leading to undesired side effects.[11,12] Also, the non-site-specific drug conjugation with antibodies may have adverse effects to compromise the immunoreactivity of the antibodies and renders irreproducibility to the manufacturing of ADCs. Moreover, the production of antibodies is often low throughput and therefore not cost efficient.

As such, small organic molecules targeting specific tumor markers have been proposed as a viable alternative to

Received: May 3, 2016
Revised: May 24, 2016
Published: June 1, 2016

DOI: 10.1021/acs.bioconjchem.6b00222

antibodies for targeted drug delivery[8,11,13] owing to the inherent advantages from their small size, nonimmunogenic nature, and much more manageable synthesis.[8,14] Indeed, several small-molecule drug conjugates (SMDCs) have been reported including ones targeting prostate specific membrane antigen (PSMA),[15] carbonic anhydrase IX,[11] or biotin receptors[16] in preclinical studies. Recently, a folic acid based SMDC (Vintafolide) targeting the folate receptors has entered the Phase III clinical trial for the treatment of platinum-resistant ovarian cancer.[13]

In company with the development of ADCs and SMDCs for targeted cancer treatment, to date considerable attention has been drawn to adding a precision medicine measure to potentiate personalized therapy for cancer patient care, as a newly emerged concept, theranostics, evolves. One strategy involves replacing the drug payload with an imaging moiety in the same modular structure of SMDCs (companion imaging).[15] However, this companion approach may not truly reflect the distribution of SMDCs inside the living subject given their chemical structural differences. Ideally, a theranostic design would allow molecular imaging to be performed using the same single agent of therapy, which provides the in vivo molecular and cellular information for patient stratification in addition to the drug distribution kinetics and dynamic tumor response. Such efforts have been seen recently with an optical imaging component embedded in SMDC designs.[17−19] Despite the promising results, the penetration depth of light in living subjects limits their applications in preclinical settings or imaging-guided intraoperative surgery.

In this study, we present a theranostic design of incorporating a PET imaging component to a SMDC system with the goal of combining both imaging and therapy functions in a single entity. Built upon a polyethylene glycol (PEG) scaffold, the T-SMDC system (Scheme 1) consists of (i) a chelating moiety for positron emission tomography (PET) imaging when labeled with ^{68}Ga, a cyclotron-independent positron-emitting radioisotope; (ii) a specific PSMA ligand for prostate cancer targeting; and (iii) a cytotoxic drug (DM1) for chemotherapy.

Scheme 1. Design of Prostate Specific Membrane Antigen (PSMA) Targeted Theranostic Small-Molecule Drug Conjugate (T-SMDC 1)

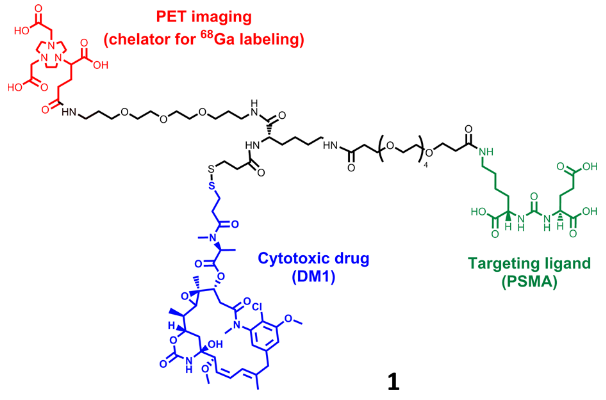

1

■ RESULTS AND DISCUSSION

Design and Synthesis of T-SMDC. The theranostic SMDC design was intended to address the inherent suboptimal in vivo kinetics of ADCs. Given the well-established role of varieties of PEGs in drug delivery,[20−23] we chose two short PEG chains anchored through amide conjugation to the carboxylic and ε-amino groups of a lysine center (Scheme 1) for the incorporation of a metal chelator, 1,4,7-triazacyclononane-1,4,7-triacetic acid (NOTA), and a PSMA-targeting moiety, Lys-Urea-Glu, respectively. The α-amino group of the lysine center was used for further conjugation with a cytotoxic chemotherapy drug, DM1, through a disulfide linkage for controlled release under the reductive conditions in tumor microenvironment.[24−26] Of note, the lysine centered PEG scaffold is versatile for the construction of other T-SMDC systems.

For proof-of-concept, herein we present a T-SMDC design targeting prostate cancer through PSMA, which is often found overexpressed in prostate cancer up to 1000-fold[27] and positively correlated with the aggressiveness of prostate cancer.[28] In addition, PSMA can form complexes with its specific ligands, which results in active internalization.[29] This feature can be leveraged for intracellular delivery of drugs to PSMA expressing prostate cancer cells. To date, many small organic molecules have been reported with low nanomolar or even subnanomolar binding affinities to PSMA.[15,30−34] In this work, we selected such a PSMA-targeting moiety containing the Lys-Urea-Glu motif, which has advanced to clinical trials of PSMA targeted PET imaging.[35−37]

Given that the circulation half-life of our designed T-SMDC in vivo is likely within hours,[6,11] the radioisotopes of choice can be either ^{18}F (97% β^+, $t_{1/2}$ = 110 min) or ^{68}Ga (90% β^+, $t_{1/2}$ = 68 min) for PET imaging. Although ^{18}F can serve the goal of our design, it requires a cyclotron onsite or in close proximity. Recently, ^{68}Ga has gained considerable attention in the field of PET mainly because it is a generator (^{68}Ge/^{68}Ga) produced radioisotope. With approximately one year of shelf life, ^{68}Ge/^{68}Ga generators have been in the market for decades to make ^{68}Ga readily available as needed. Furthermore, gallium also has a long-lived isotope (^{67}Ga: γ, $t_{1/2}$ = 3.26 days), which has been in nuclear medicine practice for gamma scintigraphy and recently single photon emission computed tomography (SPECT). With identical chemical properties to ^{68}Ga, ^{67}Ga can be used instead of ^{68}Ga for in vitro assay or SPECT imaging as necessary. To date, a variety of bifunctional chelators have been developed for gallium radiopharmaceuticals including a NOTA chelator scaffold featuring its neutral complex formation with Ga(III) without compromising its stability and with a purposely added functionality for further conjugation.[38] The chelator scaffold can form a stable complex as well with ^{64}Cu (17% β^+, $t_{1/2}$ = 12.7 h), another common radioisotope to enable PET. This further indicates the versatility of our T-SMDC design.

An effective T-SMDC requires a highly potent cytotoxic drug to potentially overcome the dose difference between diagnostics and therapeutics, which is the main challenge facing the development of theranostics. For our work, the injected amount of T-SMDC must be controlled to be sufficient to ensure the PSMA-targeted therapy but under the level that may saturate the targeted PSMA binding sites. Because of the existence of PSMA-mediated internalization, such an injection can be administered multiple times if necessary, in particular, to deliver a required dose for the targeted cancer cell kill. As such, one of the main determinants for a successful theranostics is the availability of a highly potent cytotoxic drug for the targeted disease. DM1, a cytotoxic maytansinoid that is too toxic to be used alone, is such a drug molecule for us to construct the first generation of our T-

Scheme 2. Synthesis Route to T-SMDC 1[a]

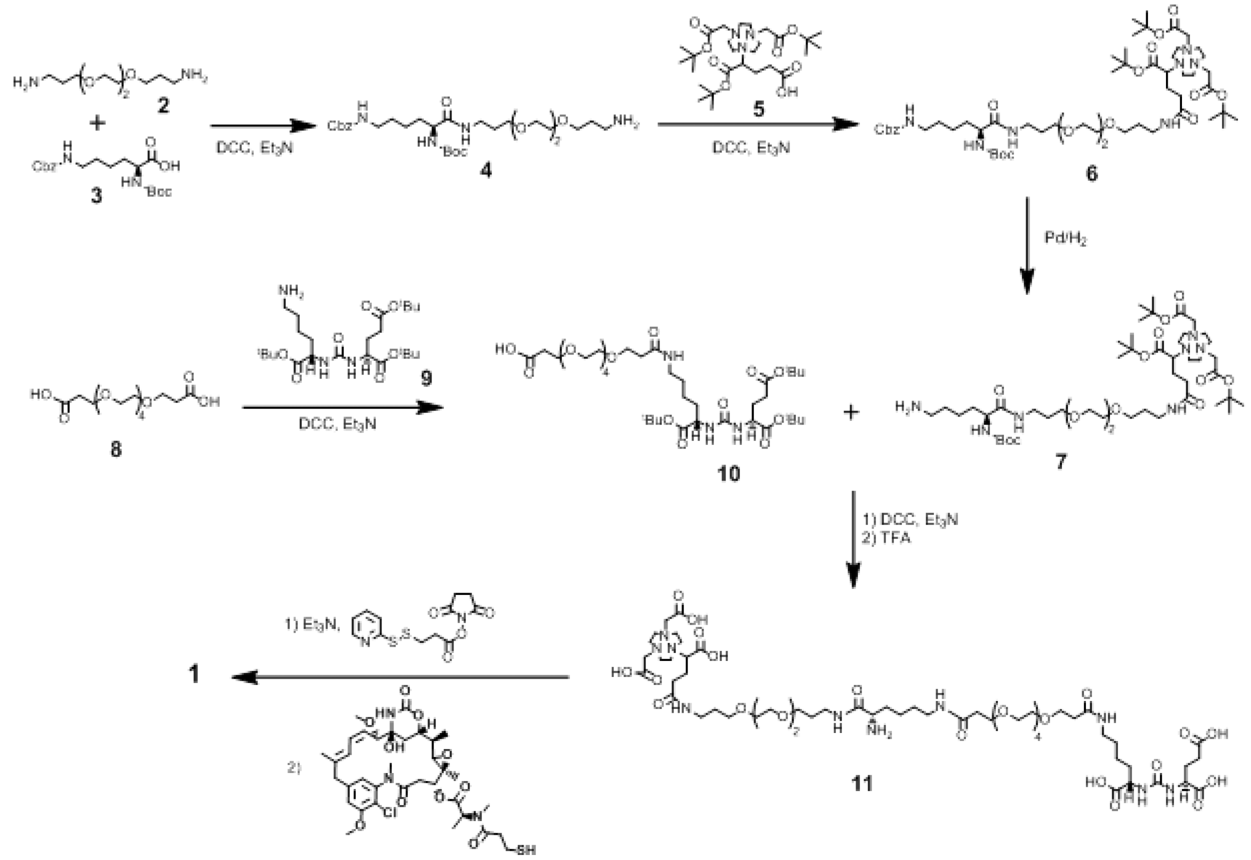

[a] Cbz: carboxybenzyl; DCC: *N,N′*-dicyclohexylcarbodiimide; TFA: trifluoroacetic acid; Boc: *tert*-butyloxycarbonyl.

SMDC. Indeed, DM1 has been used to construct ADCs for cancer treatment. For instance, trastuzumab emtansine, an ADC with DM1 conjugated to trastuzumab, was approved in 2013 by US-FDA for clinical treatment of advanced HER2 positive breast cancer.[6,11] In addition, DM1 possesses good aqueous stability and solubility, which is much needed for our T-SMDC design. For controlled release under reductive conductions within tumor microenvironment (e.g., glutathione, 1−10 mM), a disulfide linkage was introduced for DM1's anchorage at the α-amino position of the lysine center (Scheme 1).

To form a central frame, a PEG based diamino linker **2** was conjugated using carbodimide coupling to the carboxylic group of a lysine derivative **3**, in which the two amino groups were orthogonally protected (Scheme 2). The product **4** was obtained in 22% yield after purification. It was then reacted with **5**, a NOTA chelator synthesized according to our published procedure,[38] through its free side carboxy group to afford the fully protected **6** in 61% yield. The protecting group of ε-amine, carboxylbenzyl (Cbz), was removed from **6** via hydrogenation to give scaffold **7** in 91% yield for T-SMDC construction. Strategically the lysine center of **7** was chosen to provide two amino groups for the incorporation of the PSMA targeting moiety at ε-position and the DM1 molecule at the α-position. The presence of a free and one protected amine makes **7** a versatile and flexible scaffold for further T-SMDC construction.

In parallel, the tetraethylene glycol based linker **8** was attached to the ε-amine handle of a PSMA ligand containing Lys-Urea-Glu **9**,[39] using carbodiimde chemistry to give a carboxy terminated PSMA targeting ligand **10** in 25% yield. The long linker separating the PSMA targeting ligand from the rest part of T-SMDC was chosen for its reported capability of retaining the PSMA binding affinity.[30] The extended arm of ligand **10** carrying a carboxy group was coupled to the unprotected ε-amino of **7**. The resultant product was isolated and deprotected using trifluoroacetic acid to give **11** in 35% yield. Compound **11** had six carboxylic and one amino group at the α-position of the central lysine, which was intended for drug conjugation.

In order to build in a disulfide linkage between the DM1 drug molecule and **11**, a commercially available succinimidyl 3-(2-pyridyldithio)propionate (SPDP) linker was first reacted with the α-amine in **11** to give an activated disulfide bond, which was readily converted to the desired T-SMDC **1** (NO3A-DM1-Lys-Urea-Glu) upon reaction with the thiol terminated DM1 drug molecule in 51% yield. Because of the instability of disulfide and high cost of DM1, the drug was incorporated to the entire T-SMDC at the last step.

Radiolabeling and Serum Stability. NO3A-DM1-Lys-Urea-Glu (15 μg) was efficiently labeled by ^{68}Ga^{3+} (148−222 MBq) within 15 min in quantitative yield as monitored by radio-HPLC when the reaction was carried out in 4 M NaOAc buffer (pH 4−4.5) at 60 °C. At lower temperatures, 25 or 37 °C, the radiolabeling was incomplete within 15 min. For both in vitro and in vivo evaluations, the radiochemical purity of ^{68}Ga-NO3A-DM1-Lys-Urea-Glu was maintained at >95% as determined by radio-HPLC. The highest achievable specific activity was in the range of 50−80 GBq/μmol. Tested in human serum, ^{68}Ga-NO3A-DM1-Lys-Urea-Glu remained >98% intact out to 3 h.

In Vitro Cell Assays. To maintain the PSMA binding affinity of the Lys-Urea-Glu motif, a PEG-based spacer was introduced to separate the PSMA ligand from the rest part of T-SMDC. To verify the design, the PSMA binding affinity of T-SMDC **1** was measured by a competitive binding assay in LNCaP cells (PSMA positive) using an ^{125}I-labeled Lys-Urea-Glu analog (^{125}I-**12**, Figure 1) as the radioligand. Because the Lys-Urea-Glu analog has no available functional group for direct radioiodination, a Bolton-Hunter moiety was introduced. The specific activity of ^{125}I-**12** was over 74 GBq/μmol based on the HPLC measurement. The in vitro PSMA binding affinities of T-SMDC **1** were calculated by measuring the concentration of T-SMDC required to displace 50% of LNCaP cell bound ^{125}I-**12**. The free Lys-Urea-Glu ligand served as the positive control. T-SMDC **1** inhibits the binding of ^{125}I-**12** to LNCaP cells in a dose-dependent manner as shown in Figure 1. A slight decrease of PSMA binding affinity was observed for T-SMDC **1** (IC$_{50}$ (inhibitory concentration where 50% of the ^{125}I-**12** bound on LNCaP cells were displaced): 187 ± 41 nM) as compared to the unmodified Lys-Urea-Glu ligand (IC$_{50}$: 96 ± 16 nM) indicating the PSMA targeting property of T-SMDC **1** was not significantly compromised by our chemical modifications.

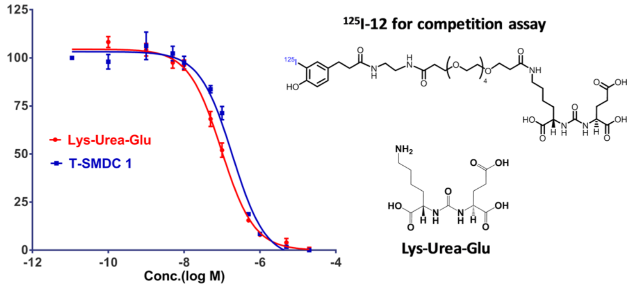

Figure 1. In vitro cell binding assay. The PSMA binding affinities of Lys-Urea-Glu and T-SMDC **1** were measured by a competitive cell-binding assay using PSMA positive LNCaP cell line and ^{125}I-**12** as the PSMA-specific radioligand. The IC$_{50}$ values of Lys-Urea-Glu and T-SMDC **1** were determined to be 96 ± 16 (coefficient of determination $R^2 = 0.99$) and 187 ± 41 nM ($R^2 = 0.98$), respectively.

The PSMA-mediated uptake and internalization of ^{68}Ga-NO3A-DM1-Lys-Urea-Glu were evaluated using LNCaP cells and PC-3 cells. The nonspecific uptake of ^{68}Ga-NO3A-DM1-Lys-Urea-Glu in LNCaP and PC-3 cells was assessed in the presence of the Lys-Urea-Glu ligand at 1 mM. The total cell uptake versus nonspecific uptake of ^{68}Ga-NO3A-DM1-Lys-Urea-Glu in LNCaP cells was significantly higher than in PC-3 cells (Figure 2A). When normalized to the cell numbers, the uptake in LNCaP cells becomes even higher than in PC-3 cells (Figure 2B). This observation indicates that the cell uptake of ^{68}Ga-NO3A-DM1-Lys-Urea-Glu is mediated by PSMA. As expected, ^{68}Ga-NO3A-DM1-Lys-Urea-Glu displayed an appreciable level of internalization in a time-dependent manner in the absence of Lys-Urea-Glu ligand (Figure 2C). This serves as the mechanism for intracellular delivery of T-SMDC for PSMA-targeted imaging and therapy.

Toxicity Determination. The cytotoxicity of NO3A-DM1-Lys-Urea-Glu was measured on three prostate cancer cell lines with different PSMA expression levels. The DM1 free drug was included in the assays as an internal positive standard to compare the toxicity of NO3A-DM1-Lys-Urea-Glu among the three cell lines. The normalized toxicity data in each cell line are shown in Figure 2D. The T-SMDC of NO3A-DM1-Lys-Urea-Glu presented the highest toxicity in LNCaP cells. The decreasing toxicity trend (LNCaP > C4-2 > PC-3) observed correlates with the PSMA expression levels in the cells (LNCaP > C4-2 > PC-3, Figure 2E). In comparison to the free DM1 drug, NO3A-DM1-Lys-Urea-Glu was less toxic in all three cell lines. The reduced toxicity of the T-SMDC is desirable to alleviate the acute side effects of the drug carried (DM1) to normal tissues when systematically administered.

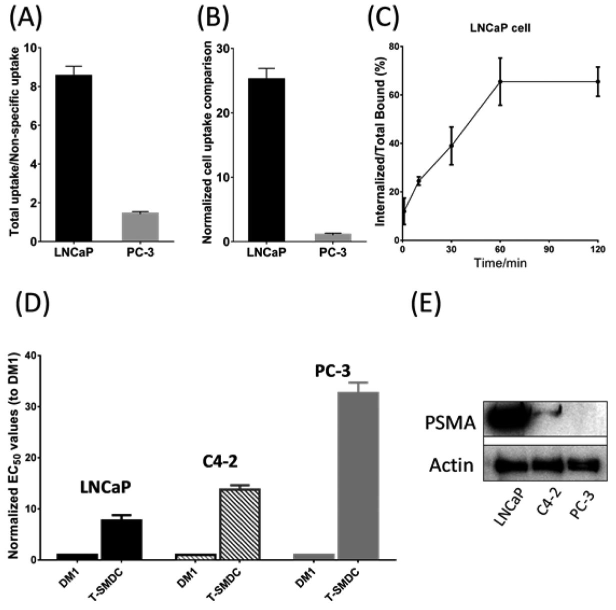

Figure 2. In vitro cell assays. (A) Total cell uptake versus nonspecific uptake of ^{68}Ga-NO3A-DM1-Lys-Urea-Glu in the absence and presence of Lys-Urea-Glu ligand (1 mM), respectively. (B) Normalized uptake of ^{68}Ga-NO3A-DM1-Lys-Urea-Glu in LNCaP and PC-3 cells; the uptake in PC-3 cells is set at 1.0. (C) Internalization of ^{68}Ga-NO3A-DM1-Lys-Urea-Glu in LNCaP cells. (D) Comparative EC$_{50}$ values of NO3A-DM1-Lys-Urea-Glu in LNCaP, C4-2, and PC-3 cells (the EC$_{50}$ of DM1 in each cell line is set at 1.0). The EC$_{50}$ value (half maximal effective concentration) was measured and averaged by three independent experiments. (E) Western blot assays of PSMA in LNCaP, C4-2, and PC-3 cells.

Small Animal PET/CT Imaging. Small animal PET/CT imaging studies were conducted in SCID mice bearing both PC3-PIP (PSMA positive, left shoulder) and PC3-Flu (PSMA negative, right shoulder) xenografts to evaluate the designed PSMA-specific imaging potential of ^{68}Ga-NO3A-DM1-Lys-Urea-Glu. The representative PET/CT images presented as the maximum intensity projection (MIP) are shown in Figure 3A. As expected, the PSMA positive PC3-PIP tumor (4.30 ± 0.20%ID/g) was clearly visualized at 1 h postinjection (p.i.), while the contrast of the PSMA negative PC3-Flu tumor was barely above the background. The quantitative analysis of the images demonstrated a significant uptake difference of ^{68}Ga-NO3A-DM1-Lys-Urea-Glu in PC3-PIP (4.30 ± 0.20%ID/g) and PC3-Flu (1.12 ± 0.42%ID/g) tumors ($p < 0.01$; $n = 3$), indicating the anticipated PSMA imaging specificity of ^{68}Ga-NO3A-DM1-Lys-Urea-Glu. At 1 h p.i., most radioactivity had been excreted into the urine from most of normal organs except for the kidneys. The observed high renal uptake (7.33 ± 2.25% ID/g) resulted from the well-recognized PSMA expression in

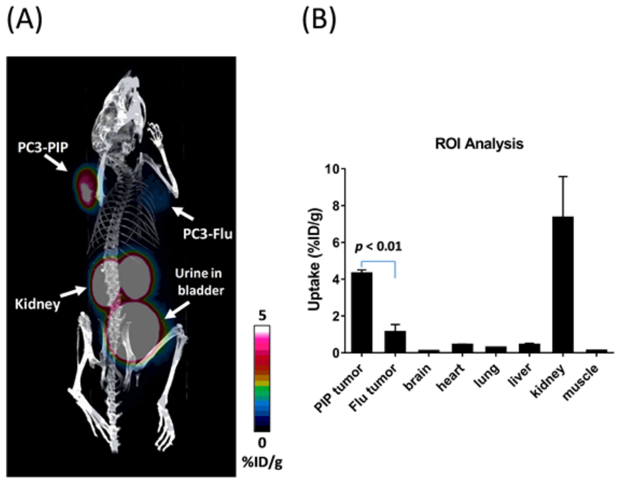

Figure 3. (A) Representative PET/CT image of ^{68}Ga-NO3A-DM1-Lys-Urea-Glu in SCID mice bearing PC3-PIP (PSMA positive, left shoulder) and PC3-Flu (PSMA negative, right shoulder) xenografts (n = 3). (B) Quantitative organ uptake (%ID/g) derived from the PET images. ROI: regions of interest.

rodent proximal renal tubules, which is not of concern in humans.[28,40] Liver, a major organ clearing the free DM1 drug, did not show a significant level of the radioactivity accumulation (0.42 ± 0.10%ID/g), indicating a desirable in vivo distribution profile of the T-SMDC for reduction of the systemic toxicity of DM1.

In summary, we have designed a targeted theranostic small-molecule drug conjugate (T-SMDC) system, and successfully synthesized a sample compound of T-SMDC, which consists of a PSMA-specific ligand, a PET imaging moiety, and a cytotoxic drug. The resulted T-SMDC retains the PSMA binding affinity and exhibits PSMA-dependent toxicity. When labeled with ^{68}Ga, the T-SMDC is capable of specific imaging PSMA-expressing cancer xenografts in mice. We recognize that the DM1 drug carried by the T-SMDC in the injected dose for PET imaging is low (ca. 0.1 nmol) to elicit the desired anticancer effects. In addition to taking advantage of the multivalent NOTA scaffold for multipresentation of DM1, we will consider three other approaches in our future work to realize the goal of the theranostic design concept for precision cancer patient care: (i) increase the injection dose to the level that specific PSMA binding allows; (ii) fractionate a therapeutic dose into multiple imaging doses. The PSMA-mediated internalization mechanism can be exploited for multiple administrations of an imaging dose until the desired DM1 dose is delivered, of which only one ^{68}Ga-NO3A-DM1-Lys-Urea-Glu dose is needed while others are its cold gallium counterpart to avoid unnecessary radiation exposure; (iii) have PET imaging with ^{68}Ga-NO3A-DM1-Lys-Urea-Glu only serve the companion purpose for precision chemotherapy of DM1 delivered by the T-SMDC formulated with cold Ga(III). It is noteworthy that the T-SMDC design is versatile in that it can be applied to other targeting systems for developing theranostics of the corresponding diseases.

■ MATERIALS AND METHODS

All chemicals, unless otherwise noted, were acquired from Sigma-Aldrich (St. Louis, MO) and used as received without further purification. All water used for buffer preparation was ultrapure (Milli-Q, Millipore, Billerica, MA) and passed through a 10 cm column of Chelex resin (Bio-Rad Laboratories, Hercules, CA) before use. NMR (Nuclear magnetic resonance) spectroscopy was performed on a Bruker 400 MHz NMR. HPLC was performed using a Waters HPLC equipped with a Waters Xterra Shield RP18 semiprep column (250 × 10 mm, 10 μm) and read by a Waters 2996 photodiode array detector and an in-line Shell Jr. 2000 radiodetector, using a gradient of 0:100 MeCN/H_2O (both with 0.1% TFA) to 100:0 MeCN/H_2O within 50 min. Bulk solvents were removed using rotary evaporator under reduced pressure at 40 °C. For accurate quantification of radioactivity, experimental samples were counted for 1 min on a calibrated PerkinElmer (Waltham, MA) Automatic Wizard2 Gamma Counter. The ^{68}Ge/^{68}Ga generator system was purchased from iThemba Laboratories (Somerset west, South Africa). Radiolabeled conjugates were purified by Light C-18 Sep-Pak cartridges (Waters, Milford, MA). Mass spectrum characterization was performed by LC-MS (Agilent 6540 Accurate-Mass Quadrupole Time-of-Flight LC/MS equipped with 1290 UPLC).

Compound 4. To a solution of the acid **3** (5.0 g, 13.1 mmol) in dry THF (10.0 mL) was added the solution of amine **2** (8.69 g, 39.4 mmol) dissolved in dry THF (10.0 mL). To the resulting mixture was added triethyl amine (1.59 g, 15.7 mmol) and *N,N'*-dicyclohexylcarbodiimide (3.25 g, 15.7 mmol). The resulting solution was stirred overnight at room temperature. The reaction mixture was then filtered and the solvent was removed under vacuum to afford a crude product. The crude product was purified by silica gel based flash chromatography to give colorless viscous oil **4** (1.68 g, 2.89 mmol, 22%). ^{1}H NMR (300 MHz, $CHCl_3$): δ 1.36 (s, 9H, *t*-Bu's), 1.40−1.60 (m, 4H), 1.68 (m, 4H), 1.88 (m, 2H), 3.09 (m, 4H), 3.23 (m, 2H), 3.38−3.64 (m, 12H), 3.99 (m, 1H), 5.02 (s, 1H), 7.59 (m, 2H), 7.84 (m, 3H). ^{13}C NMR (75 MHz, $CHCl_3$): δ 22.5, 26.3, 28.1, 28.9, 31.9, 36.7, 39.5, 40.3, 49.6, 54.7, 66.2, 68.4, 69.5, 69.9, 79.6, 127.8, 128.3, 136.6, 155.9, 156.8, 173.3. MS (ESI) m/z calcd for $C_{29}H_{50}N_4O_8$: 582.3; found: 583.3 ($[M + H]^+$).

Compound 6. To a solution of the acid **5** (0.5 g, 0.92 mmol) in dry THF (5.0 mL) was added the solution of amine **4** (0.64 g, 1.11 mmol) dissolved in dry THF (5.0 mL). To the resulting mixture was added triethylamine (0.11 g, 1.11 mmol) and *N,N'*-dicyclohexylcarbodiimide (0.23 g, 1.11 mmol). The resulting solution was stirred overnight at room temperature. The reaction mixture was then filtered and the solvent was removed under vacuum to afford a crude product, which was purified by silica gel based flash chromatography to give colorless viscous oil **6** (0.62 g, 0.56 mmol, 61%). ^{1}H NMR (300 MHz, $CHCl_3$): δ 1.12−1.56 (m, 36H, *t*-Bu's), 1.62−2.41 (m, 10H), 2.55−3.36 (m, 20H), 3.36−3.72 (m, 12H), 3.74−4.19 (m, 6H), 4.72 (m, 1H), 5.01 (s, 2H), 7.23 (m, 2H), 7.58 (m, 2H). ^{13}C NMR (75 MHz, $CHCl_3$): δ 22.4, 25.5, 27.7, 27.8, 28.1, 28.9, 32.3, 36.7, 36.9, 40.2, 45.8, 49.5, 50.6, 54.5, 55.5, 63.3, 65.9, 66.8, 68.8, 69.7, 70.0, 79.2, 82.0, 127.5, 127.7, 128.2, 136.7, 155.7, 156.7, 171.4, 172.5. MS (ESI) m/z calcd for $C_{56}H_{97}N_7O_{15}$: 1107.7; found: 1108.7 ($[M + H]^+$).

Compound 7. Carboxylbenzyl protected compound **6** (0.62 g, 0.56 mmol) was dissolved in 5 mL of ethanol and the solution was degassed (N_2) for 5 min. To the above solution was added 10% Pd/C (10 mg). The suspension was shaken in a hydrogenator (Parr, Moline, Illionis) at room temperature for 16 h under a H_2 atmosphere (60 psi). The suspension was filtered through Celite and the solvent was evaporated under vacuum. The obtained crude oil was purified by column chromatography to provide viscous oil **7** (0.56 g, 0.51 mmol, 91%). ^{1}H NMR (300 MHz, $CHCl_3$): δ 1.07−1.49 (m, 36H, *t*-Bu's), 1.63 (m, 10H), 1.73−2.06 (m, 4H), 2.26 (m, 2H), 2.62−3.02 (m, 10H), 3.04−3.35 (m, 10H), 3.35−3.57 (m, 12H), 3.63−4.02 (m, 5H). ^{13}C NMR (75 MHz, $CHCl_3$): δ 22.1, 25.4, 26.5, 27.8, 28.1, 28.8, 32.3, 37.1, 39.4, 45.8, 49.6, 50.7, 54.4, 55.6, 63.2, 66.9, 69.4, 69.9, 79.5, 82.4, 160.3, 160.6, 171.1, 172.9. MS (ESI) *m*/*z* calcd for $C_{48}H_{91}N_7O_{13}$: 973.6; found: 974.6 ([M + H]$^+$).

Compound 8. **8** was synthesized per the published procedure.[41]

Compound 9. **9** was synthesized per the published procedure.[39]

Compound 10. To a solution of the acid **8** (10.15 g, 18.5 mmol) in dry THF (10.0 mL) was added the solution of amine **9** (3 g, 6.15 mmol) dissolved in dry THF (10.0 mL). To the resulting mixture was added triethylamine (1.24 g, 12.3 mmol) and *N,N*′-dicyclohexylcarbodiimide (1.77 g, 8.61 mmol). The resulting solution was stirred overnight at room temperature. The reaction mixture was then filtered and the solvent was removed under vacuum to afford a crude product, which was purified by silica based flash chromatography to give colorless viscous oil **10** (1.24 g, 1.53 mmol, 25%). ^{1}H NMR (300 MHz, $CHCl_3$): δ 1.0−1.30 (m, 27H, *t*-Bu's), 1.46−2.04 (m, 8H), 2.15−2.39 (m, 2H), 2.73−3.53 (m, 24H), 3.81−4.12 (m, 2H), 6.9−7.45 (bm, 3H, NHs), 10.16 (bs, 1H, COOH). ^{13}C NMR (75 MHz, $CHCl_3$): δ 22.2, 27.7, 31.3, 34.7, 36.2, 38.7, 45.9, 52.7, 53.4, 66.9, 70.0, 80.2, 81.1, 81.5, 157.7, 172.1, 172.3, 173.7. MS (ESI) *m*/*z* calcd for $C_{38}H_{69}N_3O_{15}$: 807.5; found: 808.5 ([M + H]$^+$).

Compound 11. To a solution of the acid **10** (0.49 g, 0.61 mmol) in dry THF (4.0 mL) was added the solution of amine **7** (0.56 g, 0.51 mmol) dissolved in dry THF (3.0 mL). To the resulting mixture was added triethylamine (0.06 g, 0.61 mmol) and *N,N*′-dicyclohexylcarbodiimide (0.13 g, 0.61 mmol). The resulting solution was stirred overnight at room temperature. The reaction mixture was then filtered and the solvent was removed under vacuum to afford a crude product, which was purified by silica gel based flash chromatography to give colorless viscous oil with six *tert*-butyl groups and one Boc group. (0.31 g, 0.18 mmol, 35%). ^{13}C NMR (75 MHz, $CHCl_3$): δ 22.2, 22.6, 24.6, 25.2, 25.6, 27.8, 28.1, 28.7, 30.2, 31.4, 31.8, 32.0, 32.9, 36.1, 37.5, 38.9, 45.8, 49.7, 50.6, 52.9, 53.4, 55.6, 56.5, 63.3, 66.9, 68.8, 69.1, 69.8, 69.9, 80.5, 81.4, 81.9, 82.5, 159.5, 159.9, 171.1, 172.2, 172.9, 173.1. MS (ESI) *m*/*z* calcd for $C_{86}H_{158}N_{10}O_{27}$: 1763.1; found: 1764.1 ([M + H]$^+$).

To the protected conjugate (0.31 g, 0.18 mmol) was added trifluoroacetic acid (5.0 mL). The resulting solution was stirred overnight at room temperature. The solvent was then removed under vacuum to afford a crude product which was purified over reversed-phase HPLC (5% Acetonitrile/95% H_2O to 50% Acetonitrile/50% H_2O over 30 min, all solvent contained 0.1% TFA), fractions containing the product were pooled and lyophilized to give colorless viscous oil **11** (0.31 g, 0.15 mmol, 81%). MS (ESI) *m*/*z* calcd for $C_{57}H_{102}N_{10}O_{25}$: 1326.7; found: 1327.7 ([M + H]$^+$).

Compound 1. To a solution of primary amine **11** (10 mg, 7.52 μmol) in dry DMF (1.0 mL) was added succinimidyl 3-(2-pyridyldithio)propionate (SPDP, Thermo Scientific Pierce, 3 mg, 9.61 μmol). To the resulting mixture was added triethylamine (1 mg, 9.9 μmol) and the resulting solution was stirred overnight at room temperature for 6 h. The solvent was then removed under vacuum to afford a crude product which was purified over reversed-phase HPLC (5% Acetonitrile/95% H_2O to 50% Acetonitrile/50% H_2O over 25 min, all solvent contained 0.1% TFA), fractions containing the product were pooled and lyophilized to give colorless viscous oil with activated disulfide bond. (6 mg, 3.84 μmol, 51%). MS (ESI) *m*/*z* calcd for $C_{65}H_{109}N_{11}O_{26}S_2$: 1523.7; found: 1524.7 ([M + H]$^+$).

Activated compound (5 mg, 3.3 μmol) and the thiol terminated DM1 drug (3 mg, 4.0 μmol) were dissolved in degassed MeOH (0.5 mL) and stirred for 6 h at room temperature. The reaction mixture was directly purified over reversed-phase HPLC (5% Acetonitrile/95% H_2O to 50% Acetonitrile/50% H_2O over 25 min, all solvent contained 0.1% TFA), fractions containing the product were pooled and lyophilized to give colorless viscous oil **1** (2 mg, 1.0 μmol, 31%). MS (ESI) *m*/*z* calcd for $C_{89}H_{140}ClN_{13}O_{33}S_2$: 2018.8; found: 2019.8 ([M + H]$^+$).

Compound 12. To a solution of the acid **10** (0.5 g, 0.62 mmol) in dry THF (4.0 mL) was added the solution of ethylenediamine (0.13 g, 0.62 mmol) dissolved in dry THF (4.0 mL). To the resulting mixture was added triethylamine (0.06 g, 0.61 mmol) and *N,N*′-dicyclohexylcarbodiimide (0.13 g, 0.61 mmol). The resulting solution was stirred overnight at room temperature. The reaction mixture was then filtered and the solvent removed under vacuum to afford a crude product. To this, was added trifluoroacetic acid (5.0 mL). The resulting solution was stirred overnight at room temperature. The solvent was then removed under vacuum to afford a crude product which was purified over reversed-phase HPLC (5% Acetonitrile/95% H_2O to 50% Acetonitrile/50% H_2O over 30 min, all solvent contained 0.1% TFA), fractions containing the product were pooled and lyophilized to give the intermediate compound. This intermediate compound was further reacted with *N*-sulfosuccinimidyl-3-(4-hydroxyphenyl)propionate to provide colorless viscous oil **12** (0.11 g, 0.13 mmol, 22%) after HPLC purification. MS (ESI) *m*/*z* calcd for $C_{37}H_{59}N_5O_{16}$: 829.4; found: 830.4 ([M + H]$^+$).

Cell Culture and Animal Model. LNCaP, PC-3, and C4-2 cell lines were obtained from the American Type Culture Collection (ATCC, Manassas, VA). The PC-3 cell line was cultured in T-media (Invitrogen Corporation, CA) supplemented with 5% fetal bovine serum (FBS) and 1% Penicillin/Streptomycin (PS). LNCaP cells were cultured in RPMI 1640 media (HyClone, Thermo Scientific, IL), with 2.05 mM L-glutamine supplemented with 10% FBS. C4-2 cell line was cultured in DMEM media (Invitrogen Corporation, CA) supplemented with 5% FBS. The PC3-PIP and PC3-Flu cell lines were kindly provided by Dr. Martin G. Pomper from John Hopkins University. The PC3-PIP and PC3-Flu cell lines were cultured in RPMI media with FBS (10%), penicillin/streptomycin, and 2 μg/mL of Puromycin. All cells were cultured at 37 °C in an atmosphere of 5% CO_2 and passaged at 75−90% confluency.

For animal model, PC3-PIP cell suspension was injected subcutaneously (2×10^6 cells in 100 μL Hank's Buffered Salt Solution) into the left shoulder, and PC3-Flu cell suspension (1.5×10^6 cells in 100 μL Hank's Buffered Salt Solution) was injected subcutaneously into the right shoulder on the same mouse. After injection, animals were monitored twice a week by general observations.

Radiochemistry. To a 1.5 mL vial containing 15 μg of NO3A-DM1-Lys-Urea-Glu conjugate in 90 μL of 4.0 M NaOAc solution, 148−222 MBq of $^{68}Ga^{3+}$ in 0.3 mL of 0.6 M HCl was added. The pH of the final reaction mixture was

4.0–4.5. The reaction mixture was incubated at 60 °C for 15 min. The radiolabeling yields were determined by radio-HPLC. The mobile phase was H_2O with 0.1% TFA (solvent A) and acetonitrile with 0.1% TFA (solvent B), and the gradient consisted of 20% B to 100% B in 0–20 min at 1.5 mL/min flow rate. ^{68}Ga-NO3A-DM1-Lys-Urea-Glu was eluted out at 9.8 min from the Agilent Eclipse Plus C18 column (3.5 μm, 100 × 4.6 mm).

Serum Stability Assay. The in vitro stability test was performed in rat serum. Briefly, ^{68}Ga-NO3A-DM1-Lys-Urea-Glu (2 MBq, 20 μL) was added into 400 μL of human serum and incubated at 37 °C for 1 and 3 h. A 100 μL of sample was taken out and filtered by a 0.2 μm filter. The resulting solution was analyzed by radio-HPLC.

Preparation of ^{125}I-12. A Pierce precoated iodination tube was wetted with 1 mL of Tris buffer (pH 7.5). To the prewetted tube was added 100 μL of Tris buffer, followed by 5 μL (37 MBq) of Na^{125}I (PerkinElmer). The iodide was activated for 6 min at r.t. and then added to compound **12** solution (0.5 μg in 0.025 mL H_2O). After 9 min reaction at r.t., the mixture was directly applied to semipreparative HPLC (0% Acetonitrile/100% H_2O to 100% Acetonitrile/0% H_2O over 50 min, all solvent contained 0.1% TFA). HPLC fractions of ^{125}I-**12** were collected between 20 and 21 min and then concentrated by a Sep-Pak Light C18 cartridge.

Competition Assay. The PSMA binding affinities of NO3A-DM1-Lys-Urea-Glu were determined by a competitive cell-binding assay using ^{125}I-**12** as the radioligand. The urea Lys-urea-Glu was included as a positive control. Suspended LNCaP cells in Tris-buffered saline (TBS) were seeded on multiwell DV plates (Millipore) with 5 × 10^4 cells per well, and then incubated with ^{125}I-**12** (33 000 cpm/well) in the presence of increasing concentrations (0–10 000 nM) of Lys-Urea-Glu ligand and NO3A-DM1-Lys-Urea-Glu at r.t. for 2 h ($n = 4$). The final volume in each well was maintained at 200 μL. At the end of incubation, unbound ^{125}I-**12** was removed by filtration followed by five-time rinses with cold TBS buffer. The filters were collected and their radioactivity was measured. The best-fit IC_{50} values of Lys-Urea-Glu ligand and NO3A-DM1-Lys-Urea-Glu were calculated by fitting the data with nonlinear regression using GraphPad Prism 6.0.

Cell Uptake Assay. Cell uptake experiments were performed in the PSMA positive LNCaP cell line and the PSMA negative PC-3 cell line. The 6-well plates were seeded with 5.0 × 10^5 cells and incubated overnight in a humidified incubator at 37 °C with 5% CO_2. Cells were rinsed with binding buffer (20 mM Tris, 150 mM NaCl, pH 7.4) and then incubated with 500 μL binding buffer containing ~6.0 × 10^5 CPM ^{68}Ga-NO3A-DM1-Lys-Urea-Glu at 37 °C for 1 h. To account for nonspecific binding cells from additional 6-well plates were incubated with 1 mM Lys-Urea-Glu ligand in addition to the ^{68}Ga-NO3A-DM1-Lys-Urea-Glu. After incubation, the cells were washed with cold binding buffer and then trypsinized. Trypsinized cells were placed in culture tubes and the radioactivity associated with the cells was counted in a 2480 automatic gamma counter (PerkinElmer). The amount of cells per well was measured using a TC10 automated cell counter (Bio-Rad).

Internalization Assay. Cell internalization experiment was performed in PSMA positive LNCaP cell line. The 12-well plates were seeded with 2.0 × 10^5 cells and incubated overnight in a humidified incubator at 37 °C with 5% CO_2. Cells were washed once with binding buffer (20 mM Tris, 150 mM NaCl, pH 7.4). Cells were then incubated with ~6.0 × 10^5 CPM ^{68}Ga-NO3A-DM1-Lys-Urea-Glu in 0.4 mL binding buffer for 1, 10, 30, 60, and 120 min. At the end of incubation cells were washed once with ice-cold binding buffer and then incubated twice for 5 min with 0.5 mL ice-cold low pH stripping buffer (150 mM NaCl, 50 mM glycine, pH 3.0) to remove surface bound ^{68}Ga-NO3A-DM1-Lys-Urea-Glu and the fractions combined and saved in a culture tube. Cells were then incubated with 0.5 mL 4 M NaOH at 37 °C for 15 min. NaOH solubilized cells that contained the internalized ^{68}Ga-NO3A-DM1-Lys-Urea-Glu were placed in separate culture tubes. Both surface bound and internalized radioactivity were counted in a 2480 automatic gamma counter (PerkinElmer). Internalized ^{68}Ga-NO3A-DM1-Lys-Urea-Glu was expressed as the percent of internalized activity to the total bound activity.

Toxicity Assay (Crystal Violet Method). C4-2, LNCaP, and PC-3 cell lines were regularly maintained in RPMI 1640 (Life Technologies) supplemented with 10% fetal bovine serum (FBS). For the growth curves, 4000 cells were seeded per well in 96-well plates. Twenty-four hours after seeding, the cells were treated with DM1 and NO3A-DM1-Lys-Urea-Glu respectively at a series of concentrations (0.3, 1, 3, 10, 30, 100, 300, 1000, and 3000 nM; $n = 6$ per concentration). After 36 h of treatment, cells were washed once by PBS, then fixed in 100 μL/well 1% glutaraldehyde (Sigma-Aldrich) for 15 min, then stained with 100 μL/well 0.5% crystal violet (Sigma-Aldrich) for 15 min and each well was gently washed with running water. Then crystal violet was dissolved in 100 μL/well Sorenson's solution and the relative cell number was determined by absorbance reading at 560 nm. This experiment was repeated three times in total.

Western Blot Assay. The cell lysates were harvested, and equivalent amounts of protein were separated on Bolt 4–12% Bis-tris Plus gel and transferred to nitrocellulose membranes. The membranes were blocked with 5% skim milk and then incubated with primary antibodies indicated overnight at 4 °C. The membranes were then incubated with horseradish peroxidase-conjugated secondary antibodies, and signals were collected by an enhanced chemiluminescent detection system (Pierce, Rockford, IL) with SuperSignal West Dura extended duration substrate kit (Thermo). The PSMA antibodies used in experiment were purchased from Abcam (cat: ab19071).

Small Animal PET/CT Imaging. Small animal PET/CT imaging was performed with a Siemens Inveon PET/CT Multimodality System in tumor-bearing SCID mice intravenously received ca. 3.7 MBq of ^{68}Ga-NO3A-DM1-Lys-Urea-Glu in 100 μL via the tail vein ($n = 3$). Prior to imaging, the mouse was sedated on the imaging bed under 2% isoflurane anesthesia for the duration of imaging. Immediately after the CT data acquisition that was performed at 80 kV and 500 μA with a focal spot of 58 μm, static PET scans were conducted at 1 h p.i. for 7.5 min. Both CT and PET images were reconstructed with manufacturer's software. Reconstructed CT and PET images were fused for quantitative data analysis; regions of interest (ROIs) were drawn as guided by CT and quantitatively expressed as percent injected dose per gram of tissue (%ID/g).

Statistical Analysis. Statistical analyses were performed using GraphPad Prism. A p value less than 0.05 (unpaired t test) was considered statistically significant. All results are presented as mean ± standard deviation.

AUTHOR INFORMATION

Corresponding Authors

*E-mail: guiyang.hao@utsouthwestern.edu.
*E-mail: Xiankai.Sun@UTSouthwestern.edu.

Author Contributions

The manuscript was written through contributions of all authors./All authors have given approval to the final version of the manuscript.

Notes

The authors declare no competing financial interest.

ACKNOWLEDGMENTS

This study was partially supported by a grant from the National Institutes of Health (R01 CA159144), a Synergistic Idea Award from the Department of Defense (W81XWH-12-1-0336), the Simmons Cancer Center Grant (NIH 5P30 CA 142543), and the Dr. Jack Krohmer Professorship Funds. The PC3-PIP and PC3-Flu cell lines were kindly provided by Dr. Martin G. Pomper at John Hopkins University.

REFERENCES

(1) Siegel, R. L., Miller, K. D., and Jemal, A. (2016) Cancer statistics, 2016. *Ca-Cancer J. Clin. 66*, 7−30.

(2) Tannock, I. F., de Wit, R., Berry, W. R., Horti, J., Pluzanska, A., Chi, K. N., Oudard, S., Theodore, C., James, N. D., Turesson, I., Rosenthal, M. A., Eisenberger, M. A., and Investigators, T. A. X. (2004) Docetaxel plus prednisone or mitoxantrone plus prednisone for advanced prostate cancer. *N. Engl. J. Med. 351*, 1502−12.

(3) Petrylak, D. P., Tangen, C. M., Hussain, M. H., Lara, P. N., Jr., Jones, J. A., Taplin, M. E., Burch, P. A., Berry, D., Moinpour, C., Kohli, M., Benson, M. C., Small, E. J., Raghavan, D., and Crawford, E. D. (2004) Docetaxel and estramustine compared with mitoxantrone and prednisone for advanced refractory prostate cancer. *N. Engl. J. Med. 351*, 1513−20.

(4) Schweizer, M. T., and Antonarakis, E. S. (2014) Chemotherapy and its evolving role in the management of advanced prostate cancer. *Asian J. Androl. 16*, 334−40.

(5) Cetnar, J. P., and Beer, T. M. (2014) Personalizing prostate cancer therapy: the way forward. *Drug Discovery Today 19*, 1483−1487.

(6) Chari, R. V., Miller, M. L., and Widdison, W. C. (2014) Antibody-drug conjugates: an emerging concept in cancer therapy. *Angew. Chem., Int. Ed. 53*, 3796−827.

(7) Zolot, R. S., Basu, S., and Million, R. P. (2013) Antibody-drug conjugates. *Nat. Rev. Drug Discovery 12*, 259−260.

(8) Krall, N., Scheuermann, J., and Neri, D. (2013) Small Targeted Cytotoxics: Current State and Promises from DNA-Encoded Chemical Libraries. *Angew. Chem., Int. Ed. 52*, 1384−1402.

(9) Dennis, M. S., Jin, H., Dugger, D., Yang, R., McFarland, L., Ogasawara, A., Williams, S., Cole, M. J., Ross, S., and Schwall, R. (2007) Imaging Tumors with an Albumin-Binding Fab, a Novel Tumor-Targeting Agent. *Cancer Res. 67*, 254−261.

(10) Carrasco-Triguero, M., Yi, J.-H., Dere, R., Qiu, Z. J., Lei, C., Li, Y., Mahood, C., Wang, B., Leipold, D., Poon, K. A., and Kaur, S. (2013) Immunogenicity assays for antibody−drug conjugates: case study with ado-trastuzumab emtansine. *Bioanalysis 5*, 1007−1023.

(11) Krall, N., Pretto, F., Decurtins, W., Bernardes, G. J. L., Supuran, C. T., and Neri, D. (2014) A Small-Molecule Drug Conjugate for the Treatment of Carbonic Anhydrase IX Expressing Tumors. *Angew. Chem., Int. Ed. 53*, 4231−4235.

(12) Borsi, L., Balza, E., Bestagno, M., Castellani, P., Carnemolla, B., Biro, A., Leprini, A., Sepulveda, J., Burrone, O., Neri, D., and Zardi, L. (2002) Selective targeting of tumoral vasculature: Comparison of different formats of an antibody (L19) to the ED-B domain of fibronectin. *Int. J. Cancer 102*, 75−85.

(13) Vlahov, I. R., and Leamon, C. P. (2012) Engineering Folate−Drug Conjugates to Target Cancer: From Chemistry to Clinic. *Bioconjugate Chem. 23*, 1357−1369.

(14) Furqan, M., Akinleye, A., Mukhi, N., Mittal, V., Chen, Y., and Liu, D. (2013) STAT inhibitors for cancer therapy. *J. Hematol. Oncol. 6*, 90.

(15) Kularatne, S. A., Wang, K., Santhapuram, H.-K. R., and Low, P. S. (2009) Prostate-Specific Membrane Antigen Targeted Imaging and Therapy of Prostate Cancer Using a PSMA Inhibitor as a Homing Ligand. *Mol. Pharmaceutics 6*, 780−789.

(16) Bhuniya, S., Maiti, S., Kim, E.-J., Lee, H., Sessler, J. L., Hong, K. S., and Kim, J. S. (2014) An Activatable Theranostic for Targeted Cancer Therapy and Imaging. *Angew. Chem., Int. Ed. 53*, 4469−4474.

(17) Wu, X., Sun, X., Guo, Z., Tang, J., Shen, Y., James, T. D., Tian, H., and Zhu, W. (2014) In Vivo and in Situ Tracking Cancer Chemotherapy by Highly Photostable NIR Fluorescent Theranostic Prodrug. *J. Am. Chem. Soc. 136*, 3579−3588.

(18) Wu, J. B., Lin, T. P., Gallagher, J. D., Kushal, S., Chung, L. W., Zhau, H. E., Olenyuk, B. Z., and Shih, J. C. (2015) Monoamine oxidase A inhibitor-near-infrared dye conjugate reduces prostate tumor growth. *J. Am. Chem. Soc. 137*, 2366−74.

(19) Santra, S., Kaittanis, C., Santiesteban, O. J., and Perez, J. M. (2011) Cell-Specific, Activatable, and Theranostic Prodrug for Dual-Targeted Cancer Imaging and Therapy. *J. Am. Chem. Soc. 133*, 16680−16688.

(20) Kumar, A., Zhang, S., Hao, G., Hassan, G., Ramezani, S., Sagiyama, K., Lo, S. T., Takahashi, M., Sherry, A. D., Oz, O. K., Kovacs, Z., and Sun, X. (2015) Molecular platform for design and synthesis of targeted dual-modality imaging probes. *Bioconjugate Chem. 26*, 549−58.

(21) Suk, J. S., Xu, Q., Kim, N., Hanes, J., and Ensign, L. M. (2016) PEGylation as a strategy for improving nanoparticle-based drug and gene delivery. *Adv. Drug Delivery Rev. 99*, 28−51.

(22) Turecek, P. L., Bossard, M. J., Schoetens, F., and Ivens, I. A. (2016) PEGylation of Biopharmaceuticals: A Review of Chemistry and Nonclinical Safety Information of Approved Drugs. *J. Pharm. Sci. 105*, 460−75.

(23) Molineux, G. (2003) Pegylation: engineering improved biopharmaceuticals for oncology. *Pharmacotherapy 23*, 3S−8S.

(24) Ostrakhovitch, E. A. (2011) Redox environment and its meaning for breast cancer cells fate. *Curr. Cancer Drug Targets 11*, 479−95.

(25) Lee, Y., Koo, H., Jin, G. W., Mo, H., Cho, M. Y., Park, J. Y., Choi, J. S., and Park, J. S. (2005) Poly(ethylene oxide sulfide): new poly(ethylene glycol) derivatives degradable in reductive conditions. *Biomacromolecules 6*, 24−6.

(26) Schluga, P., Hartinger, C. G., Egger, A., Reisner, E., Galanski, M., Jakupec, M. A., and Keppler, B. K. (2006) Redox behavior of tumor-inhibiting ruthenium(III) complexes and effects of physiological reductants on their binding to GMP. *Dalton Trans.*, 1796−802.

(27) Ghosh, A., and Heston, W. D. W. (2004) Tumor target prostate specific membrane antigen (PSMA) and its regulation in prostate cancer. *J. Cell. Biochem. 91*, 528−539.

(28) Silver, D. A., Pellicer, I., Fair, W. R., Heston, W. D., and Cordon-Cardo, C. (1997) Prostate-specific membrane antigen expression in normal and malignant human tissues. *Clin. Cancer Res. 3*, 81−5.

(29) Rajasekaran, S. A., Anilkumar, G., Oshima, E., Bowie, J. U., Liu, H., Heston, W., Bander, N. H., and Rajasekaran, A. K. (2003) A novel cytoplasmic tail MXXXL motif mediates the internalization of prostate-specific membrane antigen. *Mol. Biol. Cell 14*, 4835−45.

(30) Banerjee, S. R., Foss, C. A., Castanares, M., Mease, R. C., Byun, Y., Fox, J. J., Hilton, J., Lupold, S. E., Kozikowski, A. P., and Pomper, M. G. (2008) Synthesis and Evaluation of Technetium-99m- and Rhenium-Labeled Inhibitors of the Prostate-Specific Membrane Antigen (PSMA). *J. Med. Chem. 51*, 4504−4517.

(31) Banerjee, S. R., Pullambhatla, M., Byun, Y., Nimmagadda, S., Green, G., Fox, J. J., Horti, A., Mease, R. C., and Pomper, M. G. (2010) ^{68}Ga-Labeled Inhibitors of Prostate-Specific Membrane

Antigen (PSMA) for Imaging Prostate Cancer. *J. Med. Chem. 53*, 5333−5341.

(32) Hillier, S. M., Kern, A. M., Maresca, K. P., Marquis, J. C., Eckelman, W. C., Joyal, J. L., and Babich, J. W. (2011) ^{123}I-MIP-1072, a Small-Molecule Inhibitor of Prostate-Specific Membrane Antigen, Is Effective at Monitoring Tumor Response to Taxane Therapy. *J. Nucl. Med. 52*, 1087−1093.

(33) Nedrow-Byers, J. R., Jabbes, M., Jewett, C., Ganguly, T., He, H., Liu, T., Benny, P., Bryan, J. N., and Berkman, C. E. (2012) A phosphoramidate-based prostate-specific membrane antigen-targeted SPECT agent. *Prostate 72*, 904−912.

(34) Hao, G., Kumar, A., Dobin, T., Öz, O. K., Hsieh, J.-T., and Sun, X. (2013) A Multivalent Approach of Imaging Probe Design To Overcome an Endogenous Anion Binding Competition for Noninvasive Assessment of Prostate Specific Membrane Antigen. *Mol. Pharmaceutics 10*, 2975−2985.

(35) Barrett, J. A., Coleman, R. E., Goldsmith, S. J., Vallabhajosula, S., Petry, N. A., Cho, S., Armor, T., Stubbs, J. B., Maresca, K. P., Stabin, M. G., Joyal, J. L., Eckelman, W. C., and Babich, J. W. (2013) First-in-man evaluation of 2 high-affinity PSMA-avid small molecules for imaging prostate cancer. *J. Nucl. Med. 54*, 380−7.

(36) Zechmann, C. M., Afshar-Oromieh, A., Armor, T., Stubbs, J. B., Mier, W., Hadaschik, B., Joyal, J., Kopka, K., Debus, J., Babich, J. W., and Haberkorn, U. (2014) Radiation dosimetry and first therapy results with a ^{124}I/^{131}I-labeled small molecule (MIP-1095) targeting PSMA for prostate cancer therapy. *Eur. J. Nucl. Med. Mol. Imaging 41*, 1280−92.

(37) Rowe, S. P., Gage, K. L., Faraj, S. F., Macura, K. J., Cornish, T. C., Gonzalez-Roibon, N., Guner, G., Munari, E., Partin, A. W., Pavlovich, C. P., Han, M., Carter, H. B., Bivalacqua, T. J., Blackford, A., Holt, D., Dannals, R. F., Netto, G. J., Lodge, M. A., Mease, R. C., Pomper, M. G., and Cho, S. Y. (2015) ^{18}F-DCFBC PET/CT for PSMA-Based Detection and Characterization of Primary Prostate Cancer. *J. Nucl. Med. 56*, 1003−10.

(38) Singh, A. N., Liu, W., Hao, G., Kumar, A., Gupta, A., Öz, O. K., Hsieh, J.-T., and Sun, X. (2011) Multivalent Bifunctional Chelator Scaffolds for Gallium-68 Based Positron Emission Tomography Imaging Probe Design: Signal Amplification via Multivalency. *Bioconjugate Chem. 22*, 1650−1662.

(39) Banerjee, S. R., Pullambhatla, M., Foss, C. A., Nimmagadda, S., Ferdani, R., Anderson, C. J., Mease, R. C., and Pomper, M. G. (2014) ^{64}Cu-Labeled Inhibitors of Prostate-Specific Membrane Antigen for PET Imaging of Prostate Cancer. *J. Med. Chem. 57*, 2657−2669.

(40) Kinoshita, Y., Kuratsukuri, K., Landas, S., Imaida, K., Rovito, P. M., Jr., Wang, C. Y., and Haas, G. P. (2006) Expression of prostate-specific membrane antigen in normal and malignant human tissues. *World J. Surg. 30*, 628−36.

(41) Kumar, A., Hao, G., Liu, L., Ramezani, S., Hsieh, J.-T., Öz, O. K., and Sun, X. (2015) Click-Chemistry Strategy for Labeling Antibodies with Copper-64 via a Cross-Bridged Tetraazamacrocyclic Chelator Scaffold. *Bioconjugate Chem. 26*, 782−789.

DOI: 10.1021/acs.bioconjchem.6b00222
Bioconjugate Chem. 2016, 27, 1681−1689